

**The Origin and Structure of Trailing Vortices
in Aerodynamics**

Final Report

By

A.T. Conlisk, P. I.

and

N. M. Komerath, Co-PI¹

Department of Mechanical Engineering
The Ohio State University
Columbus, Ohio 43210-1107

The U. S. Army Research Office

Contract AG55-97-I-0264

July 2001

Approved for Public Release;

Distribution Unlimited.

¹ School of Aerospace Engineering, Georgia Institute of Technology, Atlanta, Georgia, 30332.

20010725 030

REPORT DOCUMENTATION PAGE

Form Approved
OMB NO. 0704-0188

Public reporting burden for this collection of information is estimated to average 1 hour per response, including the time for reviewing instructions, searching existing data sources, gathering and maintaining the data needed, and completing and reviewing the collection of information. Send comment regarding this burden estimate or any other aspect of this collection of information, including suggestions for reducing this burden, to Washington Headquarters Services, Directorate for Information Operations and Reports, 1215 Jefferson Davis Highway, Suite 1204, Arlington, VA 22202-4302, and to the Office of Management and Budget, Paperwork Reduction Project (0704-0188), Washington, DC 20503.

1. AGENCY USE ONLY (Leave blank)		2. REPORT DATE July 6, 2001		3. REPORT TYPE AND DATES COVERED Final 5/01/97-4/30/01 31 Mar 01	
4. TITLE AND SUBTITLE The Origin and Structure of Trailing Vortices in Aerodynamics				5. FUNDING NUMBERS G DAA655-97-1-0264	
6. AUTHOR(S) A.T. Conlisk and N.M. Komerath					
7. PERFORMING ORGANIZATION NAMES(S) AND ADDRESS(ES) The Ohio State University Research Foundation 1960 Kenny Rd. Columbus, OH 43210				8. PERFORMING ORGANIZATION REPORT NUMBER 733920	
9. SPONSORING / MONITORING AGENCY NAME(S) AND ADDRESS(ES) U.S. Army Research Office P.O. Box 12211 Research Triangle Park, NC 27709-2211				10. SPONSORING / MONITORING AGENCY REPORT NUMBER 36435.2-EG	
11. SUPPLEMENTARY NOTES The views, opinions and/or findings contained in this report are those of the author(s) and should not be construed as an official Department of the Army position, policy or decision, unless so designated by other documentation.					
12a. DISTRIBUTION / AVAILABILITY STATEMENT Approved for public release; distribution unlimited.				12 b. DISTRIBUTION CODE	
13. ABSTRACT (Maximum 200 words) The helicopter rotor wake is among the most complex flow-fields in aerodynamics. Despite the fact that a large amount of computational and experimental work on the rotor wake has been published, little of a quantitative nature is known about the origin of the main component of the rotor wake, the tip-vortex, as a function of the rotor speed, rotor blade geometry, and angle of attack. The primary objective of this work is to predict the formation of the rotor tip vortex as a function of physical parameters such as angle of attack, rotor speed, and blade aspect ratio. While the rotor-blade tip-vortex is of primary interest, the techniques developed are applicable to fixed wings as well.					
14. SUBJECT TERMS Helicopter Aerodynamics, tip - vortex				15. NUMBER OF PAGES 231	
				16. PRICE CODE	
17. SECURITY CLASSIFICATION OF REPORT UNCLASSIFIED	18. SECURITY CLASSIFICATION OF THIS PAGE UNCLASSIFIED	19. SECURITY CLASSIFICATION OF ABSTRACT UNCLASSIFIED	20. LIMITATION OF ABSTRACT UL		

The views, opinions, and/or findings contained in this report are those of the author(s) and should not be construed as an official Department of the Army position, policy, or decision, unless so designated by other documentation.

Contents

1	Introduction	1
1.1	Background	1
1.2	The Fixed Wing Wake	2
1.3	The Rotor Wake	6
1.3.1	The Helicopter	6
1.3.2	Helicopter Aerodynamics	6
1.3.3	The Rotor Wake	7
1.3.4	Wake Models	14
1.3.5	Current Work	16
2	Panel Methods	21
2.1	Background	21
2.2	Two-Dimensional Airfoil Aerodynamics	21
2.3	Three-Dimensional Wing Solutions	30
3	Asymptotics of Lifting Line and Lifting Surface Theory for a Fixed Wing	37
3.1	Introduction	37
3.2	Theoretical Considerations	38
3.3	The Lifting-Line Integral Equation For the Semi-infinite Fixed Wing	39
3.4	Lifting Surface Theory For the Semi-Infinite Fixed Wing . . .	42
3.4.1	Panel Representation of the Semi-Infinite Wing	43
3.4.2	Results for a Rectangular Wing	52
3.4.3	Comparison with Experiment	63
3.5	Summary	74

4	Asymptotics of Lifting-Line and Lifting-Surface Theory for a Rotary Wing without Rotor-Wake Contraction	75
4.1	Introduction	75
4.2	Rotor Aerodynamics: Downwash and Vorticity in the Cylindrical Slipstream of a Hovering Rotor	76
4.3	The Solution for a Rotary Wing Near the Rotor Tip	79
4.3.1	The Inner Solution For the Lifting-Line Integral Equation	79
4.3.2	The Lifting Surface	84
4.3.3	The Formation of the Rotor Tip-vortex	86
4.4	The Uniformly-Valid Solution for the Bound Circulation for the Rotary Wing	103
4.5	Summary	109
5	Rotor-Wake Contraction Effects on the Formation of the Tip-Vortex	110
5.1	Introduction	110
5.2	The Vortex-Cylinder Model	111
5.3	The Discrete Vortex-Ring Model	118
5.3.1	Numerical Scheme	118
5.3.2	Results for the Discrete Vortex-Ring Model	121
5.4	Summary	121
6	The Boundary Layer on the Blade	126
6.1	Introduction	126
6.2	The inviscid flow	127
6.3	The Boundary-Layer Equations	127
6.4	Grid Distribution and Numerical Solution	129
6.5	Results	130
6.6	Summary	130
7	Experiments	131
7.1	Introduction	131
7.1.1	Measurement Issues - Blade Proximity	137
7.2	Experimental Setup	138
7.2.1	Rotor Interference	139
7.2.2	Measurement Grids	139
7.3	Vortex Formation	145
7.3.1	Overall Velocity Field	145

7.3.2	Evolution of the circumferential velocity	146
7.3.3	Circulation and Core Size	153
7.3.4	Axial Velocity	156
7.3.5	Vortex Location During Formation	159
7.3.6	Observations on the Vortex Formation Process	159
7.3.7	Blade Tip Location	160
7.4	Evolution to the Near Wake	161
7.4.1	Evolution of Core Axial Velocity	161
7.4.2	Evolution of Circumferential Velocity	162
7.4.3	Vortex Size	168
7.4.4	Wake Boundaries	168
7.4.5	Tip Vortex Turbulence	168
7.5	Seed Particle Dynamics	172
7.5.1	Formulation of the Seed Particle Dynamics Problem	172
7.5.2	Predicted Difference Between Seed Particle and Fluid Velocity	174
7.5.3	Error in Radial Growth of Vortex Core	176
7.5.4	Velocity Error	178
7.5.5	Particle Number Density	178
7.5.6	Accuracy of the Simulation	180
7.6	Density Variations in the Vortex Core	183
7.6.1	Analytical Model	183
7.6.2	Vortex Density Distribution	188
7.6.3	Relation Between Vortex Density and Light Intensity	192
7.6.4	Observations	194
7.7	Web-based Tip Vortex Database	196
7.7.1	Correlation of Circulation Measurements from Several Rotary Wing Experiments	200
7.8	Summary	204
8	Summary and Future Work	205
8.1	Summary	205
8.2	Future Work	210
A	Papers, Presentations, and Degrees Awarded	211

B	Lifting-line Theory for a Multi-bladed Rotor in Hover for the Untwisted Rectangular Blade	214
B.1	Derivation of the Integral Equation	215
B.2	Solution of the Integral Equation	217
C	The Velocity Induced by a Rotor Wake Modelled as a Dis- crete Distribution of Vortex Rings	219
C.1	The Elementary Vortex Ring	219
C.2	The Strength and Location of the Trailing Vortices	221
C.3	The Asymptotic Slipstream	222

List of Figures

1.1	Vortex wake of a fixed wing as photographed by Head [1982]. .	3
1.2	A summary of specific flow problems involving helicopter aerodynamics. From Caradonna [1992].	8
1.3	Rotor disk, showing definition of ψ and r . ψ is indicative of vortex age, while ϕ (not shown) is the rotor azimuthal angle. $\psi = \phi$ for the first revolution. From Johnson [1980].	9
1.4	Sketch of the trailing vorticity γ_t and the shed vorticity γ_s . . .	10
1.5	Sketch of typical radial distribution of the blade lift L , bound circulation Γ and trailing vorticity γ_t . From Johnson [1980]. .	11
1.6	Sketch of a helicopter rotor wake for a single blade. From Gray [1956].	12
1.7	Definition of the inner and outer problems for the calculation of the flow past a two-bladed rotor.	17
1.8	Sketch of the bound circulation for a semi-infinite fixed wing; in the region where the bound circulation varies, the individual vortex filaments would be expected to wind around each other to form the tip-vortex.	18
1.9	Qualitative sketch of the bound circulation for a rectangular, untwisted rotary wing. In the tip region where the bound circulation drops to zero at the tip quickly, the individual vortex filaments would be expected to wind around each other to form the strong single tip-vortex. In the inboard portion of the blade, the bound circulation drops off gradually to zero at the root and hence there is an inboard sheet with the opposite sign to the tip-vortex.	19
2.1	Potential flow over a two-dimensional airfoil.	22

2.2	Implementation of the two dimensional Kutta condition on an airfoil when using surface vortex distribution. The vorticity at the trailing edge $\gamma_{T.E.}$ which is the sum of the corresponding upper and lower surface vorticities γ_U and γ_L must vanish. Also the shed vorticity γ_W is aligned with the local flow direction.	23
2.3	Continuous vortex distribution on a zero thickness, symmetric airfoil. Note y axis is normal to x-z plane and outward.	24
2.4	Plot of the transformation $x = \frac{c}{2}(1 - \cos\theta)$.	25
2.5	Nondimensional vorticity distribution on a flat, zero thickness, symmetric airfoil at an angle of attack α_0 . The two dimensional Kutta condition is satisfied at the trailing edge of the airfoil $\gamma(c) = 0$.	26
2.6	The "lumped-vortex" element structure.	28
2.7	Point vortex representation of the thin, lifting airfoil.	29
2.8	Approximation of the wing surface by panel elements.	32
2.9	Influence of panel j on collocation point P_k .	33
2.10	A vortex ring element.	33
2.11	Vortex ring model.	35
2.12	Horseshoe vortex model.	36
3.1	(a) Cartesian coordinate system relative to a fixed wing. (b) For large aspect ratio A, the wing appears as if it were a line in the outer region; i.e. the lifting line.	41
3.2	Horseshoe-vortex panel implementation of a semi-infinite wing. (a) Definition of the global coordinates. Only three chordwise panels are shown here. In the numerical calculation, ten chordwise panels are used. (b) Definition of the local panel coordinates. The solid box represents a surface panel which is replaced by a horseshoe vortex (represented by dash lines).	44
3.3	The velocity at P induced by a three-dimensional vortex using the Biot-Savart law.	45
3.4	Velocity induced by a straight vortex segment.	46
3.5	Velocity induced by a horseshoe-vortex segment. (a) shows the swirl velocity and (b) shows the x and z components of the swirl velocity.	47

3.6	The trailing vortex system emanates from the quarter-chord line of each panel (hollow circles), extending through the trailing edge of the wing to infinity downstream. Arrows denote the direction of the normal velocity at the panel three-quarter chord line. Solid circles denote panel edges.	51
3.7	Comparison of the computational results for different number of panels used in the lifting surface code. Here '*' represents the computational results with one chordwise and twenty spanwise panels, the box represents the computational results with four chordwise and twenty spanwise panels, 'o' represents the computational results with ten chordwise and twenty spanwise panels and '+' represents the computational results with twenty chordwise and forty spanwise panels. The angle of attack is 12°	53
3.8	Circulation distribution for a semi-infinite rectangular wing. The solid line is the analytical solution of Stewartson [1960] for the lifting line. The circle is the computational results from the lifting-surface code with ten chordwise and twenty spanwise panels. The angle of attack is 12°	54
3.9	Level curves of the circulation for each panel. The angle of attack is 12°	55
3.10	Section view of the roll-up process of trailing vortices for the fixed semi-infinite wing. The core radius converges at $x = 3.25$ after 350 iterations. A single chordwise panel is used. The angle of attack is 12° . (a) X-Y plot. (b) X-Z plot.	58
3.11	Three-dimensional view of the roll-over process of the trailing vortices. The angle of attack is 12° . A single chordwise panel is used.	59
3.12	The definition of the circulation of the tip-vortex.	60
3.13	The circulation of the tip-vortex at different x . The maximum bound circulation is 0.651 and the angle of attack is 12° . Here '*' represents the result for a single chordwise panel and 'o' represents the result for four chordwise panels.	61
3.14	The core radius of the tip-vortex \bar{r} measured from the centroid at different downstream location up to $x = 3.2$. A single chordwise panel is used.	62

3.15	Section view of the roll-up process of trailing vortices for the fixed semi-infinite wing. (a) X-Y plot. (b) X-Z plot. Four chordwise panels and twenty spanwise panels are used. The angle of attack is 12°	64
3.16	3-D view of the rolling-over process for a semi-infinite wing at angle of attack 12° . Four chordwise and twenty spanwise panels are used.	65
3.17	Section view of the roll-up process of trailing vortices for the fixed semi-infinite wing. The core radius converges at $x = 3.25$ after 309 iterations. A single chordwise panel is used. The angle of attack is 8° . (a) X-Y plot. (b) X-Z plot.	66
3.18	3-D view of the roll-over process of the trailing vortices. The angle of attack is 8° . A single chordwise panel is used.	67
3.19	The circulation of the tip-vortex at different x . The maximum bound circulation is 0.436 and the angle of attack is 8° . A single chordwise panel is used.	68
3.20	The comparison of the bound circulation for wings at different angles of attack.	69
3.21	The comparison of the experimental data of McAlister and Takahashi [1991] and computations for the bound circulation. Here '*' represents the experimental data and solid line represents the computational results from the horseshoe panel model where ten chordwise and twenty spanwise panels are used. The angle of attack is 12°	70
3.22	The vertical velocity at $x = 1.1$ chord behind the trailing edge of different fixed wings from the data of McAlister and Takahashi [1991]. Here the '+' represents wing 1, the 'o' represents wing 2, '*' represents wing 3 and 'x' represents wing 4. The vertical velocity is plotted at $z = 0$; the z -coordinate measures distance normal to the $X - Y$ plane of Figure 3.2. $Y = 0$ is the wing tip and $Y > 0$ is inboard. The parameters of wings are shown in Table 3.1.	71
3.23	The vertical velocity at $x = 1.1$ chord behind the trailing edge of the wing compared with the experimental data of McAlister and Takahashi [1991], at $z = 0$ for $Re = 1.44 \times 10^6$ (wing 2). Here '*' represents the experimental data and solid line represents the computational data. $Y = 0$ is the wing tip and $Y > 0$ is inboard. A single chordwise panel is used.	72

3.24	The vertical velocity at $x = 3.0$ chord behind the trailing edge of the wing compared with the experimental data of McAlister and Takahashi[1991], at $z = 0$ for $Re = 1.44 \times 10^6$ (wing 2). Here '*' represents the experimental data and solid line represents the computational data. $Y = 0$ is the wing tip and $Y > 0$ is inboard. A single chordwise panel is used.	73
4.1	Vortex cylinder coordinate system.	77
4.2	Induced downwash in the plane of the rotor as a function of the parameter $\lambda = \frac{\alpha_0 a}{nc}$	80
4.3	Circulation distribution for a single-bladed rotor in hover as a function of the parameter $\lambda = \frac{\alpha_0 a}{nc}$	81
4.4	Leading order solution for the bound circulation on a rotary wing as a function of $\lambda = \frac{\alpha_0 a}{nc}$	85
4.5	Comparison of the computational results with different number of panels in the lifting surface code. Here 'o' represents the computational results with ten chordwise and twenty spanwise panels and '+' represents the computational results with twenty chordwise and forty spanwise panels.	87
4.6	Comparison of the inner solution for the bound circulation for a rotary wing between the lifting surface code and the modified Stewartson's equation (4.18). The solid line is the analytical solution of the modified Stewartson's equation. The circles are the computational results from the lifting surface code with ten chordwise and twenty spanwise panels.	88
4.7	The comparison of inner solutions of the bound circulation for the rotor given in Table 4.1 with the rotor at $\alpha_0 = 12^\circ$ and other parameters unchanged.	90
4.8	Section view of the roll-up process of trailing vortices for the rotor. The core radius converges at $x = 3.25$ after 110 iterations. A single chordwise panel is used. The angle of attack is 8°	92
4.9	Section view of the roll-up process of trailing vortices for the rotor. The core radius converges at $x = 30.0$ after 252 iterations. A single chordwise panel is used. The angle of attack is 8°	93

4.10	3-D view of the roll-over process of the trailing vortices. The angle of attack is 8° and the core radius is converged until $x = 30.0$. A single chordwise panel is used.	94
4.11	The comparison of the circulation of the tip-vortex for convergence achieved at different x . The maximum bound circulation is 0.153 and the angle of attack is 8° . A single chordwise panel is used.	95
4.12	Comparison of the core radius of the tip-vortex \bar{r} measured from the centroid at different downstream location up to $x = 3.25$ and $x = 30.0$. A single chordwise panel is used.	96
4.13	Section view of the roll-up process of trailing vortices for the fixed semi-infinite wing. The core radius converges at $x = 3.25$ after 121 iterations. A single chordwise panel is used. The angle of attack is 12°	98
4.14	3-D view of the roll-over process of the trailing vortices. The angle of attack is 12° . A single chordwise panel is used.	99
4.15	The circulation of the tip-vortex at different x . The maximum bound circulation is 0.274 and the angle of attack is 12° . '*' represents the result for a single chordwise panel and 'o' represents the result for four chordwise panels.	100
4.16	Section view of the roll-up process of trailing vortices for a rotary wing. (a) X-Y plot. (b) X-Z plot. Four chordwise panels and twenty spanwise panels are used. The angle of attack is 12°	101
4.17	3-D view of the roll-over process of the trailing vortices. The angle of attack is 12° . A single chordwise panel is used.	102
4.18	The vertical velocity at $x = 1.5$ chord behind the trailing edge of the rotor compared with the experimental data at $z = 0$. Here '*' represents the experimental data and solid line represents the computational data. $Y = 0$ is the rotor tip and $Y > 0$ is inboard. A single chordwise panel is used.	104
4.19	The vertical velocity at $x = 4.0$ chord behind the trailing edge of the rotor compared with the experimental data at $z = 0$. Here '*' represents the experimental data and solid line represents the computational data. $Y = 0$ is the rotor tip and $Y > 0$ is inboard. A single chordwise panel is used.	105

4.20	The comparison of inner solutions for the bound circulation for two-bladed rotors with different aspect ratios. The angle of attack is 8°	106
4.21	The comparison of the induced vertical velocity at $x = 1.5c$ behind different aspect ration wings.	107
4.22	The uniformly-valid solutions without wake contraction for different λ . $\alpha_0 = 8^\circ$	108
5.1	The vortex cylinder model for the rotor wake contraction at a single downstream location.	112
5.2	The comparison of the uniformly-valid solutions without wake contraction with the solutions with wake contraction for different λ . The dotted lines represent the solutions without wake contraction and the solid lines represent the solutions with wake contraction. $\alpha_0 = 8^\circ$	116
5.3	The comparison of the computational solutions with the experimental data of Caradonna and Tung [1981] for several values of angle of attack. The solid lines represent the numerical solutions with wake contraction, the dotted lines represent the numerical solutions without wake contraction, '+' represents the experimental data for $\alpha_0 = 12^\circ$, 'o' represents the experimental data for $\alpha_0 = 8^\circ$ and '*' represents the experimental data for $\alpha_0 = 5^\circ$	117
5.4	The discrete vortex ring model. The dashed lines represent the vortex rings on the m^{th} elemental surface. After the last vortex ring K, the mth elemental surface has been represented by a semi-infinite vortex cylinder with uniformly distributed vorticity. After a revolution time $\frac{2\pi\Omega}{n}$, vortex ring k convects with the local induced velocity to vortex ring k+1.	119
5.5	Vortex ring representation of the rotor wake (axial view). M spanwise elemental slipstream surfaces.	120

5.6	Comparison of the induced downwash in the plane of the rotor (outer solution). The solid line represents the Burggraf's theoretical solution, the dotted line represents the result for the vortex-cylinder model, '*' represents the result for $M = 4$ and $\mu = 0.16$, 'o' represents the result for $M = 4$ and $\mu = 0.28$, '◊' represents the result for $M = 4$ and $\mu = 0.35$, the right pointing triangle represents the result for $M = 8$ and $\mu = 0.28$ and the box represents the result for $M = 8$ and $\mu = 0.35$. M is the number of the elemental surfaces and μ is the cut-off parameter used in the numerical calculation.	122
5.7	Comparison of the bound circulation(outer solution). The solid line represents the Burggraf's theoretical solution, the dotted line represents the result for the vortex-cylinder model, '*' represents the result for $M = 4$ and $\mu = 0.16$, 'o' represents the result for $M = 4$ and $\mu = 0.28$, '◊' represents the result for $M = 4$ and $\mu = 0.35$, the right pointing triangle represents the result for $M = 8$ and $\mu = 0.28$ and the box represents the result for $M = 8$ and $\mu = 0.35$. M is the number of the elemental surfaces and μ is the cut-off parameter used in the numerical calculation.	123
5.8	Comparison of the slipstream. The solid line represents Burggraf's first-order approximation, dotted line represents the result of Landgrebe's [1972] formula (5.2) where $A = 0.78$, $C_T = 0.0001$ and $\lambda_l = 0.04$. Here '*' represents the result for the vortex ring model with $M = 4$ and $\mu = 0.35$	124
7.1	Beam blockage by blade.	140
7.2	Vortex origins measurement grid.	141
7.3	Near wake measurement grid on both sides of the rotor.	142
7.4	Near wake measurement grid, front and rear.	143
7.5	Blade tip flow field, approximate blade position shown, $x/c = 0.8$. Here x measures distance from the leading edge of the blade.	144
7.6	Circumferential velocity profile. Horizontal cut (left), Vertical cut (right), $x/c = 0.47$	146
7.7	Circumferential velocity profile. Horizontal cut (left), Vertical cut (right), $x/c = 0.51$	147

7.8	Circumferential velocity profile. Horizontal cut (left), Vertical cut (right), $x/c = 0.55$.	147
7.9	Circumferential velocity profile. Horizontal cut (left), Vertical cut (right), $x/c = 0.59$.	148
7.10	Circumferential velocity profile. Horizontal cut (left), Vertical cut (right), $x/c = 0.63$.	148
7.11	Circumferential velocity profile. Horizontal cut (left), Vertical cut (right), $x/c = 0.68$.	149
7.12	Circumferential velocity profile. Horizontal cut (left), Vertical cut (right), $x/c = 0.72$.	149
7.13	Circumferential velocity profile. Horizontal cut (left), Vertical cut (right), $x/c = 0.76$.	150
7.14	Circumferential velocity profile. Horizontal cut (left), Vertical cut (right), $x/c = 0.80$.	150
7.15	Circumferential velocity profile. Horizontal cut (left), Vertical cut (right), $x/c = 0.85$.	151
7.16	Circumferential velocity profile. Horizontal cut (left), Vertical cut (right), $x/c = 0.89$.	151
7.17	Circumferential velocity profile. Horizontal cut (left), Vertical cut (right), $x/c = 0.93$.	152
7.18	Circumferential velocity profile. Horizontal cut (left), Vertical cut (right), $x/c = 0.97$.	152
7.19	Circumferential velocity profile. Horizontal cut (left), Vertical cut (right), $x/c = 1.02$.	153
7.20	Evolution of circulation and width/2.	154
7.21	Evolution of circulation and height/2.	155
7.22	Horizontal vortex location.	157
7.23	Vertical vortex location.	158
7.24	Evolution of the peak axial velocity.	161
7.25	Evolution of the peak circumferential velocity.	163
7.26	Peak Circumferential velocity, ABS.	165
7.27	Evolution of the vortex core radius.	166
7.28	Evolution of the vortex core radius, ABS	167
7.29	Wake boundaries on the ABS and RBS.	169
7.30	Wake boundaries on the front and rear.	170
7.31	Core axial velocity profile, ABS, $Age = 12^\circ$	171
7.32	Particle at time t .	173
7.33	Non-dimensional velocity.	175

7.34	Radial position. Circles represent one revolution.	177
7.35	Comparison of measured core size with 2-D predictions for various sizes of particles.	179
7.36	Reynolds numbers of the particles.	181
7.37	Comparison of drag predictions.	182
7.38	Vortex velocity profiles.	187
7.39	Density distribution for Rankine($n = \infty$), Scully($n = 1$) and $n = 2$ vortex models, $\lambda = 0.14$	190
7.40	The effect of λ on the density distribution for $n = 2$ vortex model.	191
7.41	Refraction of light passing through a local density variation (Bagai <i>et al.</i> [1993]).	193
7.42	Computed light intensity for Rankine($n = \infty$), Scully($n = 1$) and $n = 2$ vortex models, $\lambda = 0.14$	194
7.43	The effect of λ on the light intensity profile for $n = 2$ vortex model.	195
7.44	Range of aspect ratio and Reynolds number over which data exist.	197
7.45	Range of aspect ratio and thrust coefficients over which data exist.	198
7.46	Range of aspect ratio and downstream distance over which data exist.	199
7.47	Correlation of several experiments with estimated tip-vortex circulation.	203

List of Tables

3.1	The parameters for the wings investigated by McAlister and Takahashi [1991].	63
4.1	The parameters for the rotor investigated by McAlister <i>et al</i> [1995].	89
4.2	The circulation of the tip-vortex for both fixed and rotary wings.	97
5.1	The comparison of $W(1)$ and $W_c(1)$	115
7.1	Rotor properties.	138
7.2	Measured flapping angles, $\mu = 0.10$, 1050RPM	160
7.3	Particle's Stokes numbers	175
7.4	Time to reach various radial locations	176

ACKNOWLEDGEMENTS

The authors wish to express their appreciation to the contract monitor Dr. Thomas L. Doligalski for his support and guidance during the course of this research. Professor Odus R. Burggraf has also been an integral part of this effort and is responsible for many of the ideas discussed in connection with an analytical model for the wake. In addition, the co-authors acknowledge the student personnel who have contributed significantly to the production of this document; these include Raghav Mahalingam(GT), Oliver Wong(GT), Hui Li(OSU), Santosh Kini(OSU), and Vishwanath Godavarty(OSU). The Ohio Supercomputer Center has provided computer time for which the authors are also grateful.

EXECUTIVE SUMMARY

The helicopter-rotor wake is among the most complex flow-fields in aerodynamics. This is due to the fact that the wake is fully three-dimensional and unsteady; moreover, many experiments have focused on trimmed conditions which involve cyclic pitch that complicates the wake and makes both experiments and computations difficult. As is well known, it is difficult and expensive to calculate accurately the wake position beyond one revolution of the rotor. The primary focus of this work is to study the formation of the rotor wake in both hover and forward flight.

The major objective of the analytical and computational work is to investigate whether classical inviscid lifting line and lifting surface methods applied locally near the wing tip can describe the origin of the tip-vortex. If so, this will result in the ability to predict circulation, asymptotic core radius, initial tip-vortex position, and local blade loads accurately. It may seem odd to describe the formation of the tip-vortex in this manner when viscous flow methods have been used. To further address the problem, a comprehensive set of experiments have been conducted.

The primary results and major accomplishments of this work are

- A lifting surface code for a semi-infinite three-dimensional fixed and rotary wing has been developed for use as the inner solution at the wing tip and the formation of the vortex has been described by rollover of vortex filaments near the wing tip.
- An analytical lifting-line analysis for the semi-infinite fixed wing has been compared with the full lifting surface code and the results are very good.
- The analytical lifting surface code results for the development of the tip vortex shed by both fixed and rotary wings have been compared with experiment and the results are encouraging.
- The calculations show that the circulation of the tip-vortex is about 80 – 90% of the maximum bound circulation in hover and the tip-vortex is formed within one revolution. The experiments suggest that the circulation is $\sim 40\%$ of the maximum bound circulation in low-speed forward flight. The reason for the large discrepancy is unknown.

- Experimental data obtained in the last few decades by researchers all over the world has been correlated.
- An internet database has been setup where results from several fixed-, rotary- and oscillating- wing tests have been tabulated.
- Circulation measurements from this database have been correlated with an expression developed for trailed circulation in the vortex in terms of geometric angle of attack and aspect ratio.
- Laser velocimetry has been performed near the blade tip on the advancing side of a 2-bladed rotor in forward flight in the Harper Wind Tunnel. Vortex trajectories over the blade tip, as well as velocity fields in the vortex formation region have been obtained from these measurements.
- The experiments have shown that the vortex increases in strength and size during the formation process. This, coupled with secondary features observed in the velocity profiles, suggests that the formation process may be due to the rollup of discrete vortex filaments. This is precisely what is seen in the computations.
- Laser velocimetry was also used to obtain velocity data in the very near wake of the rotor blade in a fixed wing configuration. These are intended to serve as direct comparisons to the rotary wing data under the same free-stream turbulence levels.
- Axial velocity values within the vortex can reach 96% of the tip speed.

Chapter 1

Introduction

1.1 Background

The helicopter-rotor wake is among the most complex flow-fields in aerodynamics. This is due to the fact that the wake is fully three-dimensional and unsteady; moreover, many experiments have focused on trimmed conditions which involve cyclic pitch that complicates the wake and makes both experiments and computations difficult. As is well known, it is difficult and expensive to calculate accurately the wake position beyond one revolution of the rotor (Tung and Lee [1994], Tung *et al.* [1996]). The major objective of the analytical and computational work is to investigate whether classical inviscid lifting line and lifting surface methods applied locally near the wing tip can describe the origin of the tip-vortex. If so, this will result in the ability to predict circulation, asymptotic core radius, initial tip-vortex position, and local blade loads accurately. It may seem odd to describe the formation of the tip-vortex in this manner when viscous flow methods have been used. However, correlation of experimental data by several authors (Mahalingam [1998], Bhagwat and Leishman [1998]) has revealed little dependence on the Reynolds number if the flow remains substantially unseparated.

In this chapter, we review the literature dealing with the formation of the tip-vortex on both fixed and rotary wings together with a brief introduction to the helicopter and helicopter aerodynamics.

1.2 The Fixed Wing Wake

The accurate calculation of the strength and the position of the tip-vortex shed from a lifting wing is a critical problem for aircraft because the flow in the tip region can have a great influence on the performance of the wing. In the tip region, the bound circulation drops to zero and vorticity must be shed. The shed vorticity forms the trailing vortex system which is responsible for the downwash and the induced drag and consequently has a major effect on the performance of the wing. In addition, for a large wing, the shed vortices can be very strong (strong rotational flow and strong downwash) and long-lasting. If a following aircraft encounters this wake at a shallow angle of incidence, it can experience a large roll movement due to the strong rotating flow or a strong downwash and result in a significant loss of altitude. If such an encounter occurs when the aircraft is already near the ground in landing or takeoff regimes, the result can be disastrous.

The region immediately downstream of the wing, referred to as the near wake or rollup region, is strongly three-dimensional. In the tip region, the bound circulation drops to zero rapidly and because the vorticity of the vortex filament is associated with the gradient of the bound circulation, the vortex filaments in the tip region will roll up with each other quickly and form a strong single tip-vortex.

Many researchers have investigated the fixed wing trailing vortex wake including Batchelor [1964], McCormick *et al.* [1968], Brown [1973], Moore and Saffman [1973], Francis and Kennedy [1978], McAlister and Takahashi [1991], Dacles-Mariani *et al.* [1995], Denvenport [1996] and Christopher *et al.* [1999]. As noted by Francis and Kennedy [1978], vortex formation begins to occur almost at the leading edge of the wing. This results in the picture of the tip-vortex as a collection of vortex-like lines shed from those discrete positions on the wing which appear helical in nature as depicted in the photograph on Figure 1.1; these streakline patterns show the behavior of trailing vortices shed from those discrete positions and illuminate the region around the vortex core; note that some of the vortex-like lines wrap from the underside. Such a filament-like structure for the tip-vortex is mentioned by Lanchester [1991] indicating a long history of this interpretation. However, no computational model of the tip-vortex incorporating a model of this type has been constructed.

A central feature of tip-vortices is the presence of axial flow in the core. Batchelor [1964] has shown that, in the absence of viscosity, the axial velocity

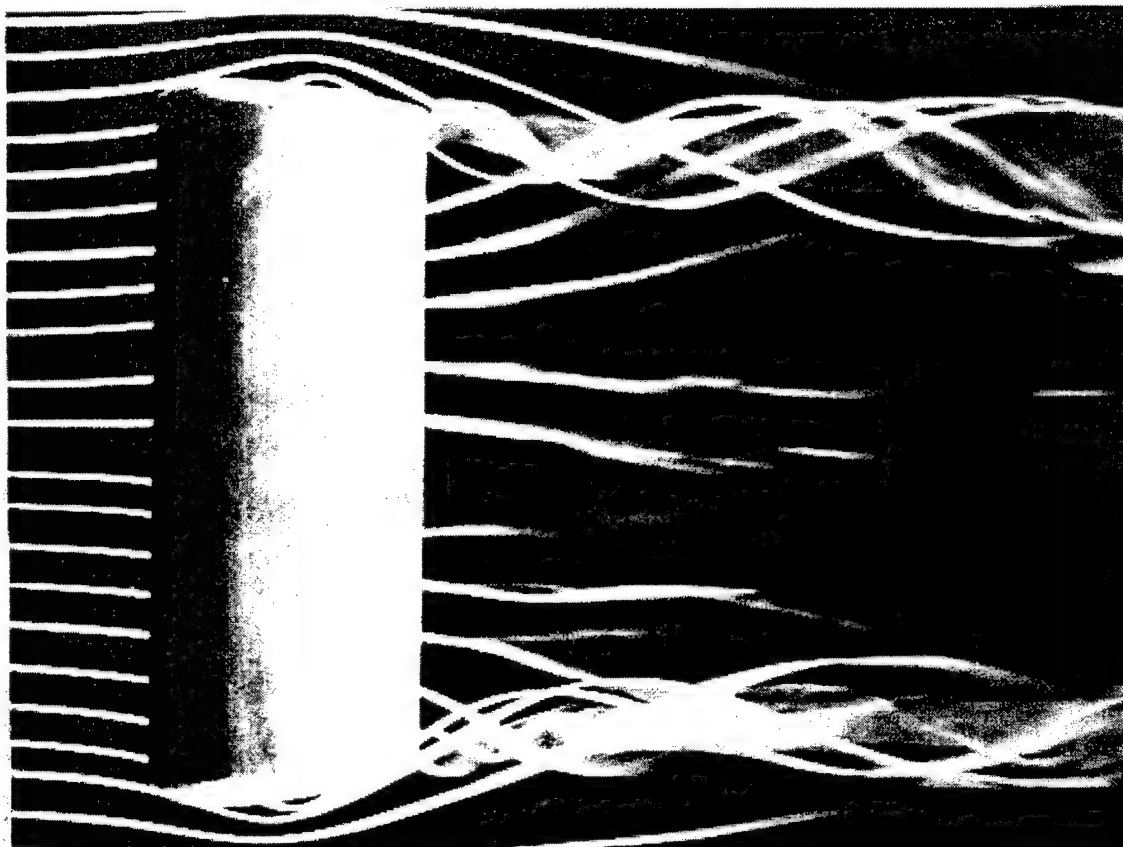


Figure 1.1: Vortex wake of a fixed wing as photographed by Head [1982].

is jet-like in the sense that the velocity at the center of the vortex along the direction of the core is larger than the velocity in the surrounding free stream. On the other hand, Moore and Saffman [1973] point out that a velocity deficit has been observed in experiments. Batchelor [1964] has shown that the effect of viscosity is to induce a deficit in the axial velocity profile, however, his analysis is confined to distances far downstream of the blade tip. Moore and Saffman [1973] have investigated the near wake region and found that there is a viscous inner core in which axial velocities in the opposite directions can occur; however, the influence of blade geometry is not addressed.

The recent model of Rule and Bliss [1996] suggests a jet-like axial flow in the far wake of a fixed-wing aircraft. McAlister and Takahashi [1991] found both jet-like and wake-like axial velocity directions in the tip-vortex of a straight fixed wing, beyond a few chord lengths. They postulated a difference between the axial velocity from a square-edged rotor tip versus a rounded tip.

Devenport *et al.* [1996] studied the structure of the wing-tip vortex shed by NACA 0012 half-wing and measured the velocity in the vortices using hot-wire probe. They found that inside the core of the vortex, the flow is laminar and therefore the core radius, peak tangential velocity and axial velocity develop very slowly. Outside the core, the turbulence structure of the spiral is dominated by the remainder of the wing wake which winds into an approximately self-similar form. They also suggested that, at the upstream locations, the core has a two-layered structure: an outer core that appears to be a remnant of a secondary vortex formed during the roll-up process and an inner core which grows within the outer core with distance downstream.

On the computational side, there are mainly two approaches to describe the wake vortex system. One is the panel method (vortex lattice method) which is used in the current work, and the other is the direct Euler/Navier-Stokes simulation. Each of these methods has its own advantages and disadvantages. Although the panel method can roughly consider the effect of compressibility by introducing the compressibility factor β , the panel method is mainly used to study an irrotational inviscid incompressible flow (potential flow) problem, while there is no limitations on applying the Euler/Navier-Stokes simulation. On the other hand, the Euler/Navier-Stokes methods suffer from large numerical diffusion contained in their solutions, while the panel method, in which the vortex structure can be specified to a large extent, is almost free of numerical diffusion.

Roger [1991] used a second-order Euler method together with an adaptive-

grid solver to study the tip-vortex flow fields around NACA 0015 airfoil. The predicted results for the surface pressures and integrated lift agree well with experiments. However, the core radius is larger and the peak induced tangential velocity behind the wing is less than the experimental data. This appears to be caused by high numerical diffusion in the numerical approximation.

Dacles-Mariani *et al.* [1995] report solutions for the fixed wing in which up to one million points with grid clustering have been used. They report that they could resolve the outer portion of the vortex but could not resolve the viscous portion of the core owing to high numerical diffusion. However, the viscous core of the vortex is important because it determines the form of the axial flow and the magnitude of the circulation of the tip-vortex.

Christopher *et al.* [1999] apply a fourth-order accurate differencing approximation in both space and time to study the near-wake development of the flow past a NACA 0012 airfoil. They use a total of 1.33 million grid points to compute the tangential velocity behind the wing and determine the trajectory of the tip-vortex and the pressure contours. They suggest that the numerical dissipation can be reduced by applying the high-order differencing approximation because their results are better than those obtained by using the low-order NASA CFD code: CFL3D.

Yeh and Plotkin [1985] apply the first-order "linear vortex" panel method to calculate the three-dimensional wake roll-up process behind a large aspect ratio, thin wing, in a steady inviscid incompressible flow. They divide the wake into three regions: the adjoining region, near region and far region. In the adjoining region and the near region, the wake has been represented by triangular panels with linearly distributed spanwise vorticity and constant chordwise vorticity. The collocation points are chosen to be at the geometric center of each panel. In the far wake, the wake has been represented by straight semi-infinite vortex segment extending to infinity. The wake geometry is evaluated in an iterative scheme and the converged wake geometry compares well with the result of constant doublet panel method applied by Suciu and Morino [1976].

Osama *et al.* [1983] apply a "nonlinear hybrid vortex" method on a lifting wing at high angle of attack. For the near field calculation, they use vortex panels with linear vorticity distribution. In the far field, the distribution of vorticity is reduced to vortex lines where the modified Biot-Savart law is employed to calculate the induced velocity field. This coupling of a continuous vortex-sheet representation in the near field and a concentrated vortex-line representation in the far field for solving the nonlinear lifting surface problem

is this so called the “nonlinear hybrid vortex” method. They study both steady and unsteady flow problems for a lifting wing. For the unsteady flow, they solve the steady flow first and take the steady solution as the initial condition for the unsteady problem. The net pressure distribution and lift coefficient they obtained compare well with experimental data. However, they did not present results for the formation of the tip-vortex.

1.3 The Rotor Wake

1.3.1 The Helicopter

Helicopter is an aircraft that uses rotating wings (rotors) to provide lift, propulsion and control. In contrast with the fixed-wing aircraft, a helicopter can generate these forces even when the velocity of the helicopter is zero. Therefore, helicopter is used to perform tasks which fixed wing aircraft can not do, such as hover and vertical flight, including vertical take-off and landing. Thrust supports the helicopter weight and the propulsive force balances both the aircraft and the rotor drag in forward flight, some other forces and moments are required to control the helicopter position, attitude and velocity. All these forces and moments are supplied by the helicopter rotor. The rotor generates such forces as a result of its relative motion with respect to the air. There are four regimes in which the helicopter operates; namely hover, vertical climb, vertical descent and forward flight.

When a rotor provides the lift, it shed a trailing vortex system which interacts with the rotor and the helicopter body. These interactions make the flow field around the helicopter very complex; moreover, they are source of considerable noise and vibration.

The primary focus of this work is to study the formation of the rotor wake. The rotor wake computation and other study areas dealing with the flow around the helicopter form the field of helicopter aerodynamics. In the next section, a very brief review of the helicopter aerodynamics is presented.

1.3.2 Helicopter Aerodynamics

Helicopter aerodynamics studies the flow field around the helicopter. Figure 1.2 from Caradonna [1992] depicts various major rotor craft problems. It shows several fluid dynamic problems. As the blades rotate, the tip-vortex

shed from one of the blades may encounter with the following blades; this phenomenon is called blade-vortex interaction (BVI) which is a major source of the rotor noise. The blade-vortex interactions are most severe in vertical descent and landing. Another important aerodynamic interaction is the vortex-fuselage in which the tip-vortex convects down away from the rotor and collides with the airframe. Also there is vortex interaction between the tail rotor and the main rotor. In forward flight, the helicopter has a translatory velocity and thus the rotor blades have different relative air velocities as shown on Figure 1.3. The advancing blade has a velocity relative to the air higher than the retreating blade. Due to the different relative velocities, the rotor needs to be trimmed. This requires periodic adjustment of the angle of attack of the rotor blades azimuthly in order to balance the moment arising due to the lift force. On the retreating side, the velocity relative to air is low and thus the angle of attack has to be increased. This may lead to stalled flow and viscous effects can become important. On the advancing side, the flow may be transonic; thus near the tip of the blade shock waves can form.

1.3.3 The Rotor Wake

On a three-dimensional blade, conservation of vorticity requires that the bound circulation be shed into the wake from the tip to the root. Also vorticity is left in the rotor wake as a consequence of radial and azimuthal changes in the bound circulation. The trailed vorticity γ_t is generated owing to the radial variation of the bound circulation and is normal to the trailing edge of the rotor blade. Near the tip and root, the trailing vortices roll over each other and form the tip and root vortex; while in the inboard portion of the blade, there is a vortex sheet as shown on Figure 1.4. For unsteady state, rotating blade causes the azimuthal variation of the bound circulation and thus the trailing vorticity is not constant downstream and correspondingly, the shed vorticity is generated. The shed vorticity γ_s , due to the variation of the trailing vorticity, is parallel to the trailing edge of the rotor blade. γ_t and γ_s are defined in Johnson [1980] as

$$\gamma_t = \frac{\partial \Gamma}{\partial r} \quad (1.1)$$

$$\gamma_s = -\frac{1}{u_T} \frac{\partial \Gamma}{\partial \phi} \quad (1.2)$$

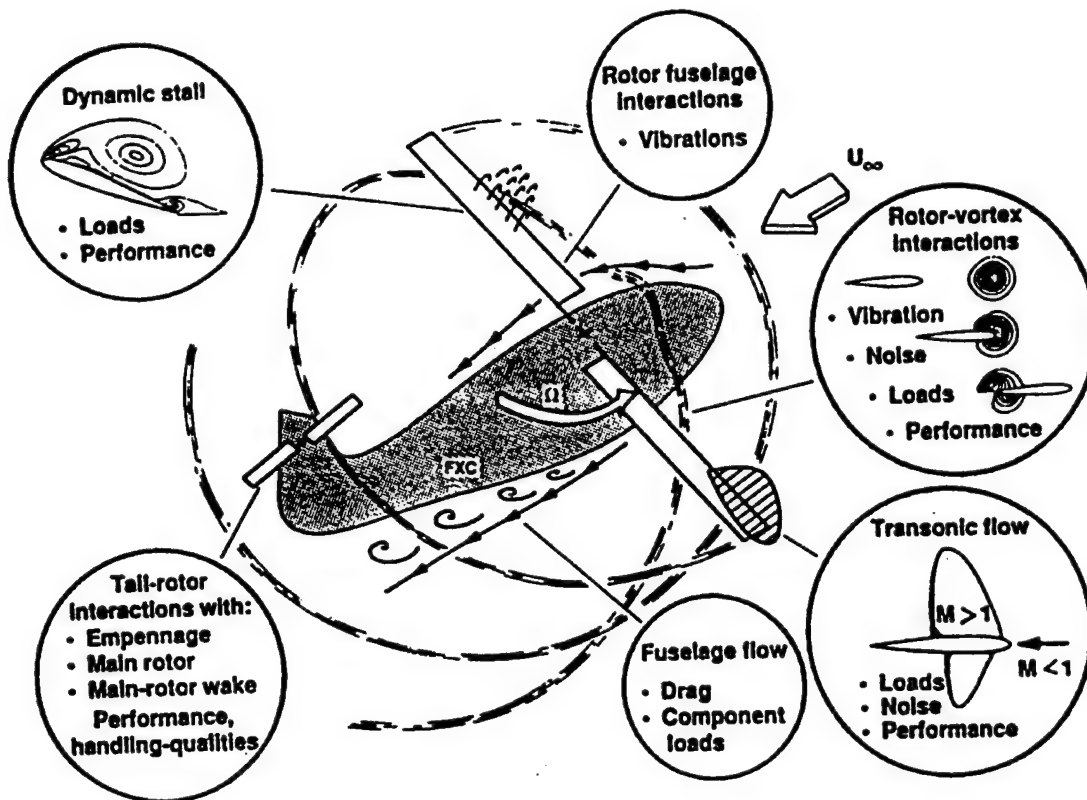


Figure 1.2: A summary of specific flow problems involving helicopter aerodynamics. From Caradonna [1992].

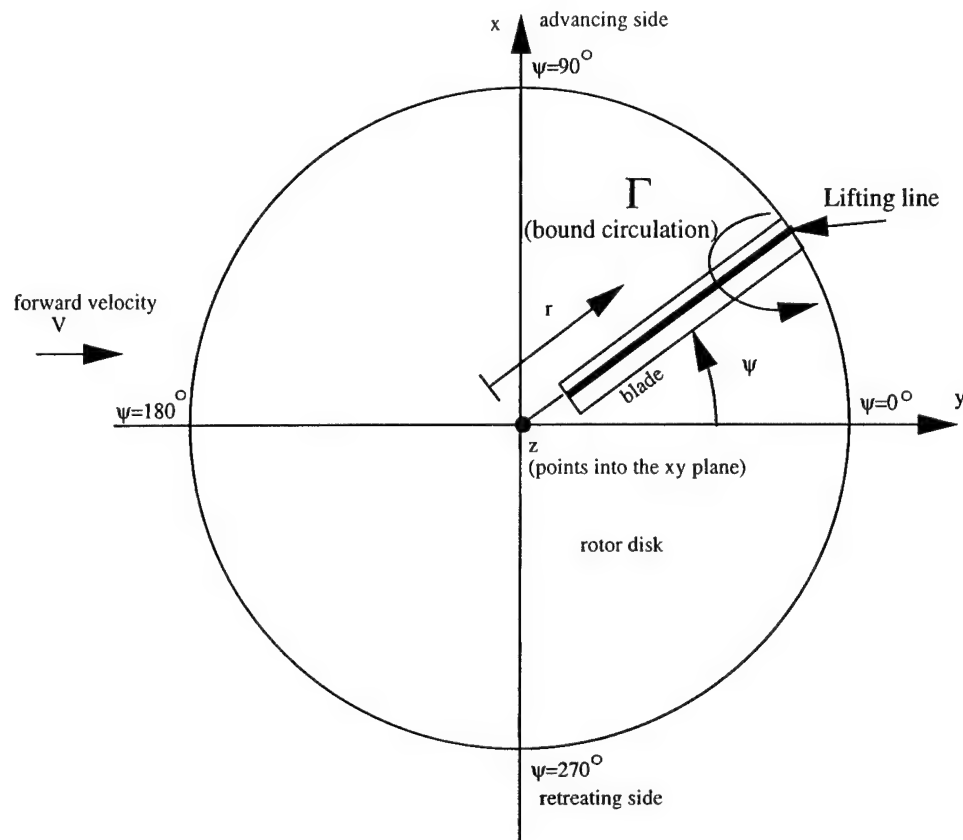


Figure 1.3: Rotor disk, showing definition of ψ and r . ψ is indicative of vortex age, while ϕ (not shown) is the rotor azimuthal angle. $\psi = \phi$ for the first revolution. From Johnson [1980].

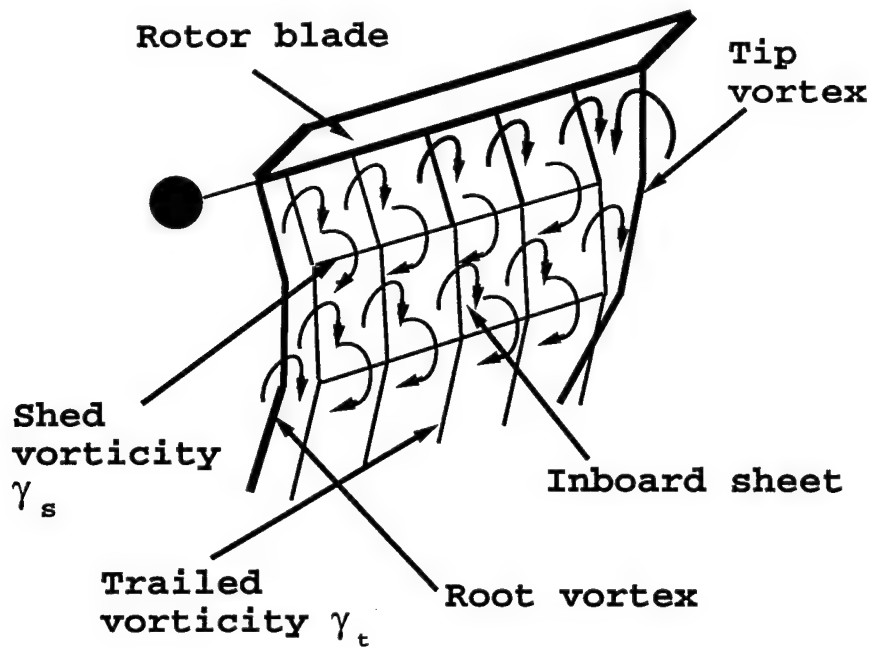


Figure 1.4: Sketch of the trailing vorticity γ_t and the shed vorticity γ_s .

where Γ is the bound circulation, r is the radial position on the blade, ϕ is the rotor azimuth angle (see Figure 1.3) and u_T is relative air velocity of blade section tangent to the disk plane. All these derivatives of the bound circulation are evaluated at the time the wake element leaves the trailing edge of the blade. The typical variation of lift L , the bound circulation Γ and the corresponding trailed vorticity γ_t are depicted on Figure 1.5.

As described in Johnson [1980], owing to the rotation of the blade, the lift and the corresponding circulation are concentrated at the tip. In the tip region, the circulation drops quickly to zero over a finite distance. Owing to the high rate of change in the circulation, the strength of the shed vorticity is very strong, which causes the shed vortices to quickly roll up into a strong single tip-vortex. In the inboard portion of the blade, the bound circulation drops off gradually to zero at the root. Hence there is an inboard sheet of trailed vorticity in the wake with the opposite sign to the tip-vortex. Since the radial variation of the bound circulation is small away from the rotor-tip, the inboard vortex sheet is generally much weaker and more diffuse than the tip-vortex. Figure 1.6 depicts the complexity of the shed wake of a single bladed rotor from Gray [1956].

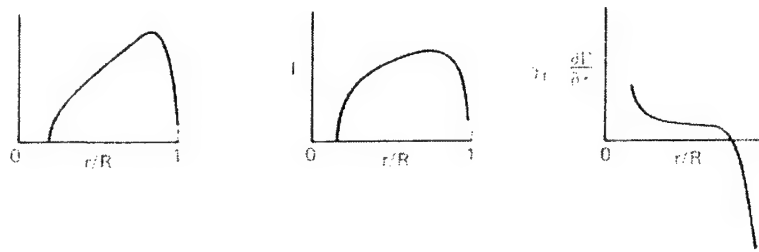


Figure 1.5: Sketch of typical radial distribution of the blade lift L , bound circulation Γ and trailing vorticity γ_t . From Johnson [1980].

From the viewpoint of pressure, the tip region contains a complex three-dimensional viscous flow field which results from the pressure difference on the upper and lower surfaces on a lifting airfoil. Because at the wing tip, pressure discontinuity is not possible, the pressure difference on the blade is gradually relieved towards the tip and finally the pressure difference is zero at the wing tip. Associated with this pressure field, near the wing tip, the fluid particles roll up and form the tip-vortex which is convected downstream by the local streamwise velocity. The core radius of the tip-vortex is defined as the half distance between the minimum and maximum tangential velocities.

Many experimental investigations have focused on the wakes of helicopter rotor blades and a survey of these results is presented in Conlisk [1997]. A relevant paper on the influence of tip-shape on various integrated properties such as lift and moment coefficients is by Berry and Mineck [1980]. However, detailed velocity and pressure measurements of the very near wake of a rotor blade have, in general, not been available until very recently.

McAlister *et al.* [1995] have measured the fully three-dimensional velocity field for a rigid rotor blade; the measurements include data at 0.3-chord length downstream where origin of the tip-vortex in particular can be analyzed. According to McAlister *et al.* [1995], the vortex begins to form near the point of maximum thickness on the top of the blade. The center of the vortex is offset inboard a small amount and the circulation within the vortex varies with the rotor phase angle. The vortices leave the wing in the chord-wise direction at the trailing edge as in the case when the classical Kutta condition is applied.

Most rotor-tip vortices are helical, with a strong velocity component directed along the axis of the core. As with the fixed wing, there is a surpris-

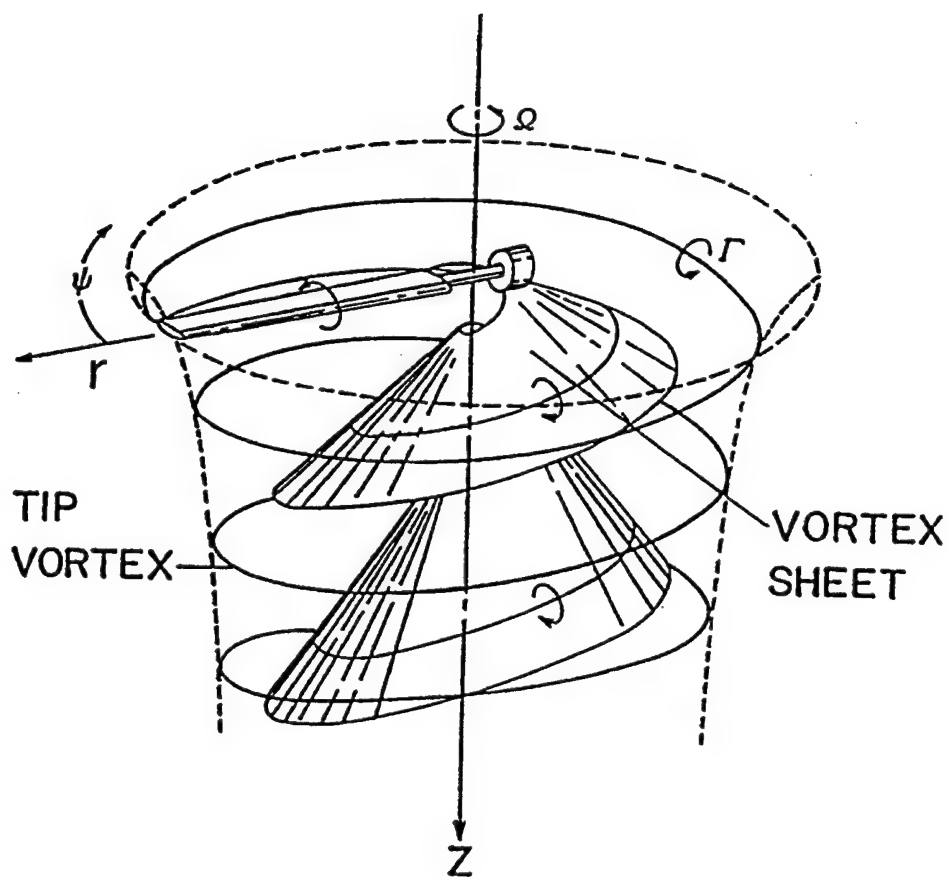


Figure 1.6: Sketch of a helicopter rotor wake for a single blade. From Gray [1956].

ing amount of disagreement regarding the axial velocity in the vortex core, even about its sign. Shivananda *et al.* [1978] used a split-film anemometer to resolve all three components of velocity in the wake of a single-bladed, square-edged NACA0012 rotor in hover. They found a wake-like core: the axial velocity was directed back along the trajectory of the vortex toward the blade. The measurements by McAlister *et al.* [1995] and McAlister [1996] show that, at three chord-lengths downstream of square-tipped NACA0012 rotor blade in hover, the axial velocity of the tip-vortex is directed back toward the blade and of the same order of magnitude as the peak swirl, and is about 9% of the tip speed.

Komerath *et al.* [1998] studied the same rotor-blade wake, and resolved all three components of velocity in the vortex using laser velocimetry. They were able to achieve high data rates using an off-axis light receiving system, and incense smoke particles which stayed inside the core. They showed not only a wake-like vortex core, but also secondary features inside the core indicating several layers of vortex sheet roll-up. There is some flow visualization evidence in the literature on propeller wakes which supports this finding (Cook [1972]). Other experiments (Mahalingam [1996]) in the wake of NACA0015 rotor in forward flight show large wake-like axial velocity both in the tip vortex and in the inboard sheet and strong evidence of secondary features in the core.

Bhagwat and Leishman [1998] use a three-component Laser Doppler Velocimetry to study the tip-vortex flow field. They report that the peak value of the induced tangential velocity decays and the core radius grows in a logarithmic trend downstream which indicates viscous diffusion in the tip-vortex. They find Reynolds number not to appear to have a strong effect in the flow field. They also correlate the maximum bound circulation with the strength of the tip-vortex which is formed from the roll-over trailing vortices. The measurements show the strength of the tip-vortex to be approximately 85 percent of the maximum bound circulation and the remaining to be contained in the inner vortex sheet.

With the improvement in the speed and storage of modern supercomputers and the development of parallel processing, direct Euler/Navier-Stokes simulations have been conducted in the rotor wake calculation by applying higher-order accurate approximation in both space and time (Tang and Baeder [1999], Christopher *et al.* [1999] and Hariharan and Sanker [1999]). Tang and Baeder [1999] apply an improved third-order accurate Euler/Navier Stokes solver and a grid redistribution method to simulate the hovering rotor

flow field. They used about half a million grid points and computed the tangential induced velocity behind the rotor. They compared the results with the code without a grid adaptation and suggested that numerical diffusion is reduced by applying both a higher-order Euler/Navier Stokes solver and the grid adaptation. Christopher *et al.* [1999] apply the fourth-order accuracy in both space and time and also demonstrate low dissipation.

Hariharan and Sanker [1999] apply a seventh order spatially accurate ENO (Essentially Non-Oscillatory) method to study the unsteady rotor tip-vortex structure. They report that it is necessary to capture the correct axial velocity (jet-like versus wake-like) because the axial velocity is very important in calculating the tangential velocity accurately. If the axial velocity is jet-like, then the peak-to-peak variation of the tangential velocity remains at a certain value. If the axial velocity switches to a wake-like structure owing to numerical dissipation downstream, the peak-to-peak variation of the tangential velocity changes to a different lower value downstream. They suggest that the axial component can be correctly captured over 50 chord lengths with a grid of 270,000 points by implementing the seventh order spatially accurate ENO method.

As mentioned above, different from the Euler/Navier-Stokes simulation, in panel method (vortex lattice method), the wake structure can be specified to a large extent. Generally, there are three types of wake models used in the panel method namely; Rigid Wake, Prescribed Wake and Free Wake models. A brief discussion on each of them is presented subsequently.

1.3.4 Wake Models

A good review of the development of the wake model from the rigid wake model, prescribed wake model to free wake model is given by Gray [1991]. The rigid wake model assumes that the wake consists of a series of vortex lines. Each vortex line forms a skewed helix, whose geometry is set by the forward speed of the helicopter and the mean inflow velocity (axial flow) through the tip path plane. The wake is not allowed to deform. The problem in using this model is that the wake does not contract and therefore, the results do not agree with the experiments.

The prescribed wake model overcomes this disadvantage by utilizing experimental data to predict the wake geometry including the tip vortex and the inner vortex sheets. But this model is not truly predictive because it requires experimental data.

A free wake model allows the wake to develop under the influence of all the components i.e., the free stream velocity, the self-induced velocity, the effect of the blade. This is the standard way now to calculate the wake and the blade loads. Although the free wake model has demonstrated improved performance predictions over most of the blade, it is not appropriate near the rotor-tip because the free wake model assumes that the tip-vortex rolls up completely at the trailing edge of the rotor blade where it emanates. This deficiency leads to a considerable difference between the numerical calculations and experiments in the spanwise distribution of the bound circulation near the rotor-tip. Therefore, it is necessary to develop a satisfactory model to account for the formation and downstream development of the tip-vortex for the blade load calculation in the tip region which is the main concern of the current work.

Prescribed, free wake model together with lifting-line or lifting surface methods have been widely used to study the rotor hovering performance and propellers (Kocurek *et al.* [1976], Miller [1982], Shenoy and Gray [1980] and Hess and Valarezo [1985]).

Katz and Maskew [1986] applied panel method to study the unsteady low-speed flow over both fixed wings and rotors. A modified potential-flow panel method is used together with a time-dependent vortex wake model to simulate the wake. Unlike the wake models mentioned before, the zero normal velocity on the body surface is related to time, and the corresponding time-dependent equivalent Kutta condition is applied to the wake model. At every time interval, a new wake element with constant strength which satisfies the Kutta condition is shed from each panel on the trailing edge of the wing and moves with the local stream velocity, which is due to the free stream flow and the induced velocity by other vortex elements. The shed wake elements are allowed to roll up. Katz and Maskew [1986] applied this method to study the spanwise lift distribution for a two-bladed rotor and they found a large difference between the experimental results and the computational results due to the undeveloped wake. They suggested this deficiency can be improved by adding a far wake model or running the code for more time steps (at least three complete revolutions). Because this wake model considers the roll-up process of the shed vortices, it can obtain good agreement with the experimental data near the tip-region. However, the problem in using this method is time consuming because of two reasons. First, every time interval, new wake panel element must be shed from the separation line of each panel on the trailing edge of the wing and moves with the local stream velocity

and then the bound circulation on the wing is calculated. Second, after up to three complete revolutions, the numerical result for the bound circulation agrees well with the experimental data. We will show that using Burggraf's [1999] theory and a simple rotor wake-contraction model, similar results can be obtained analytically.

1.3.5 Current Work

The present work is to delineate the major features of the origin of the tip-vortex and the rotor wake computationally, resulting in the ability to predict accurately circulation, asymptotic core radius, initial tip-vortex position, and local blade loads. While the rotor tip-vortex is of primary interest, the techniques developed would be applicable to fixed wings as well. The lifting surface theory is applied in the bound circulation calculation and thus a brief introduction to the panel method is presented in the next chapter.

From the analytical and computational perspectives, the flow near the wing tip can be viewed as the inner solution in a matched asymptotic expansion in the small parameter defined as the ratio of the chord to length of the rotor blade. This situation is depicted in Figure 1.7. This idea is not new; Van Dyke [1964] alluded to this in his discussion of the fixed wing case. It is shown that for a fixed wing, in the tip region, to leading order, the lifting-line integral equation for the bound circulation has an analytical solution given by Stewartson [1960] and a sketch of the result is presented on Figure 1.8. Far from the tip, the circulation is constant and so to leading order, no vorticity is shed there, while in the region where the circulation varies, the individual vortex filaments would be expected to roll over each other and form a strong tip-vortex. We apply the lifting surface method to obtain the chordwise and spanwise distributions for the bound circulation and the vertical induced velocity behind the wing and compare these results with the experimental data of McAlister and Takahashi [1991]. The roll-over process of the trailing vortices is presented as well.

The rotary wing case is considered next. For a rotary wing, the leading order-inner solution for the bound circulation has been derived using Burggraf's lifting-line theory [1999]. It is shown that in the tip region, to leading order, the rotary wing is similar to the semi-infinite fixed wing and the difference is only a parameter which is dependent on the aspect ratio, the angle of attack and the number of the blades. The analytical uniformly-

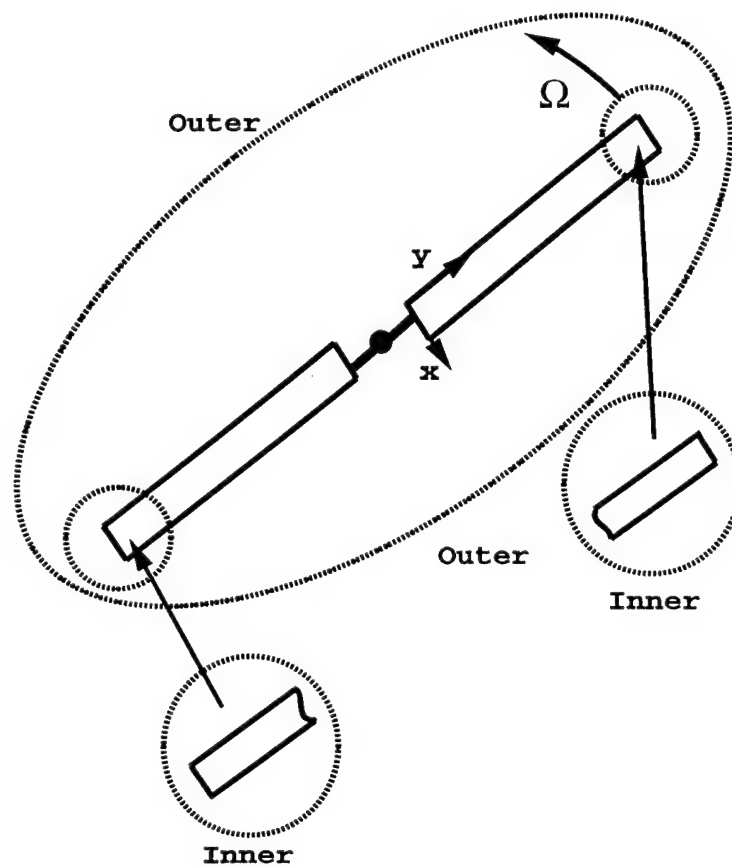


Figure 1.7: Definition of the inner and outer problems for the calculation of the flow past a two-bladed rotor.

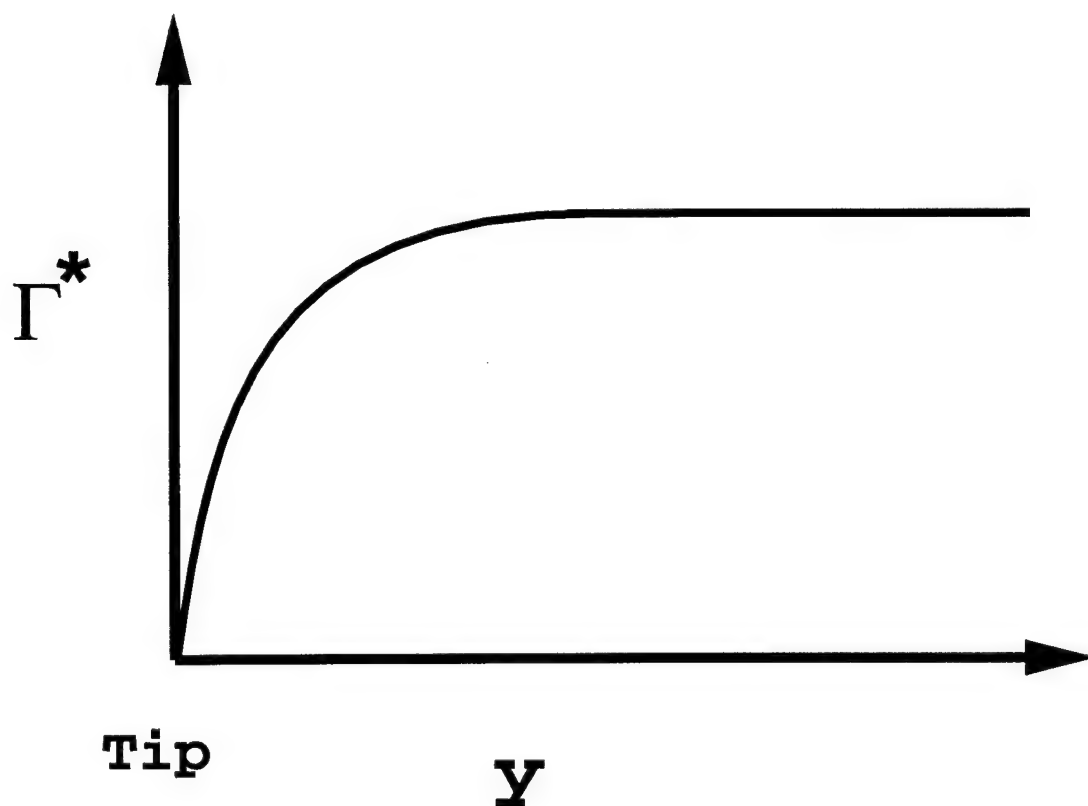


Figure 1.8: Sketch of the bound circulation for a semi-infinite fixed wing; in the region where the bound circulation varies, the individual vortex filaments would be expected to wind around each other to form the tip-vortex.

valid solution for the bound circulation is presented. Next, the lifting-surface method is applied and the roll-over process of the trailing vortices is illustrated. The induced vertical velocity is calculated numerically and compares well with McAlister *et al.* [1995]. Using “multiplicative composition” to combine the inner and outer solutions, the uniformly-valid solution is obtained for the bound circulation over the whole rotor blade. A sketch of the bound circulation is shown on Figure 1.9.

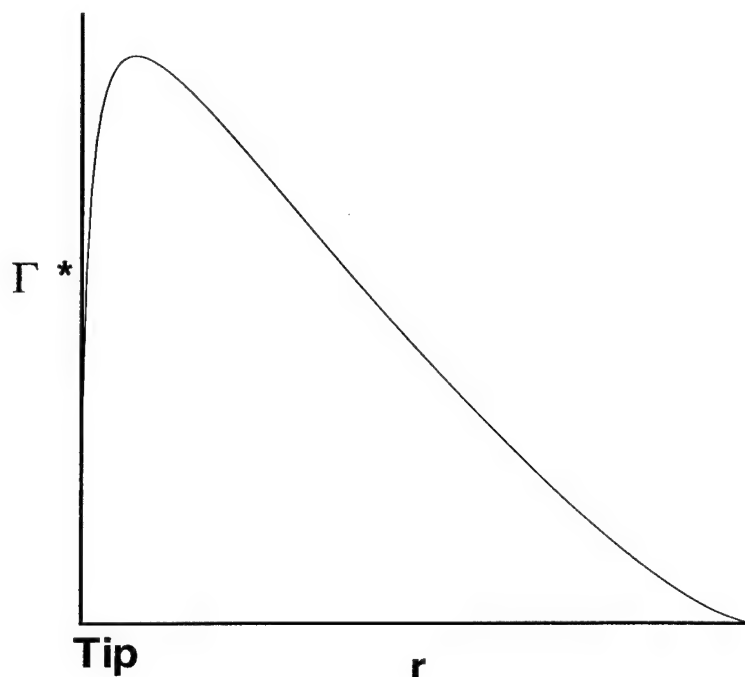


Figure 1.9: Qualitative sketch of the bound circulation for a rectangular, untwisted rotary wing. In the tip region where the bound circulation drops to zero at the tip quickly, the individual vortex filaments would be expected to wind around each other to form the strong single tip-vortex. In the inboard portion of the blade, the bound circulation drops off gradually to zero at the root and hence there is an inboard sheet with the opposite sign to the tip-vortex.

The influence of rotor-wake contraction on the bound circulation is considered next. Two types of wake models are applied: the vortex cylinder model and the discrete vortex ring model. First, the vortex cylinder model is used to represent the rotor wake contraction and the computed bound circulations compare fairly well with the experimental data from Caradonna and Tung [1981]. The weakness of this vortex-cylinder model is that the vorticity is assumed to be uniformly distributed along each semi-infinite cylinder and this assumption is not accurate. The discrete vortex-ring model overcomes this weakness and the results using this model compare well with Landgrebe's [1972] results.

Finally, laser velocimetry measurements were conducted on the wake of a two bladed teetering rotor in forward flight to gain an understanding of both the vortex formation process and how the vortex properties evolve into the near wake. Circumferential velocity profiles of the vortex during the formation process were first observed at a chordwise location of 0.47. In the past four years, the experiments have been directed towards:

- Collecting and correlating experimental results and data on fixed-wing and rotary wing vortices.
- Performing experiments on rotary wing vortices to answer some key unknowns.
- Estimate measurement errors due to particle "spinout".
- Developing methods of measuring the tip vortex strength and structure efficiently.

Chapter 2

Panel Methods

2.1 Background

In the current work, lifting-surface theory is applied to the flow near the wingtip by using a panel method. Panel methods are used to solve potential flow problems and are a logical extension of the analytical methods to deal with the complicated surface geometry. By applying the panel method, the solution to the potential-flow problem is reduced to finding strengths of singularity elements (source, doublet or vortex) distributed over the body surface. In this work, the flow field in the tip region is assumed to be incompressible, inviscid and irrotational and thus it is appropriate to apply the panel method to investigate the flow field. In this chapter, a brief introduction to the panel method is presented. First, we review its application to two-dimensional airfoil problems. Then, we extend the solutions for two-dimensional airfoils to the three-dimensional wings used in this work.

2.2 Two-Dimensional Airfoil Aerodynamics

Consider a two-dimensional airfoil immersed in a potential flow as shown on Figure 2.1; then the total potential Φ_{total} can be expressed as a sum of a perturbation potential Φ and the free-stream potential Φ_{∞} :

$$\Phi_{total} = \Phi + \Phi_{\infty} \quad (2.1)$$

and

$$\nabla^2 \Phi_{total} = 0 \quad (2.2)$$

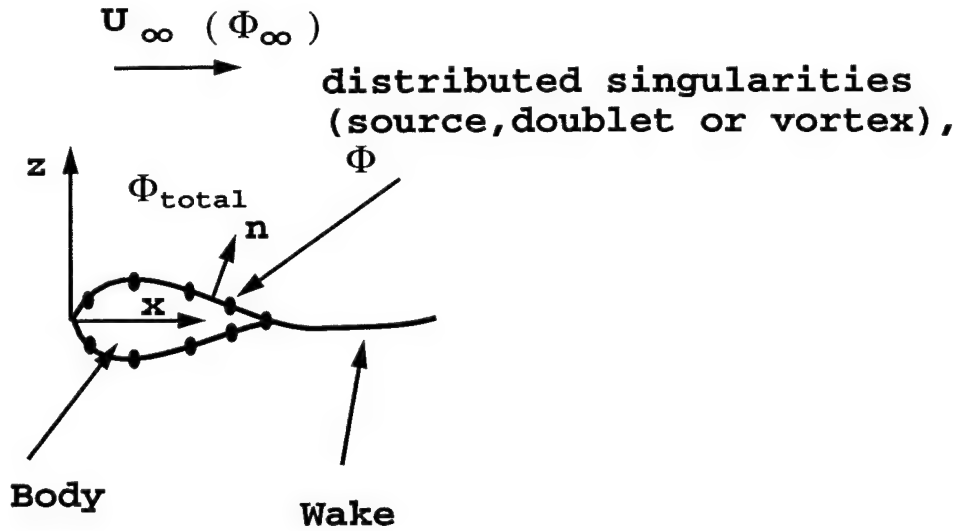


Figure 2.1: Potential flow over a two-dimensional airfoil.

The total potential Φ_{total} satisfies two boundary conditions. Firstly, the normal velocity at the body surface vanishes and this condition can be expressed by

$$\nabla \Phi \cdot \vec{n} = 0 \quad (2.3)$$

where \vec{n} is the surface vector. Second, the flow disturbance due to the body's motion relative to the free stream flow vanishes far from the body. This boundary condition is expressed as

$$\lim_{r \rightarrow \infty} \nabla \Phi = 0 \quad (2.4)$$

where r is the position vector, i.e., distance from the body. This condition is automatically satisfied for all the singularity distributions of source, vortex or doublet types (Katz and Plotkin [1991]) and thus the problem has been reduced to finding the strengths of the singularity elements on the body surface which satisfy (2.3).

The solution to (2.3) is not unique even after selecting a desirable combination of singularity elements (source, doublet or vortex) and thus an additional condition must be applied in the flow field. According to Helmholtz theorem, a vortex can not start or end in the flow field, so the bound circulation on the wing must be shed into the flow field correspondingly. To make the solution unique, the wake must be shed at the trailing edge; i.e., Kutta

condition is applied to the flow. One statement of the Kutta condition is that the flow is required to be parallel to the trailing edge of the wing as it leaves, thus fixing the circulation generated by the airfoil. Mathematically, Kutta condition requires the vorticity component parallel to the trailing edge $\gamma_{T.E.}$ to be zero,

$$\gamma_{T.E.} = \gamma_U + \gamma_L = 0 \quad (2.5)$$

where γ_U and γ_L are the corresponding upper and lower surface vorticities. Kutta condition also requires the shed vorticity γ_W to be aligned with the local flow direction. Figure 2.2 illustrates the implementation of the two-

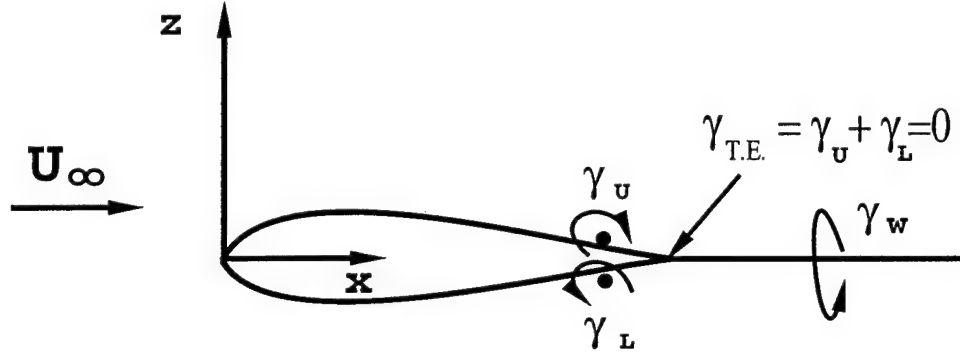


Figure 2.2: Implementation of the two dimensional Kutta condition on an airfoil when using surface vortex distribution. The vorticity at the trailing edge $\gamma_{T.E.}$ which is the sum of the corresponding upper and lower surface vorticities γ_U and γ_L must vanish. Also the shed vorticity γ_W is aligned with the local flow direction.

dimensional Kutta condition for a vortex distribution on an airfoil.

Now we consider a zero thickness, symmetric airfoil at an angle of attack α_0 submerged in an inviscid, incompressible and irrotational flow as shown on Figure 2.3. The leading and trailing edge of the airfoil are located at $x = 0$ and $x = c$ respectively and U_∞ is the free stream velocity. We apply unknown continuous vorticity distribution $\gamma(x)$ (circulation per unit length) on the airfoil. On the plane $z = 0$, the velocity induced at x_0 by vorticity $\gamma(x)$ located at the point x is $-\frac{\gamma(x)}{2\pi(x_0 - x)}$. Integrating $\gamma(x)$ from the leading edge ($x = 0$) to the trailing edge ($x = c$), the zero normal-velocity boundary condition at the given point x_0 becomes

$$\frac{1}{2\pi} \int_0^c \gamma(x) \frac{dx}{x_0 - x} = U_\infty \alpha_0 \quad (2.6)$$

where $0 < x_0 < c$.

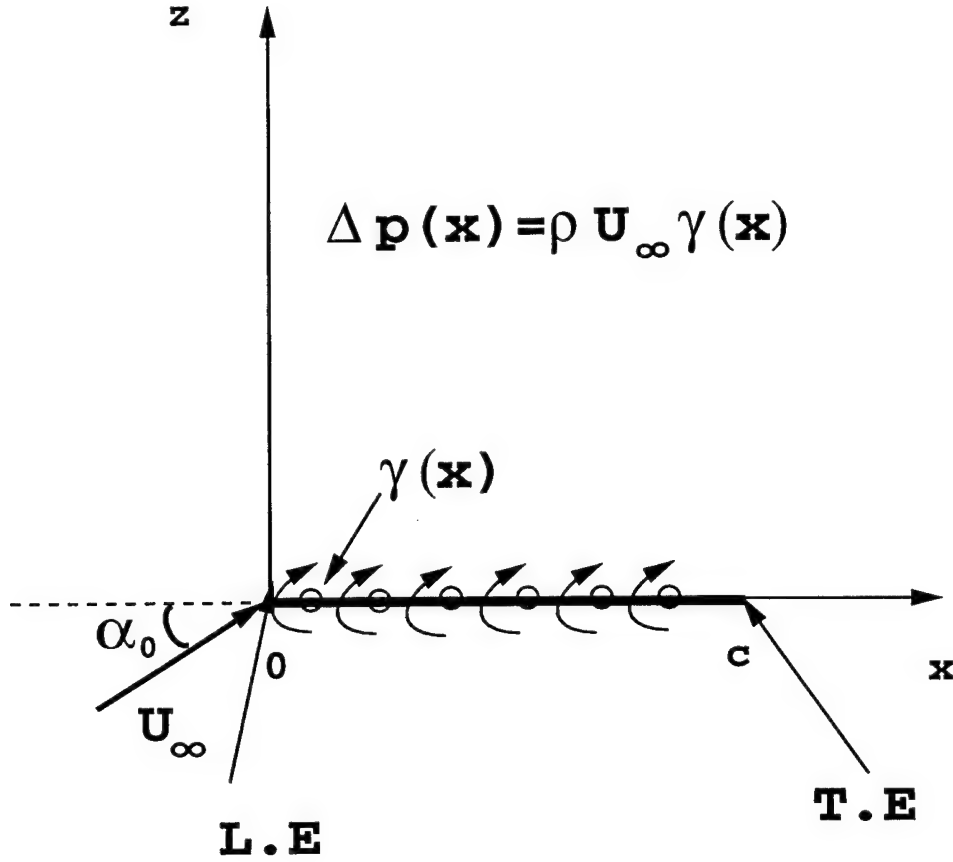


Figure 2.3: Continuous vortex distribution on a zero thickness, symmetric airfoil. Note y axis is normal to x-z plane and outward.

As mentioned above, the solution for equation (2.6) is not unique and thus the two dimensional Kutta condition is applied, requiring $\gamma(c) = 0$. The analytical solution for equation (2.6) is given by Glauert [1948] as

$$\gamma(\theta) = 2U_{\infty}\alpha_0 \frac{1 + \cos\theta}{\sin\theta} \quad (2.7)$$

where θ is defined by

$$x = \frac{c}{2}(1 - \cos\theta) \quad (2.8)$$

which is shown on Figure 2.4. Figure 2.5 shows the distribution of $\gamma(x)$.

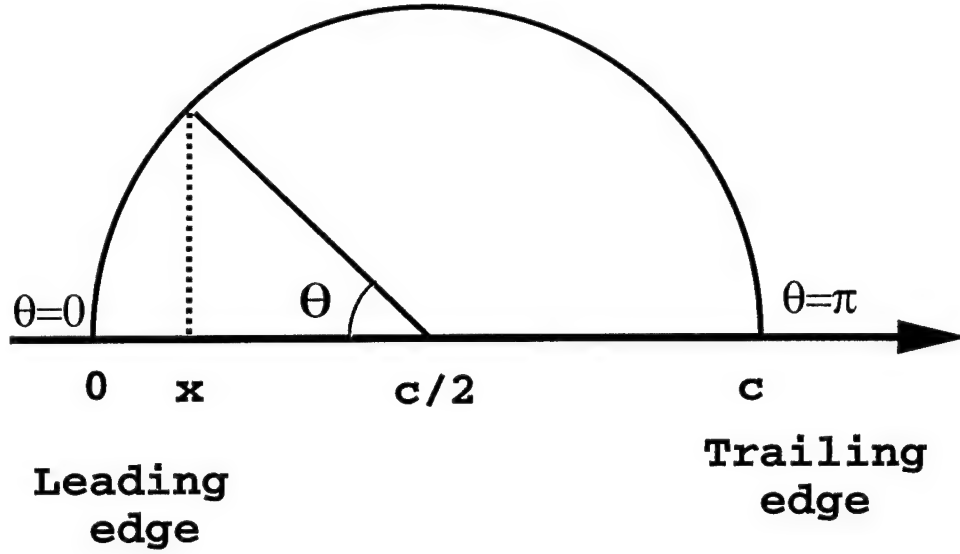


Figure 2.4: Plot of the transformation $x = \frac{c}{2}(1 - \cos\theta)$.

Having obtained the distribution of vorticity on the two-dimensional lifting airfoil, the pressure, lift and moment can be calculated. The pressure difference $\Delta p(x)$ between the upper surface p_u and lower surface p_l is obtained by applying the steady state Bernoulli equation on the airfoil boundary. In a steady-state flow, the velocity at any point u in the flow field is a combination of the free stream velocity and the perturbation velocity, as $(U_\infty \cos\alpha_0 + \frac{\partial\Phi}{\partial x}, U_\infty \sin\alpha_0 + \frac{\partial\Phi}{\partial z})$. Substituting u into the Bernoulli equation and taking into account the small-disturbance assumptions ($\frac{\partial\Phi}{\partial z}$ and $\frac{\partial\Phi}{\partial x} \ll U_\infty$ and $\alpha_0 \ll 1$), we have the linearized Bernoulli equation:

$$p - p_\infty = -\frac{\rho}{2}(u^2 - U_\infty^2) \quad (2.9)$$

$$\approx -\rho U_\infty(u - U_\infty) \quad (2.10)$$

$$= -\rho U_\infty \frac{\partial\Phi}{\partial x} \quad (2.11)$$

where p is the local pressure and p_∞ is the pressure at infinity. For a vorticity distribution $\gamma(x)$, $\frac{\partial\Phi}{\partial x}(x, 0^+) = \frac{\gamma(x)}{2}$ and at $z = 0^+$ plane, $\frac{\partial\Phi}{\partial x}(x, 0^-) = -\frac{\gamma(x)}{2}$ on the plane $z = 0^-$ (Katz and Plotkin 1991). Hence the pressure difference between the upper and lower surface Δp is

$$\Delta p(x) = p_l - p_u \quad (2.12)$$

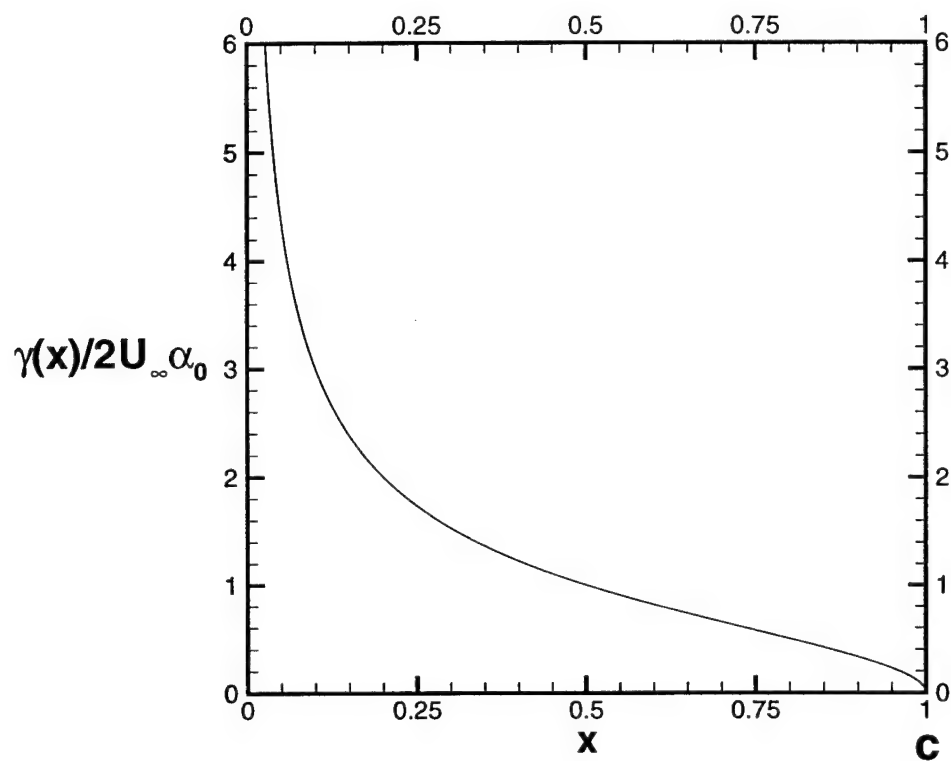


Figure 2.5: Nondimensional vorticity distribution on a flat, zero thickness, symmetric airfoil at an angle of attack α_0 . The two dimensional Kutta condition is satisfied at the trailing edge of the airfoil $\gamma(c) = 0$.

$$= \rho U_{\infty} \gamma(x) \quad (2.13)$$

The lifting force L is obtained by integrating $\Delta p(x)$ over the airfoil:

$$L = \int_0^c \Delta p(x) dx = \int_0^c \rho U_{\infty} \gamma(x) dx \quad (2.14)$$

Substituting Glauert's [1948] solution(2.7) into equation(2.14), we obtain the lift force acting on a thin, symmetric airfoil at an angle of attack α_0

$$L = \rho U_{\infty}^2 \pi c \alpha_0 \quad (2.15)$$

The pitching moment M_0 about the leading edge is

$$M_0 = \int_0^c \Delta p(x) x dx = \int_0^c \rho U_{\infty} \gamma(x) x dx \quad (2.16)$$

Hence for this zero-thickness symmetric airfoil,

$$M_0 = \rho U_{\infty}^2 \pi \frac{c^2}{4} \alpha_0 \quad (2.17)$$

The center of pressure x_{cp} , where the moment is zero (this also can be considered to be the point where the lift force acts), can be obtained by balancing the pitching moment and the product of the lift force and x_{cp}

$$x_{cp} = \frac{M_0}{L} \quad (2.18)$$

Substituting M_0 and L into equation (2.18), we find that for a zero-thickness symmetric airfoil at an angle of attack α_0 , x_{cp} is located at the one-quarter chord ($x_{cp} = \frac{1}{4}c$). Because the lift force acts at the one-quarter chord, a single point vortex with the strength $\Gamma = \int_0^c \gamma(x) dx$ is applied at this point to replace the continuous vortex distribution $\gamma(x)$. Note that the two dimensional-Kutta condition is satisfied automatically by Glauert's [1948] solution(2.7) (recall $\gamma(c) = 0$). Since the vorticity distribution $\gamma(x)$ is represented by a single point vortex Γ , the zero normal-velocity boundary condition at the surface can be specified correspondingly at a single point (collocation point) and the location of this point is obtained by solving

$$\frac{\Gamma}{2\pi(x_{col} - x_{cp})} = U_{\infty} \alpha_0 \quad (2.19)$$

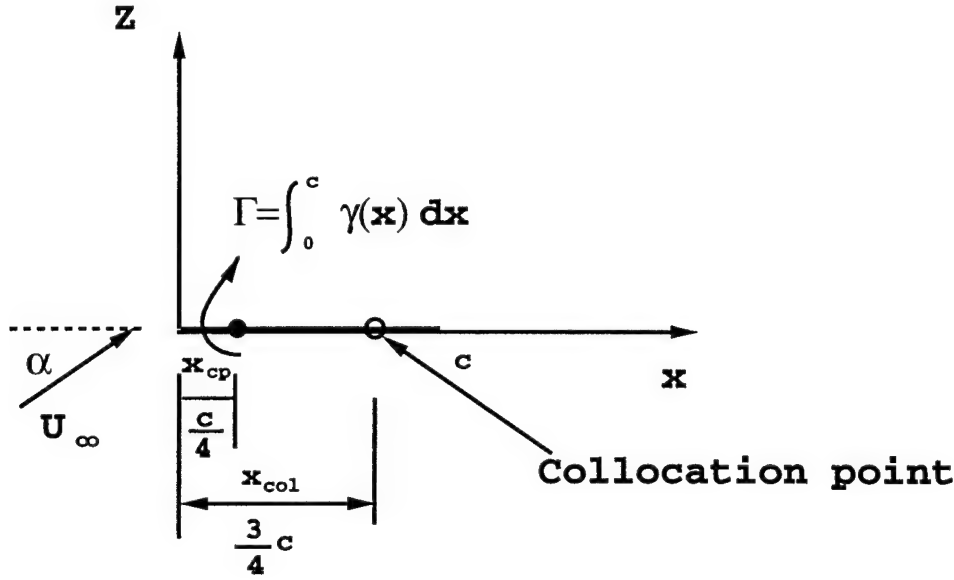


Figure 2.6: The "lumped-vortex" element structure.

and $x_{col} = \frac{3}{4}c$ as shown on Figure 2.6. In Figure 2.6, the concentrated point vortex is located at the one-quarter chord and the collocation point at the three-quarter chord and this two-dimensional point-vortex singularity may be called a "lumped vortex" element.

Now we apply the "lumped-vortex" element to a two dimensional airfoil. We divide a thin airfoil camberline into N panels and each panel has been replaced by a "lumped vortex element" as shown on Figure 2.7. Because the "lumped vortex" element satisfies the Kutta condition automatically, the last panel (panel 5 in the figure) inherently fulfills this requirement and no additional specification of the Kutta condition is needed. For a collocation point on panel k ($k=1, \dots, N$), the normal velocity induced by panel j is defined as the influence coefficient $A_{k,j}$, $j = 1, \dots, N$. Taking the circulation of the point vortex on panel j as Γ_j , evaluating the normal velocity at each collocation point and applying the zero normal-velocity condition on each of the N collocation points results in N equations:

$$\begin{pmatrix} A_{11} & A_{12} & \cdots & A_{1N} \\ A_{21} & A_{22} & \cdots & A_{2N} \\ \cdots & \cdots & \cdots & \cdots \\ A_{N1} & A_{N2} & \cdots & A_{NN} \end{pmatrix} \begin{pmatrix} \Gamma_1 \\ \Gamma_2 \\ \cdots \\ \Gamma_N \end{pmatrix} = \begin{pmatrix} R_1 \\ R_2 \\ \cdots \\ R_N \end{pmatrix} \quad (2.20)$$

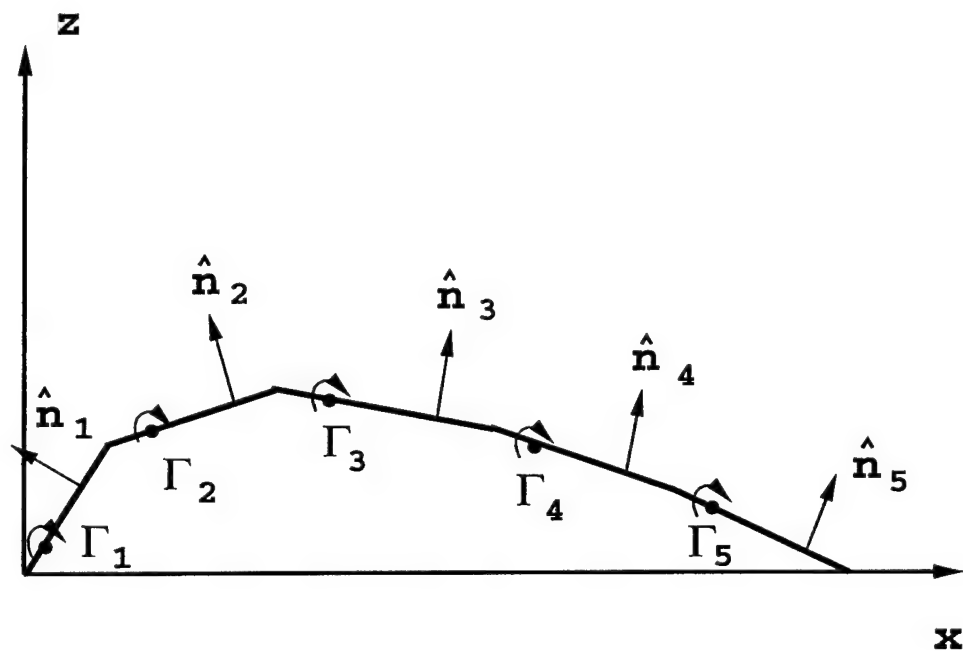


Figure 2.7: Point vortex representation of the thin, lifting airfoil.

where $R_k, k = 1, \dots, N$, is the normal component of the free stream velocity at each collocation point and is balanced by the total normal velocities induced by all the panels. The values of $\Gamma_j, j = 1, \dots, N$ can be computed numerically by solving this fully-dense-matrix equation. Having solved for the value of Γ_j , when assuming incompressible flow, the pressure on the surface and the fluid dynamic loads can be calculated using Bernoulli's equation.

Compressibility can be incorporated by introducing the Prandtl-Glauert compressibility factor β defined as

$$\beta = \sqrt{1 - M^2} \quad (2.21)$$

where M is the Mach number; however, the viscous effects are more complicated because the boundary layer must be considered in the solution (see Katz and Plotkin 1991 for more details).

The scheme illustrated above can be extended to introduce time-dependent terms from the boundary condition (2.3) when \vec{n} varies with time. The time-equivalent Kutta condition is also applied (see Katz and Plotkin 1991 for more details).

2.3 Three-Dimensional Wing Solutions

In this section, we extend the numerical solution developed for two-dimensional airfoil problems to three-dimensional wings. We divide the wing surface into N surface panels and N_w wake panels as shown on Figure 2.8. As mentioned above, for a two-dimensional airfoil, each panel has been replaced by a two-dimensional point vortex (i. e. the "lumped vortex" element); while for a three-dimensional wing, each surface panel is represented by a three-dimensional singularity (discussed below). Also, a collocation point is selected on each body surface panel where the zero normal velocity boundary condition is satisfied. For a collocation point P on a wing surface panel $k (k = 1, \dots, N)$ shown on Figure 2.9, the normal velocity induced by panel j is defined as the influence coefficient $A_{k,j}, j = 1, \dots, N + N_w$. Taking the strength of singularity element on the wing surface panel as $\mu_j, j = 1, \dots, N$ and on the wake as $\sigma_i, i = 1, \dots, N_w$, evaluating the normal velocity induced at each of the N collocation points and applying the zero normal-velocity boundary condition at each of the N collocation points results in N equa-

tions:

$$\begin{pmatrix} A_{11} & A_{12} & \cdots & A_{1N} & \cdots & A_{1N+N_w} \\ A_{21} & A_{22} & \cdots & A_{2N} & \cdots & A_{2N+N_w} \\ \cdots & \cdots & \cdots & \cdots & \cdots & \cdots \\ A_{N1} & A_{N2} & \cdots & A_{NN} & \cdots & A_{NN+N_w} \end{pmatrix} \begin{pmatrix} \mu_1 \\ \mu_2 \\ \cdots \\ \mu_N \\ \sigma_1 \\ \cdots \\ \sigma_{N_w} \end{pmatrix} = \begin{pmatrix} R_1 \\ R_2 \\ \cdots \\ R_N \end{pmatrix} \quad (2.22)$$

where $R_k, k = 1, \dots, N$ is the normal component of the free stream velocity at each collocation point and is balanced by the total normal velocities induced by all the panels. Applying the Kutta condition, the strength of each singularity element on the wake panel σ_i can be expressed in the corresponding upper and lower wing-surface singularity elements μ_j . Therefore, these N equations can be written as:

$$\begin{pmatrix} A'_{11} & A'_{12} & \cdots & A'_{1N} \\ A'_{21} & A'_{22} & \cdots & A'_{2N} \\ \cdots & \cdots & \cdots & \cdots \\ A'_{N1} & A'_{N2} & \cdots & A'_{NN} \end{pmatrix} \begin{pmatrix} \mu_1 \\ \mu_2 \\ \cdots \\ \mu_N \end{pmatrix} = \begin{pmatrix} R'_1 \\ R'_2 \\ \cdots \\ R'_N \end{pmatrix} \quad (2.23)$$

The values of $\mu_j, j = 1, \dots, N$ can be computed numerically by solving this fully-dense-matrix equation. Having solved for the value of μ_j , the pressure on the surface and the fluid dynamic loads can be calculated using the incompressible Bernoulli equation.

Now we consider the three-dimensional singularity elements. Among the three dimensional singularity elements, the vortex-ring and horseshoe-vortex element are commonly used to represent the lifting-wing surface in the helicopter rotor-performance calculation.

- Vortex ring

A vortex ring consists of four line vortex segments with the same circulation. Figure 2.10 shows a vortex ring composed of four straight line vortices: AB, BC, CD and DA. The velocity induced by each segment is evaluated using the Biot-Savart law. This vortex ring model is applied to represent both the wing surface and the wake panels.

Let us consider the wake panel first. For a steady-state flow, the Kutta condition requires that the wake circulation be constant in the stream-wise direction and equal to the surface circulation at the trailing edge

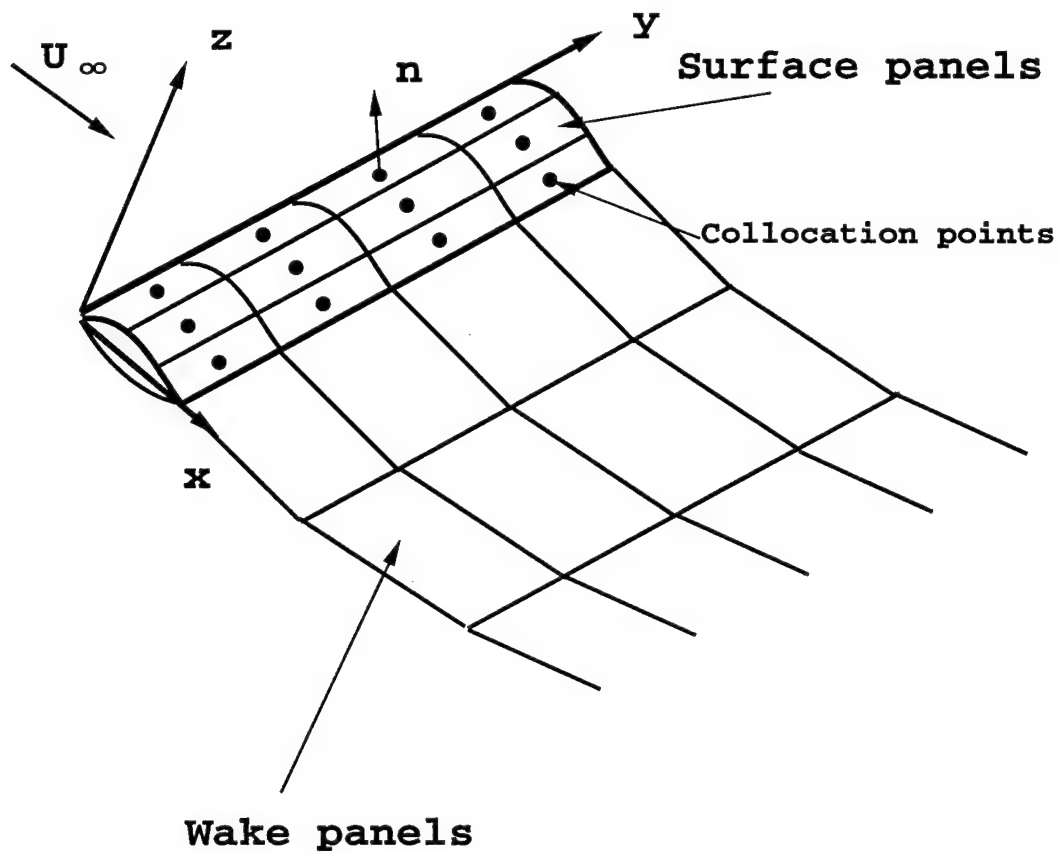


Figure 2.8: Approximation of the wing surface by panel elements.

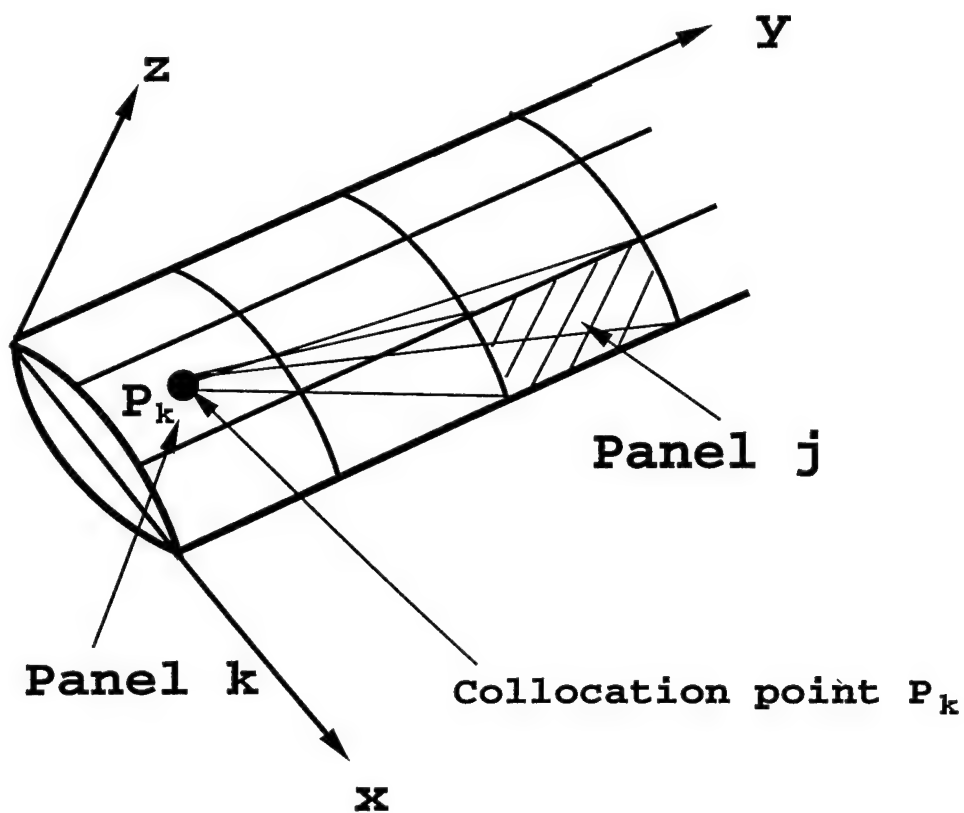


Figure 2.9: Influence of panel j on collocation point P_k .

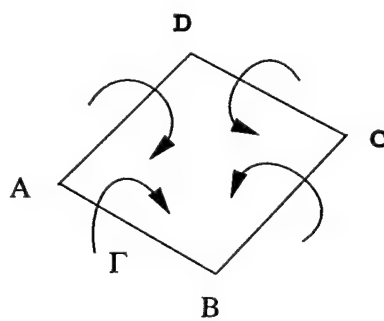


Figure 2.10: A vortex ring element.

of the wing where it emanates. In effect, the wake panels are trailing strips of vorticity.

Now we replace each surface panel with the vortex ring. Each panel edge is represented by a straight-line vortex and thus a rectangular vortex ring is formed. The collocation point is located at the geometric center of each panel as shown on Figure 2.11. Kocurek *et al.*[1976] applied this method to represent the rotor blade in a hover-performance calculation. The shortcoming with such replacement is that for each last chordwise panel (i.e. those on the trailing edge of the wing), the Kutta condition is not satisfied because the bound vortex is not located at the one-quarter chord line (recall the "lumped vortex element"). The horseshoe vortex panel method overcomes this disadvantage and is discussed subsequently.

- Horseshoe vortex

In the current work, the three-dimensional horseshoe vortex is applied. Now we explain how to replace each surface panel by a horseshoe vortex and how to select the collocation point to satisfy the three-dimensional Kutta condition.

A horseshoe vortex is a simplified case of the vortex ring. A horseshoe vortex consists of a bound vortex along the panel quarter-chord line together with two trailing vortices lying along the panel edges and extending to infinity downstream. The boundary condition of zero normal velocity on the wing surface is satisfied at the three-quarter chord point on the centerline of each panel (collocation point) and the trailing vortices emanate from the panel quarter-chord line (see Figure 2.12). Actually, this model is based on the two-dimensional "lumped vortex" element model discussed above. By placing the leading vortex segment of the horseshoe vortex at the quarter chord line of the panel, the two-dimensional Kutta condition is satisfied along the chord and it is assumed that the two-dimensional Kutta condition satisfactorily accounts for the three-dimensional Kutta condition.

Applying N horseshoe panels over the three-dimensional wing surface (small lift, thin airfoil and large aspect ratio), the solution can be obtained by solving the $N \times N$ fully-dense-matrix equation.

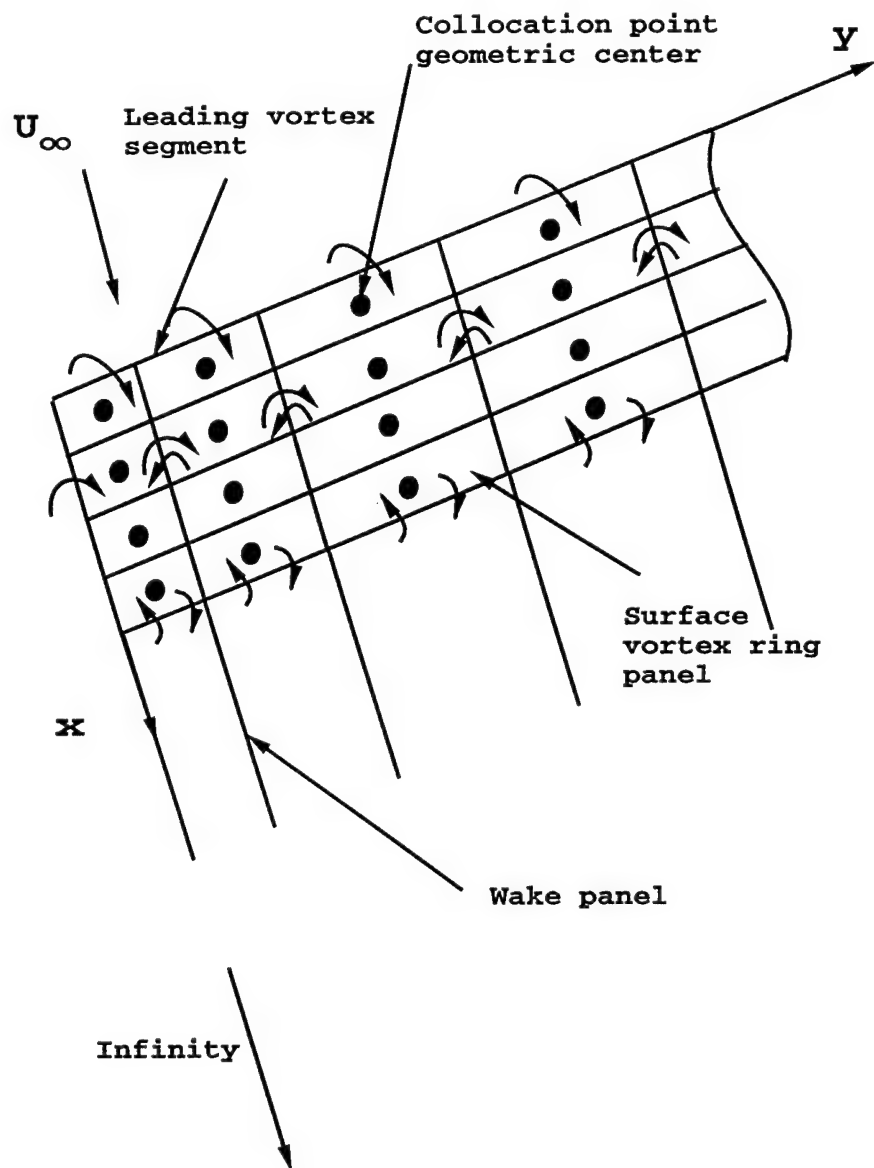


Figure 2.11: Vortex ring model.

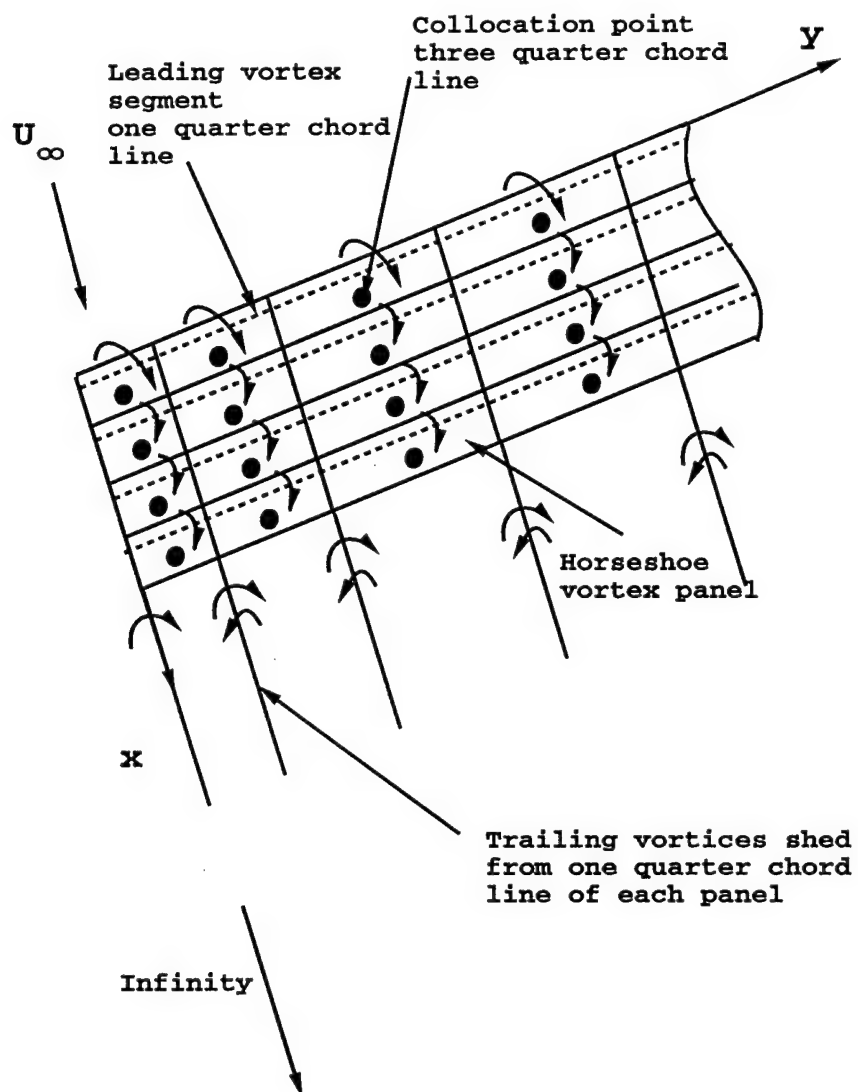


Figure 2.12: Horseshoe vortex model.

Chapter 3

Asymptotics of Lifting Line and Lifting Surface Theory for a Fixed Wing

3.1 Introduction

The basic structure of the vortex wake of a fixed wing is that the shed vorticity ultimately rolls up into a strong tip-vortex. Because the flow in the tip region is highly three-dimensional and unsteady, it makes both experiments and computations extremely difficult. A brief review of the consequence and complexity of the tip-vortex and the means to reduce the tip-vortex strength has been presented by Jain-Ming James Wu [1992].

In this chapter, we consider a fixed wing of large aspect ratio. From the analytical and computational perspective, the flow near the tip can be viewed as the flow over a semi-infinite wing. For a semi-infinite wing, using the method of matched asymptotic expansions in terms of a small parameter defined as the inverse aspect ratio, Van Dyke [1964] has shown that the classical inviscid lifting-line integral equation is obtained. It is shown here that this lifting-line equation has an analytical solution given by Stewartson[1960] for the inner region near the tip. A similar analysis for the lifting-surface theory is performed and the numerical results compare well with Stewartson[1960]'s analytical solutions and the experimental data of McAlister and Takahashi [1991].

The bound circulation drops to zero at the wingtip, while away from the

tip, it approaches a constant. Corresponding to this spanwise variation of the bound circulation, the trailing vortices in the tip region roll over each other quickly and form a strong single tip-vortex downstream. However, in the region away from the tip, the trailing vortices roll up very slowly.

We applied our numerical technique to compute the induced vertical velocity behind the wing and compare it with the experimental data of McAlister and Takahashi [1991] and the comparison is encouraging. This indicates that viscosity and turbulence have only a minor effect on the initial formation of the tip-vortex.

3.2 Theoretical Considerations

A mathematical basis for lifting-line theory for a fixed wing is given in Van Dyke [1975] in which the method of matched asymptotic expansions is used to construct the solution for the circulation and hence the effective angle of attack α_e . The effective angle of attack α_e is defined as

$$\alpha_e = \alpha_0 - \alpha_i \quad (3.1)$$

where α_0 is the geometric angle of attack and α_i is the result of the downwash induced by the wake

$$\alpha_i = \frac{w_i}{U_\infty} \quad (3.2)$$

where w_i is the downwash induced by the wake and U_∞ is the free-stream velocity. As illustrated by Van Dyke [1975], an outer region, in which the complete wing is represented as a line of singularities, is matched with an inner region represented as a locally two dimensional airfoil. The inverse of the aspect ratio is taken as the small parameter for a series expansion. The results for the lift-curve slope for the elliptic wing using this method can be made more accurate as more terms are added to the asymptotic series (Van Dyke [1975], p.175); this is important since the classical lifting-surface method is much more computationally demanding than lifting-line theory.

It is clear, however, that Van Dyke's [1975] analysis, carried out for a cusp-shape tip for which there is no tip-vortex, breaks down near the noncusp-shape tip, requiring an additional inner expansion for the region around the tip (Van Dyke [1964, 1975]). In his analysis, the classical lifting-line model breaks down in a region of width $O(A^{-2})$ where A is the aspect ratio of the

wing. It is for this reason that the tip-vortex circulation cannot be estimated from lifting-line theory alone since the theory does not hold at the tip. Consequently, the tip-vortex circulation must be estimated by some other means. Since the circulation directly influences the subsequent position of the tip-vortex and the intensity of the subsequent interactions with other components of the wake, it is important to determine the circulation as precisely as possible. We use lifting-surface theory to evaluate the inner solution, valid near the tip.

3.3 The Lifting-Line Integral Equation For the Semi-infinite Fixed Wing

In this section we develop a model to obtain the circulation of the tip vortex by using the fundamental lifting-line integral equation. This is appropriate since the large aspect ratio wing is, to leading order in the large aspect ratio, a lifting line. We consider the steady incompressible flow past a fixed wing.

The integral equation of lifting-line theory has been derived for the case of a fixed wing in many text books and the result is Katz and Plotkin[1991]

$$\Gamma^*(y^*) = \frac{1}{2}mc \left(U_\infty \alpha_0 - \frac{1}{4\pi} \int_{-\frac{b}{2}}^{\frac{b}{2}} \frac{d\Gamma^*}{dy_0^*} \frac{dy_0^*}{y^* - y_0^*} \right) \quad (3.3)$$

where Γ^* is the circulation, U_∞ is the speed far from the wing and b is the span of the wing; also $c(y)$ is the local value of the chord. Here m is a constant equivalent to the lift curve slope which is airfoil dependent. For a flat plate, $m = 2\pi$. If the plane of the wing varies with span, $c = c(y)$. It is important to understand the assumptions of linearized theory associated with the derivation of this equation. First the trailing wake is assumed to remain in the plane of the wing $z = 0$ for all time. Second, the pressure difference between the bottom and the top of the wing must approach zero at the tip, and so $\Gamma^* = 0$ there also.

Let us non-dimensionalize this equation by writing

$$\Gamma = \frac{\Gamma^*}{U_\infty b}$$

Then equation (3.3) becomes

$$\Gamma(y) = \frac{m}{2} A^{-1} C(y) \left(\alpha_0 - \frac{1}{4\pi} \int_{-\frac{1}{2}}^{\frac{1}{2}} \frac{d\Gamma}{dy_0} \frac{dy_0}{y - y_0} \right) \quad (3.4)$$

where y is dimensionless and $y = \frac{y^*}{b}$, $c(y) = c_0 C(y)$ and c_0 is the dimensional reference chord, $c_0 = \frac{b^2}{S}$ where S is the wing area. Thus $A = \frac{b}{c_0}$ is the aspect ratio of the wing, assumed to be large. In the limit of very large aspect ratio, to an observer placed a distance of the order of the semi-span away from the wing, the wing profile (Figure 3.1(a)) looks as if it were a line, i.e. the lifting line, as indicated by Figure 3.1(b). Away from the wing tip, since A is large, the circulation can be expanded in powers of A^{-1} and the leading order outer solution is

$$\Gamma(y) \sim \frac{\frac{m}{2} \alpha_0 C(y)}{A}. \quad (3.5)$$

Note that this value of the bound circulation is non-zero at the tip (provided $C(y) \neq 0$) and so this solution breaks down near the tip of the wing where the bound circulation must vanish. This error results in a tip-singularity in higher-order terms.

To analyze the behavior of the bound circulation near the tip, we make the transformation

$$Y = \left(\frac{1}{2} - y\right) A^\beta$$

where β is a constant. Substituting into equation (3.4) we find that to balance both sides, $\beta = 1$. If we assume that Γ remains $O(A^{-1})$ near the tip, and a finite chord at the tip, then Γ may be expanded as

$$\Gamma = A^{-1} \Gamma_1 + A^{-2} \Gamma_2 + \dots$$

and substituting in equation (3.4) above, we get

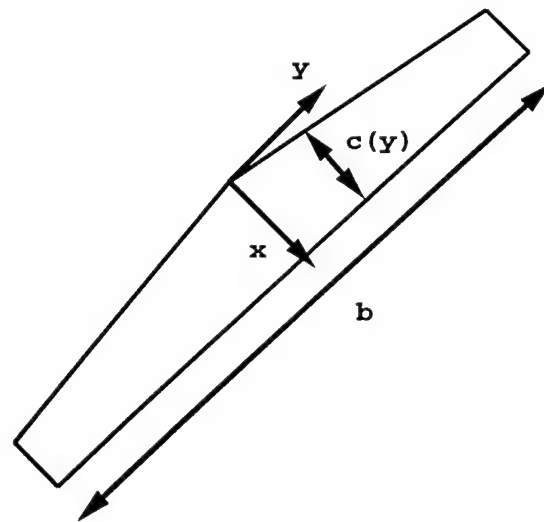
$$\Gamma_1(Y) = \frac{m}{2} C_{tip} \left(\alpha_0 - \frac{1}{4\pi} \int_0^\infty \frac{d\Gamma_1}{dY_0} \frac{dY_0}{Y - Y_0} \right) \quad (3.6)$$

and

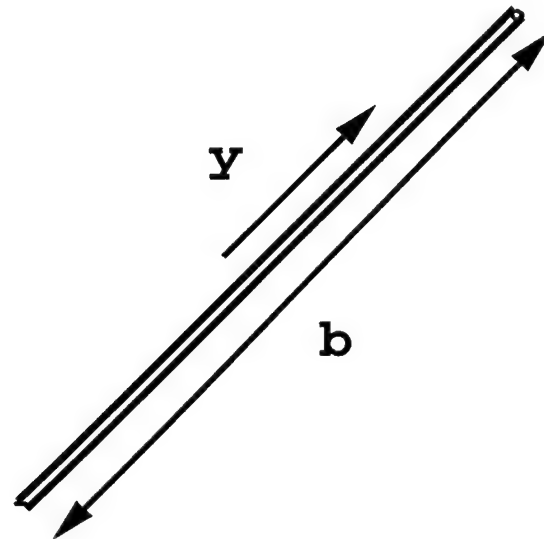
$$\Gamma_2(Y) = \frac{1}{4\pi} \int_0^\infty \frac{d\Gamma_2}{dY_0} \frac{dY_0}{Y - Y_0} \quad (3.7)$$

Note that for a rectangular wing $C_{tip} = 1$ and equation (3.6) is precisely the equation solved by Stewartson [1960]. Thus to leading order near the tip, the wing appears infinite in length and the solution is that of Stewartson [1960]

$$\Gamma_1(Y) = \frac{m}{2} \alpha_0 \left(1 - \frac{1}{\pi} \int_0^\infty \frac{e^{-tY}}{(1+t^2)^{3/4}} e^{-\frac{1}{\pi} \int_0^t \frac{\log \theta d\theta}{1+\theta^2}} dt \right) \quad (3.8)$$



(a)



(b)

Figure 3.1: (a) Cartesian coordinate system relative to a fixed wing. (b) For large aspect ratio A , the wing appears as if it were a line in the outer region; i.e. the lifting line.

Equation (3.8) defines the bound circulation on the wing near the tip to leading-order and this is the so-called inner solution. This solution compares very well with the results of a numerical lifting-surface calculation which is discussed in the next section.

3.4 Lifting Surface Theory For the Semi-Infinite Fixed Wing

In this section we consider the lifting surface analog of lifting-line theory for the semi-infinite wing. As with lifting line theory, the leading-order inner solution near the wing tip corresponds to a semi-infinite wing.

The lifting surface equation for the finite fixed wing is given by Katz and Plotkin[1991] where we have assumed a flat plate airfoil.

$$-\frac{1}{4\pi} \int_{-\frac{1}{2}}^{\frac{1}{2}} \int_0^{\epsilon c(y)} \frac{\gamma_y(x-x_0) + \gamma_x(y-y_0)}{[(x-x_0)^2 + (y-y_0)^2]^{\frac{3}{2}}} dx_0 dy_0 + \alpha_0 = 0 \quad (3.9)$$

where all lengths are made dimensionless on the semi-span and velocities on the freestream speed U_∞ and $\epsilon = \frac{c}{b}$. Solution of this equation for the circulation per unit length γ_x and γ_y give the solution in the x and y direction. To focus on the region near the tip $y = \frac{1}{2}$, the inner solution, as in the previous section, we define the inner variable as

$$X = xA$$

$$Y = \left(\frac{1}{2} - y\right)A$$

so that the lifting surface equation becomes

$$-\frac{1}{4\pi} \int_0^\infty \int_0^{c_{tip}} \frac{\gamma_Y(X-X_0) + \gamma_X(Y-Y_0)}{[(X-X_0)^2 + (Y-Y_0)^2]^{\frac{3}{2}}} dX_0 dY_0 + \alpha_0 = 0 \quad (3.10)$$

This is the same equation as for the outer solution except for the limits on the integration in Y . This means that to leading order, the inner solution for the lifting surface is also for a semi-infinite wing. Unlike the lifting-line equation, the analytical solution to this two-dimensional integral equation is unknown and so we solve it numerically using a panel method.

3.4.1 Panel Representation of the Semi-Infinite Wing

According to the method of Schlichting and Thomas [1947], the semi-infinite wing may be represented by vortex panels distributed over its surface, as illustrated on Figure 3.2 (a). In Figure 3.2 (a), only three chordwise and nine spanwise panels including semi-infinite panels (discussed below) are shown, while in the numerical calculation, ten chordwise and twenty spanwise panels were used. Each wing panel consists of a horseshoe vortex system with a bound vortex along the panel quarter-chord line together with trailing vortices lying along the panel edges and extending through the trailing edge of the wing to infinity downstream. Figure 3.2 (b) shows a wing surface panel replaced by a horseshoe vortex.

In the classical lifting-line theory, the shed wake is assumed to form in the plane of the wing and the vortices are assumed to be straight line vortices, which is a small-lift assumption, consistent with other assumptions in the theory.

We now define local panel-based coordinates; define the x -axis to be oriented in the chordwise direction, the y -axis spanwise, and the z -axis vertical as shown in Figure 3.2 (b). x and y are measured from the midpoint of the selected panel, and z from the plane of the wing. The panel-width dimensions are $2a$ by $2b^1$ in the chordwise and spanwise directions respectively. Then the velocity induced by each horseshoe vortex segment is evaluated using the Biot-Savart law with a cut-off parameter μ as shown on Figure 3.3:

$$d\vec{V} = \frac{\Gamma}{4\pi\bar{R}^3} d\vec{S} \times \vec{R} \quad (3.11)$$

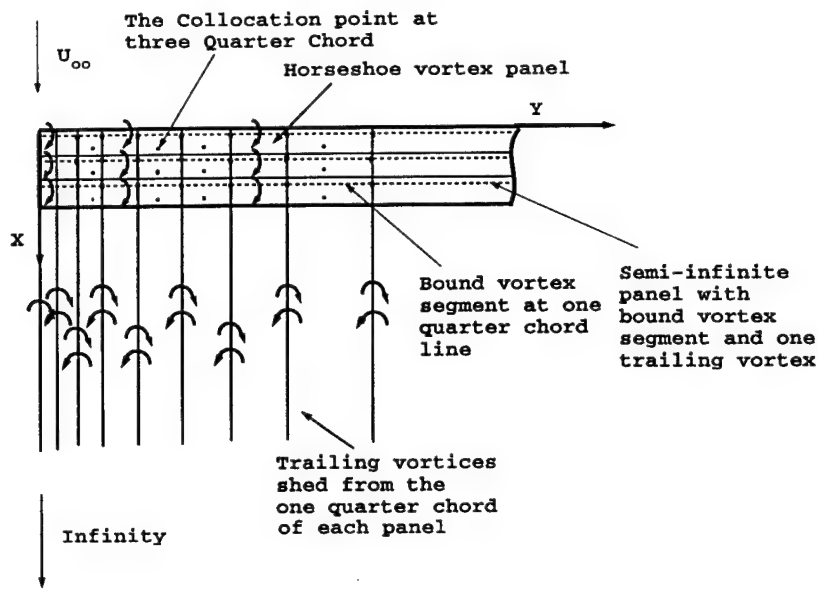
where $\bar{R} = \sqrt{R^2 + \mu^2}$.

The swirl velocity induced by a straight vortex segment with unit strength as shown on Figure 3.4, is given as (Glauert 1948)

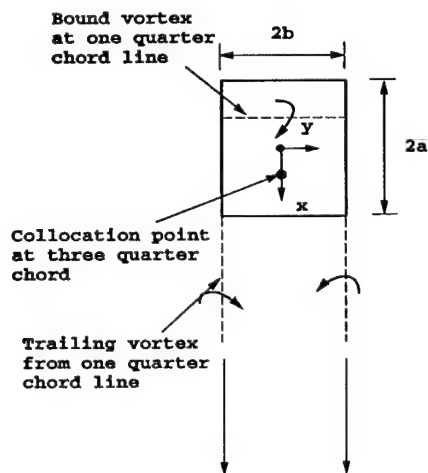
$$V_{swirl} = \frac{1}{4\pi d} (\cos\beta_1 - \cos\beta_2) \quad (3.12)$$

By applying equation (3.12) to each straight vortex segment of a horseshoe vortex, the velocity induced by the entire horseshoe vortex is obtained. Now we derive the velocity induced by the unit bound-vortex segment from the Biot-Savart law. Figure 3.5 (a) shows a horseshoe vortex segment ABCD

¹The variable b used in this section refers to the panel-width and not the wing span as on Figure 3.1. The x, y, z coordinate system used in this portion of the section refers to local panel coordinates as well.



(a)



(b)

Figure 3.2: Horseshoe-vortex panel implementation of a semi-infinite wing. (a) Definition of the global coordinates. Only three chordwise panels are shown here. In the numerical calculation, ten chordwise panels are used. (b) Definition of the local panel coordinates. The solid box represents a surface panel which is replaced by a horseshoe vortex (represented by dash lines).

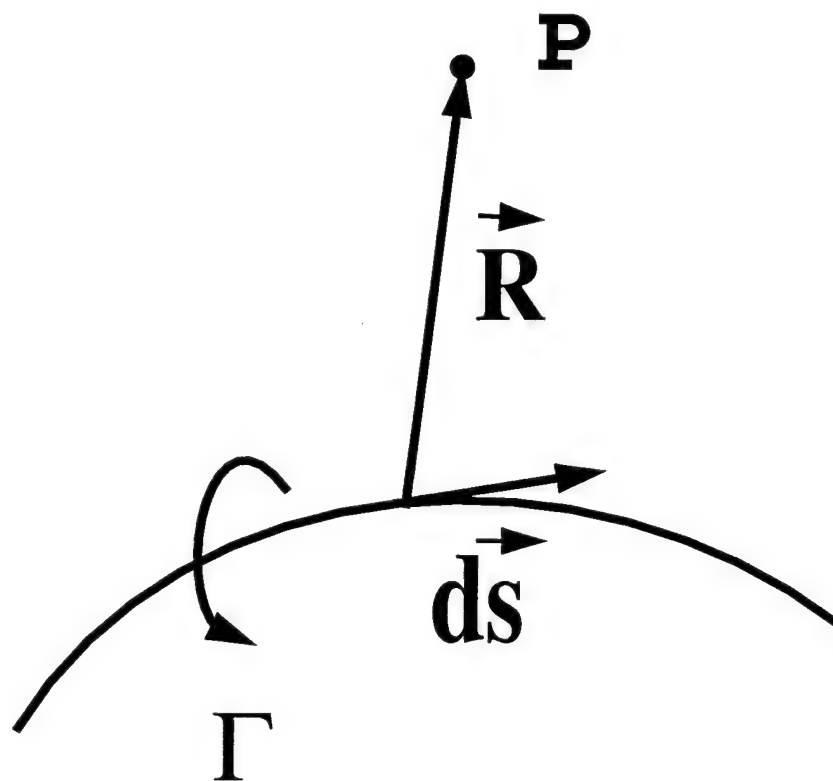


Figure 3.3: The velocity at P induced by a three-dimensional vortex using the Biot-Savart law.

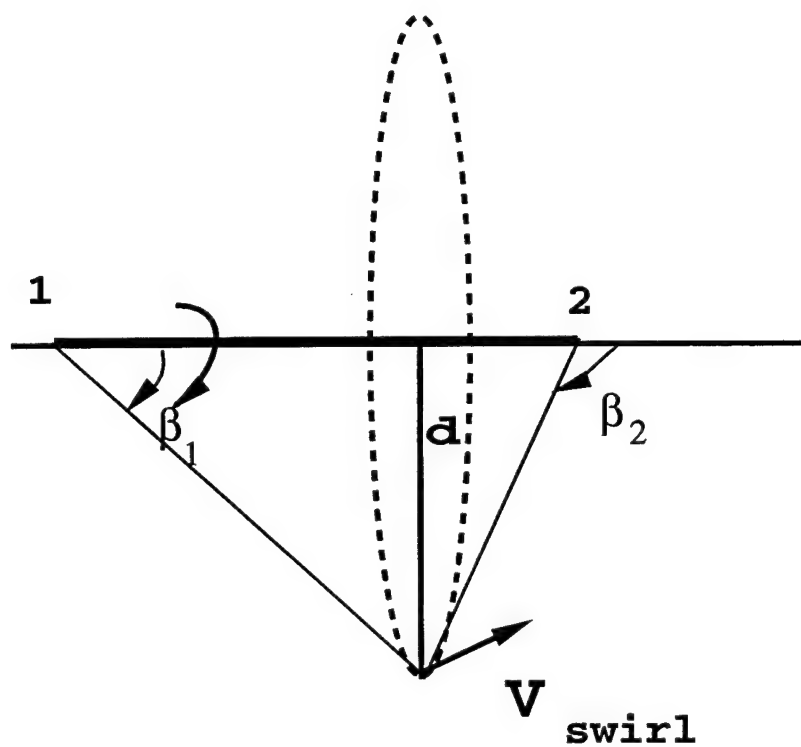
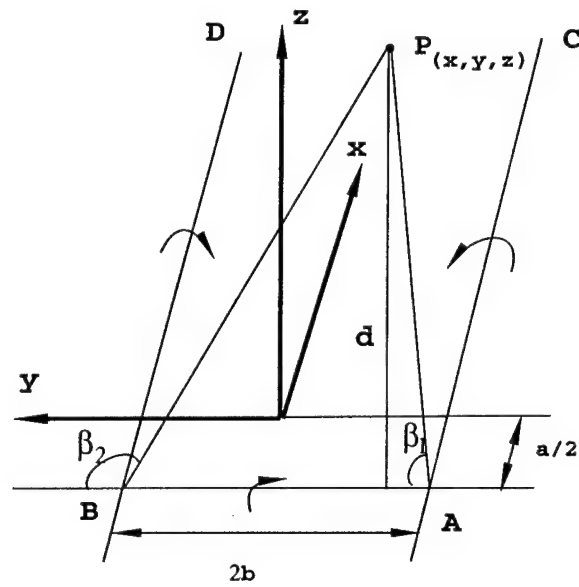
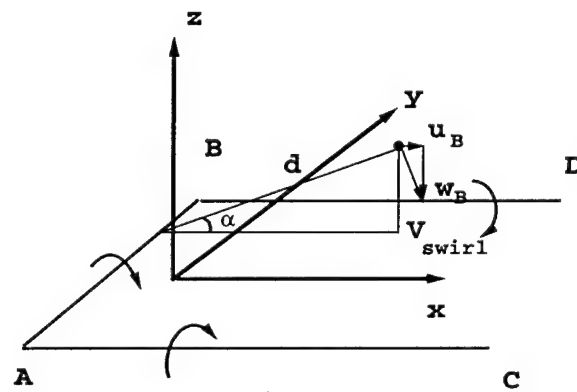


Figure 3.4: Velocity induced by a straight vortex segment.



(a)



(b)

Figure 3.5: Velocity induced by a horseshoe-vortex segment. (a) shows the swirl velocity and (b) shows the x and z components of the swirl velocity.

with the unit strength. For the velocity induced by the bound vortex AB at P(x,y,z), the swirl velocity can be calculated as

$$\cos\beta_1 = \frac{y+b}{\sqrt{(x+\frac{a}{2})^2 + (y+b)^2 + z^2}} \quad (3.13)$$

$$\cos\beta_2 = \frac{y-b}{\sqrt{(x+\frac{a}{2})^2 + (y-b)^2 + z^2}} \quad (3.14)$$

and

$$d = \sqrt{(x+\frac{a}{2})^2 + z^2} \quad (3.15)$$

so the swirl velocity at P induced by AB is

$$V_{swirl} = \frac{1}{4\pi\sqrt{(x+\frac{a}{2})^2 + z^2}} \left(\frac{y+b}{\sqrt{(x+\frac{a}{2})^2 + (y+b)^2 + z^2}} - \frac{y-b}{\sqrt{(x+\frac{a}{2})^2 + (y-b)^2 + z^2}} \right) \quad (3.16)$$

Now we consider the x and z components of the swirl velocity. Because the bound-vortex segment AB is parallel to the y axis, so the y component is zero. From Figure 3.5 (b),

$$u_B(x, y, z) = V_{swirl}\sin\alpha \quad (3.17)$$

$$w_B(x, y, z) = V_{swirl}\cos\alpha \quad (3.18)$$

and

$$\sin\alpha = \frac{z}{\sqrt{(x+\frac{a}{2})^2 + z^2}} \quad (3.19)$$

$$\cos\alpha = \frac{x+\frac{a}{2}}{\sqrt{(x+\frac{a}{2})^2 + z^2}} \quad (3.20)$$

Substituting equation (3.16) into equations above, we have

$$u_B(x, y, z) = \frac{1}{4\pi} \frac{z}{(x+\frac{a}{2})^2 + z^2} \times \left[\frac{y+b}{\sqrt{(x+\frac{a}{2})^2 + (y+b)^2 + z^2}} - \frac{y-b}{\sqrt{(x+\frac{a}{2})^2 + (y-b)^2 + z^2}} \right]$$

$$w_B(x, y, z) = -\frac{1}{4\pi} \frac{x + \frac{a}{2}}{(x + \frac{a}{2})^2 + z^2} \times \\ \left[\frac{y + b}{\sqrt{(x + \frac{a}{2})^2 + (y + b)^2 + z^2}} - \frac{y - b}{\sqrt{(x + \frac{a}{2})^2 + (y - b)^2 + z^2}} \right]$$

while the two unit trailing vortices produce the contributions can be obtained similarly

$$v_{T_1}(x, y, z) = \frac{1}{4\pi} \frac{z}{(y + b)^2 + z^2} \times \\ \left[\frac{x + \frac{a}{2}}{\sqrt{(x + \frac{a}{2})^2 + (y + b)^2 + z^2}} + 1 \right]$$

$$w_{T_1}(x, y, z) = \frac{-1}{4\pi} \frac{y + b}{(y + b)^2 + z^2} \times \\ \left[\frac{x + \frac{a}{2}}{\sqrt{(x + \frac{a}{2})^2 + (y + b)^2 + z^2}} + 1 \right]$$

and

$$v_{T_2}(x, y, z) = \frac{-1}{4\pi} \frac{z}{(y - b)^2 + z^2} \times \\ \left[\frac{x + \frac{a}{2}}{\sqrt{(x + \frac{a}{2})^2 + (y - b)^2 + z^2}} + 1 \right]$$

$$w_{T_2}(x, y, z) = \frac{1}{4\pi} \frac{y - b}{(y - b)^2 + z^2} \times \\ \left[\frac{x + \frac{a}{2}}{\sqrt{(x + \frac{a}{2})^2 + (y - b)^2 + z^2}} + 1 \right]$$

where u , v and w are the x , y and z velocity components respectively. Subscript B represents the bound-vortex segment and T_1 , T_2 represent two trailing vortices respectively.

Now we consider the global coordinates. Define the x -axis to be oriented in the chordwise direction, originating at the leading edge of the wing, the y -axis spanwise, originating at the wing-tip, positive inboard, and the z -axis, vertical as shown on Figure 3.2 (a). The panel-influence coefficients A_{kj} are given by the normal velocity induced in the plane of the wing at the 3/4 chord position on panel k due to the horseshoe vortex of unit circulation with the bound vortex at the 1/4 chord position on panel j , as

$$A_{kj} = w_B(x_{kj}, y_{kj}, 0) + w_{T_1}(x_{kj}, y_{kj}, 0) + w_{T_2}(x_{kj}, y_{kj}, 0)$$

where

$$x_{kj} = x_k - x_j + \frac{a}{2}$$

and

$$y_{kj} = y_k - y_j$$

Note x_k, x_j, y_k, y_j are global variables and x_{kj}, y_{kj} are the local variables $x_k - x_j + \frac{a}{2}$ and $y_k - y_j$.

The boundary condition of zero normal velocity on the wing surface is satisfied at the three-quarter chord point on the centerline of each panel and the trailing vortices emanate from the panel quarter-chord line (see Figure 3.6). Thus the panel circulations $\Gamma_k, k = 1, \dots, N$ may be evaluated from the surface boundary condition, expressed as the linear equation

$$\sum_{j=1}^N A_{kj} \Gamma_j = -w_\infty$$

For a flat-plate airfoil, the right side vector w_∞ is just the vertical component of the freestream velocity vector; i.e., $U_\infty \alpha_0$ in linearized theory.

Because of the strong variation of circulation near the wing-tip, it is helpful to use panels of variable width. Guided by lifting-line theory, we have chosen the variation

$$y = \bar{b} \tan \theta, 0 < \theta < \pi/2$$

where \bar{b} is the computational span of the wing. Thus distributing the panels uniformly in the θ variable increases the density of panels near the wingtips. A constant chordwise width was used for each panel, since it was found less important to have a similar distribution in the chordwise variable x .

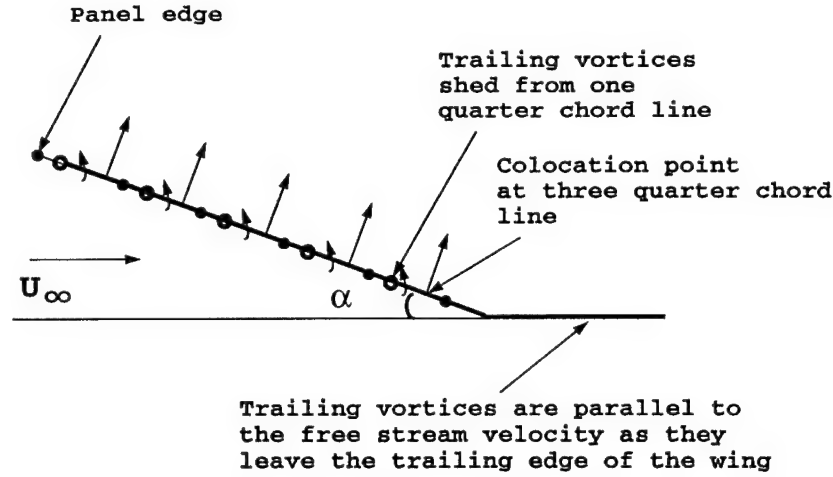


Figure 3.6: The trailing vortex system emanates from the quarter-chord line of each panel (hollow circles), extending through the trailing edge of the wing to infinity downstream. Arrows denote the direction of the normal velocity at the panel three-quarter chord line. Solid circles denote panel edges.

For the numerical computation, the semi-infinite wing is represented by a finite number of panels outboard of a semi-infinite panel. The baseline configuration uses twenty chordwise panels and forty spanwise panels. The semi-infinite panels have been applied beyond the fortieth spanwise panel at each chordwise location to model the semi-infinite aspect of the problem. Each of the semi-infinite panels has only one bound vortex and one trailing vortex, i.e., half of a horseshoe vortex. The bound vortex extends to infinity spanwise and the trailing vortex extends to infinity downstream as shown on Figure 3.2(a). The boundary condition of finite circulation at infinity is represented by requiring the values of bound circulation of each of the semi-infinite panels to be equal to those of the panels next to them. The velocities induced by the leading bound-vortex segment of the semi-infinite panel are

$$u_{B\infty}(x, y, z) = \frac{1}{4\pi} \frac{z}{(x + \frac{a}{2})^2 + z^2} \times [1 - \frac{y + b}{\sqrt{(x + \frac{a}{2})^2 + (y + b)^2 + z^2}}]$$

$$w_{B\infty}(x, y, z) = -\frac{1}{4\pi} \frac{x + \frac{a}{2}}{(x + \frac{a}{2})^2 + z^2} \times$$

$$\left[1 - \frac{y + b}{\sqrt{(x + \frac{a}{2})^2 + (y + b)^2 + z^2}}\right]$$

3.4.2 Results for a Rectangular Wing

We have applied the horseshoe-vortex panel model to the case of a rectangular wing. A few of these results are of interest to show how the lift is distributed over the surface of the wing, and how the vorticity is shed from the wing, particularly how the flow rolls up around the wingtip to initiate the trailing wingtip vortex. The results to follow are for the inner region near the wingtip. The bound circulation is defined as

$$\Gamma(Y_k) = \sum_{j=1}^{n_x} \Gamma_{jk}, k = 1 \dots n_y \quad (3.21)$$

where n_x and n_y are the number of chordwise and spanwise panels respectively. Y_j is the spanwise location of the center point of panel j .

The trailing vorticity becomes small at a distance of the order of a chord length from the wingtip. Consequently accurate computation of the trailing vorticity requires a strong concentration of the horseshoe-vortex panels in the region near the wingtip, as discussed above. Figure 3.7 shows the effect of the number of panels used in the lifting surface code. Note that there is little difference among the four results. The result with one chordwise panel is fairly good and the result with ten chordwise panels is satisfactory. This suggests that ten chordwise panels and twenty spanwise panels are sufficient for the bound circulation computations.

Figure 3.8 shows the results of the lifting-surface computation for the bound circulation on the wing. Note the excellent comparison of the numerical results with the formula of Stewartson[1960]. In the region of sharp drop-off of the bound circulation, the individual vortex filaments will roll around each other to form the tip-vortex. In the region away from the tip, where the spanwise variation of the bound circulation approaches zero, no vorticity is shed to leading-order.

Figure 3.9 shows the circulation for each panel. Here we have used twenty chordwise panels and forty spanwise panels. Note that the distribution of circulation has its maximum value near the leading edge (i.e. at the one quarter chord point of the most forward panel) and sharply decreases toward zero away from the leading edge.

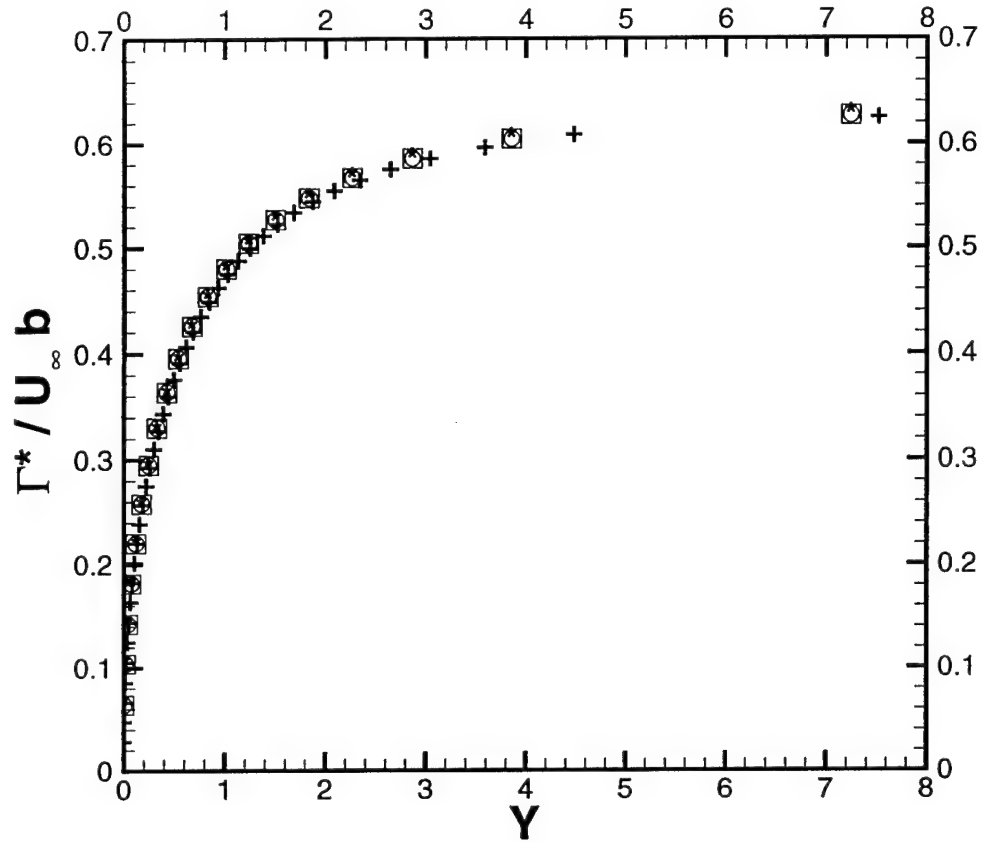


Figure 3.7: Comparison of the computational results for different number of panels used in the lifting surface code. Here '*' represents the computational results with one chordwise and twenty spanwise panels, the box represents the computational results with four chordwise and twenty spanwise panels, 'o' represents the computational results with ten chordwise and twenty spanwise panels and '+' represents the computational results with twenty chordwise and forty spanwise panels. The angle of attack is 12° .

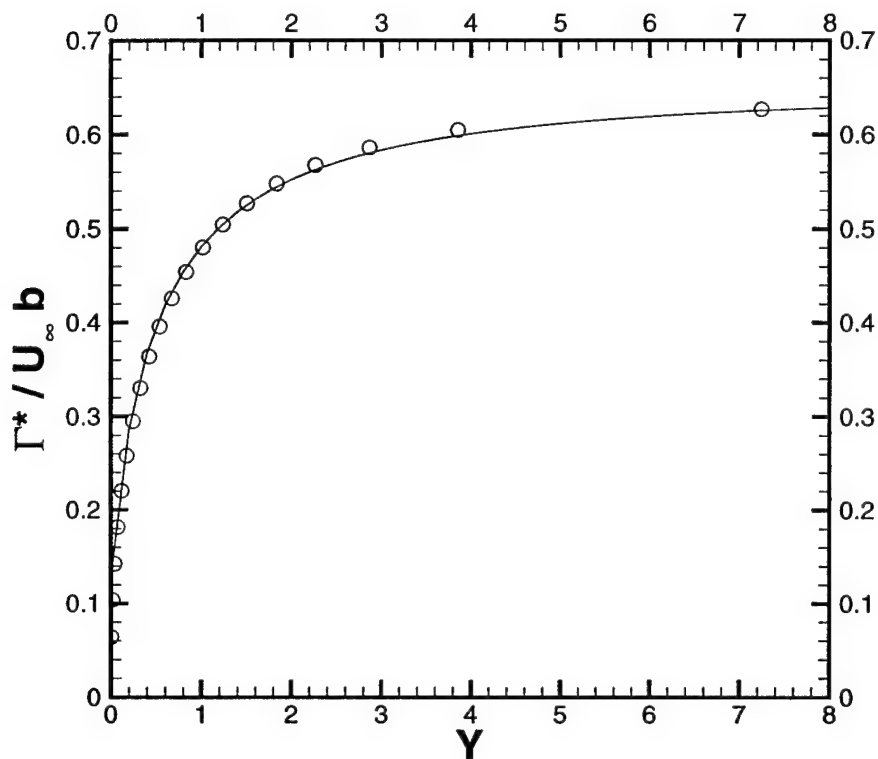


Figure 3.8: Circulation distribution for a semi-infinite rectangular wing. The solid line is the analytical solution of Stewartson [1960] for the lifting line. The circle is the computational results from the lifting-surface code with ten chordwise and twenty spanwise panels. The angle of attack is 12° .

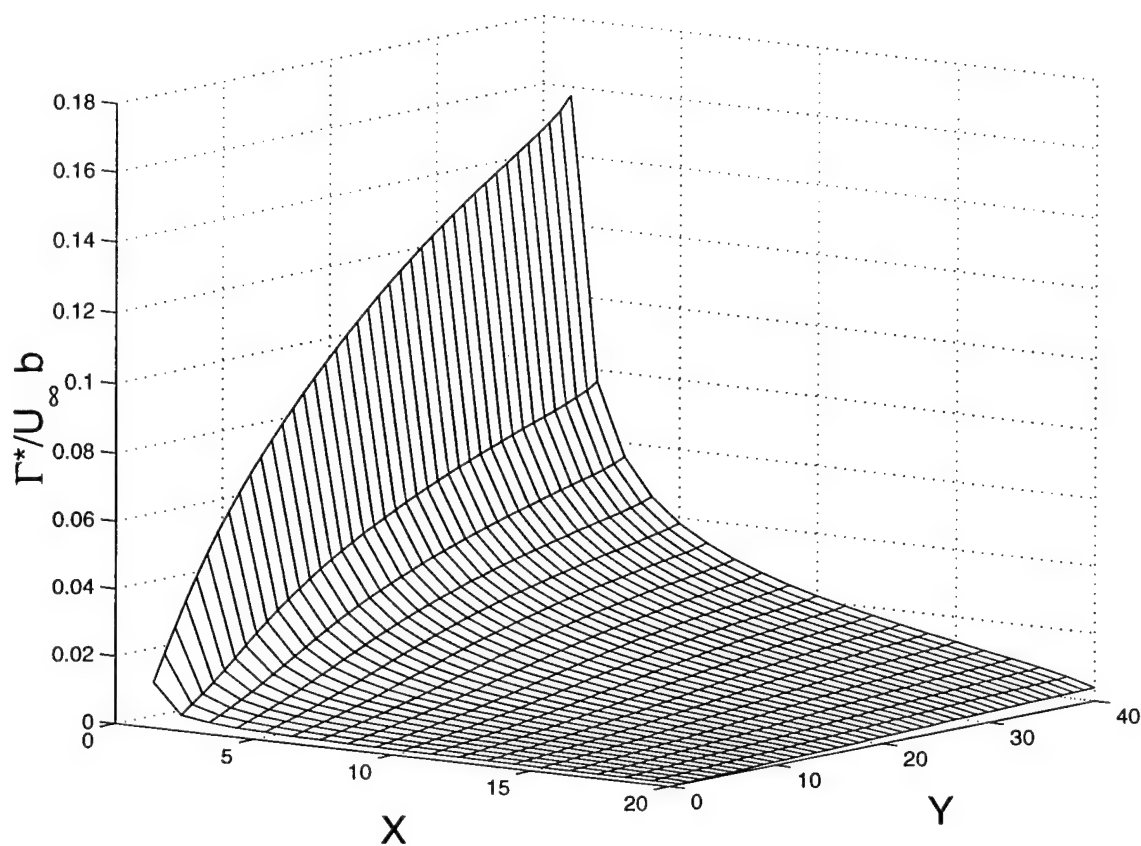


Figure 3.9: Level curves of the circulation for each panel. The angle of attack is 12° .

Having obtained the spanwise distribution of the bound circulation, we can calculate the positions of the shed vortices behind the wing. In a steady inviscid-flow field, the trailing vortex lines are also streamlines. Therefore, we can obtain the positions of vortex lines by solving the set of equations

$$\frac{dy}{dx} = \frac{v}{U_\infty} \quad (3.22)$$

$$\frac{dz}{dx} = \frac{w + \sin\alpha_0}{U_\infty} \quad (3.23)$$

where we have put $u = U_\infty = 1$ corresponding to linearized theory. The symbols v and w represent the y and z velocity components induced by the wake. Here x is the independent variable measured from leading edge of the wing. The vortices are initiated at the one-quarter chord position of each panel at the beginning of the numerical integration for every iteration. For the initial condition, $z = 0$ and y is the spanwise location of the trailing vortex shed from the one-quarter chord of each panel. The trailing vortices are forced to stay on the wing surface up to the trailing edge of the wing but can be displaced in the y direction by the induced velocity. This set of ordinary differential equations was solved numerically by the Adams-Moulton method. Note that the velocity components were calculated for straight-line trailing vortices in the first iteration.

In order to obtain the initial positions of the trailing vortices, we introduce three parameters to describe the roll-up process. They are \bar{y} , \bar{z} which are the y and z components of the center of the tip-vortex core and \bar{r} which defines the core radius measured from the centroid. We define

$$\bar{y} = \frac{\sum_{k=1}^n \sum_{j=1}^{n_x} \Gamma_{j,k} y_{j,k}}{\sum_{k=1}^n \sum_{j=1}^{n_x} \Gamma_{j,k}} \quad (3.24)$$

$$\bar{z} = \frac{\sum_{k=1}^n \sum_{j=1}^{n_x} \Gamma_{j,k} z_{j,k}}{\sum_{k=1}^n \sum_{j=1}^{n_x} \Gamma_{j,k}} \quad (3.25)$$

where n is the number of trailing vortices which are rolling over each other, n_x is the number of chordwise panels and $\Gamma_{j,k}$ is the circulation of the panel (j, k) . The core radius r has been defined as

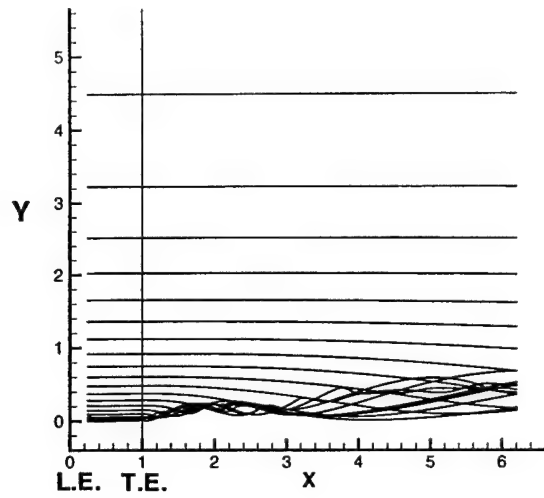
$$\bar{r} = \sqrt{\frac{\sum_{k=1}^n \sum_{j=1}^{n_x} (\bar{y} - y_{j,k})^2 + (\bar{z} - z_{j,k})^2}{n \times n_x}} \quad (3.26)$$

The iterative process was assumed to be convergent when $\frac{\bar{\Gamma}_{new} - \bar{\Gamma}_{old}}{\bar{\Gamma}_{old}}$ is less than 10^{-4} at each given value of x . Here we have used one chordwise panel, twenty spanwise panels on the wing surface and one hundred and twenty nodes on each of the trailing vortices. The separation between the nodes on each of the trailing vortices is 0.05. Beyond the last node, the trailing vortex is represented by a semi-infinite, horizontal straight vortex line extending to $x = +\infty$ and parallel to the free-stream velocity.

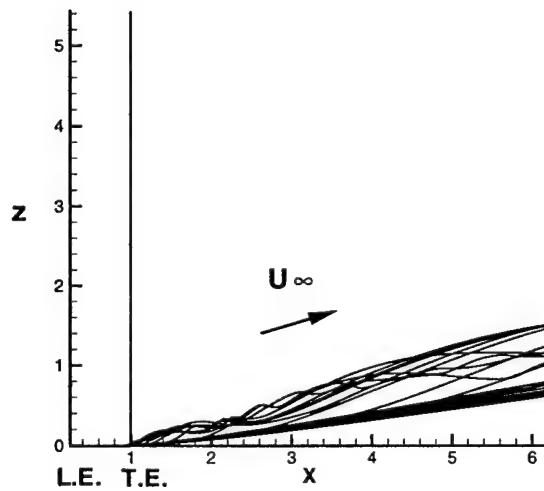
Figure 3.10 presents the roll-up process for the semi-infinite fixed wing at $\alpha_0 = 12^\circ$ with a single chordwise panel after 350 iterations at which the $\frac{\bar{\Gamma}_{new} - \bar{\Gamma}_{old}}{\bar{\Gamma}_{old}}$ converges up to $x = 3.25$, with more iterations required for larger x . Here the vortex lines emanating from each panel are shown on Figure 3.10 (a) and these suggest the behavior of the streamlines photographed by Head [1982] (Figure 1.1). Note that the trailing vortices near the tip region roll over and form a strong trailing vortex. However, in the region away from the tip, the trailing vortices do not roll up in distances of the order shown here. At $x = 3.25$, the tip-vortex has moved inboard which is also shown in Figure 1.1. Figure 3.10 (b) shows the X-Z plot of the roll-over process of the trailing vortices. Note that the trailing vortices leave the wing surface at the trailing edge and move with the local velocity which is the sum of the free stream velocity and the velocity induced by the wake. To satisfy the Kutta condition, the flow is parallel to the free-stream velocity at infinite distance downstream. Figure 3.11 shows a 3-D view of the roll-over process of the trailing vortices.

The circulation of the tip-vortex is defined as the sum of the circulations of all the rolled-up trailing vortices as shown on Figure 3.12, which shows the Y-Z plot at $x = 3.4$ for the fixed wing at $\alpha_0 = 12^\circ$. At any given downstream location, we plot a Y-Z view of the trailing vortices. From the Y-Z view plot, we draw a box to count all the rolling-over trailing vortices. The left and right edges of the box are determined by the left-most and the right-most rolling-over trailing vortices and the lower edge is determined by the lowest rolling-over trailing vortex. All the trailing vortices in this box are counted as the rolling-over trailing vortices. The circulation of the tip-vortex is defined as the sum of the trailing vortices in the box.

Figure 3.13 shows the growth of the circulation of the tip-vortex as a function of x (symbol '*'). At $x = 6.0$, the circulation of the tip-vortex is about 74.8 percent of the maximum bound circulation. Hence the tip-vortex does not completely roll up at the trailing edge of the wing as some authors have



(a)



(b)

Figure 3.10: Section view of the roll-up process of trailing vortices for the fixed semi-infinite wing. The core radius converges at $x = 3.25$ after 350 iterations. A single chordwise panel is used. The angle of attack is 12° . (a) X-Y plot. (b) X-Z plot.

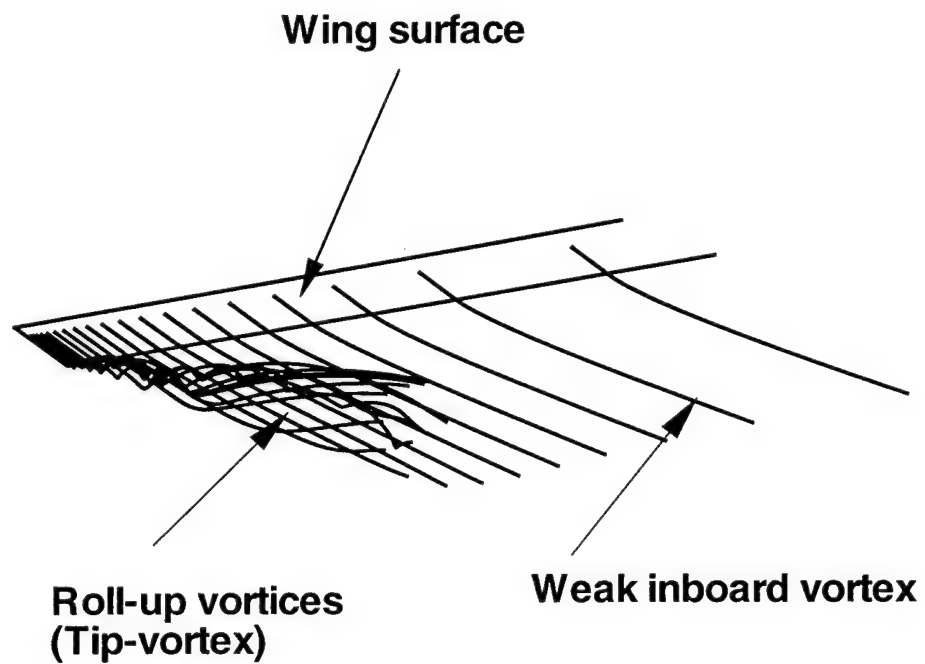


Figure 3.11: Three-dimensional view of the roll-over process of the trailing vortices. The angle of attack is 12° . A single chordwise panel is used.

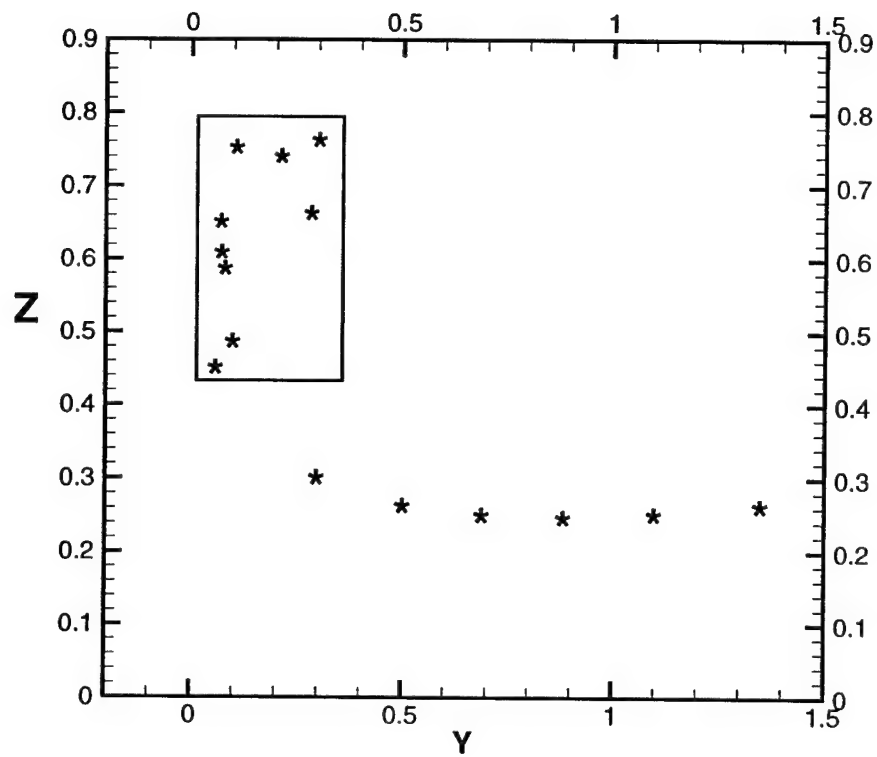


Figure 3.12: The definition of the circulation of the tip-vortex.

stated. Instead, the circulation of the tip-vortex develops downstream and approaches a constant asymptotically. At an infinite distance downstream, the circulation of the tip-vortex approaches the maximum bound circulation.

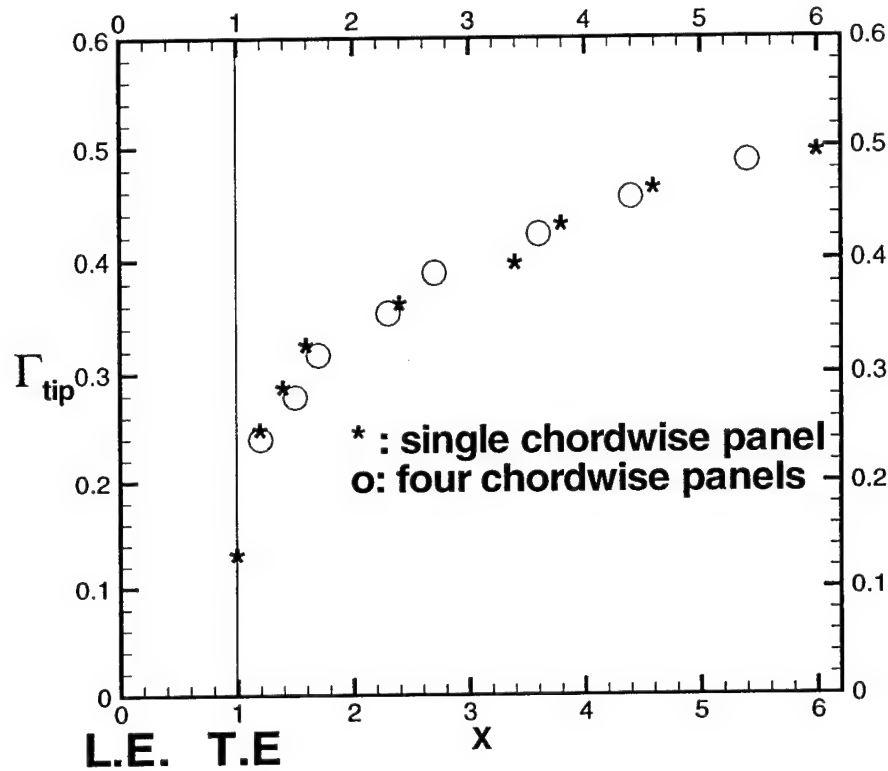


Figure 3.13: The circulation of the tip-vortex at different x . The maximum bound circulation is 0.651 and the angle of attack is 12° . Here '*' represents the result for a single chordwise panel and 'o' represents the result for four chordwise panels.

Figure 3.14 shows the downstream growth of the core radius \bar{r} of the tip-vortex measured from the centroid. The core radii \bar{r} in Figure 3.14 were calculated at each downstream location x at which an additional trailing vortex enters into the rolling-over trailing vortices. Note that the core radius develops downstream and approaches a constant asymptotically which is

similar to the development of the circulation of the tip-vortex.

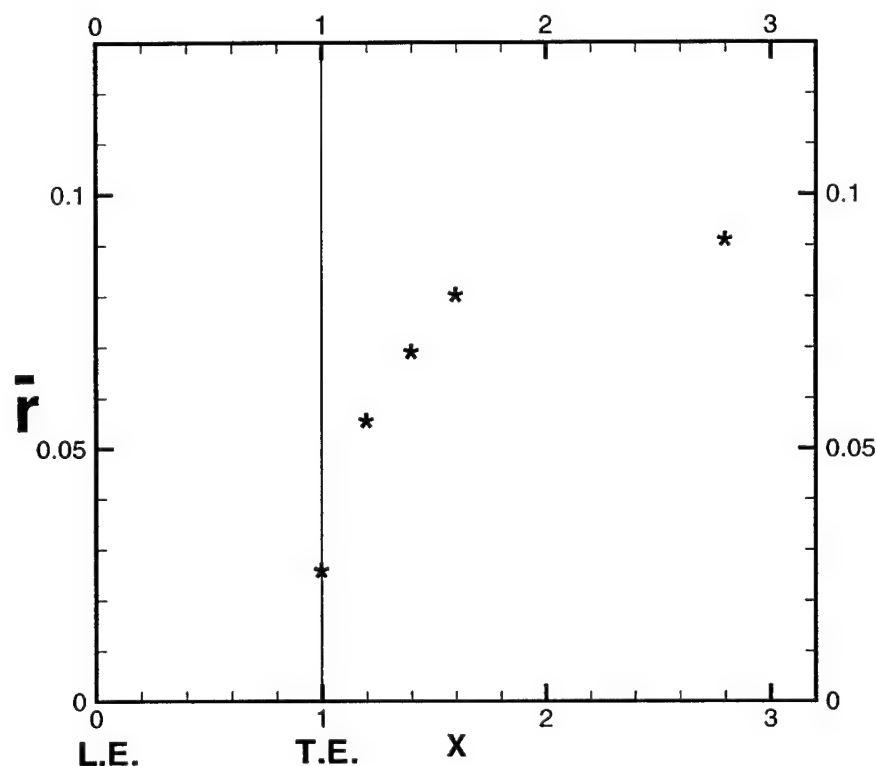


Figure 3.14: The core radius of the tip-vortex \bar{r} measured from the centroid at different downstream location up to $x = 3.2$. A single chordwise panel is used.

Figure 3.15 (a) and (b) show the X-Y and X-Z views of the roll-up process for the semi-infinite wing at $\alpha_0 = 12^\circ$ with four chordwise and twenty spanwise panels and the 3-D view is presented on Figure 3.16. The iterative process was convergent after 490 iterations when $\frac{\bar{r}_{new} - \bar{r}_{old}}{\bar{r}_{old}}$ is less than 10^{-4} at $x = 3.25$. The downstream development of the circulation is shown on Figure 3.13 by the circles. Note that the agreement with the result for one chordwise panel (represented by '*') is fairly good. The trailing vortices shed from different chordwise panels but from the same spanwise location roll into the single strong tip-vortex at different downstream locations. The

trailing vortices emanate from the panels closer to the leading edge of the wing roll into the tip-vortex more quickly due to the velocity induced by the wake. With more chordwise panels, the downstream development of the circulation and core radius can be calculated more accurately. However, the computation time has been greatly increased because the computation time is approximately expressed by $n_y^2 \times n_x^2 \times n_s^2$ where n_s is the number of segments on each trailing vortex.

Figure 3.17 (a) and (b) show the X-Y and X-Z plot of the roll-up process for a semi-infinite wing at $\alpha_0 = 8^\circ$ with a single chordwise panel. After 309 iterations, the core radius \bar{r} converges at $x = 3.25$. At $x = 3.25$, the center of the core has moved inboard. Figure 3.18 shows the 3-D view of the roll-over process. Figure 3.19 shows the growth of the circulation of the tip-vortex with x . At $x = 6.0$, the circulation of the tip-vortex is about 65.1 percent of the maximum bound circulation, while for $\alpha_0 = 12^\circ$, this value is 74.8 percent. This difference might be attributed to the steeper gradient of the bound circulation near the wingtip for a wing at higher angle of attack, as shown on Figure 3.20.

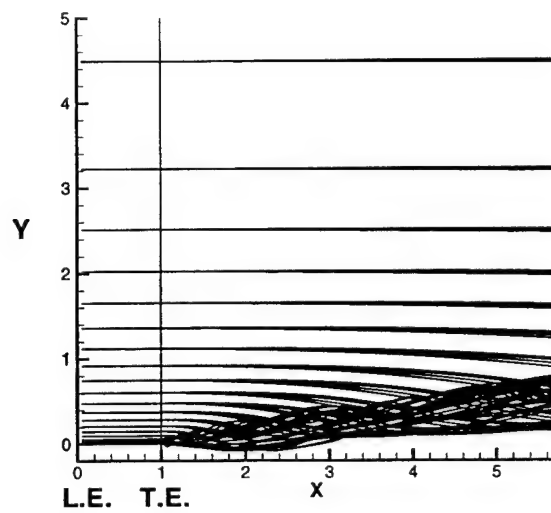
3.4.3 Comparison with Experiment

In this section we compare the computational results with the experiments of McAlister and Takahashi [1991]. The parameters of the experiment are given in Table 3.1. Figure 3.21 shows the comparison of the bound circulation of the experimental data with the computational data. The data are for a fixed wing whose the aspect ratio is 6.6 and the angle of attack is 12° . The computational and experimental results agree fairly well.

Wing	Chord	AR	AOA	Re
1	304.8mm	6.6	12.0	1.43×10^6
2	304.8mm	9.6	12.0	1.44×10^6
3	518.2mm	6.6	12.0	1.49×10^6
4	518.2mm	6.6	12.0	1.98×10^6

Table 3.1: The parameters for the wings investigated by McAlister and Takahashi [1991].

Figure 3.22 presents the vertical velocity results of McAlister and Takahashi [1991] for wings of different aspect ratios and different chords. Note



(a)

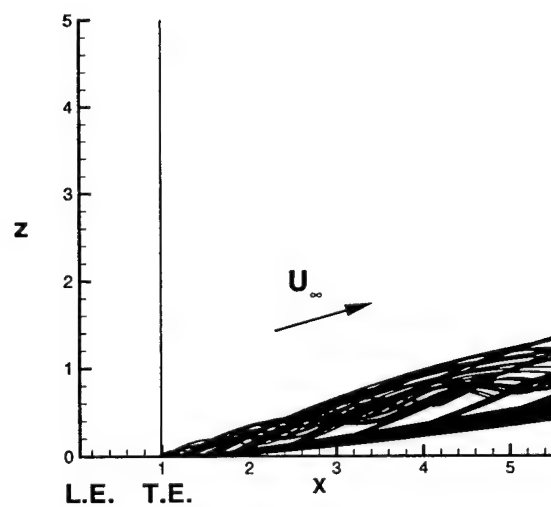


Figure 3.15: Section view of the roll-up process of trailing vortices for the fixed semi-infinite wing. (a) X-Y plot. (b) X-Z plot. Four chordwise panels and twenty spanwise panels are used. The angle of attack is 12° .

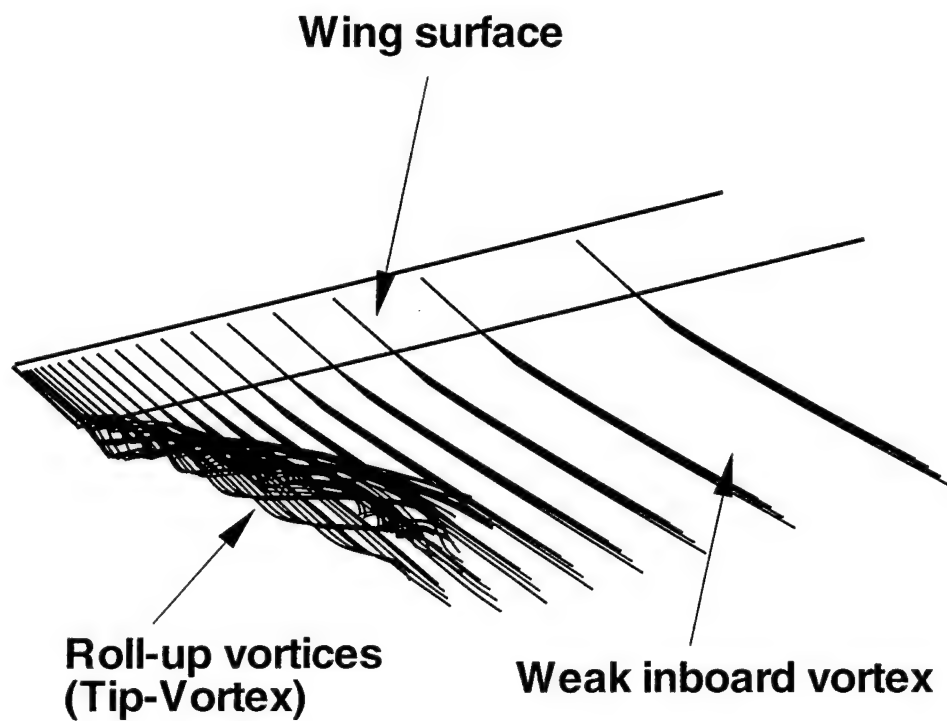
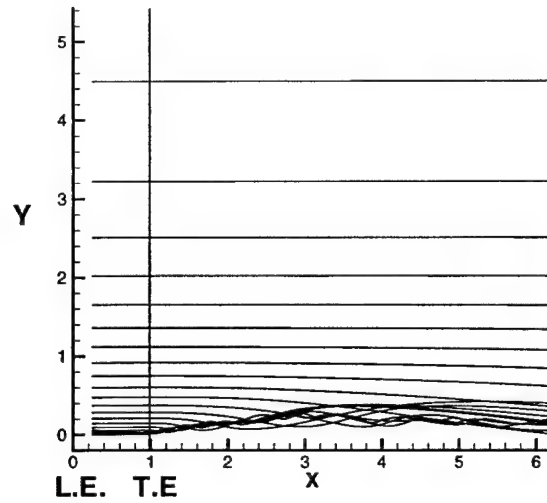
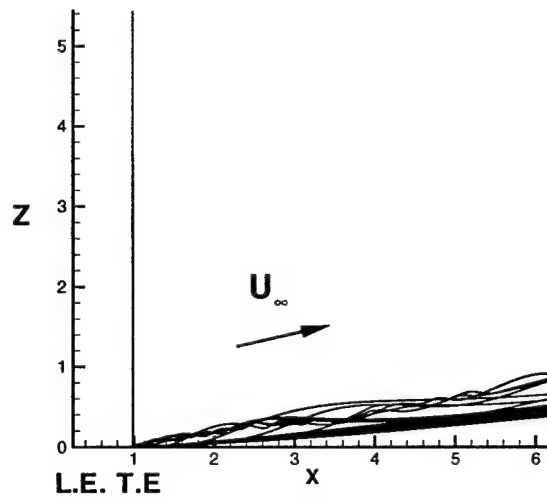


Figure 3.16: 3-D view of the rolling-over process for a semi-infinite wing at angle of attack 12° . Four chordwise and twenty spanwise panels are used.



(a)



(b)

Figure 3.17: Section view of the roll-up process of trailing vortices for the fixed semi-infinite wing. The core radius converges at $x = 3.25$ after 309 iterations. A single chordwise panel is used. The angle of attack is 8° . (a) X-Y plot. (b) X-Z plot.

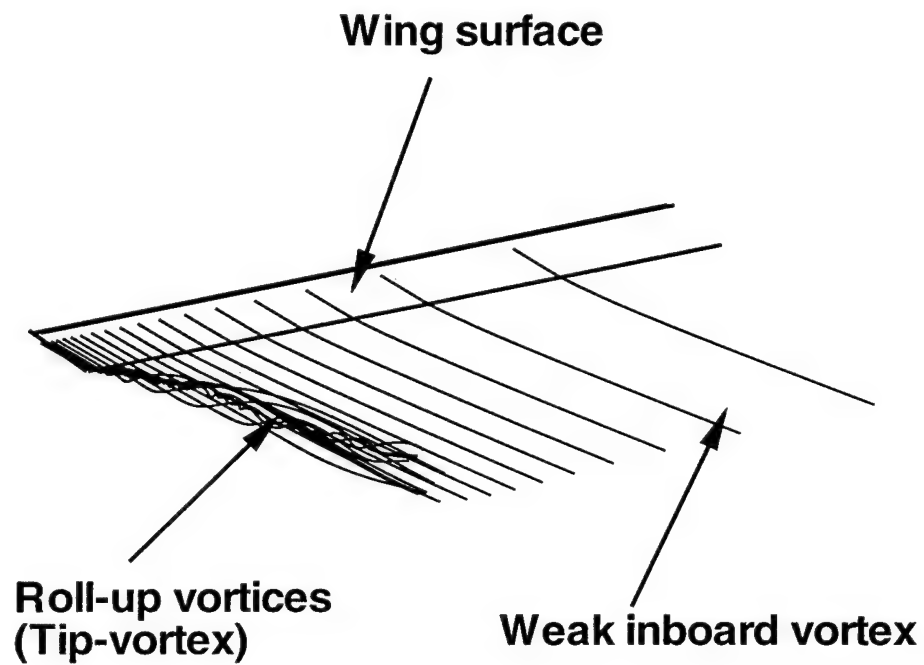


Figure 3.18: 3-D view of the roll-over process of the trailing vortices. The angle of attack is 8° . A single chordwise panel is used.

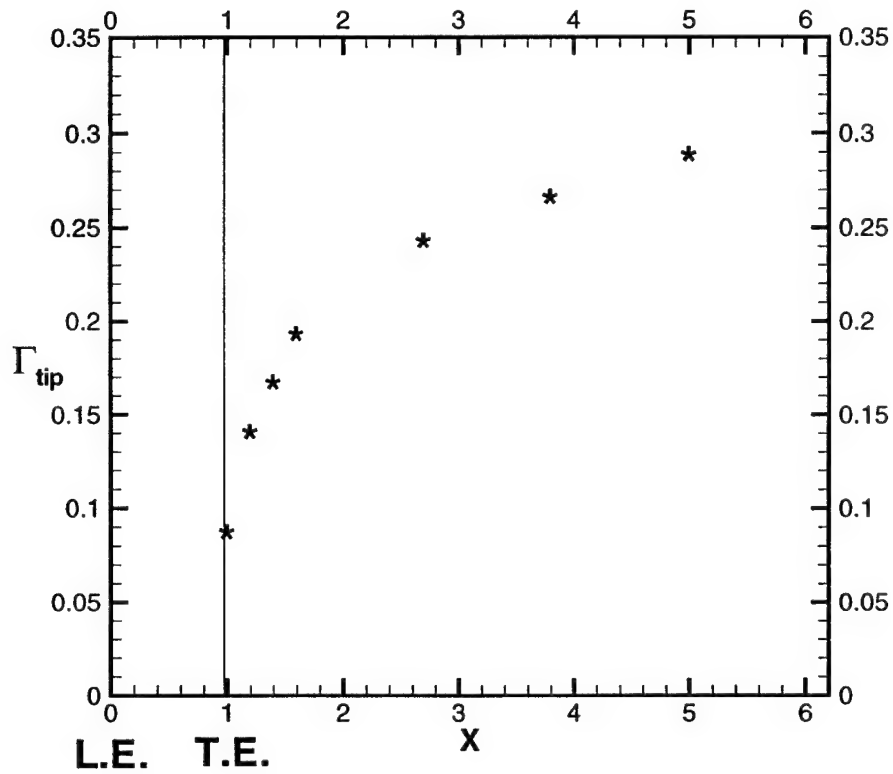


Figure 3.19: The circulation of the tip-vortex at different x . The maximum bound circulation is 0.436 and the angle of attack is 8° . A single chordwise panel is used.

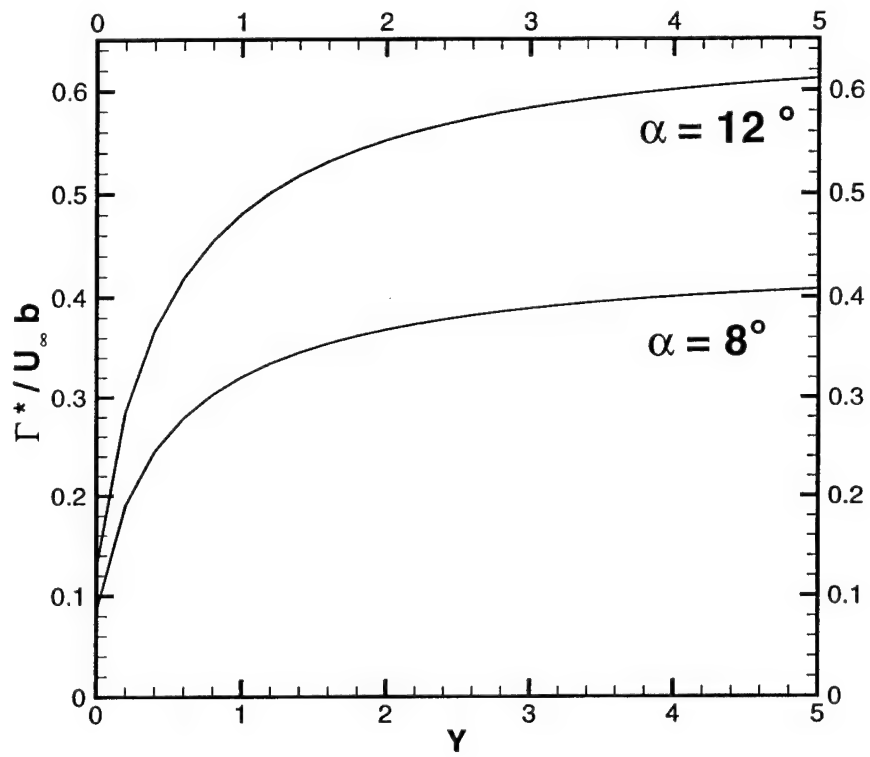


Figure 3.20: The comparison of the bound circulation for wings at different angles of attack.

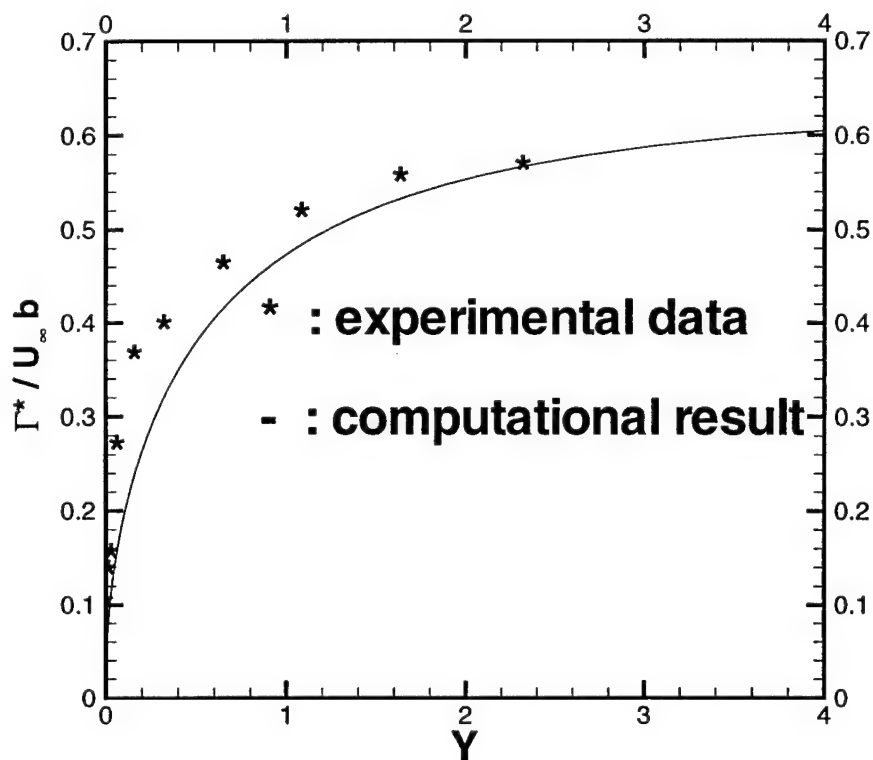


Figure 3.21: The comparison of the experimental data of McAlister and Takahashi [1991] and computations for the bound circulation. Here '*' represents the experimental data and solid line represents the computational results from the horseshoe panel model where ten chordwise and twenty spanwise panels are used. The angle of attack is 12° .

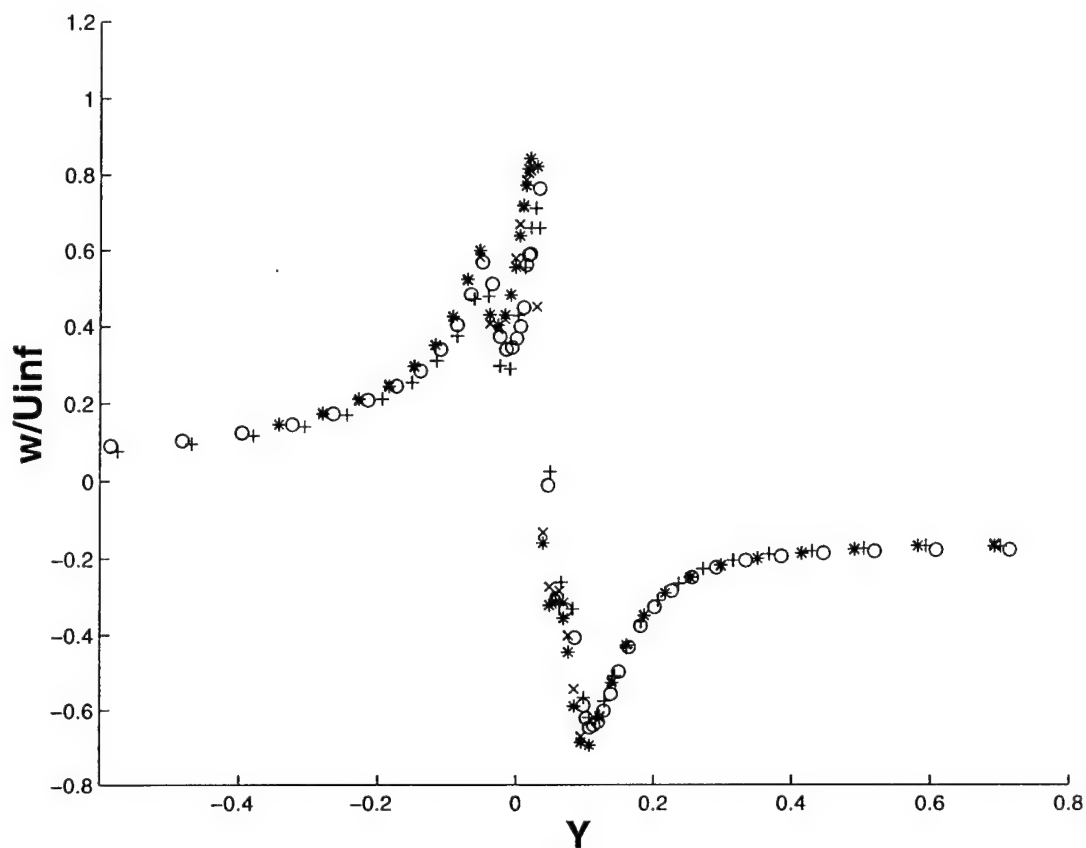


Figure 3.22: The vertical velocity at $x = 1.1$ chord behind the trailing edge of different fixed wings from the data of McAlister and Takahashi [1991]. Here the '+' represents wing 1, the 'o' represents wing 2, '*' represents wing 3 and 'x' represents wing 4. The vertical velocity is plotted at $z = 0$; the z -coordinate measures distance normal to the $X - Y$ plane of Figure 3.2. $Y = 0$ is the wing tip and $Y > 0$ is inboard. The parameters of wings are shown in Table 3.1.

that the influence of the aspect ratio and the chord on the vertical velocity behind the wing is small. Therefore, to leading order, near the wing tip, the flow is independent of aspect ratio and chord and hence the wing may be viewed as being semi-infinite over the range of Y represented on the figure even though each aspect ratio is less than 10. It also suggests that in the range of the Reynolds number from 1.43×10^6 to 1.98×10^6 , the viscosity has minor influence on the formation of the tip-vortex.

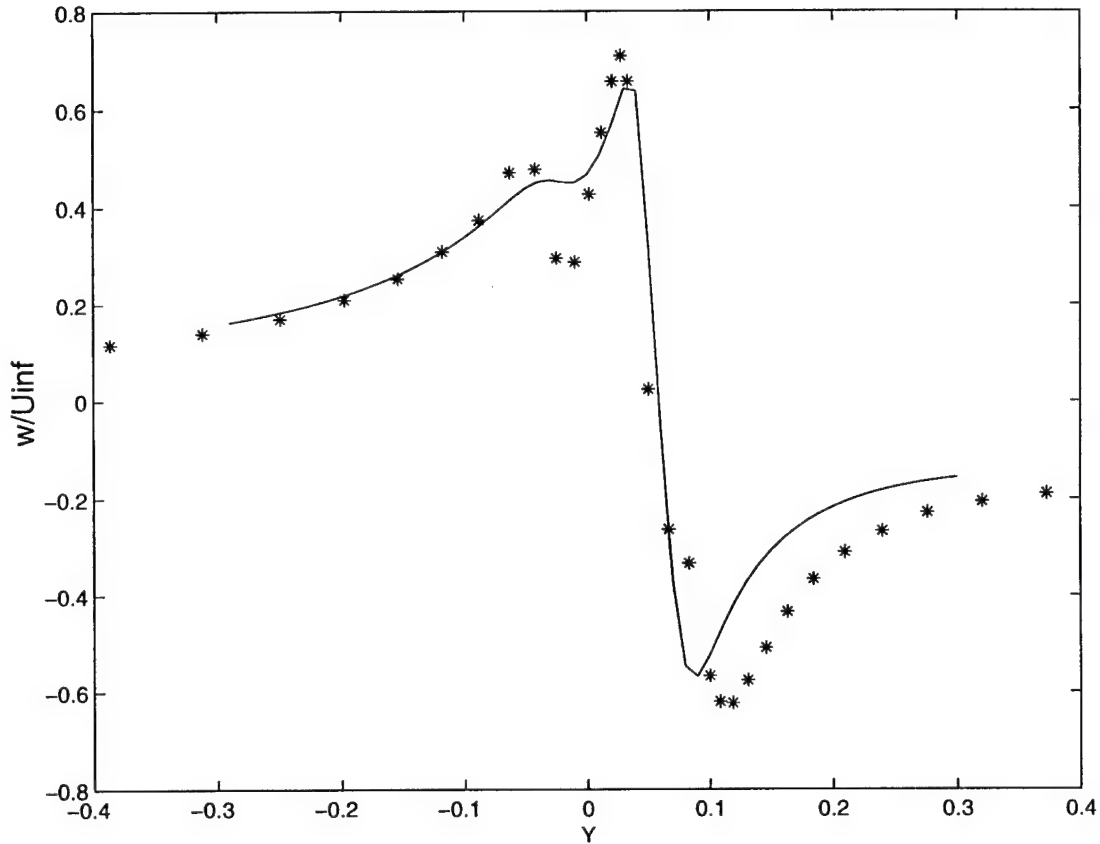


Figure 3.23: The vertical velocity at $x = 1.1$ chord behind the trailing edge of the wing compared with the experimental data of McAlister and Takahashi [1991], at $z = 0$ for $Re = 1.44 \times 10^6$ (wing 2). Here '*' represents the experimental data and solid line represents the computational data. $Y = 0$ is the wing tip and $Y > 0$ is inboard. A single chordwise panel is used.

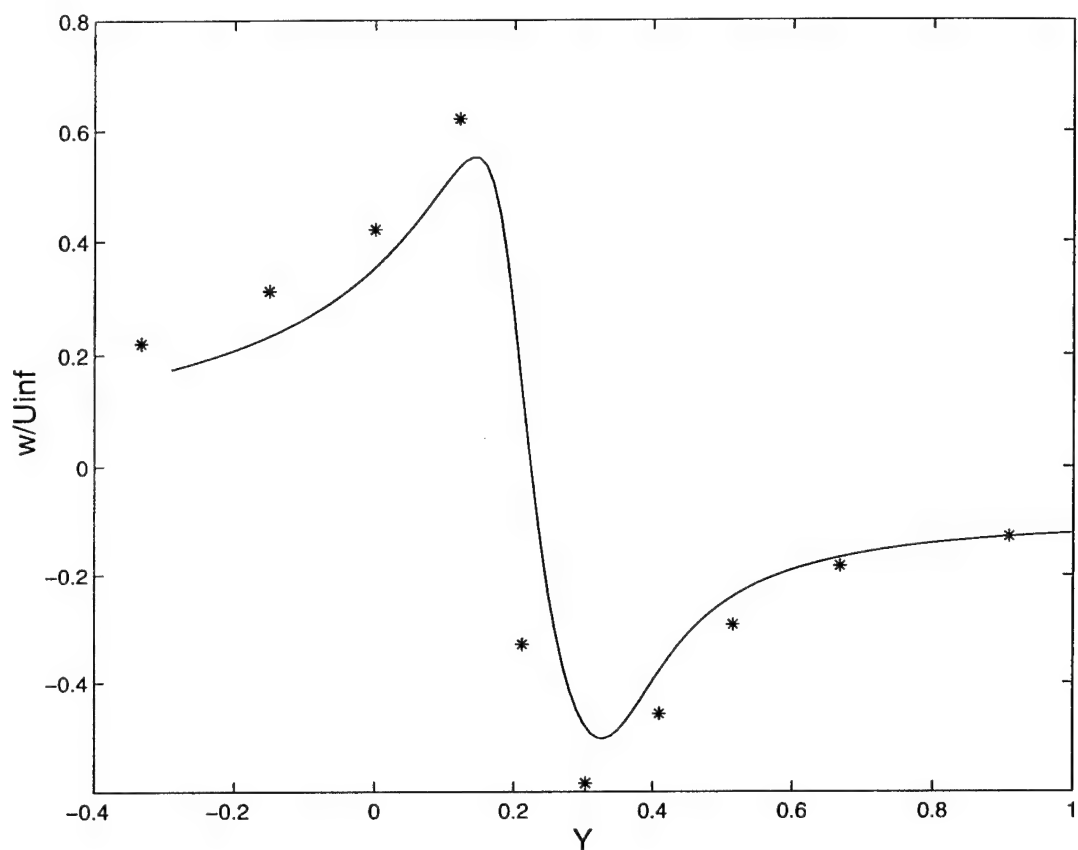


Figure 3.24: The vertical velocity at $x = 3.0$ chord behind the trailing edge of the wing compared with the experimental data of McAlister and Takahashi[1991], at $z = 0$ for $Re = 1.44 \times 10^6$ (wing 2). Here '*' represents the experimental data and solid line represents the computational data. $Y = 0$ is the wing tip and $Y > 0$ is inboard. A single chordwise panel is used.

Figures 3.23 and 3.24 compare the numerical results for the vertical velocity at $x = 1.1$ and $x = 3.0$ chords behind the trailing edge of the wing with the experimental data of McAlister and Takahashi [1991] at the same location for wing 2 of Table 3.1. Note that at $x = 1.1$ the comparison is good except that the maximum of the velocity is underpredicted, as is the dip outboard of the wingtip. At $x = 3.0$, the tip-vortex has moved further inboard. The comparison is surprisingly good since the experiments were performed at Reynolds numbers where the flow would be expected to be turbulent, suggesting that viscosity and turbulence have only a minor influence on the roll-up process.

3.5 Summary

The computation of the formation of a fixed wing tip-vortex is described in this chapter. It is shown that to leading order, the flow near the tip of a large aspect-ratio wing is equivalent to the flow past a semi-infinite wing. The leading-order inner solution for the lifting-line integral equation has an analytical solution given by Stewartson[1960]. A similar analysis was performed for the lifting-surface theory using a horseshoe panel method. The numerical results compare fairly well with experimental data, suggesting that viscosity and turbulence have only a minor influence on the formation of the fixed wing tip-vortex.

It is shown that the tip-vortex develops downstream and its circulation approaches a constant asymptotically. At an infinite distance downstream, the circulation of the tip-vortex approaches the maximum bound circulation. Hence the tip-vortex does not roll up completely at the trailing edge of the wing; instead, the core radius and the circulation develop asymptotically downstream.

Chapter 4

Asymptotics of Lifting-Line and Lifting-Surface Theory for a Rotary Wing without Rotor-Wake Contraction

4.1 Introduction

In this chapter, the rotary wing computation is presented. Unlike the fixed wing wake, it is observed that for a rotary wing, the shed vortices are driven downward away from the rotor tip-path plane and form a more-or-less helical rotor wake. Therefore, the lifting-line integral equation (3.3) can not be applied to the rotary wing directly since the influence of the helical rotor wake must be considered. In this chapter, Burggraf's [1999] lifting-line theory for rotors is applied first to obtain the influence of the helical rotor wake on the distribution of the bound circulation in the outer region away from the rotor-tip. Then the leading order lifting-line integral equation is established in the tip region. In the tip region, because the curvature of the most recently shed trailing vortices is much greater than the length scale of the inner region (the chord c), the most recently shed trailing vortices can be viewed as straight vortex lines. However, unlike the fixed wing case, the trailing vortices are also driven downward away from the rotor tip-path plane and form a more-or-less helical wake and thus the lifting-line integral equation for a fixed wing can be applied in the tip region with a modification accounting

for the helical wake effect. It is shown that near the rotor-tip, to leading order, an analytical solution for the bound circulation can be obtained by a simple modification of the Stewartson[1960] solution. Next the lifting-surface method is applied and its results compare well with the modified Stewartson [1960] solutions. The roll-up process for the trailing vortices is also presented. We calculate the induced vertical velocity and compare the numerical result with the experimental data of McAlister *et al*[1995]. The uniformly valid solution for the bound circulation is obtained by using “multiplicative composition”.

4.2 Rotor Aerodynamics: Downwash and Vorticity in the Cylindrical Slipstream of a Hovering Rotor

Burggraf [1999] has developed a theory for the interaction between an assumed cylindrical slipstream and the bound circulation for an n -bladed rotor (see Appendix B for more details). The concepts of Prandtl’s lifting-line theory were applied to formulate an integro-differential equation governing the aerodynamics of a rotor operating in hover (static thrust). In Prandtl’s theory, the high aspect-ratio wing is represented by a line vortex (the lifting line) and the aerodynamic properties of each spanwise section are approximated locally by the two-dimensional characteristics from linearized airfoil theory. However, the free stream of the local section is replaced by the relative wind, i.e., the effective angle of attack is the geometric angle of attack reduced by the local downwash induced by the trailing vortices.

Corresponding to the variation of bound circulation, vortices are shed all across the rotor, forming an approximately cylindrical slipstream filled with concentric helical vortices. These discrete helical vortices are approximated by uniform cylindrical sheets of vorticity. For purposes of computing the downwash, these elemental vortex cylinders may be viewed as composed of vortex rings, whose strength is approximately constant on each cylinder. The axial component of the helical vortices, that is, the component of the circulation oriented in a direction normal to the tip-path plane may be ignored for present purpose, since it does not contribute to the downwash.

A cylindrical coordinate system (r, θ, z) is convenient, where r is the radial coordinate, θ the azimuthal coordinate, z the axial coordinate (see Figure

4.1). These elemental vortex cylinders, formed from the inboard vortex sheet, are superposed with the vortex cylinder generated by the tip-vortex to form the complete rotor slipstream.

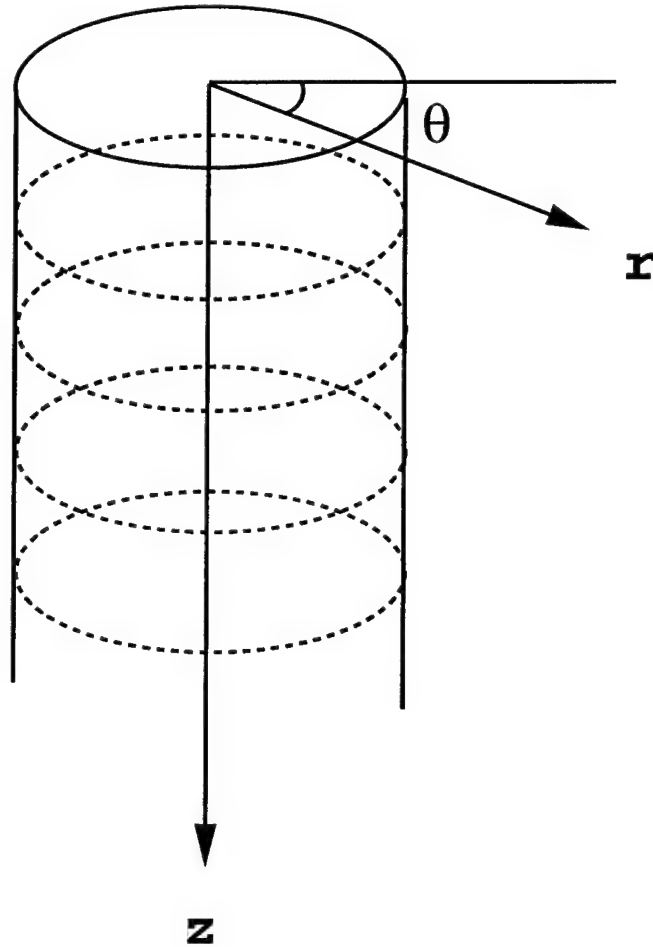


Figure 4.1: Vortex cylinder coordinate system.

For a single cylinder of vortex rings of circulation γ_θ per unit of axial length along the cylinder, it has been shown previously by Radcliff *et al.* [2000] that the axial velocity induced by the vortex ring-cylinder using the

Biot-Savart Law is given by

$$v_z(r) = \begin{cases} \gamma_\theta/2 & \text{for } r < r' \\ \gamma_\theta/4 & \text{for } r = r' \\ 0 & \text{for } r > r' \end{cases} \quad (4.1)$$

Since the downwash at radius r in the rotor plane is induced only by those cylinders of larger radius, the net downwash is given by

$$v_z(r) = \frac{1}{2} \int_r^a \gamma_{\theta i}(r') dr' + \frac{1}{2} \gamma_{\theta t} \quad (4.2)$$

where the subscripts i and t refer to the inboard vortex sheet and to the tip vortex, respectively. It is shown in Appendix A that the downwash satisfies an integro-differential equation which depends on a single parameter

$$\lambda = \frac{\alpha_0 a}{nc}$$

where a is the blade radius, α_0 is the geometric attack angle and n is the number of blades. As described by Burggraf [1999], the form of this integro-differential equation permits a simple analytical solution, unlike the apparently simpler case of the fixed wing. For the case of a rectangular blade the induced downwash has the form

$$W(R) = \frac{v_{ztip}}{\Omega a \alpha_0} = \frac{1}{4\lambda} (\sqrt{1 + 8\lambda R} - 1) \quad (4.3)$$

where $W(R)$ is the nondimensional downwash and R is the nondimensional radius which is defined as $R = \frac{r}{a}$. Ω is the rotor rotating speed.

The blade circulation is given by

$$\Gamma = \frac{\Gamma^*}{\Omega a c} = \pi \alpha_0 [R - W(R)] \quad (4.4)$$

and the effective angle of attack is

$$\alpha_e = \alpha_0 - \frac{v_{ztip}}{\Omega r} \quad (4.5)$$

$$= \alpha_0 \left[1 - \frac{W(R)}{R} \right] \quad (4.6)$$

where the leading term represents the effects of blade rotation and the second term accounts for the reduction due to downwash induced by the helical

rotor wake. This outer solution is not valid near the rotor tip and proper treatment of this anomaly requires consideration of the inner expansion which is discussed in the next section.

To study the behavior of the induced downwash $W(R)$ as a function of λ , we expand $W(R)$ as $\lambda \rightarrow 0$ and $\lambda \rightarrow \infty$. The series expansion for $W(R)$ as $\lambda \rightarrow 0$ is

$$W(R) = R - 2\lambda R^2 + 8\lambda^2 R^3 - \dots \quad (4.7)$$

and as $\lambda \rightarrow \infty$ is

$$W(R) = \left(\frac{R}{2\lambda}\right)^{\frac{1}{2}} - \frac{1}{4\lambda} + \dots \quad (4.8)$$

Equation (4.7) shows as λ goes to 0, $W(R)$ has a linear spanwise distribution. Equation (4.8) shows $W(R)$ vanishes as λ goes to infinity and thus in this case, the rotary wing is equivalent to a semi-infinite wing.

Figure 4.2 shows the induced downwash in the plane of the rotor given by the analytical solution of Burggraf [1999] and the corresponding distribution of the bound circulation is shown on Figure 4.3. It is seen that the induced downwash increases monotonically, from zero at the hub to the maximum value at the tip, the latter value depending on the parameter λ . The circulation vanishes like R^2 at the hub, and also increases monotonically with radius. As mentioned above, these outer solutions are not valid in the region near the rotor-tip and thus an inner solution is necessary, which is discussed subsequently.

4.3 The Solution for a Rotary Wing Near the Rotor Tip

4.3.1 The Inner Solution For the Lifting-Line Integral Equation

In this section, we consider the flow in the tip region as shown on Figure 1.7. In the tip region, the most recently shed trailing vortices can be approximated as straight lines and their influence is represented by the integral term in equation (3.3). However, different from the fixed-wing case, the previously shed vortices do not remain in the rotor tip-path plane; instead, they are driven downward away from the rotor tip-path plane and form the helical

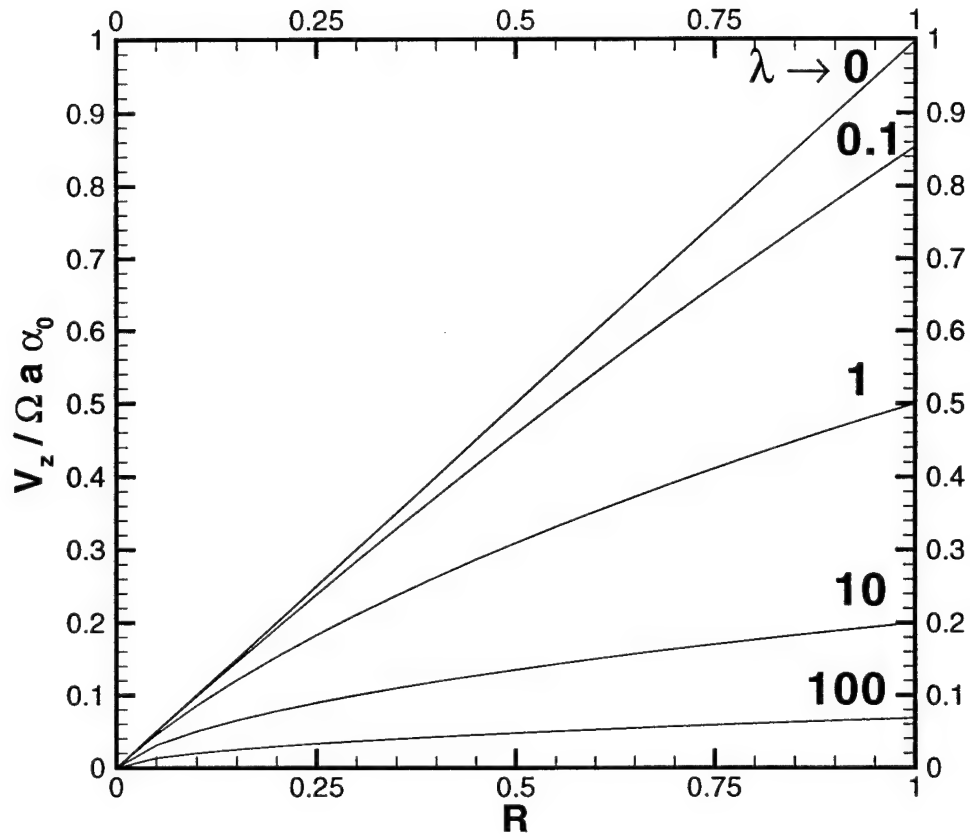


Figure 4.2: Induced downwash in the plane of the rotor as a function of the parameter $\lambda = \frac{\alpha_0 a}{nc}$.

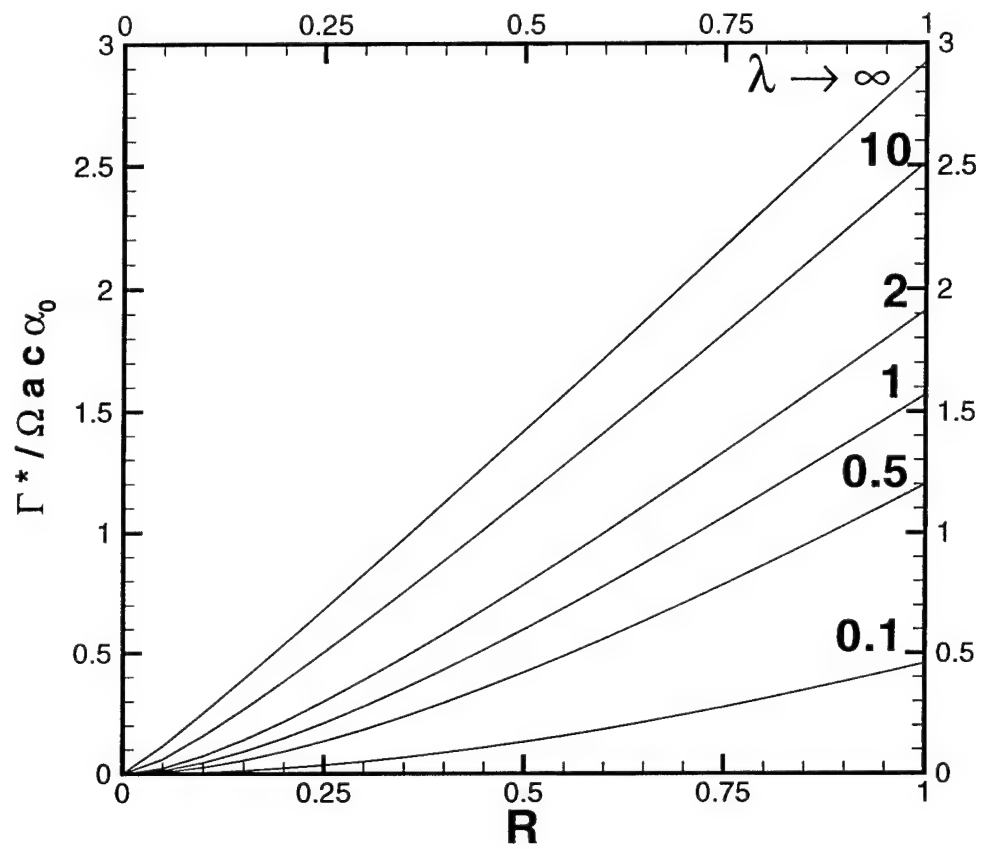


Figure 4.3: Circulation distribution for a single-bladed rotor in hover as a function of the parameter $\lambda = \frac{\Omega a}{nc}$.

rotor wake. Therefore, the influence of the helical rotor wake needs to be considered when equation (3.3) is applied in the rotor tip region.

First, we replace U_∞ and y^* in equation (3.3) with Ωr and r respectively, nondimensionlize equation (3.3) by writing

$$\Gamma = \frac{\Gamma^*}{\Omega a c}$$

and

$$R = \frac{r}{a}$$

Integrating R_0 from the rotor hub ($R_0 = 0$) to the tip ($R_0 = 1$), we have

$$\Gamma(R) = \frac{1}{2} m C(R) \left(\alpha_0 R - \frac{A^{-1}}{4\pi} \int_0^1 \frac{d\Gamma}{dR_0} \frac{dR_0}{R - R_0} \right) \quad (4.9)$$

where $C(R)$ has the same definition as $C(y)$ in the fixed wing case. For a rectangular rotor blade, $C(R) = 1$.

To focus on the tip region, we make the transformation

$$Y = (1 - R)A^\beta$$

where β is a constant. Substituting Y into equation (4.9), we find to balance both sides, $\beta = 1$. If we assume that Γ remains $O(1)$ near the rotor-tip, and the chord finite at the wing-tip, then Γ may be expanded as

$$\Gamma = \Gamma_1 + A^{-1}\Gamma_2 + \dots$$

and substituting into equation (4.9), we find to leading-order, the lifting-line integral equation for a semi-infinite wing is

$$\Gamma_1(Y) = \frac{m}{2} \left(\alpha_0 - \frac{1}{4\pi} \int_0^\infty \frac{d\Gamma_1}{dY_0} \frac{dY_0}{Y - Y_0} \right) \quad (4.10)$$

To include the effect of the helical rotor wake in the tip region, a modification must be made to equation (4.10)

$$\Gamma_1(Y) = \frac{m}{2} \left[\alpha_0 - \frac{1}{4\pi} \int_0^\infty \frac{d\Gamma_1}{dY_0} \frac{dY_0}{Y - Y_0} - \alpha_0 W_o(Y) \right] \quad (4.11)$$

where $W_o(Y)$ is the downwash induced by the helical rotor wake in the inner region and is defined just below.

Expanding the outer solution for the downwash in the rotor-tip path plane $W(R)$ in equation (4.3) with the inner variable $Y = A(1 - R)$ and substitute it into equation (4.11), we have

$$W_o(Y) = \frac{1}{4\lambda} \left\{ \sqrt{1+8\lambda} \left[1 - \frac{4\lambda A^{-1}Y}{1+8\lambda} - \frac{8\lambda^2 A^{-2}Y^2}{(1+8\lambda)^2} + O(A^{-3}) \right] - 1 \right\} \quad (4.12)$$

To leading order

$$W_o(Y) \sim \frac{\sqrt{1+8\lambda}}{4\lambda} - \frac{1}{4\lambda} \quad (4.13)$$

Substituting $W_o(Y)$ into equation (4.11), we have

$$\Gamma_1(Y) = \frac{m}{2} \left[\alpha_0 \left(1 - \frac{\sqrt{1+8\lambda}}{4\lambda} + \frac{1}{4\lambda} \right) - \frac{1}{4\pi} \int_0^\infty \frac{d\Gamma_1}{dY_0} \frac{dY_0}{Y - Y_0} \right] \quad (4.14)$$

Comparing equation (4.14) with equation (3.6), it is easy to see that to leading-order, the only difference is a parameter $1 - \frac{\sqrt{1+8\lambda}}{4\lambda} + \frac{1}{4\lambda}$. Therefore, in the tip region, to leading-order, the rotary wing is similar to the fixed wing and thus equation (4.14) has an analytical solution similar to Stewartson's [1960].

We represent the λ -grouping by the symbol D as

$$D = 1 - \frac{\sqrt{1+8\lambda}}{4\lambda} + \frac{1}{4\lambda} \quad (4.15)$$

Hence equation (4.14) becomes

$$\begin{aligned} \Gamma_1(Y) &= \frac{m}{2} \left[\alpha_0 D - \frac{1}{4\pi} \int_0^\infty \frac{d\Gamma_1}{dY_0} \frac{dY_0}{Y - Y_0} \right] \\ &= \frac{m}{2} \alpha_0 D \left[1 - \frac{1}{4\pi \alpha_0 D} \int_0^\infty \frac{d\Gamma_1}{dY_0} \frac{dY_0}{Y - Y_0} \right] \end{aligned}$$

Define the integral term in the equation above as $f(\xi)$ where $\xi = \frac{8}{m}Y$, we have

$$\Gamma_1(Y) = \frac{m}{2} \alpha_0 D [1 - f(\xi)] \quad (4.16)$$

and thus

$$\frac{d\Gamma_1}{d\xi} = -\frac{m}{2} \alpha_0 D f'(\xi) \quad (4.17)$$

$f(\xi)$ can be expressed as

$$\begin{aligned} f(\xi) &= \frac{1}{4\pi\alpha_0 D} \int_0^\infty \frac{d\Gamma_1}{dY_0} \frac{dY_0}{Y - Y_0} \\ &= \frac{1}{4\pi\alpha_0 D} \int_0^\infty \frac{d\Gamma_1}{d\xi_0} \frac{d\xi_0}{Y - Y_0} \end{aligned}$$

Substituting equation (4.17) into equation above, the same expression as Stewartson's [1960] is obtained.

$$\begin{aligned} f(\xi) &= -\frac{1}{\pi} \int_0^\infty \frac{f'(\xi_0) d\xi_0}{\xi - \xi_0} \\ &= \frac{1}{\pi} \int_0^\infty \frac{e^{-t\xi}}{(1+t^2)^{3/4}} e^{-\frac{1}{\pi} \int_0^t \frac{\log \theta d\theta}{1+\theta^2}} dt \end{aligned}$$

Finally, to leading order near the rotor tip, we have

$$\Gamma_1(Y) = \frac{m}{2} \alpha_0 D [1 - f(\xi)] \quad (4.18)$$

We call equation (4.18) the modified Stewartson's solution since it is identical to the analytical solution aside from the parameter D .

Figure 4.4 shows the leading-order inner solution for the bound circulation as a function of λ . Note that these inner solutions are matched with the outer solution shown on Figure 4.3.

4.3.2 The Lifting Surface

In this section we consider the lifting surface analog of lifting-line theory for the rotary wing. We apply the lifting-surface equation for a finite fixed wing (equation 3.9) to the rotor-tip. First, y is replaced by R and the outer integral is from the rotor hub ($R_0 = 0$) to the tip ($R_0 = 1$). Moreover, in a tip region, two more modifications must be made: transform outer variables x and y into inner variables near the rotor-tip as:

$$X = xA$$

$$Y = (1 - R)A$$

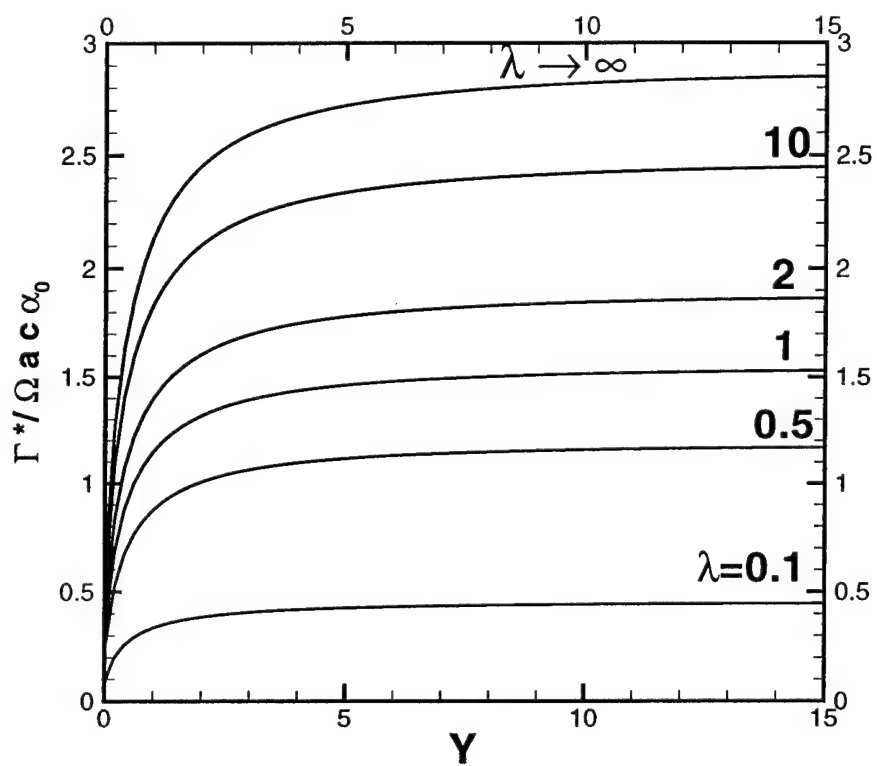


Figure 4.4: Leading order solution for the bound circulation on a rotary wing as a function of $\lambda = \frac{\alpha_0 a}{nc}$.

Also $W_0(Y)$ appears in the lifting-surface equation. Thus equation (3.9) becomes

$$\frac{1}{4\pi} \int_0^\infty \int_0^{c_{tip}} \frac{\gamma_Y(X - X_0) + \gamma_X(Y - Y_0)}{[(X - X_0)^2 + (Y - Y_0)^2]^{\frac{3}{2}}} \times \\ dX_0 dY_0 - \alpha_0 + \alpha_0 W_0(Y) = 0 \quad (4.19)$$

Note that equation 4.19 is valid only in the tip region and hence the leading-order term of the rotor speed in the tip region is 1, nondimensionalized by the rotor-tip speed. The analytical solution to this two-dimensional integral equation is unknown and so we solve it numerically. The same horse-shoe panel method as was used for the fixed wing is applied to the rotary wing near the rotor-tip.

Figure 4.5 shows the numerical results with different number of panels in the lifting surface code. Note that the comparison is good. This suggests that ten chordwise panels and twenty spanwise panels are sufficient for the computations.

Figure 4.6 shows the leading order-inner solutions for the bound circulation near the rotor-tip for the lifting surface code and the modified Stewartson's equation (4.18). Note the excellent comparison of the lifting-surface results with the modified Stewartson's equation (4.18). In the region of sharp drop-off of the bound circulation, the individual vortex filaments will roll around each other to form the rotor tip-vortex. In the region away from the tip, where the circulation approaches a constant, no vorticity is shed to leading order.

4.3.3 The Formation of the Rotor Tip-vortex

Having obtained the spanwise distribution of the bound circulation near the tip-region, we can calculate the positions of the shed vortices behind the rotor. In a steady inviscid-flow field, the trailing vortex lines are also streamlines. Therefore, we can obtain the positions of vortex lines near the rotor tip by solving the set of equations

$$\frac{dy}{dx} = \frac{v}{U_\infty} \quad (4.20)$$

$$\frac{dz}{dx} = \frac{w + \sin\alpha_0}{U_\infty} \quad (4.21)$$

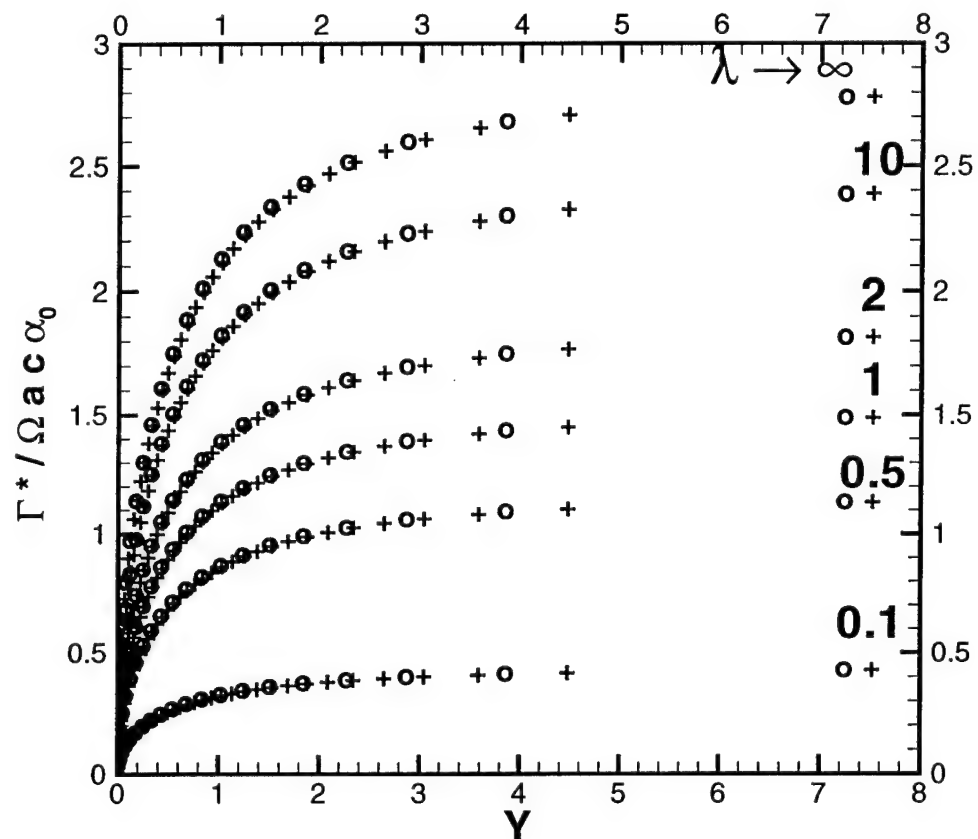


Figure 4.5: Comparison of the computational results with different number of panels in the lifting surface code. Here 'o' represents the computational results with ten chordwise and twenty spanwise panels and '+' represents the computational results with twenty chordwise and forty spanwise panels.

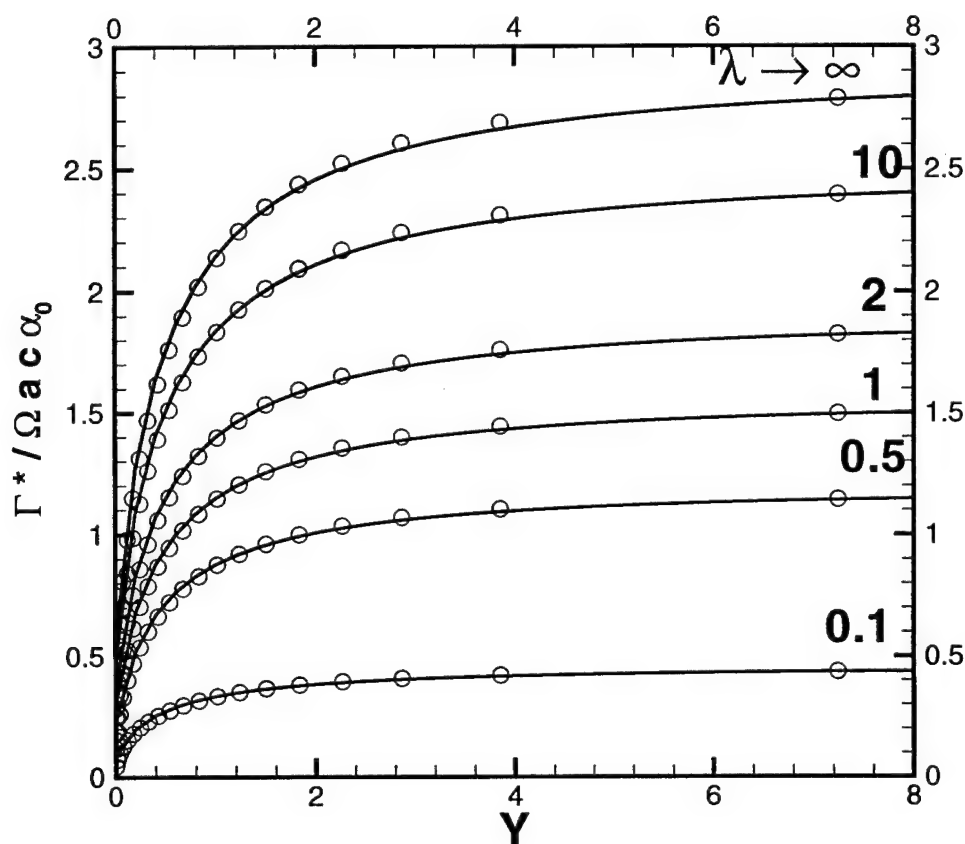


Figure 4.6: Comparison of the inner solution for the bound circulation for a rotary wing between the lifting surface code and the modified Stewartson's equation (4.18). The solid line is the analytical solution of the modified Stewartson's equation. The circles are the computational results from the lifting surface code with ten chordwise and twenty spanwise panels.

where U_∞ has been nondimensionlized by Ωa and equals 1 in the tip region, corresponding to linearized theory. The symbols v and w are the y and z velocity components induced by the wake. Here x is the independent variable measured from the leading edge of the blade. The vortices are initiated at the one-quarter chord position of each panel at the beginning of the numerical integration for every iteration. For the initial condition, $z = 0$ and y is the spanwise location of the trailing vortex shed from the one-quarter chord of each panel. For each trailing vortex, $z = 0$ all along the wing surface, while they can be bent along y direction by the induced velocity. This set of ordinary differential equations was solved numerically by the Adams-Moulton method. Note that the velocity components were calculated for straight-line trailing vortices in the first iteration.

In order to obtain the steady state positions of trailing vortices, we use the centroid of the tip-vortex core \bar{y} and \bar{z} and the core radius measured from the centroid: \bar{r} . The definitions of \bar{y} , \bar{z} and \bar{r} are the same as for the fixed wing. The iterative process was assumed to be convergent when $\frac{\bar{r}_{new} - \bar{r}_{old}}{\bar{r}_{old}}$ is less than 10^{-4} at each value of x . Here we have used one chordwise panel, twenty spanwise panels on the wing surface and one hundred and twenty nodes on each of the trailing vortices. The separation between the nodes on each of the trailing vortices is 0.05. Beyond the last node, the trailing vortex is represented by a semi-infinite, straight vortex line extending to $x = +\infty$ and parallel to the free-stream velocity.

R	1.14 m
ΩR	132 m/s
n_b	2
Chord	0.191 m
Angle of Attack	8°
λ	0.42

Table 4.1: The parameters for the rotor investigated by McAlister *et al* [1995].

Figure 4.7 presents the calculated results for the bound circulation in the inner region for the two-bladed rotor of McAlister *et al* [1995] ($\alpha_0 = 8^\circ$). The parameters of the rotor are given in Table 4.1. Figure 4.8 (a) and (b) presents the X-Y and X-Z views of the roll-up process for the rotor after 110 iterations at which the $\frac{\bar{r}_{new} - \bar{r}_{old}}{\bar{r}_{old}}$ converges up to $x = 3.25$, with more iterations required

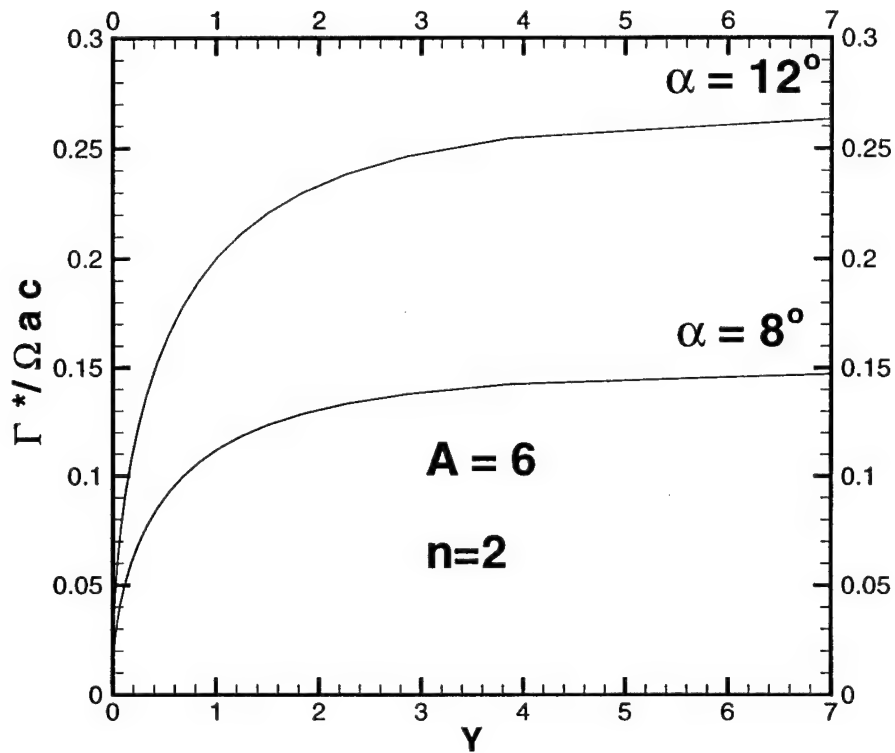


Figure 4.7: The comparison of inner solutions of the bound circulation for the rotor given in Table 4.1 with the rotor at $\alpha_0 = 12^\circ$ and other parameters unchanged.

for larger x .

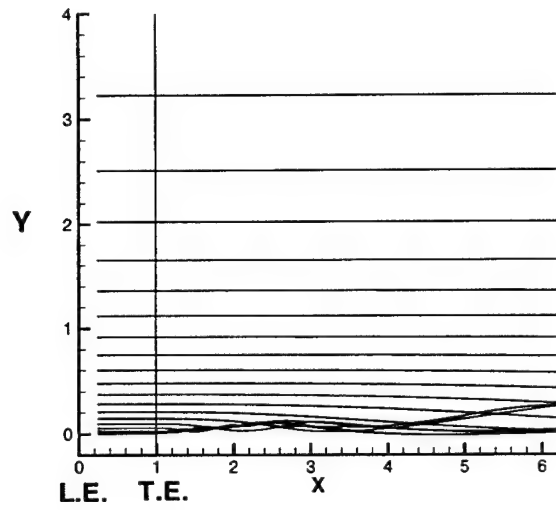
Figure 4.9 (a) and (b) presents the X-Y and X-Z views of the roll-up process for the rotor after 252 iterations at which the $\frac{\bar{\Gamma}_{new} - \bar{\Gamma}_{old}}{\bar{\Gamma}_{old}}$ converges up to $x = 30.0$. The roll-up process of the trailing vortices for the same rotor has also been investigated for convergence at $x = 10.0$ and $x = 20.0$. As we go further downstream along x , more trailing vortices were found to roll-over thereby increasing the maximum tip-circulation. For the convergence at $x = 30.0$, the non-rolled-up trailing vortices were found to contribute very little in increasing the strength of the tip-vortex. Hence, their non-inclusion in the roll-up process is assumed to be of little importance in terms of the strength of the tip-vortex. We note that there is good agreement between the X-Z views in figure 4.8 and figure 4.9 upto the position $x = 3.25$. Also from figure 4.9 (b) we see that with increasing downstream distance x the tip-vortex moves further inboard.

Note that the trailing vortices near the tip region roll over and form a strong trailing vortex. However, in the region away from the tip, the trailing vortices do not roll up in distances of the order shown here. The 3-D view of the roll-up process is presented on Figure 4.10.

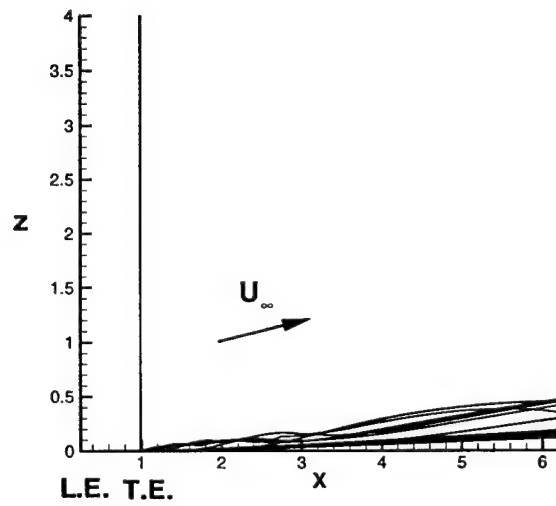
Figure 4.11 shows the comparison of the growth of the circulation of the tip-vortex as a function of convergence achieved at different x . At $x = 6.0$, the circulation of the tip-vortex is about 54.9 percent of the maximum bound circulation. Hence the rotor tip-vortex does not roll up completely at the trailing edge of the rotor blade as assumed in many wake models. Instead, it develops downstream and its circulation approaches a constant asymptotically as is seen when the convergence is achieved at $x = 30.0$, where the circulation of the tip-vortex is about 78.6 percent of the maximum bound circulation. The circulation of the tip-vortex approaches the maximum bound circulation at an infinite distance downstream.

Figure 4.12 shows the downstream development of the core radius \bar{r} of the tip-vortex measured from the centroid for two different cases; one in which convergence is achieved until $x = 3.25$ and the other in which convergence is achieved until $x = 30.0$. The core radii \bar{r} in the Figure 4.12 were calculated at each downstream location x at which an additional trailing vortex enters the rolling-over trailing vortices. Note that the \bar{r} develops downstream and approaches a constant asymptotically. Comparing with Figure 3.14, the core radius of the rotor tip-vortex develops more slowly than the fixed-wing tip-vortex.

Figure 4.13 (a) and (b) show the X-Y and X-Z views of the roll-up process

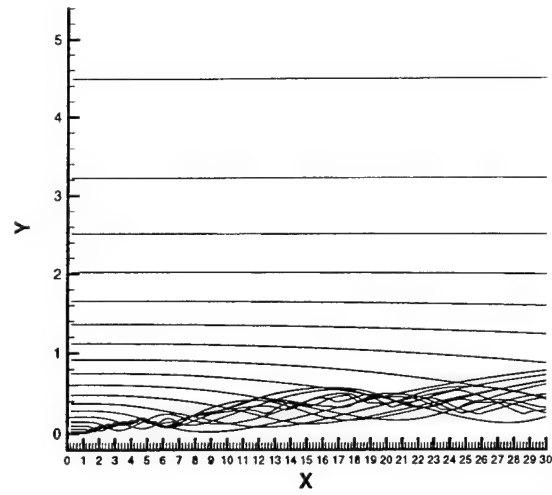


(a)

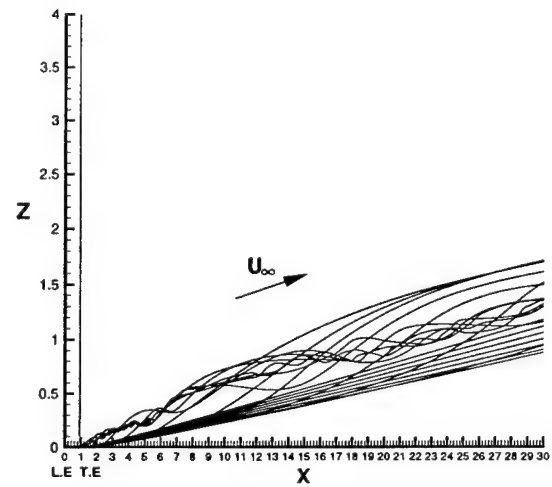


(b)

Figure 4.8: Section view of the roll-up process of trailing vortices for the rotor. The core radius converges at $x = 3.25$ after 110 iterations. A single chordwise panel is used. The angle of attack is 8° .



(a)



(b)

Figure 4.9: Section view of the roll-up process of trailing vortices for the rotor. The core radius converges at $x = 30.0$ after 252 iterations. A single chordwise panel is used. The angle of attack is 8° .

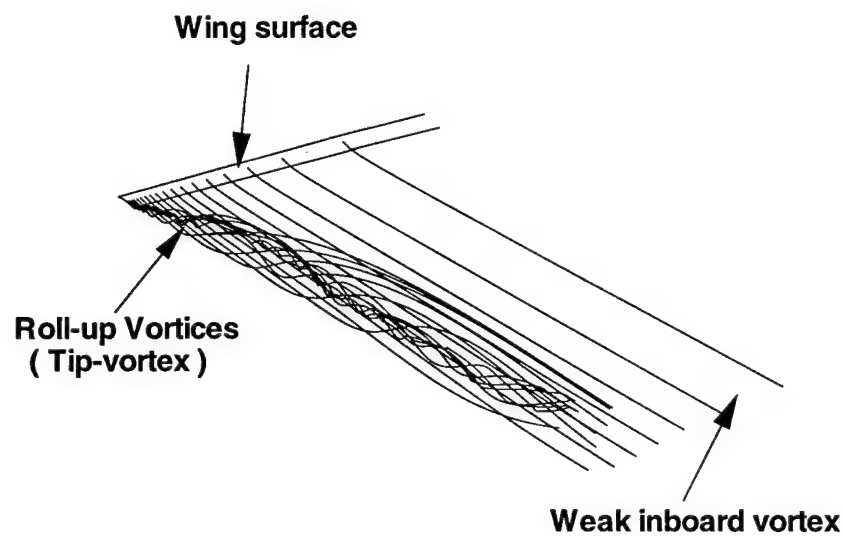


Figure 4.10: 3-D view of the roll-over process of the trailing vortices. The angle of attack is 8° and the core radius is converged until $x = 30.0$. A single chordwise panel is used.

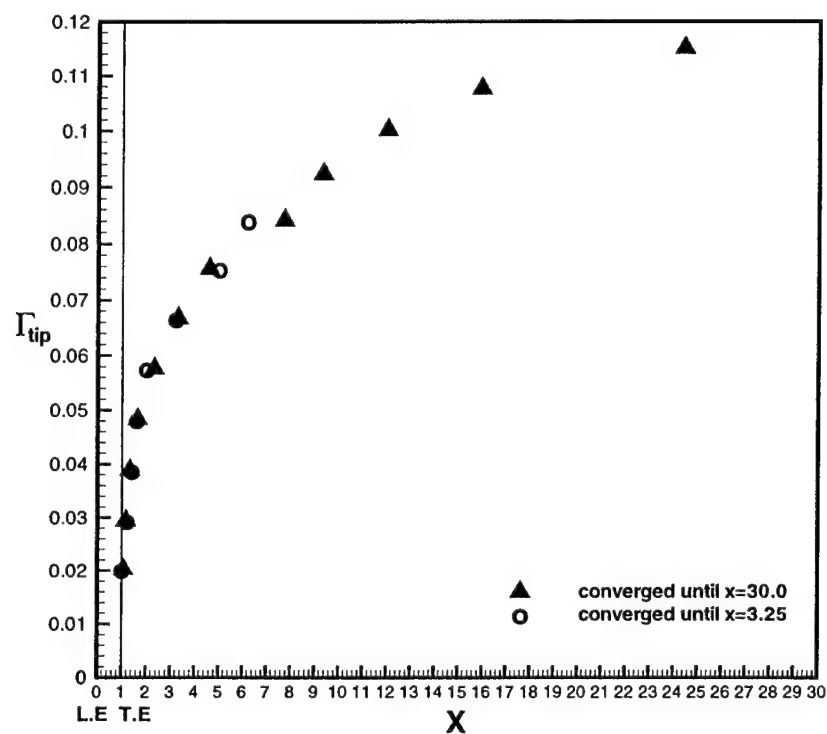


Figure 4.11: The comparison of the circulation of the tip-vortex for convergence achieved at different x . The maximum bound circulation is 0.153 and the angle of attack is 8° . A single chordwise panel is used.

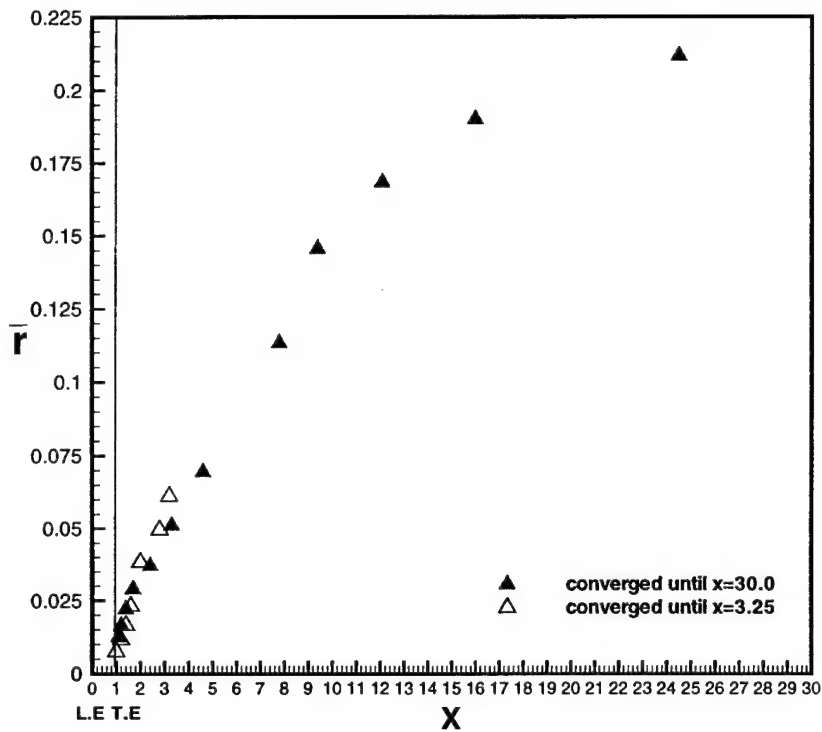


Figure 4.12: Comparison of the core radius of the tip-vortex \bar{r} measured from the centroid at different downstream location up to $x = 3.25$ and $x = 30.0$. A single chordwise panel is used.

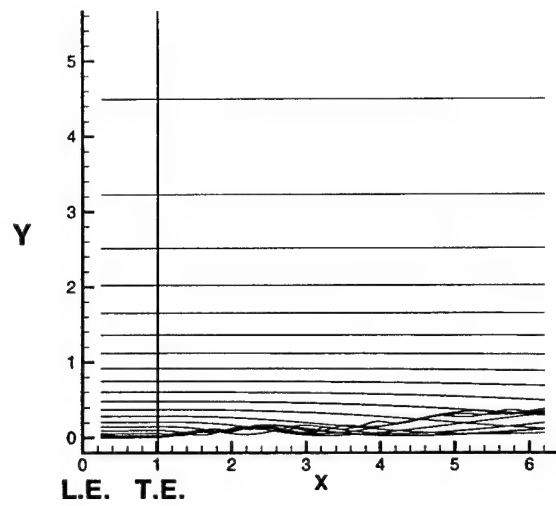
for a rotor with $\alpha_0 = 12^\circ$ and its 3-D view is shown on Figure 4.14. A single chordwise panel was used in this case. The corresponding bound circulation in the inner region is shown on Figure 4.7 ($\alpha_0 = 12^\circ$). After 121 iterations, the core radius \bar{r} converges at $x = 3.25$. At $x = 3.25$, the center of the core has moved inboard. The symbol '*' in Figure 4.15 shows the growth of the circulation of the tip-vortex with x . At $x = 6.0$, the circulation of the tip-vortex is about 60.1 percent of the maximum bound circulation, while for the rotor at $\alpha_0 = 8^\circ$, the circulation is only 54.9 percent. The reason for such difference is addressed below.

Figure 4.16 (a) and (b) show the X-Y and X-Z views of the roll-up process for the rotary wing at $\alpha_0 = 12^\circ$ with four chordwise and twenty spanwise panels. The iterative process was convergent after 132 iterations when $\frac{\bar{r}_{new} - \bar{r}_{old}}{\bar{r}_{old}}$ is less than 10^{-4} up to $x = 3.25$. Note that trailing vortices shed from different chordwise panels but from the same spanwise location roll into the single strong tip-vortex at different downstream locations. The trailing vortices emanate from the panels more close to the leading edge of the rotor blade roll into the tip-vortex more quickly. The 3-D view is shown on Figure 4.17. The downstream development of the circulation of the tip-vortex is presented by the circles in Figure 4.15. Note that they agree fairly well with the result for one chordwise panel (represented by '*').

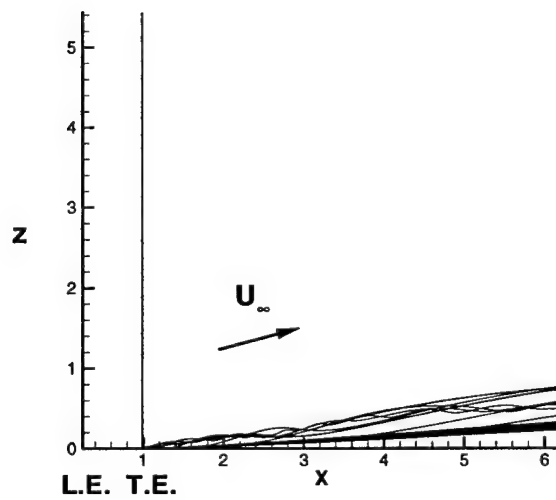
Wing	Angle of Attack	x_1	$\frac{\Gamma_{tip}}{\Gamma_{maxbnd}}$	x_2	$\frac{\Gamma_{tip}}{\Gamma_{maxbnd}}$
Fixed1	8°	3.25	0.546	6.0	0.651
Fixed2	12°	3.25	0.597	6.0	0.748
Rotary1	8°	3.25	0.436	6.0	0.549
Rotary2	12°	3.25	0.492	6.0	0.601

Table 4.2: The circulation of the tip-vortex for both fixed and rotary wings.

Table 4.2 shows the comparison of the circulations of tip-vortex for different fixed and rotary wings. At the same angle of attack and downstream location, the tip-vortex shed from a fixed wing is stronger than that for a rotary wing (Fixed wing1 and Rotary wing1, Fixed wing2 and Rotary wing2); that is, the fixed wing tip-vortex develops more quickly than the rotor tip-vortex. Moreover, the tip-vortex shed by the wing at higher angle of attack also develops more quickly than that shed by the wing at lower angle of attack. Such different downstream development is attributed to the different



(a)



(b)

Figure 4.13: Section view of the roll-up process of trailing vortices for the fixed semi-infinite wing. The core radius converges at $x = 3.25$ after 121 iterations. A single chordwise panel is used. The angle of attack is 12° .

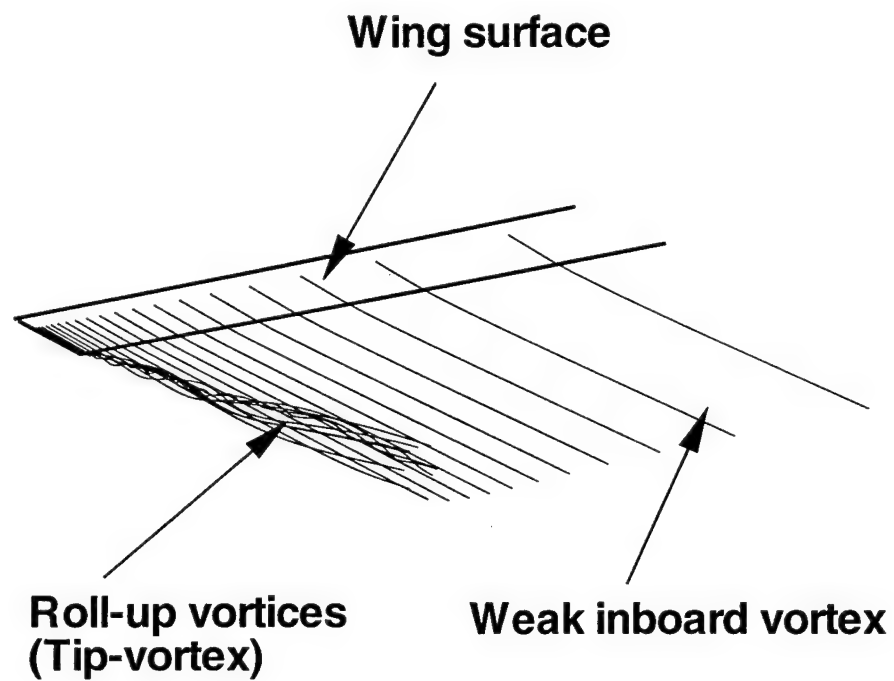


Figure 4.14: 3-D view of the roll-over process of the trailing vortices. The angle of attack is 12° . A single chordwise panel is used.

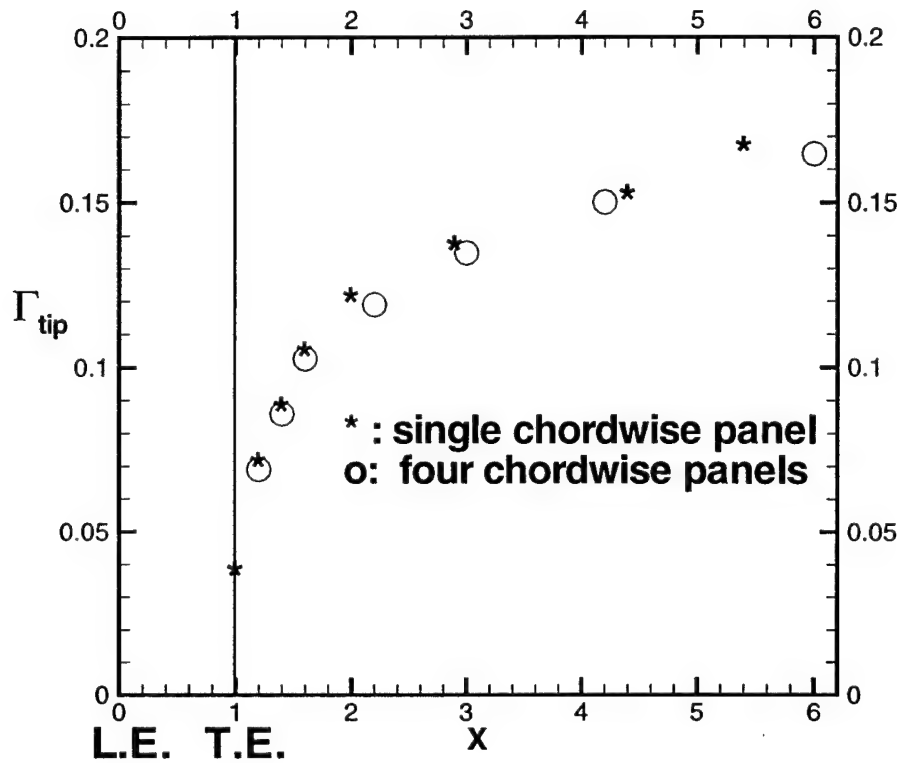
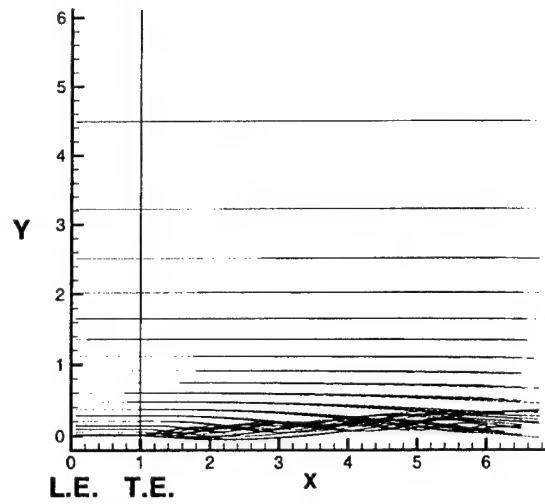
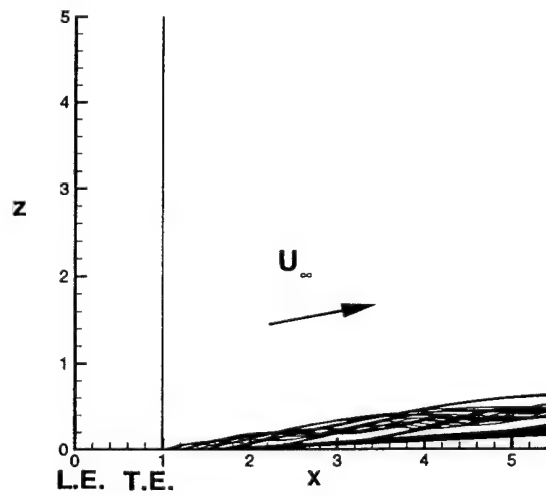


Figure 4.15: The circulation of the tip-vortex at different x . The maximum bound circulation is 0.274 and the angle of attack is 12° . '*' represents the result for a single chordwise panel and 'o' represents the result for four chordwise panels.



(a)



(b)

Figure 4.16: Section view of the roll-up process of trailing vortices for a rotary wing. (a) X-Y plot. (b) X-Z plot. Four chordwise panels and twenty spanwise panels are used. The angle of attack is 12° .

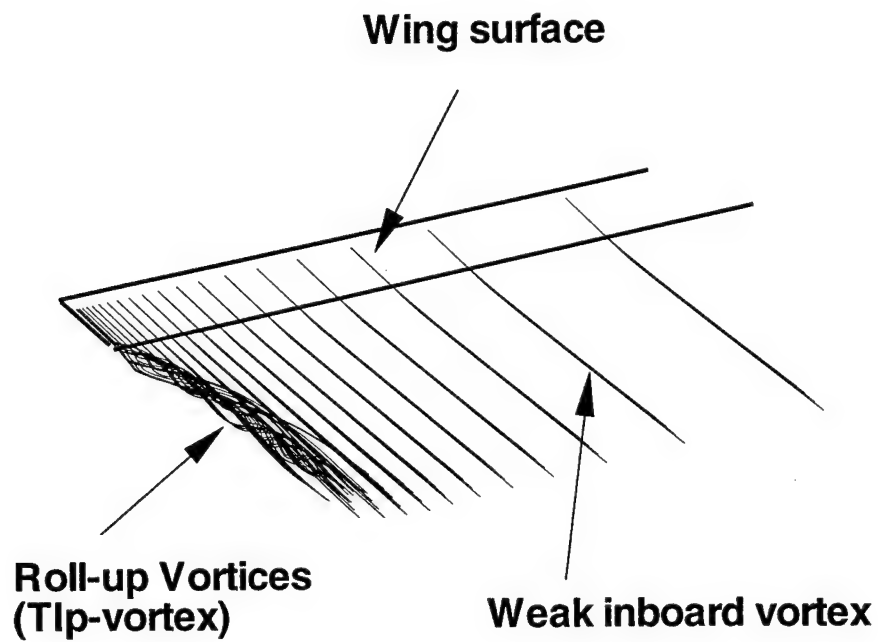


Figure 4.17: 3-D view of the roll-over process of the trailing vortices. The angle of attack is 12° . A single chordwise panel is used.

spanwise variation of the bound circulation near the tip region: a steeper spanwise gradient produces stronger tip vortices and hence a quicker development of the tip-vortex.

Figures 4.18 and 4.19 compare the numerical results for the vertical velocity with the experimental data of McAlister *et al.*[1995] at a position 0.5 and 3 chord lengths behind the trailing edge of the rotor. At $x = 1.5c$, although the maximum of the velocity is underpredicted, the comparison is surprisingly good since the experiments were performed at Reynolds numbers where the flow would be expected to be turbulent, suggesting that viscosity and turbulence have only a minor influence on the roll-up process. Note the lack of a dip outboard of the tip for the rotary wing, which was present for the fixed wing (see Figure 3.23). At $x = 4c$, the computed result shows the tip-vortex has moved more inboard while such movement is not shown by the experimental data.

In the above velocity profile comparisons we considered a rotor blade with a low aspect ratio of 6. But in assuming the rotor blade to be semi-infinite we ignored some higher-order terms in the analytical expression for the downwash induced by the helical rotor wake in the inner region $W_o(Y)$. However, the velocity field around and across the tip-vortex of a single-bladed rotor of aspect ratio 6 was computed after inducting the higher order terms in the expression for downwash. These velocity profiles compare much better with the experiments conducted by McAlister [2001] and the results will be published(Kini *et al* [2002]).

Figure 4.20 shows the calculated results for the bound circulation in the inner region for two-bladed rotors at 8° angle of attack with different aspect ratios. As the aspect ratio increases, the bound circulations come close to each other. Figure 4.21 presents the corresponding induced vertical velocities behind these rotors. Note that the induced vertical velocities for $A = 30, 40$ and 50 are very similar and this suggests that for $A = 30$, the flow behind the rotor is relatively independent of the aspect ratio.

4.4 The Uniformly-Valid Solution for the Bound Circulation for the Rotary Wing

In this section, the uniformly-valid solution for the bound circulation for a rotor is given by using the method of matched asymptotic expansion. We

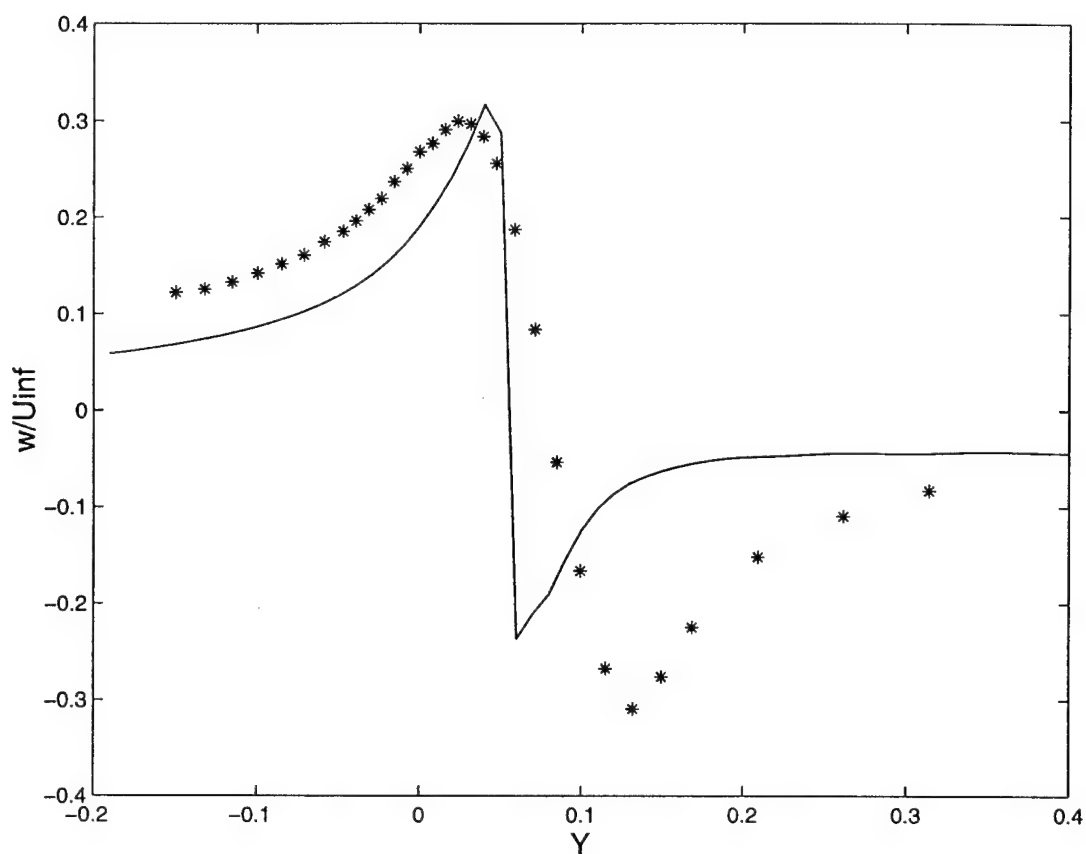


Figure 4.18: The vertical velocity at $x = 1.5$ chord behind the trailing edge of the rotor compared with the experimental data at $z = 0$. Here '*' represents the experimental data and solid line represents the computational data. $Y = 0$ is the rotor tip and $Y > 0$ is inboard. A single chordwise panel is used.

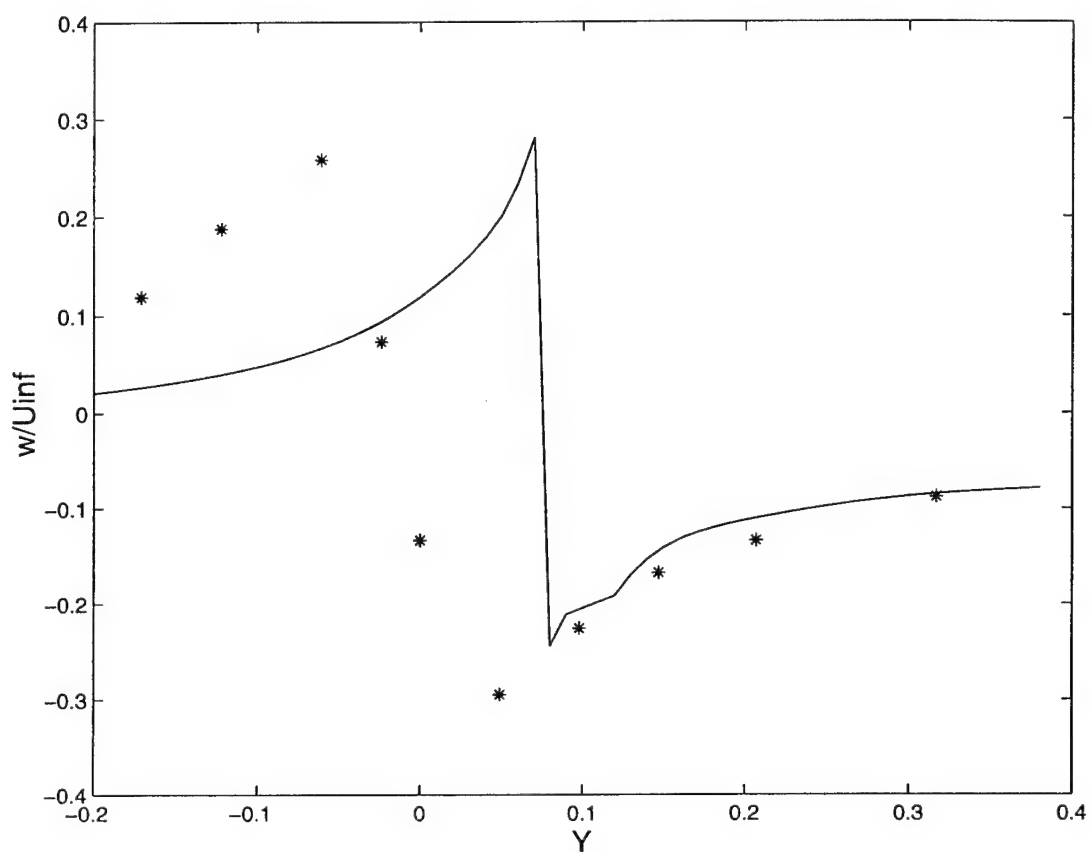


Figure 4.19: The vertical velocity at $x = 4.0$ chord behind the trailing edge of the rotor compared with the experimental data at $z = 0$. Here '*' represents the experimental data and solid line represents the computational data. $Y = 0$ is the rotor tip and $Y > 0$ is inboard. A single chordwise panel is used.

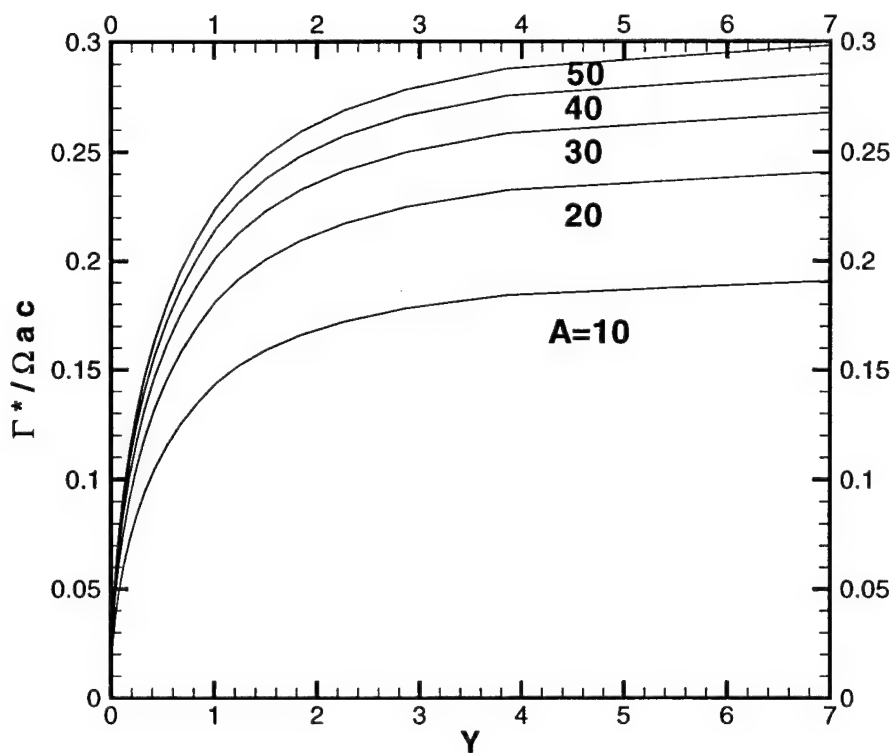


Figure 4.20: The comparison of inner solutions for the bound circulation for two-bladed rotors with different aspect ratios. The angle of attack is 8° .

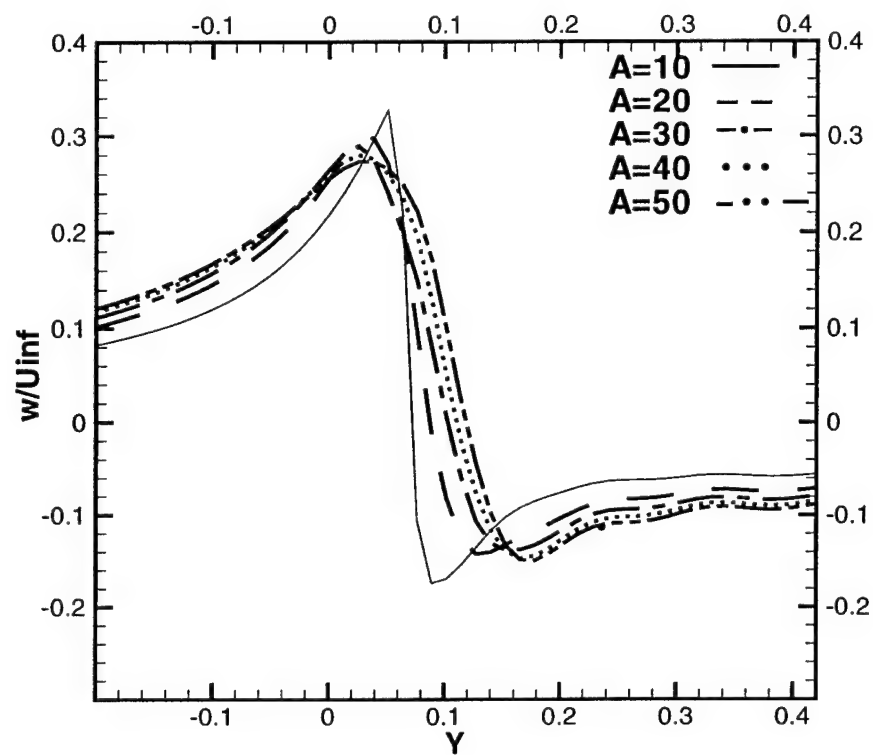


Figure 4.21: The comparison of the induced vertical velocity at $x = 1.5c$ behind different aspect ratio wings.

use “mutiplicative composition”, as defined by Van Dyke[1975], to form the uniformly-valid solution for the bound circulation

$$\Gamma_{uniform} = \frac{\Gamma_{inner} \times \Gamma_{outer}}{\Gamma_{cp}} \quad (4.22)$$

where Γ_{inner} is the inner solution of the bound circulation (near the tip region) given by the modified Stewartson[1960] or the lifting surface code, Γ_{outer} is the outer solution which is given by equation (4.4) and Γ_{cp} is the common part which is defined as the bound circulation as the outer variable $R \rightarrow 1$ or the inner variable $Y \rightarrow \infty$.

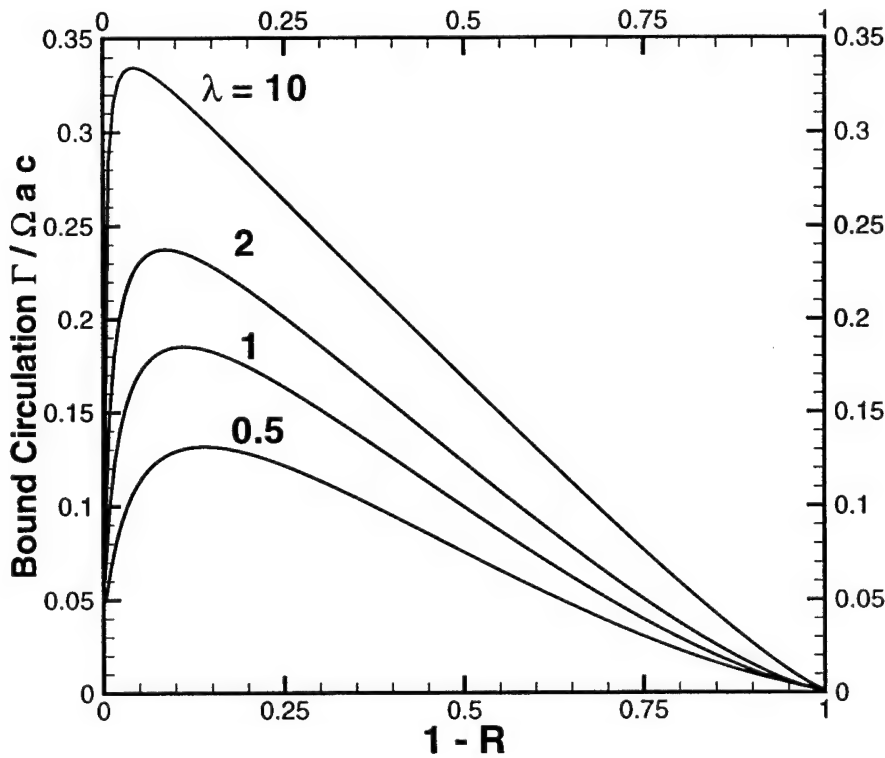


Figure 4.22: The uniformly-valid solutions without wake contraction for different λ . $\alpha_0 = 8^\circ$.

Figure 4.22 shows the resulting uniformly-valid solution without slip-

stream contraction. When the rotor-wake contraction effects are considered, the downwash induced at the tip-path plane by the contracting slipstream vortices will change and the bound circulation will change correspondingly. In order to determine the effect of contraction on the bound circulation, two types of wake models are used to represent the slipstream contraction, which will be discussed in the next chapter.

4.5 Summary

In this chapter, the rotary wing computation is performed. The most important result of this work is that by applying the classical inviscid lifting-line and lifting-surface methods, the formation of the tip-vortex including the core radius and the circulation can be predicted quantitatively as a function of the angle of attack, the aspect ratio and the number of blades.

It is shown that near the rotor-tip, to leading order, the flow past a rotary wing is equivalent to the flow over a semi-infinite wing and it has an analytical solution given by the modified Stewartson[1960] equation (4.18). The similar lifting-surface method which was developed for the fixed wing is extended to the rotary wing and its numerical results compare well with the modified Stewartson[1960] equation (4.18).

The roll-up process for the trailing vortices is presented. It is shown that the rotor tip-vortex does not roll up completely at the trailing edge of the rotor blade as assumed by many rotor wake models; instead, the core radius and the circulation develop downstream asymptotically. Compared with the fixed wing at the same angle of attack, the downstream development of the rotor tip-vortex is much slower than that for the fixed wing tip-vortex. The computational results for the induced vertical velocity compare well with McAlister *et al.* [1995]. The uniformly valid solution for the bound circulation of a rotor without rotor-wake contraction is established by the "multiplicative composition" (Van Dyke 1975).

It is observed that the rotor wake is not a perfect helix as assumed in Burggraf's lifting-line theory [1999]. In the next chapter, two types of rotor wake models (vortex cylinder model and discrete vortex ring model) are used to consider the influence of the rotor wake contraction on the bound circulation in the outer region away from the rotor-tip.

Chapter 5

Rotor-Wake Contraction Effects on the Formation of the Tip-Vortex

5.1 Introduction

Experiments show that the tip vortices appear to be fully contracted within about one rotor radius below the tip-path plane (Landgrebe [1972], Gray [1991] and Leishman *et al.* [1995]). Leishman *et al.* [1995] reported that the vertical slipstream velocity in the wake boundary is roughly doubled in magnitude as the wake contracted which is consistent with the simple one-dimensional actuator disk theory (Johnson [1980]). Outside the wake boundary, the flow is found to be relatively quiescent. The axial and radial displacement (Z_{tip} and r_{tip}) of the tip-vortex with respect to the rotor position is given empirically by Landgrebe [1972] as:

$$\frac{Z_{tip}}{R} = \begin{cases} k_1 \phi_w, & 0 \leq \phi_w \leq \frac{2\pi}{b} \\ (\frac{Z_{tip}}{R}|_{\phi_w=\frac{2\pi}{b}}) + k_2(\phi_w - \frac{2\pi}{b}), & \phi_w \geq \frac{2\pi}{b} \end{cases} \quad (5.1)$$

and

$$\frac{r_{tip}}{R} = A + (1 - A)e^{-\lambda_1 \phi_w} \quad (5.2)$$

where k_1 and k_2 are constants which are related to the blade loading and ϕ_w is the phase angle of the rotor blade. A is a constant and for the stable near-wake region $A = 0.78$ which means the asymptotic contraction is about

78 percent of the rotor radius. λ_l is defined as

$$\lambda_l = 0.145 + 27C_T \quad (5.3)$$

where C_T is the thrust coefficient.

Because of the rotor wake contraction, the induced downwash at the rotor tip-path plane by the contracting slipstream vortices will change and the bound circulation will change correspondingly. In order to determine the effect of the contraction on the bound circulation, we have used two types of wake models (vortex cylinder and discrete vortex ring model) to represent the slipstream contraction, discussed below.

5.2 The Vortex-Cylinder Model

In this section, we use a vortex cylinder model to consider the influence of the rotor wake contraction on the bound circulation. The slipstream of the tip-vortex can be obtained based on Burggraf's [1999] theory. In Burggraf's [1999] theory, the rotor wake is represented by uniformly distributed semi-infinite vortex cylinders. According to this model, the inner semi-infinite vortex cylinders have no influence on the outer-most semi-infinite vortex cylinder (i.e. the tip-vortex). Therefore, the velocity components induced at the slipstream boundary by the vorticity distributed along the outermost semi-infinite vortex cylinder are determined. The streamline passing through the edge of the rotor disk is evaluated by numerical integration, using the velocity components evaluated on the original cylinder surface as a first approximation.

By definition, the slope of a streamline is given in terms of the velocity components as

$$\frac{dr}{dz} = \frac{v_r}{v_z} \quad (5.4)$$

where v_r and v_z are velocity components induced by the outer-most semi-infinite vortex cylinder at the evaluation point. By solving these streamline equations, the slipstream boundary of the tip-vortex can be represented as the streamline passing through the edge of the rotor disk.

First we consider the rotor wake-contraction effect on the bound circulation in the outer region. In order to determine the effect of rotor-wake contraction on the bound circulation, we have used a simple model to represent the slipstream contraction. In this model, the slipstream has been

represented by a discrete sequence of vortex cylinders of finite length and different radii. The wake configuration is defined using a contraction coefficient $\epsilon = \frac{a_{i+1}}{a_i}$ with $\epsilon < 1$, where a_{i+1} and a_i ($i = 1, \dots, N$) are the radii of two downstream successive finite vortex cylinders respectively. In this case, the lifting-line model was solved by a numerical scheme, using the elliptic-integral formulas given by Radcliff *et al.* [2000] to evaluate the downwash induced by each vortex cylinder. Figure 5.1 shows the structure of this model.

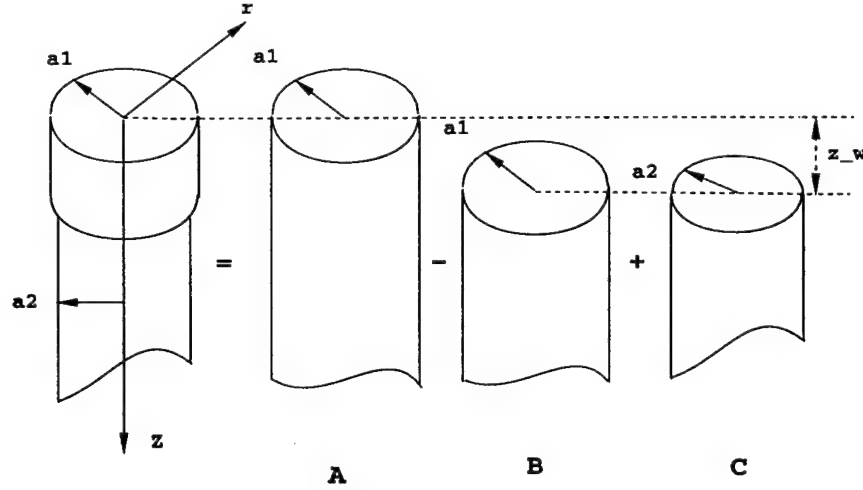


Figure 5.1: The vortex cylinder model for the rotor wake contraction at a single downstream location.

Note that we use only three vortex cylinders to illustrate the model at a single contraction location, though thirty cylinders were used in the numerical calculation.

The upper vortex cylinder has a radius of a_1 and length z_w below the rotor-tip path plane, the lower vortex cylinder has a radius of a_2 and extends to infinity downstream. The contraction coefficient $\epsilon = \frac{a_2}{a_1}$. The radial and vertical induced velocities by a semi-infinite vortex cylinder are given by Radcliff *et al.* [2000]. The axial induced velocity at the tip-path plane ($r, 0$) by the three semi-infinite vortex cylinders (A, B and C) is given by

$$v_z(r, 0) = \frac{\gamma_\theta(r')}{4} [1 + \text{sign}(r' - r)] - \frac{\gamma_\theta(r')}{4} C_B + \frac{\gamma_\theta(r')}{4f(\epsilon)} C_C \quad (5.5)$$

r' is the radius of the vortex cylinder A, $f(\epsilon)$ is a function accounting for the

variation of $\gamma_\theta(r')$ when r' changes from a_1 to a_2

$$f(\epsilon) = \epsilon \frac{v_z(r', z_w)}{v_z(r', 0)} \quad (5.6)$$

where for convenience $v_z(r', z_w)$ and $v_z(r', 0)$ are both approximated by $v_z(r', 0)$ and thus $f(\epsilon) = \epsilon$. The quantities C_B and C_C in Equation (5.5) are defined as

$$C_B = 1 + \text{sign}(r' - r) + \frac{2}{\pi} \frac{\frac{z - z_w}{r'}}{\sqrt{\left(\frac{z - z_w}{r'^2}\right)^2 + \left(\frac{r}{r'} + 1\right)^2}} \left[K(k_b) - \frac{\frac{r}{r'} - 1}{\frac{r}{r'} + 1} \Pi(\sigma_b^2, k_b) \right] \quad (5.7)$$

and

$$C_C = 1 + \text{sign}(\epsilon r' - r) + \frac{2}{\pi} \frac{\frac{z - z_w}{\epsilon r'}}{\sqrt{\left(\frac{z - z_w}{\epsilon r'^2}\right)^2 + \left(\frac{r}{\epsilon r'} + 1\right)^2}} \left[K(k_c) - \frac{\frac{r}{\epsilon r'} - 1}{\frac{r}{\epsilon r'} + 1} \Pi(\sigma_c^2, k_c) \right] \quad (5.8)$$

where K is the complete elliptic integral of the first kind and Π is the complete elliptic integral of the third kind.

Now we integrate with respect to r' from the root to the tip,

$$v_z(r, 0) = \int_0^a \left[\frac{\gamma_\theta(r')}{4} [1 + \text{sign}(r' - r)] - \frac{\gamma_\theta(r')}{4} C_B + \frac{\gamma_\theta(r')}{4f(\epsilon)} C_C \right] dr' \quad (5.9)$$

where a is the radius of the rotor. The term $\int_0^a \frac{\gamma_\theta(r')}{4} [1 + \text{sign}(r' - r)] dr'$ has been derived by Burggraf[1999]. As an approximation, we use Burggraf's [1999] result (see Appendix B) to calculate term C_B and term C_C .

Since

$$\gamma_\theta(r) = -\frac{\Omega^2 c}{2v_z(r, 0)} \left[\alpha_0 - \frac{1}{\Omega} \frac{dv_z}{dr} \right] \quad (5.10)$$

Non-dimensionlizing equation above where $R = \frac{r}{a}$ and $W(R) = \frac{v_z}{\Omega a \alpha_0}$,

$$\gamma_\theta(R) = -\frac{\Omega c}{2aW(R)} \left[1 - \frac{dW(R)}{dR} \right] \quad (5.11)$$

The velocity induced by vortex cylinder B and C is defined as v_{z_c} and

$$v_{z_c}(r, 0) = \int_0^a \left[-\frac{\gamma_\theta(r')}{4} C_B + \frac{\gamma_\theta(r')}{4f(\epsilon)} C \right] dr' \quad (5.12)$$

Non-dimensionlizing equation (5.12), we have

$$W_c(R) = \frac{1}{8\lambda} \int_0^1 \frac{1}{W(R')} \left[1 - \frac{dW(R')}{dR'} \right] \left[C_B - \frac{C_C}{f(\epsilon)} \right] dR' \quad (5.13)$$

From Appendix A, equation (B.11)

$$W(R') = \frac{1}{4\lambda} [\sqrt{1 + 8\lambda R'} - 1] \quad (5.14)$$

so that

$$\frac{dW(R')}{dR'} = \frac{1}{\sqrt{1 + 8\lambda R'}} \quad (5.15)$$

Non-dimensionlizing C_B and C_C , we have C_B

$$C_B = 1 + \text{sign}(R' - R) + \frac{2}{\pi} \frac{\frac{Z-Z_W}{R'}}{\sqrt{\frac{(Z-Z_W)^2}{R'^2} + \left(\frac{R}{R'} + 1\right)^2}} \left[K(k_b) - \frac{\frac{R}{R'} - 1}{\frac{R}{R'} + 1} \Pi(\sigma_b^2, k_b) \right] \quad (5.16)$$

where

$$k_b^2 = \frac{4 \frac{R}{R'}}{\frac{(Z-Z_W)^2}{R'^2} + \left(\frac{R}{R'} + 1\right)^2} \quad (5.17)$$

$$\sigma_b^2 = \frac{4 \frac{R}{R'}}{\left(\frac{R}{R'} + 1\right)^2} \quad (5.18)$$

and C_C

$$C_C = 1 + \text{sign}(\epsilon R' - R) + \frac{2}{\pi} \frac{\frac{Z-Z_W}{\epsilon R'}}{\sqrt{\frac{(Z-Z_W)^2}{(\epsilon R')^2} + \left(\frac{R}{\epsilon R'} + 1\right)^2}} \left[K(k_c) - \frac{\frac{R}{\epsilon R'} - 1}{\frac{R}{\epsilon R'} + 1} \Pi(\sigma_c^2, k_c) \right] \quad (5.19)$$

where

$$k_c^2 = \frac{4 \frac{R}{\epsilon R'}}{\frac{(Z-Z_W)^2}{(\epsilon R')^2} + \left(\frac{R}{\epsilon R'} + 1\right)^2} \quad (5.20)$$

$$\sigma_c^2 = \frac{4 \frac{R}{\epsilon R'}}{\left(\frac{R}{\epsilon R'} + 1\right)^2} \quad (5.21)$$

The total downwash in the rotor tip-path plane induced by these three vortex cylinders is $W(R) + W_c(R)$ where $W_c(R)$ is the correction term due

to the rotor wake contraction. Therefore, the resulting bound circulation is

$$\begin{aligned}\frac{\Gamma(R)}{\pi\alpha_0} &= R - [W(R) + W_c(R)] \\ &= R - \left[\frac{1}{4\lambda}(\sqrt{1 + 8\lambda R} - 1) + W_c(R)\right]\end{aligned}$$

We can add more semi-infinite vortex cylinders to this model only by modifying $W_c(R)$.

Burggraf[1999] has analytically derived the rotor slipstream contraction in hovering flight condition based on the velocity induced by the tip-vortex cylinder alone. z_w and ϵ for each of our interior vortex cylinders are based on Burggraf[1999] results for the tip-vortex cylinder.

Now we consider the downwash induced by the rotor-wake contraction $W_c(R)$ in the inner region where $R = 1$. Setting $R = 1$ into equation (5.13), we found $W_c(1)$ is a function of λ . Table 5.1 shows the comparison between $W(1)$ and $W_c(1)$. Note that $W_c(1)$ is much less than $W(1)$ and thus $W_c(1)$ is not included in the inner solution in this work.

λ	$W(1)$	$W_c(1)$	$\frac{W_c(1)}{W(1)}$
0.07	0.889	0.070	0.080
0.7	0.560	0.035	0.063
7	0.234	0.012	0.05

Table 5.1: The comparison of $W(1)$ and $W_c(1)$.

Figure 5.2 compares the resulting uniformly-valid solution without slipstream contraction with the solution accounting for the rotor-wake contraction. Note that as λ increases, the effect of slipstream contraction is reduced.

Figure 5.3 compares our theoretical results with the experimental data of Caradonna and Tung [1981]. Note that the theoretical values for no contraction are evaluated from purely analytical formulas. The comparison is reasonably good in each case, though the peak value is underpredicted for the smallest value of angle of attack ($\alpha = 5^\circ$). Note that for the large angle of attack ($\alpha = 12^\circ$), the wake contraction model (represented by the solid lines) produces better results than the model without wake contraction (presented by the dotted lines) except near the tip.

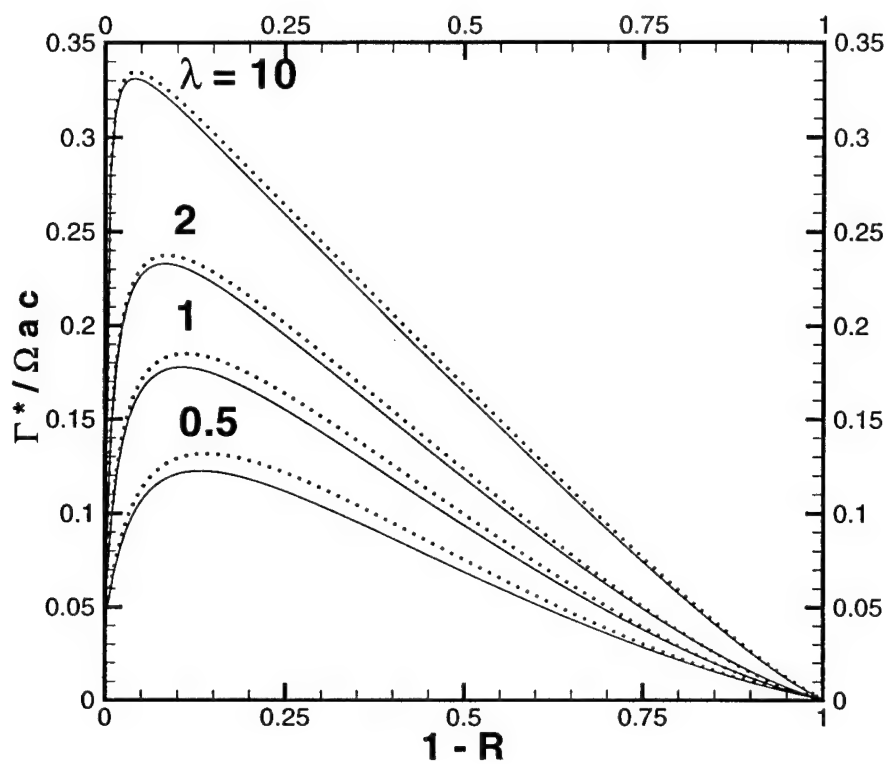


Figure 5.2: The comparison of the uniformly-valid solutions without wake contraction with the solutions with wake contraction for different λ . The dotted lines represent the solutions without wake contraction and the solid lines represent the solutions with wake contraction. $\alpha_0 = 8^\circ$.

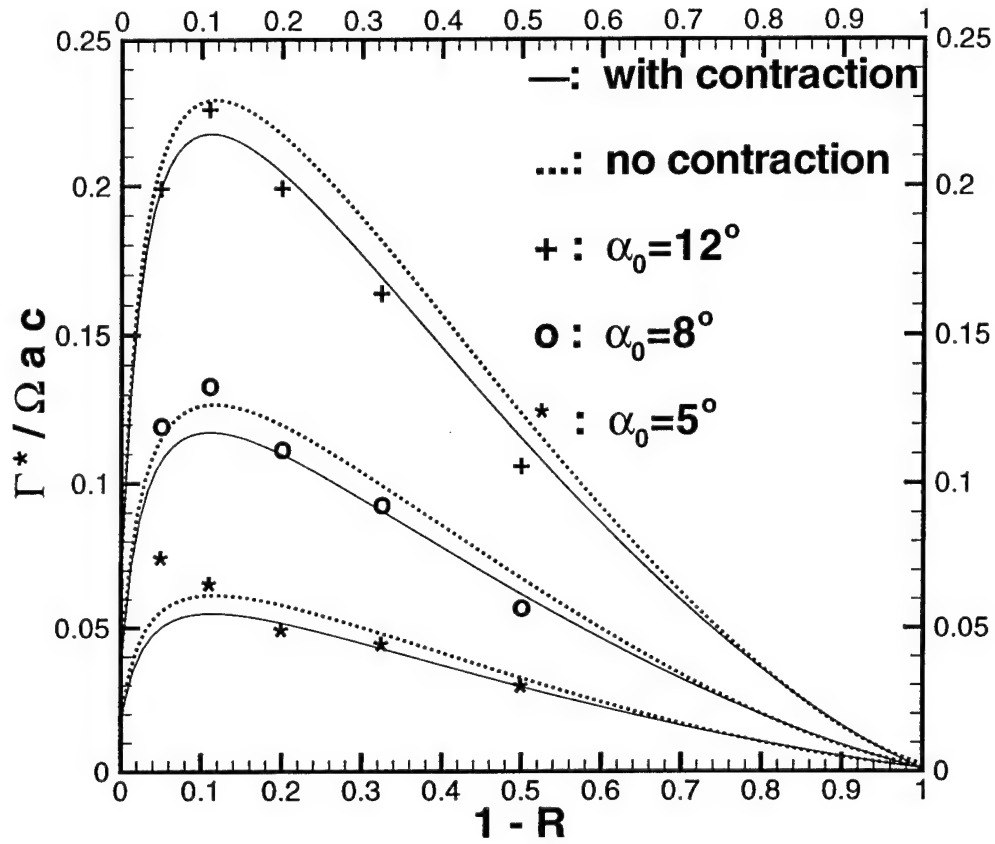


Figure 5.3: The comparison of the computational solutions with the experimental data of Caradonna and Tung [1981] for several values of angle of attack. The solid lines represent the numerical solutions with wake contraction, the dotted lines represent the numerical solutions without wake contraction, '+' represents the experimental data for $\alpha_0 = 12^\circ$, 'o' represents the experimental data for $\alpha_0 = 8^\circ$ and '*' represents the experimental data for $\alpha_0 = 5^\circ$.

The problem with this vortex cylinder model is that in Burggraf's [1999] theory, the discrete helical vortices are approximated by cylindrical sheets with uniformly distributed vorticity. However, this is not appropriate because the induced downwash is not a constant downstream on each vortex cylinder. In order to obtain a more accurate representation of the slipstream of the rotor wake and the outer solution for the bound circulation on the rotor blade, a discrete vortex-ring model is applied, as discussed below.

5.3 The Discrete Vortex-Ring Model

5.3.1 Numerical Scheme

Burggraf developed a discrete vortex-ring model to represent the discrete helical vortices (See Appendix C for more details). The more-or-less helical trailing vortices shed from the rotor across the rotor blade forms a screwlike surface winding down below the rotor plane and this screwlike surface is referred as an elemental slipstream surface. In this vortex-ring model, each elemental slipstream surface is represented by a sequence of discrete vortex rings. With every rotor revolution, each vortex ring convects along with the local induced radial and vertical velocities. The circulations of the vortex rings on the same elemental slipstream surface are constant and equal to the spanwise variation of the bound circulation on the rotor plane from which they are shed from. An iterative scheme is applied to obtain the slipstream of the trailing vortices and the corresponding bound circulation simultaneously.

For the numerical computation, initially, we use Burggraf's [1999] theoretical solution (see Appendix B) to determine the circulations of the vortex rings on each slipstream surface and the downstream distance between two successive vortex rings on the same elemental slipstream. To accurately represent the rotor-wake slipstream, we use the discrete vortex-ring representation up to a distance $L = 5$ below the rotor tip-path plane and then extend the rotor-wake slipstream from the final vortex ring on this elemental slipstream surface to infinity with a uniform distribution of azimuthal vorticity wound around a semi-infinite cylinder as shown on Figure 5.4. The iterative process begins with this initial condition.

Now we consider the iteration process. For each iteration, first, a set of streamline equations are solved numerically with the initial position at the rotor tip-path plane $(r_m, 0)$ for each elemental slipstream surface m where

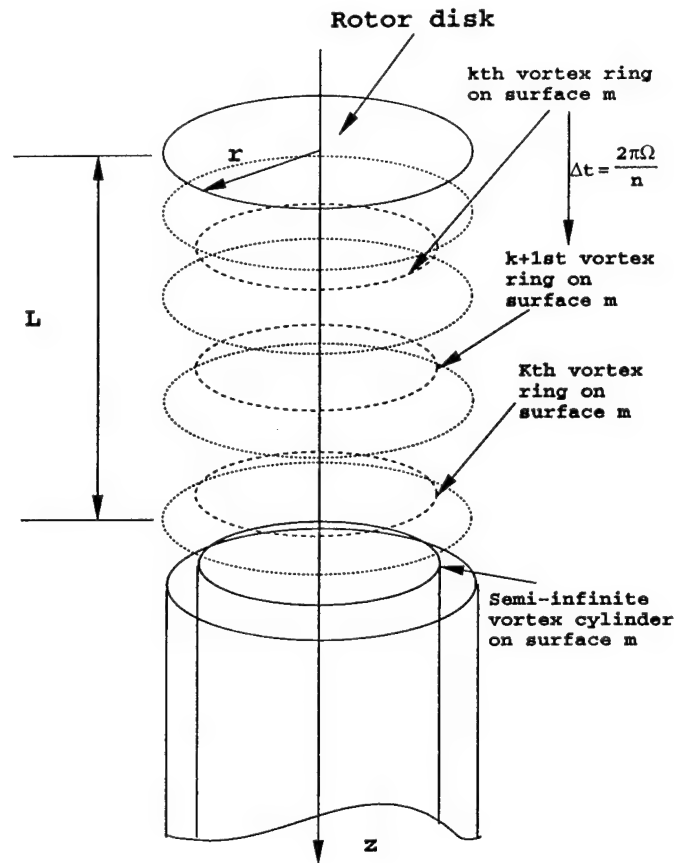


Figure 5.4: The discrete vortex ring model. The dashed lines represent the vortex rings on the m^{th} elemental surface. After the last vortex ring K , the m th elemental surface has been represented by a semi-infinite vortex cylinder with uniformly distributed vorticity. After a revolution time $\frac{2\pi\Omega}{n}$, vortex ring k convects with the local induced velocity to vortex ring $k+1$.

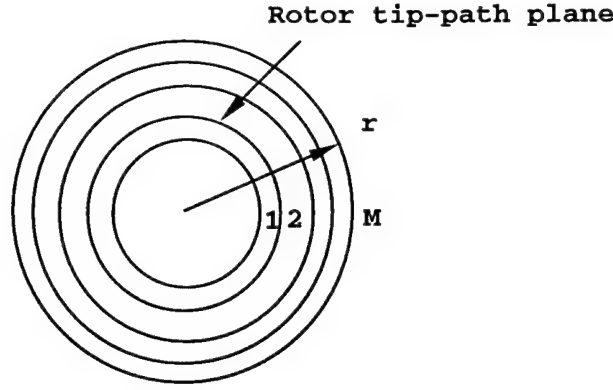


Figure 5.5: Vortex ring representation of the rotor wake (axial view). M spanwise elemental slipstream surfaces.

$m = 1, \dots, M$ (M is the total number of elemental slipstream surfaces across the rotor blade as shown on Figure 5.5), we have

$$z_{m,k+1}^{new} - z_{m,k}^{new} = \frac{2\pi}{n} \alpha_0 w \quad (5.22)$$

$$r_{m,k+1}^{new} - r_{m,k}^{new} = \frac{2\pi}{n} \alpha_0 u \quad (5.23)$$

where $z_{m,k}^{new}$ and $r_{m,k}^{new}$ are nondimensionlized downstream and radial positions (by the rotor radius a) of the vortex ring k on the elemental surface m . As mentioned above, initially, $r_{m,0}^{new} = r_m$ and $z_{m,0}^{new} = 0$. w and u are induced radial and vertical velocities nondimensionlized by $\Omega a \alpha_0$. A relaxation scheme is applied also to obtain the slipstream of trailing vortices, in the form

$$z_{m,k}^{new} = \omega z_{m,k}^{new} + (1 - \omega) z_{m,k}^{old} \quad (5.24)$$

and

$$r_{m,k}^{new} = \omega r_{m,k}^{new} + (1 - \omega) r_{m,k}^{old} \quad (5.25)$$

where ω is the relaxation coefficient. For each rotor revolution, the vortex ring on surface m convects from $(r_{m,k}^{new}, z_{m,k}^{new})$ to $(r_{m,k+1}^{new}, z_{m,k+1}^{new})$. Having obtained $z_{m,k+1}^{new}$, $r_{m,k+1}^{new}$, $z_{m,k+2}^{new}$ and $r_{m,k+2}^{new}$ can be computed similarly. Such computations are repeated until $z_{m,k}^{new}$ is greater than L . Next, the bound circulation for the rotor blade is evaluated at the center of two consecutive slipstream surfaces in the rotor plane for each iteration. The iterative process

was assumed to be convergent when the maximum absolute value of the bound circulation $\frac{\Gamma_{new} - \Gamma_{old}}{\Gamma_{old}}$ is less than the criterion given by the user.

With this discrete vortex ring model, the slipstream of the helical rotor wake can be evaluated with the local induced radial and vertical velocities by all the wake vortex segments and this makes the vortex ring model more accurate than the vortex cylinder model provided enough rings used in the computations.

5.3.2 Results for the Discrete Vortex-Ring Model

We applied the discrete vortex ring model to study a single-bladed rotor with aspect ratio $A = 6$ and geometric angle of attack $\alpha_0 = 8^\circ$. Figure 5.6 presents the comparison of the outer solutions for the induced downwash in the rotor plane and Figure 5.7 shows the comparison of the corresponding bound circulations where μ is the cut-off parameter in the numerical calculation. Note that the calculated bound circulations for the vortex ring model agree well with Burggraf's [1999] lifting-line theory in the middle of the rotor (R from 0.35 to 0.6). However, near the tip, the results for the vortex ring model are higher than the theoretical result and near the hub, they are lower than the theoretical result. This might be because that with the rotor wake contraction, the induced downwash in the rotor tip-path plane becomes smaller near the tip region but larger near the hub compared with the Burggraf's [1999] non-contracted lifting-line model as shown on Figure 5.6. Moreover, the results for the vortex ring-model are affected by the cut-off parameter μ . As μ is reduced, the results approach the theoretical curve. The minimum μ was taken to be 0.16 for $M = 4$ and 0.28 for $M = 8$. For a value of μ below these values for the corresponding M , the computations do not converge.

The converged slipstream for the rotor-wake is shown on Figure 5.8. Note that the slipstream predicted by the discrete vortex-ring model agrees fairly well with Landgrebe's experimental formula (5.2), while the slipstream of Burggraf's first-order approximation overpredicts the contraction.

5.4 Summary

In this chapter, the solution for the spanwise bound circulation for a rotary wing is computed using two types of wake model: vortex cylinder and discrete vortex ring model. In the vortex cylinder model, the contracting

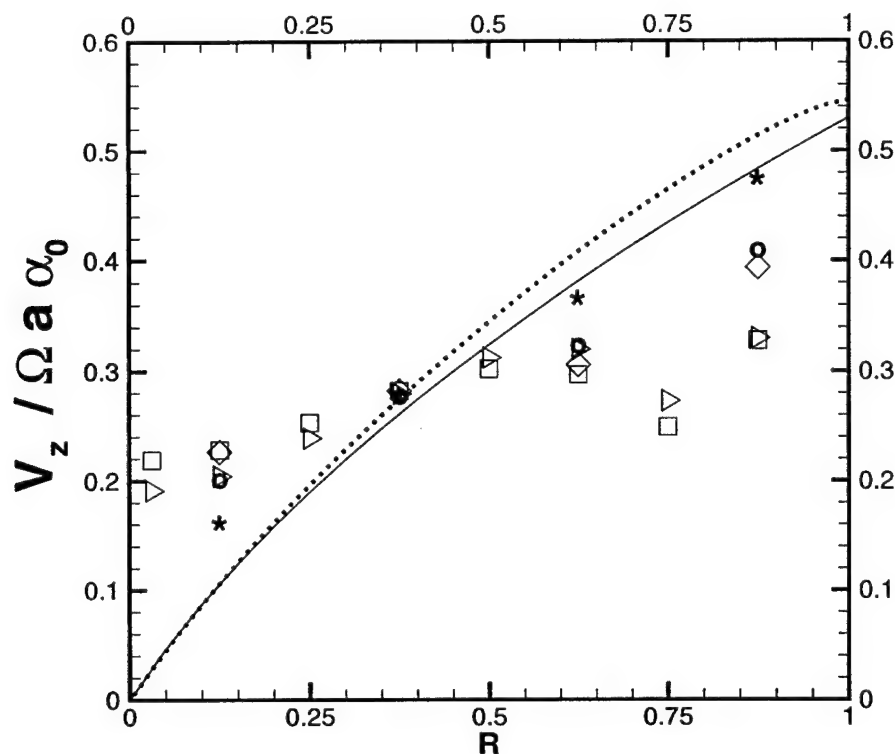


Figure 5.6: Comparison of the induced downwash in the plane of the rotor (outer solution). The solid line represents the Burggraf's theoretical solution, the dotted line represents the result for the vortex-cylinder model, '*' represents the result for $M = 4$ and $\mu = 0.16$, 'o' represents the result for $M = 4$ and $\mu = 0.28$, '◇' represents the result for $M = 4$ and $\mu = 0.35$, the right pointing triangle represents the result for $M = 8$ and $\mu = 0.28$ and the box represents the result for $M = 8$ and $\mu = 0.35$. M is the number of the elemental surfaces and μ is the cut-off parameter used in the numerical calculation.

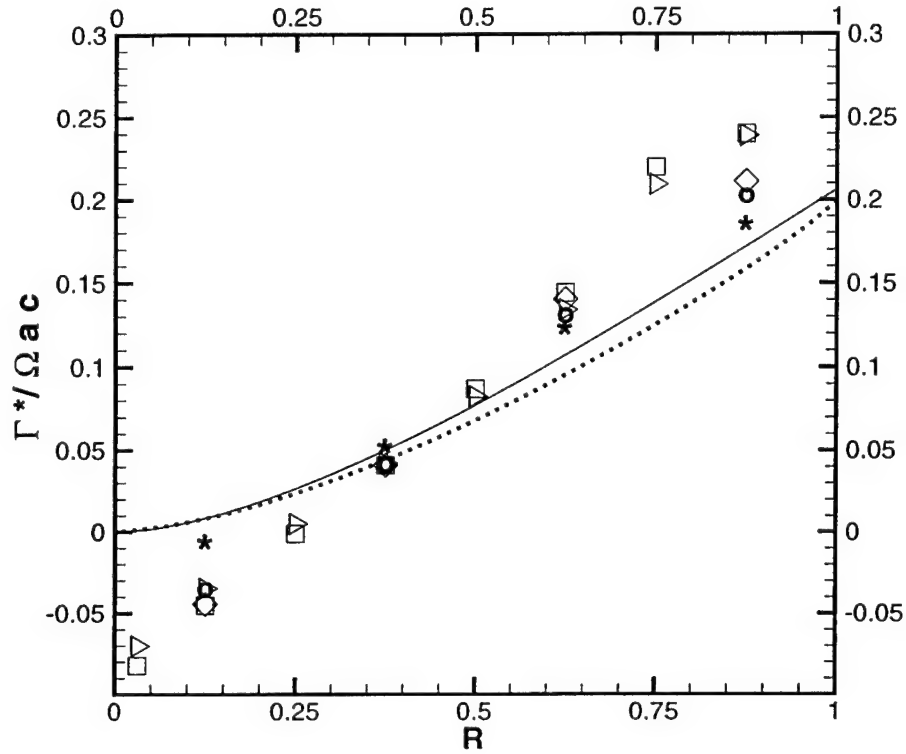


Figure 5.7: Comparison of the bound circulation(outer solution). The solid line represents the Burggraf's theoretical solution, the dotted line represents the result for the vortex-cylinder model, '*' represents the result for $M = 4$ and $\mu = 0.16$, 'o' represents the result for $M = 4$ and $\mu = 0.28$, ' \diamond ' represents the result for $M = 4$ and $\mu = 0.35$, the right pointing triangle represents the result for $M = 8$ and $\mu = 0.28$ and the box represents the result for $M = 8$ and $\mu = 0.35$. M is the number of the elemental surfaces and μ is the cut-off parameter used in the numerical calculation.

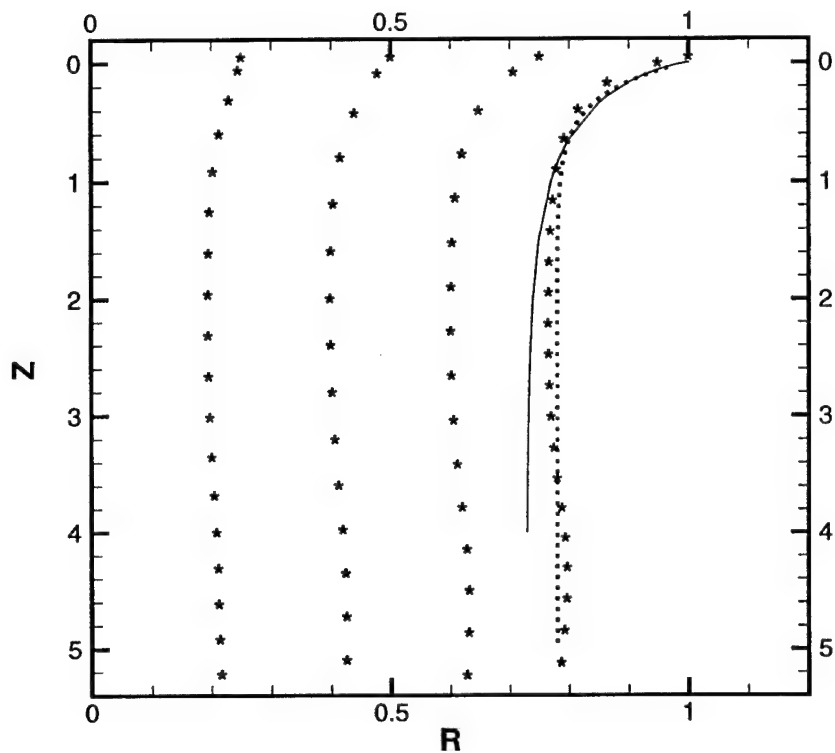


Figure 5.8: Comparison of the slipstream. The solid line represents Burggraf's first-order approximation, dotted line represents the result of Landgrebe's [1972] formula (5.2) where $A = 0.78$, $C_T = 0.0001$ and $\lambda_l = 0.04$. Here '*' represents the result for the vortex ring model with $M = 4$ and $\mu = 0.35$.

slipstream vortices has been represented by a discrete sequence of vortex cylinders of finite length and different radii. The contraction coefficient ϵ is given by Burggraf's [1999] first-order approximation. The computational results compare fairly well with the experimental data of Caradonna and Tung [1981]. The problem with this vortex cylinder model is that according to Burggraf's [1999] theory, the discrete helical vortices are approximated by cylindrical sheets with uniformly distributed azimuthal vorticity. However, this approximation may not be appropriate because the induced downwash is not a constant downstream on each vortex cylinder. In order to obtain a more accurate prediction of the slipstream of the rotor wake and the bound circulation on the rotor blade, the discrete vortex-ring model is applied. The numerical results for the bound circulation of the vortex ring model compare well with Landgrebe's [1972] empirical formula, whereas Burggraf's more approximate theory overpredicts the wake contraction when compared with Landgrebe's [1972] empirical formula.

Chapter 6

The Boundary Layer on the Blade

6.1 Introduction

The three-dimensional viscous flow near the rotor tip is one of the important and difficult problems in rotor dynamics. Most theoretical investigations that focused upon the flow in the tip region have been confined to inviscid analyses. The detailed study of the complex three-dimensional viscous flow near the tip region can play an important role in determining the generated rotor noise, rotor performances, and dynamic loading of the rotor blade.

The present work investigates the details of the viscous flow near the rotor tip by solving for the boundary-layer flow. Interpretation of the boundary-layer flow in that region is expected to explain many phenomena that arise in rotor dynamics.

Fundamental treatments of the boundary layer away from the hub and the tip and the leading and the trailing edges of the blade are found in Sears [1948], Fogarty[1951] and Tan [1953]. In particular, Fogarty[1951] found a similarity solution for the boundary layer flow in which the streamwise viscous flow (i.e. in the x-direction) reduces to the classical boundary layer flow past a wing. The spanwise velocity component is small compared with the streamwise component, and is of the order of $\frac{c}{y}$ where c is the chord of the airfoil. Tan [1953] considered the same problem as Fogarty [1951] and used regular perturbation theory to obtain a solution. In all this early boundary layer work which incorporates the outer flow of Sears [1950], the spanwise

velocity is directed outward from the hub and is small compared to the local rotational velocity $U_\infty = \Omega y$. In fact it is easy to show that away from the hub, the ratio of the spanwise to the streamwise flow is

$$\frac{v}{u} \sim \frac{c}{y} \ll 1$$

McCroskey and Yaggy[1968] extended the outer flow of Sears(1950) to the case of forward flight and they were able to obtain boundary layer solutions. In this treatment, McCroskey finds that cross flow effects due to translation are significant, while those due to rotation are small. Dwyer and McCroskey [1971] builds on this earlier work by adding the unsteady flow effects to the full single blade rotor aerodynamic problem. Results show that the Coriolis and apparent pressure gradients due to translation (i.e. potential) cross flow are significant.

6.2 The inviscid flow

For solving the boundary-layer equations, the inviscid flow-velocity components are needed as boundary conditions at the edge the boundary layer. To obtain the chordwise velocity component U and the spanwise velocity component V for the inviscid flow, the rotor blade is modeled by horseshoe-vortex panels, as described in Chapter 3. The panel circulations are calculated such that the normal velocity at collocation points are set to zero. The inviscid velocity components are calculated assuming zero circulation at the trailing edge (Kutta condition). The inviscid velocity components evaluated at the blade surface provide boundary values for solving the boundary-layer equations.

6.3 The Boundary-Layer Equations

The derivation of the boundary-layer equations near the rotor tip started by assuming the form of these equations in generalized rotating coordinates given by Mager [1964]. After some mathematical manipulations, the boundary layer equations in Cartesian coordinates have the following dimensionless form

$$\frac{\partial u}{\partial x} + \frac{\partial v}{\partial y} + \frac{\partial w}{\partial Z} = 0, \quad (6.1)$$

$$\frac{\partial u}{\partial t} + u \frac{\partial u}{\partial x} + v \frac{\partial u}{\partial y} + w \frac{\partial u}{\partial Z} = -\frac{\partial p}{\partial x} + \frac{\partial^2 u}{\partial Z^2}, \quad (6.2)$$

$$\frac{\partial v}{\partial t} + u \frac{\partial v}{\partial x} + v \frac{\partial v}{\partial y} + w \frac{\partial v}{\partial Z} = -\frac{\partial p}{\partial y} + \frac{\partial^2 v}{\partial Z^2}, \quad (6.3)$$

where Z is the boundary-layer coordinate normal to the surface, x is the chordwise coordinate and y is the inner variable in the spanwise direction; for these equations to hold, we must have the aspect ratio of the blade $A \ll Re^{1/2}$. The origin of the coordinates coincides with the leading edge of the rotor-tip chord. (u, v, w) are the velocity components in the (x, y, Z) directions, respectively. p is the dimensionless pressure, which replaces the static pressure - the dynamic pressure of the upstream flow at the rotor tip. The dimensionless variables in equations (6.1), (6.2) and (6.3) are defined by

$$\begin{aligned} x &= \frac{x^*}{a}, \quad y = \frac{y^*}{c}, \quad Z = \frac{z^*}{a} Re^{1/2}, \quad t = \frac{W_0}{a_c} t^*, \\ u &= \frac{u^*}{\Omega a}, \quad v = \frac{v^*}{\Omega a}, \quad w = \frac{w^*}{\Omega a}, \quad Re^{1/2}, \quad p = \frac{p^*}{\rho \Omega^2 l^2} \end{aligned} \quad (6.4)$$

where the superscript $*$ denotes corresponding dimensional variables, l denotes the rotor span, c is the rotor chord and Ω is the rotating speed of the rotor. Equations (6.1-6.3) are subject to the following boundary conditions:

$$\begin{aligned} u, v &\text{ specified at } t = 0, \\ \frac{\partial u}{\partial y} = \frac{\partial v}{\partial y} &= 0 \quad \text{as } y \rightarrow \pm\infty, \\ u = v = w &= 0 \quad \text{at } Z = 0, \\ u &\rightarrow U \quad \text{as } Z \rightarrow \infty, \\ v &\rightarrow V \quad \text{as } Z \rightarrow \infty, \end{aligned}$$

where U and V are the inviscid velocity components in the x and y -directions respectively. The normal coordinate Z is replaced by a Rayleigh variable defined by

$$\eta = \frac{Z}{2\sqrt{t}}. \quad (6.5)$$

Also, to cluster the points near the wall where the flow is expected to vary rapidly,

$$\eta = \frac{2\xi}{1-\xi}, \quad (6.6)$$

where ξ is the new normal coordinate and has a range of $[0,1]$; the governing equations (6.1), (6.2) and (6.3) become

$$\frac{\partial u}{\partial x} + \frac{\partial v}{\partial y} + \xi_Z \frac{\partial w}{\partial \xi} = 0, \quad (6.7)$$

$$\frac{\partial \vec{F}}{\partial t} + u \frac{\partial \vec{F}}{\partial x} + v \frac{\partial \vec{F}}{\partial y} + (\xi_t + u_r \xi_Z - \xi_{ZZ}) \frac{\partial \vec{F}}{\partial \xi} - \xi_Z^2 \frac{\partial^2 \vec{F}}{\partial \xi^2} = -\vec{P}, \quad (6.8)$$

where $\xi_t = \frac{\partial \xi}{\partial t}$, $\xi_Z = \frac{\partial \xi}{\partial Z}$ and $\xi_{ZZ} = \frac{\partial^2 \xi}{\partial Z^2}$, $\vec{F} = (u, v)$, $\vec{P} = (\partial p / \partial x, \partial p / \partial y)$. The pressure gradient vector \vec{P} is calculated using the inviscid surface speeds obtained from the panel code.

The problem is started by assuming parabolic velocity distributions inside the boundary layer for both u and v . These distributions start from zero values at the wall and reach asymptotically the values of inviscid velocity at the boundary layer edge (ξ_{max}). These parabolic distributions serve as initial conditions for the numerical solution of the boundary-layer equations.

6.4 Grid Distribution and Numerical Solution

While the grids are distributed uniformly in the chordwise direction, grid points are clustered near the rotor tip to resolve the rapid variation of inviscid flow variables there. The distributions in the spanwise direction are obtained from the same lifting surface program as is used in obtaining the bound circulation. The numerical solution contains two major steps; the first one solves the inviscid flow and the second solves the boundary-layer equations.

For solving the boundary-layer equations, the same technique of Xiao *et al* [1994] is used assuming fixed grid and non-interacting boundary layer. The boundary-layer equations are solved with the external potential flow used to evaluate the inviscid velocity and the corresponding pressure gradients. The Crank-Nicolson method is used to obtain the time derivatives in the equations. Also, the spatial derivatives are evaluated using the standard central difference operator. Different time steps Δt were used in solving the equations, and it was observed that the smaller the time step the faster the convergence of the solution. The standard central differences replace the spatial derivatives in the equation.

6.5 Results

Initial results were obtained for the case of a Blasius boundary layer in order to validate the code. In this case, the velocity in the chordwise direction (U) equals unity and zero value of (V) at all the collocation points. The results approach the Blasius boundary layer solution as time increases.

6.6 Summary

Additional results produced for the case where the inviscid flow corresponds to the actual vortex flow over the wing have been produced. These results indicate the presence of a strong spanwise flow along with a well defined, non-reversed streamwise flow. More work is required to quantify the boundary layer results further and to develop conditions under which the flow may become reversed.

Chapter 7

Experiments

7.1 Introduction

The long-term goal of this project is to arrive at a general understanding of how tip vortices form. Such an understanding would enable the synthesis of findings from various application areas, with sufficient generality and accuracy to guide the design of new tip shapes and vortex control devices. Although research on vortices is as old as hydrodynamics, a quick survey of current work in aerodynamics indicates that several efforts are underway in various application areas, where the primary uncertainty is about the origin and evolution of tip vortices. In the past four years, our effort has been directed towards:

- Collecting and correlating experimental results and data on fixed-wing and rotary wing vortices.
- Performing experiments on rotary wing vortices to answer some key unknowns.
- Estimate measurement errors due to particle "spinout".
- Developing methods of measuring the tip vortex strength and structure efficiently.

In this Chapter we introduce prior work and discuss current findings, as they relate to the long-term project goal. Vortex formation, evolution to the near wake, seed particle dynamics, work on quantifying density variations in

the vortex, and the development of a web tip vortex database are addressed.

7.1.1 Rotor Experiments

Thompson, *et al.*[1988] used LV to examine the formation process as well as the vortex properties in the near-wake of a single-bladed rotor in the Georgia Tech 9-foot hover facility in the mid-1980s. In this facility, a wake inductor refined by trial and error enabled rotor operation over a specified range of test conditions with the problems of vortex impingement on facility walls. Under these conditions, rotor-synchronized laser sheet visualization showed that the vortex followed a precisely repeating trajectory for at least the first 360 degrees and probably the first 540 degrees of vortex age. Using mineral oil seeding which showed some "spinout" (discussed later in this paper), they sliced the wake radially using an argon ion laser sheet, approximately 1mm thick, and strobed the laser beam using a chopper wheel driven on a motor synchronized to the rotor shaft. The rotor was operated at 600rpm. A 35 mm camera set on long exposure captured the vortex cores clearly for at least the first 3 turns. Aperiodicity (jitter) of even one core radius would have moved the brightest regions of the photograph (the heavily-seeded region at the edge of the core) across the darkest region the core center, smearing out the photos.

With periodicity thus assured, they used sub-micron particles of incense smoke to seed the core of the tip vortex, and measured each of the 3 components of velocity, in turn, across the vortex using a specially designed Remote-Aligned Off-Axis Receiver[1990]. With this arrangement, they obtained fairly uniform seed particle arrival rates across the entire tip vortex. They found that during formation, the vortex achieved its maximum strength at a x/c of 0.5 and 0.6 for CT values of 0.0057 and 0.0022 respectively. Thompson also observed secondary features in the circumferential velocity profiles for early wake ages. These were not understood at the time, beyond postulating that these were a manifestation of the rollup of discrete vortical filaments during the formation of the tip vortex. However, Thompson's flow visualization and measurements showed that the tip vortex of a rotor does persist with much of its initial strength for large vortex ages.

Brand, *et al.*[1989, 1990] and Liou, *et al.*[1989, 1990] examined vortex trajectories and dynamics of the two-bladed rotor used in the present paper, in forward flight in the Harper Tunnel. They showed, again, that vortex trajec-

tories repeated with precise periodicity, provided wake impingement on the tunnel floor, and wake recirculation, were prevented by going to sufficiently high advance ratio (> 0.06 in this experimental configuration). Again, the vortex was seen to maintain much of its initial strength for vortex ages over 400 degrees, which was the limit of their interest because they were studying rotor vortex/airframe interaction. This is consistent with the computational results reported in Chapter 4.

Komerath, et al.[1991] extended the single-bladed rotor with a double-swept blade tip in the 9-foot hover facility at Georgia Tech to study effects at high pitch angles. During their experiments, they observed that at certain conditions, the tip vortices impinged on the edge of the wake inductor and recirculated in the facility: this was associated with the development of severe aperiodic jitter of the vortex trajectories. Funk, et al.[1995] conducted extensive measurements of the flow field between the 2-bladed rotor and a wing in the John Harper wind tunnel. Although vortex trajectories were substantially altered by wing interaction, the results on periodic repeatability of vortex locations, and persistence of vortices to large ages, both remained unchanged.

Caradonna, et al.[1997, 1999] visualized the wake of a 2-bladed rotor in axial climb in the 30'x30' Settling Chamber of the 7'x 10' wind tunnel at Ames Research Center. Again they found that when wake recirculation was prevented, the vortex trajectories repeated quite perfectly from cycle to cycle of blade motion, even as the climb velocity was brought towards zero. Vortex cores were discernible by the seed particle patterns for several turns of the vortex, until merger between vortices smeared the patterns. The introduction of blockage beyond a certain level downstream of the rotor, (using wooden slats placed across the test section) triggered violent unsteadiness at the rotor plane and all over the wake; removal of such blockage made the wake smooth and periodic again. From the above, it is quite clear that the tip vortex of a rotor persists over long vortex ages. Also, aperiodic "jitter" of vortices is avoided. The test condition McAlister [1995] and McAlister *et al.* [1996] studied the velocity field in the near wake of a two-bladed rotor in hover using a 3-component laser velocimeter. The test conditions were a CT of 0.005 at 1100 and 550 RPM. He found that three chords downstream of the blade the vortex meander was less than one core diameter. By the time the vortex reached a vortex age of 180° , the meander had increased by an order of magnitude. McAlister also noted that changing the rotational speed did not have an effect on the core diameter, the general appearance of the

trailing vortex or the magnitude of the velocity components relative to the tip speed.

In the late 1990s, measurements were reported by Leishman, et al.[1995] using a single-bladed rotor in a hover facility, with a 3-component laser velocimeter. These measurements indicated rapid "diffusion" of the tip vortices within the first 90 degrees of vortex age. Substantial aperiodicity was observed. These phenomena were attributed to turbulence in the core, and the rapid smearing of the vortex velocity profile data was described as turbulent diffusion[1995]. The data acquisition procedures used had taken no account of aperiodicity, however, raising the possibility that vortex profile data, averaged over several cycles, had become severely smeared by cycle-to-cycle uncertainty in vortex position. Conlisk, et al.[2000] showed by analytical arguments based on orders of magnitude that turbulent diffusion was not a plausible explanation for the vortex decay of the rate reported by Leishman.

Mahalingam et al.[2000, 1998, 1998] conducted measurements on the advancing blade side (ABS) of the two-bladed rotor used in this paper, in low-speed forward flight. He showed by flow visualization and LDV measurements that the rotor flow field was periodic to better than 1 deg of rotor azimuth at an advance ratios 0.1.

7.1.2 Previous Work - Seed Particle Dynamics

Velocity measurement techniques that rely on seed particles carried by a fluid are subject to errors due to finite particle inertia. In the case of laser velocimetry, the experimenter faces a dilemma: over the large distances used for laser velocimetry in rotor facilities, it is difficult to accurately capture in back scatter mode light scattering from particles smaller than $1\mu m$. Particles larger than one micron are believed to experience substantial centrifugal drift with respect to the flow in the core of a tip vortex. Thompson, et al.[1988, 1990] dealt with this problem by developing an Off-Axis Scatter Receiver. This device could be aligned remotely to stay focused on the measurement volume as it was traversed across a large facility, and capture scattering from sub-micron particles. This is less convenient than using a backscatter LV system, however. It is also difficult when the rotor is near other objects that block the line of sight.

It is therefore necessary to use larger particles, and to subsequently quantify the error due to particle spinout. Dring, et al.[1979] has examined the

trajectories of particles in turbine cascades. He concluded that the Stokes number (St) had the greatest influence on particle behavior. Furthermore, he determined that particles with $St \leq 0.1$ would very closely follow the streamlines, and that particles with $St > 10$ would be centrifuged across streamlines. In another study, Dring[1982] integrated the equations of motion for particles in several flows to provide guidance on LV seed particle size selection. The flows included a turbine cascade, a step deceleration and exponential and sinusoidal accelerations. He determined that the Stokes number required to achieve 1% accuracy depended on the type of flow. In a turbine cascade, he found that a Stokes number of less than 0.01 was required, but in a sinusoidal flow 0.14 was tolerable.

Dring, *et al.*[1978] and Kriebel[1961] examined the behavior of particles in centrifugal particle separators. In these flows, the gas experiences solid body rotation. This is analogous to vortex core velocity profiles, except that the strong axial velocity is absent. Dring's analysis assumed that the particle and gas velocities were equal. He also used several drag models instead of assuming that Stokes relation holds. Dring[1978] asserts: "axial velocities do not alter the solution so long as the particle and fluid axial velocities are equal and constant." Kriebel's study did not place any assumptions on the particle and fluid velocities. However, he used Stokes relation to estimate drag acting on the particle. Comparison with experimental data is also provided. Neither of these analyses is valid in the potential velocity region outside the vortex core.

Leishman[1996] calculated the behavior of seed particles in a "desingularized" vortex. His study used particles ranging from 0.5 to $2.0\mu m$ and a vortex circulation of $5.6m^2s^{-1}$. Inside the vortex core, he predicted velocity errors as high as 10% and 25% for the tangential and radial velocities, respectively, for the $2\mu m$ particle. The smaller particles resulted in lower errors. His study also examined particle count distribution. The highest particle distributions occurred at r/R_c of 1.7 for the $0.5\mu m$ particles, 2.6 for the $1.0\mu m$ particles and 3.8 for the $2.0\mu m$ particles. Although intended for rotor tip vortex applications, this work did not consider the effects of the strong axial velocity in the core. It should be noted here that the vortex strengths used by Leishman [1996] are almost 7.5 times those encountered in the present rotor flow field.

The previous work on seed particle inertia has been focused on two di-

mensional models of vortices. In the rotor tip vortex core, there is a very substantial axial velocity (for example Caradonna *et al.* [1997, 1999]). The resulting sink-like effects on the flow field should cause an inward-directed radial fluid velocity, which should considerably inhibit the drift of particles out of the middle of the core, where the centrifugal acceleration is much lower than at the core edge. Considering experimental results obtained at the present authors' laboratory with cleanly-periodic, well-resolved vortices, it is evident that the estimates of seed-particle inertia error cited, for example, in Leishman [1996] convey overly conservative picture. This issue needs to be considered, and upper bounds are sought for these types of errors.

7.1.3 Vortex Core Density Field

Intense vortices are present in many natural fluid flows. Specially, the flow fields of fixed and rotary wings are composed of many vortical flow structures. The most dominant and important structures are trailing tip vortices from wings or rotor-blade tips. In some cases, the tip vortices associated with high-speed aircraft or high-performance helicopters may be so intense that the compressibility effect is important in the vortex cores [1953].

There has been much research studying the inner structure of vortex core, however not many have studied the effects of axial flow, compressibility and viscosity. There is little information and understanding on the inner structure of vortex core including details on the pressure and density distributions. The knowledge of this information is especially important to the further development and validation of advanced CFD model.

Many experiments have been performed to measure the structure of fixed-wing and rotary-wing tip vortices. Several experimental methods have been used to this purpose. Intrusive methods such as pressure probes, hot-wire anemometry, are questionable because the existence of probes alter the vortex structure and increase the uncertainty (Chigier and Corsiglia [1971], Tung *et al.* [1983]). Non-intrusive methods such as LDV also encounter difficulty for tip vortex structure measurements, because seed particles which are large enough to provide good signal-to-noise ratio are also subject to inertial drift radially from the vortex core, leaving the core void of particles beyond some age.

Some optical density gradient methods such as laser speckle velocimetry and shadowgraphy can also be used to examine the structure of tip vortices. These methods are completely non-intrusive, and the use of seeding particles

is not required. Laser speckle velocimetry uses changes in the index of refraction caused by local changes in the density due to turbulent eddies. The changes in index of refraction are integrated over the path length of the laser and result in speckles in the beam. Flow velocity can then be determined by tracking the motion of the speckles. Hence, the most important requirement for this method is that the density field of the flow must contain inhomogeneities and the relation between light intensity and density variation of the flow field should be known. Therefore, this work will present a simple analytical result for the density variation of a three-dimensional compressible viscous vortex and the relation between density gradient and intensity of light.

7.1.4 Measurement Issues - Blade Proximity

Measuring the velocities during the formation process is fundamentally difficult due to the proximity of the measurement points to the blade surface and the length scales involved. Measurement techniques that require physical probes, such as hotwires, cannot be employed for these measurements. There is too much potential for physical interference between the probe and the rotor. Since the length scales are so small, there is also the risk of the probe influencing the flow. Because of these risks, laser velocimetry is often used. Its primary advantage is that probe interference and interaction with anything in the flow is avoided. However, its performance also suffers in blade tip measurements. This can be due to low signal to noise ratio. There are two factors contributing to the low signal to noise ratio. The first is that positive and negative velocities on the order of the rotor tip speed are expected. Therefore, the frequency shift and the bandwidth of the bandpass filter must be increased to capture the entire expected velocity range. Both of these contribute to a noisy signal. Reflections off of the blade surface due to the proximity of the measurement points to the blade also decrease the signal to noise ratio.

Another issue that increases the complexity of these measurements is beam blockage. At certain rotor azimuths, the rotor blade blocks one or more of the LV beams, resulting in a lack of data in portions of the rotor cycle. Careful positioning of the beams or other schemes must be used to capture data at all points over the complete rotor cycle.

7.2 Experimental Setup

These experiments were conducted in the John Harper Wind Tunnel on the Georgia Tech campus. The Tunnel is a closed return tunnel with a 7'x9' test section. The tunnel is powered by a 600hp electric motor coupled to a four-bladed fan via an eddy current clutch. This provides continuously variable speed control up to 200fps. Turbulence intensity is approximately 0.5%. Extending through the ceiling of the test section is the shaft for the rotor. It is tilted forward by 6 deg to simulate forward flight. A photodetector provides a pulse once per revolution for phase averaging the data. Attached to the end of the shaft is a two bladed untwisted, untapered, teetering NACA 0015 rotor. The characteristics of this rotor are shown in Table 7.1. For these

Airfoil	NACA 0015
Radius	18"
Chord	3.375"
Collective	10°
Solidity, σ	0.12
CT	0.0089
Tip Chord Re	2.87×10^5

Table 7.1: Rotor properties.

experiments an advance ratio, μ , of 0.10 was used. Rotor RPM was 1050 corresponding to a tunnel freestream of 16.4 ft/s.

The vortex properties were measured using laser velocimetry (LV). The tunnel LV system is a single component system consisting of a 5W argon ion laser, conditioning and fiber optics and a probe mounted in the test section. The laser's output is split, frequency shifted and coupled to fiber optics in a TSI Colorburst module. The fibers terminate in the probe, which is mounted to a three axis linear traverse in the tunnel test section. It is computer controlled and moves the measurement volume to the desired location. The traverse is located far enough outside of the wake that it has little affect on the flow. Focusing lenses of 350mm and 750mm were used. The corresponding probe volumes using these lenses were 1.31mm x 90.5 μ m and 5.80mm x 190.0 μ m, respectively. Frequency shifts between 1Mhz and 10MHz were used. The LV processor is a counter-type processor. Between 8 and 128

fringes were counted using a 1% tolerance for the 5/8 crossing criteria.

Seeding for the LV measurements consisted of atomized mineral oil droplets. These droplets have been sized in the test section to range between 1 and $5\mu m$. As previously discussed, the flow field in this experimental setup is periodic to better than 1 deg of rotor azimuth. Therefore, the three-dimensional flow field can be reconstructed from three separate single component measurements.

7.2.1 Rotor Interference

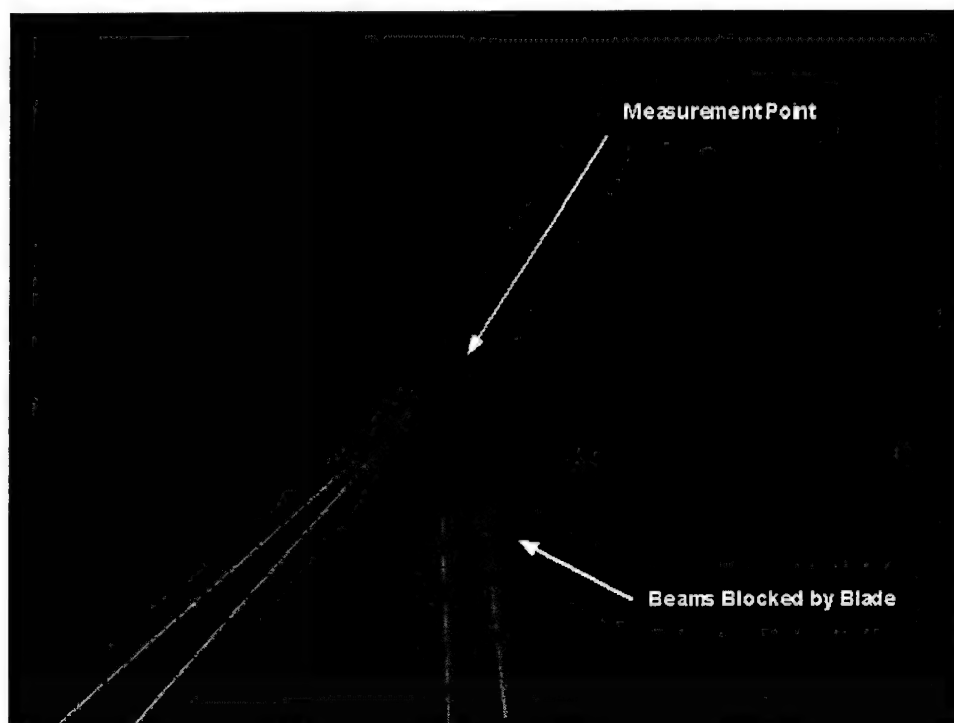


Figure 7.1: Beam blockage by blade.

Beam blockage and noise due to reflections were addressed by measuring each velocity component using two different probe orientations (Figure 7.1). In the figure, the beams from the bottom are measuring the lateral velocity

component. However, due to rotor interference, it cannot measure the points above the rotor for the azimuth shown. Positioning the probe behind the rotor allows measurements of the lateral velocity component to be made at positions above the blade for the azimuth shown, but it will also contain a void in its data set. Measurements in front of the blade are not possible due to beam blockage. However, by stitching together the two datasets, one complete dataset can be created. A code was written to do so. For a given azimuth, data from grid locations containing a zero velocity and points per bin were replaced from the same grid point from the second dataset.

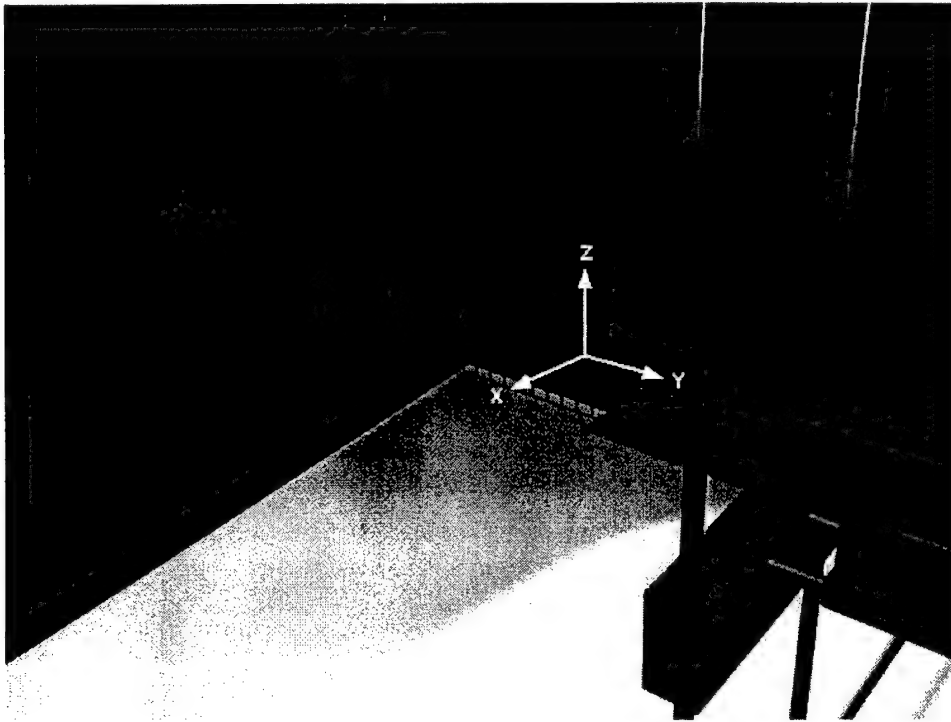


Figure 7.2: Vortex origins measurement grid.

7.2.2 Measurement Grids

Vortex formation measurements were conducted on the advancing blade side (ABS) and retreating blade side (RBS) of the rotor. On the ABS the mea-

surement grid origin was located at the trailing edge of the tip of the blade when $\phi = 90^\circ$ (Figure 7.2). It should be noted that (a) the measurement grid is only parallel to the blade at $\psi = 90^\circ$, and (b) for the other azimuths where the blade intersects the measurement grid there is an angle between the blade and the measurement grid. This becomes an issue when determining the location of the blade in the measurement grid. The measurement grid on the RBS side was the same with the exception of when $\phi = 270^\circ$.

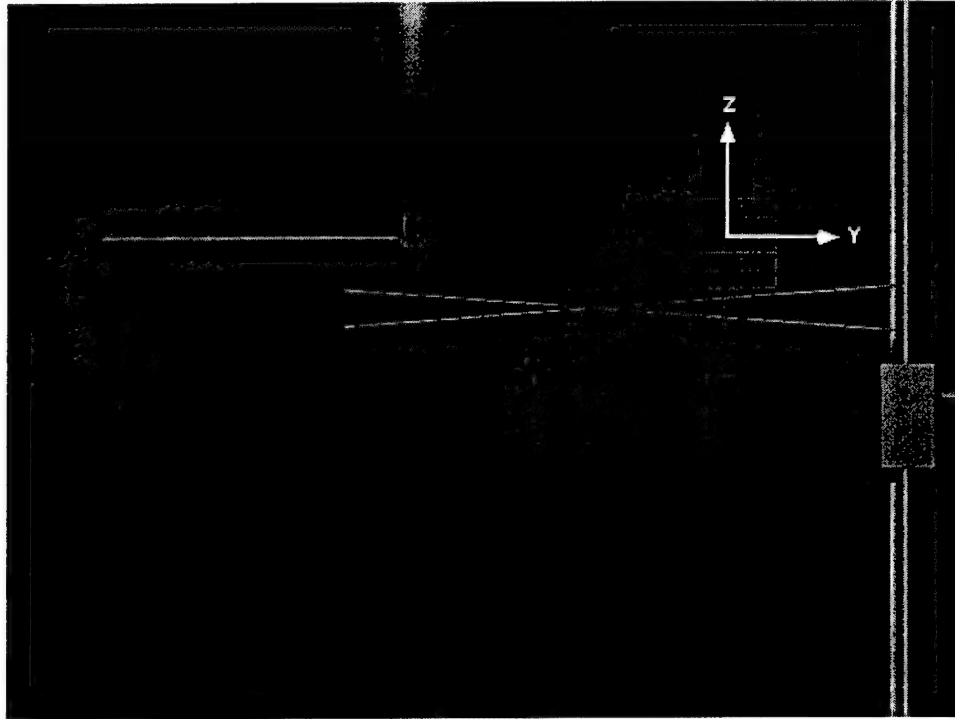


Figure 7.3: Near wake measurement grid on both sides of the rotor.

In forward flight, the vortex properties are a function of the rotor azimuth at which they were shed. Measurements were made at four azimuth locations, the minimum number of locations to capture all of the shedding possibilities. The measurement grids for these are shown in Figure 7.3 and Figure 7.4.



Figure 7.4: Near wake measurement grid, front and rear.

7.3 Vortex Formation

7.3.1 Overall Velocity Field

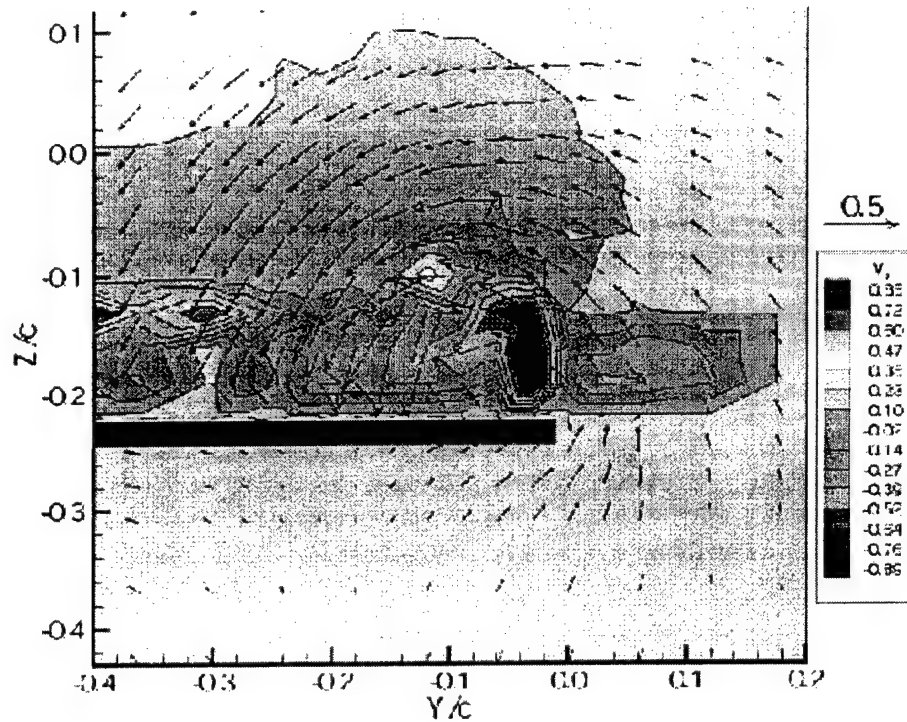


Figure 7.5: Blade tip flow field, approximate blade position shown, $x/c = 0.8$. Here x measures distance from the leading edge of the blade.

The flow field surrounding the blade is highly three-dimensional. As illustrated in Figure 7.5, in addition to the substantial rotation due to the vortex, there is also a strong component of velocity directed upstream. Note that the blade position shown is only approximate. Its position was estimated from artifacts in the data. Perhaps the most prominent feature is the tip

vortex. Its influence is apparent in all of the measurement locations above and outboard of the blade. The fluid spilling around the edge of the blade and rolling up into the tip vortex can also be seen. On the top surface, or suction side of the blade, there is a substantial spanwise flow directed toward the blade tip. On the pressure side of the blade, there is a bifurcation point located around $y/c = -0.2$. For locations closer to the tip than $y/c = -0.2$, the flow is directed outward towards the tip. On the other side, the flow is directed towards the rotor hub. The bifurcation point may be due to the influence of the vortex shed by the previous blade. That vortex has moved off of the measurement grid, and therefore is not seen.

There is considerable asymmetry in the tip vortex. The vortex core, as defined by the distribution of the circumferential velocities, is elliptical. The circumferential velocities also show considerable asymmetry. Unlike vortices observed at older ages, the circumferential velocities are not of the same magnitude as one traces the perimeter of the vortex. Circumferential velocities approaching 60% of tip speed are observed on the inboard and top portion of the core. The velocities on the bottom and the outboard sides are significantly weaker, ranging between 20 and 30% of the tip speed. The peak axial velocity is not located in the vortex "center". It is instead shifted toward the outboard edge of the vortex core. Peak axial velocities approaching 90% of tip speed in the upstream direction are observed. Several "blobs" containing high axial velocity are also apparent in regions that appear to be outside of the vortex core ($y/c = -0.3$).

A vortex is typically characterized by measuring both its peak circumferential and axial velocities and radius, since it is assumed to be symmetric. However, a single number cannot be used to characterize the observed vortex due to its asymmetry.

7.3.2 Evolution of the circumferential velocity

Due to the asymmetry of the vortex, the circumferential velocity profiles across the horizontal and vertical axis of the vortex were examined. The vortex location was determined by searching the horizontal lines of the measurement grid for the vortex signature. This resulted in the velocity profile along the horizontal axis of the vortex as well as vortex position. Using the vortex position, velocity measurements along the vertical measurement line

passing through the vortex center were plotted to obtain the velocity profiles along the vertical axis. Sometimes the center of the vortex did not coincide with a vertical measurement grid line. In these cases the two measurement lines closest to the vortex center were plotted.

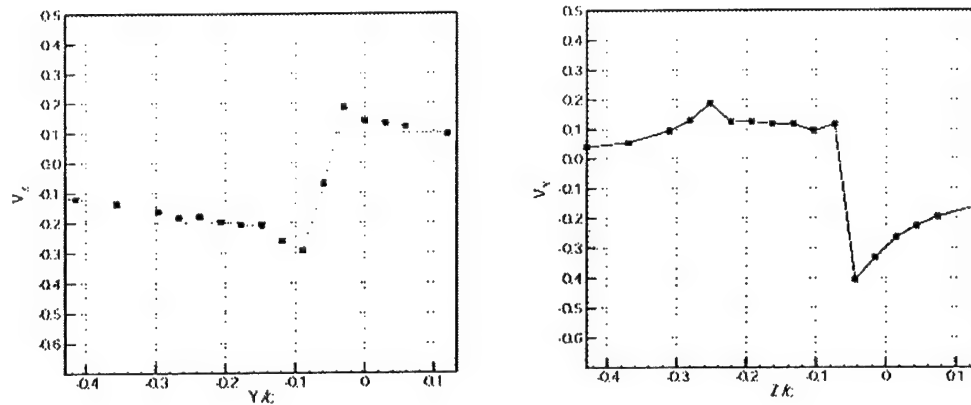


Figure 7.6: Circumferential velocity profile. Horizontal cut (left), Vertical cut (right), $x/c = 0.47$.

The circumferential velocity profiles along both axes during vortex formation are shown in Figure 7.6 - Figure 7.19. Velocity profiles along the horizontal axes are shown on the left, and those along the vertical axes are on the right of each figure. The first clear circumferential velocity profile is apparent at a x/c of 0.47. At this position, along the horizontal axis, there is a region of solid body rotation with a radius of 3% of the chord. Outside of this region, the expected $1/r$ velocity decay is not present. Along the vertical axis velocity profile also shows a region of solid body rotation. On the top of the vortex, it exhibits a $1/r$ type decay outside of the vortex core. However, the bottom exhibits behavior similar to that observed along the horizontal axis (Figure 7.6). A $1/r$ decay is observed forming on the inboard and bottom of the vortex as early as $x/c = 0.55$ (Figure 7.8). The outboard side of the vortex does not exhibit this behavior until a chordwise location of 0.63 (Figure 7.10). In general, the highest circumferential velocities are found on the top of the vortex; the inboard side is a close second. Velocities observed

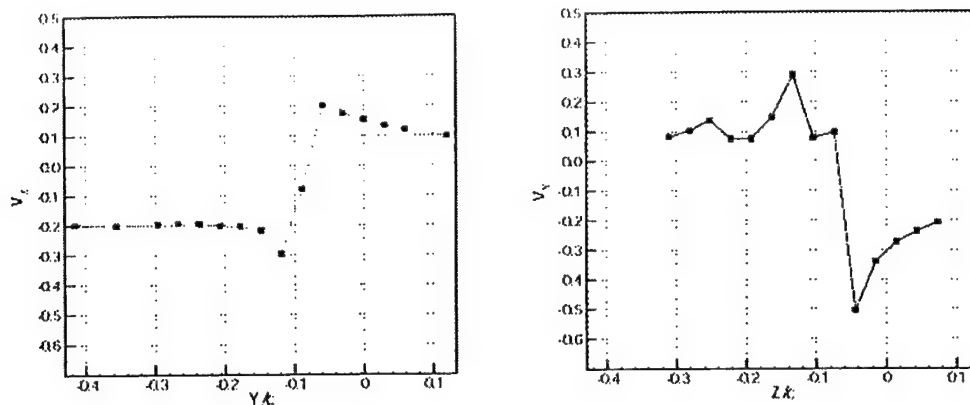


Figure 7.7: Circumferential velocity profile. Horizontal cut (left), Vertical cut (right), $x/c = 0.51$.

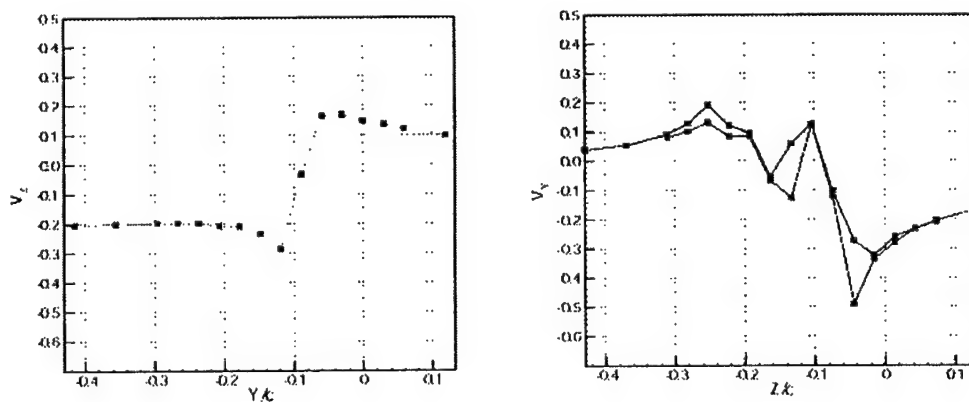


Figure 7.8: Circumferential velocity profile. Horizontal cut (left), Vertical cut (right), $x/c = 0.55$.

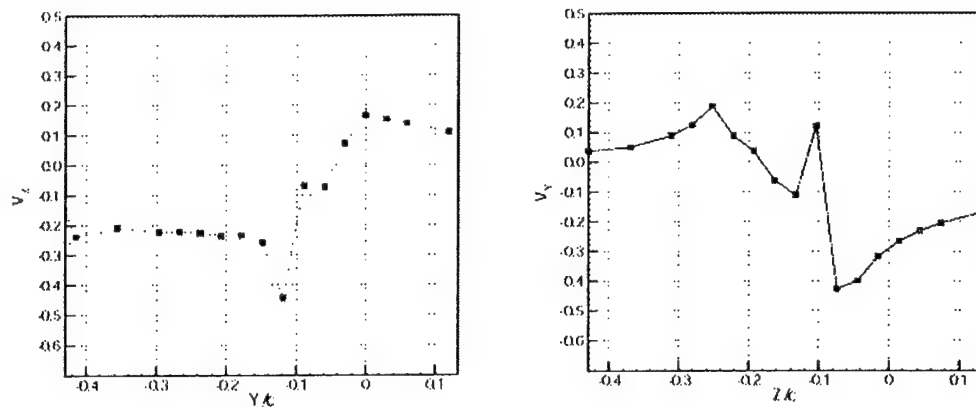


Figure 7.9: Circumferential velocity profile. Horizontal cut (left), Vertical cut (right), $x/c = 0.59$.

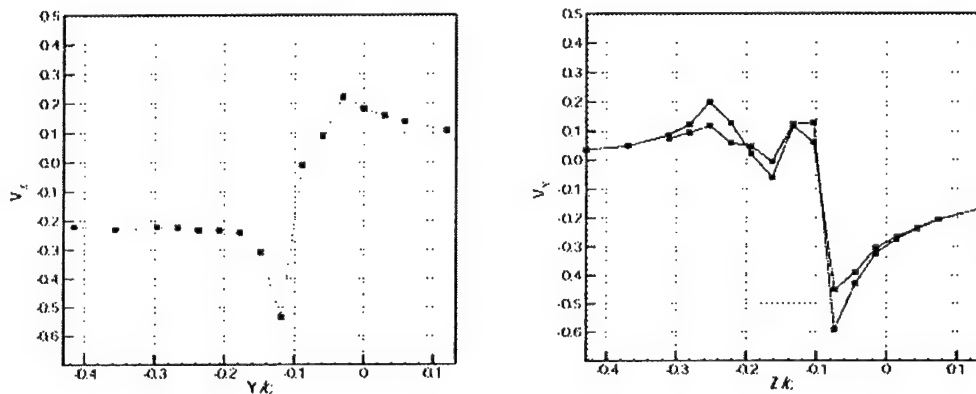


Figure 7.10: Circumferential velocity profile. Horizontal cut (left), Vertical cut (right), $x/c = 0.63$.

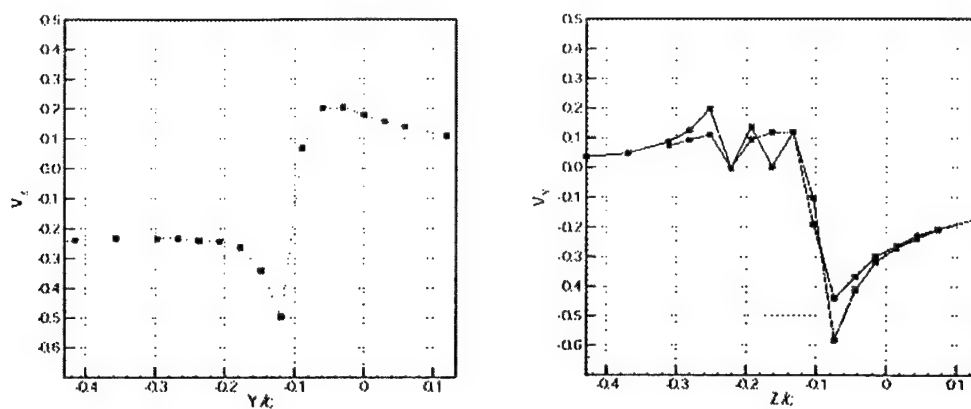


Figure 7.11: Circumferential velocity profile. Horizontal cut (left), Vertical cut (right), $x/c = 0.68$.

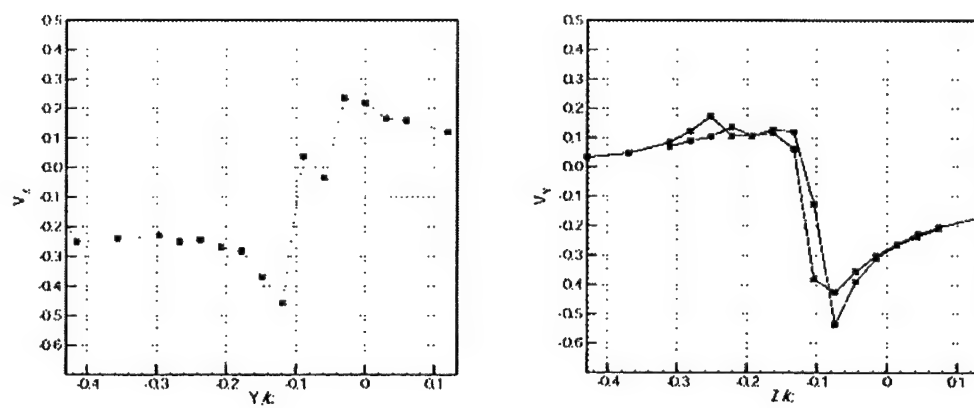


Figure 7.12: Circumferential velocity profile. Horizontal cut (left), Vertical cut (right), $x/c = 0.72$.

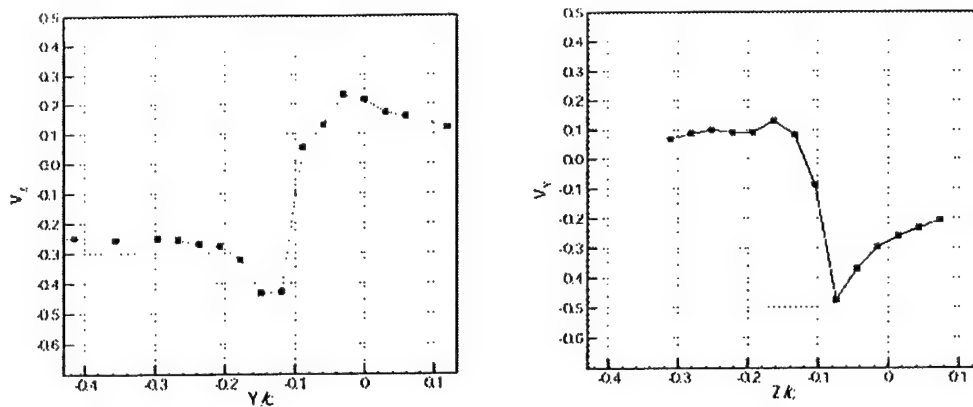


Figure 7.13: Circumferential velocity profile. Horizontal cut (left), Vertical cut (right), $x/c = 0.76$.

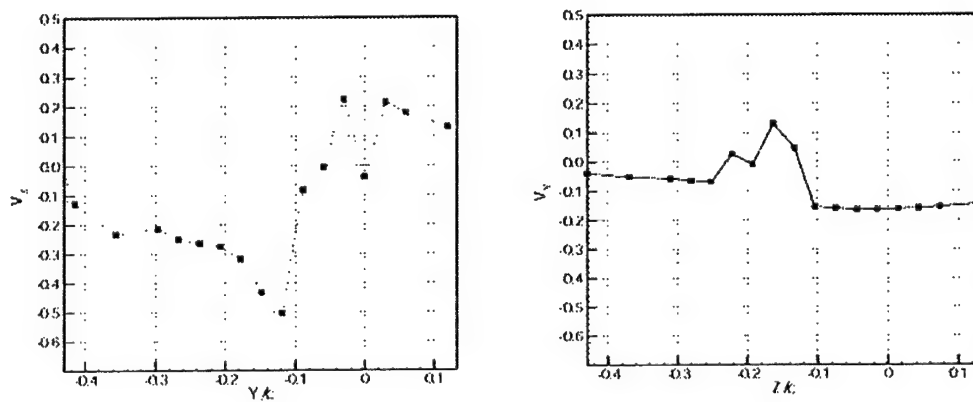


Figure 7.14: Circumferential velocity profile. Horizontal cut (left), Vertical cut (right), $x/c = 0.80$.

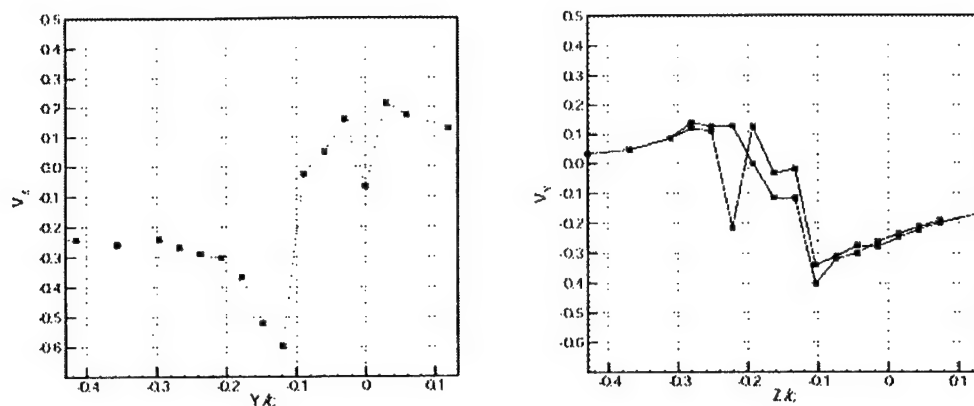


Figure 7.15: Circumferential velocity profile. Horizontal cut (left), Vertical cut (right), $x/c = 0.85$.

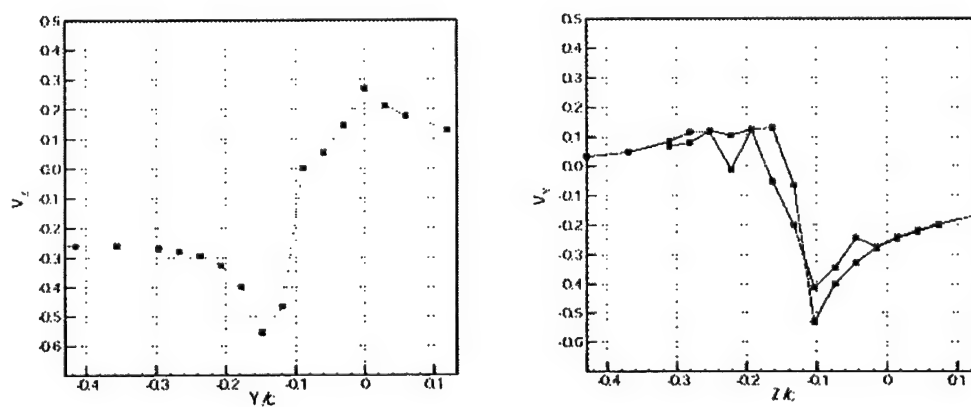


Figure 7.16: Circumferential velocity profile. Horizontal cut (left), Vertical cut (right), $x/c = 0.89$.

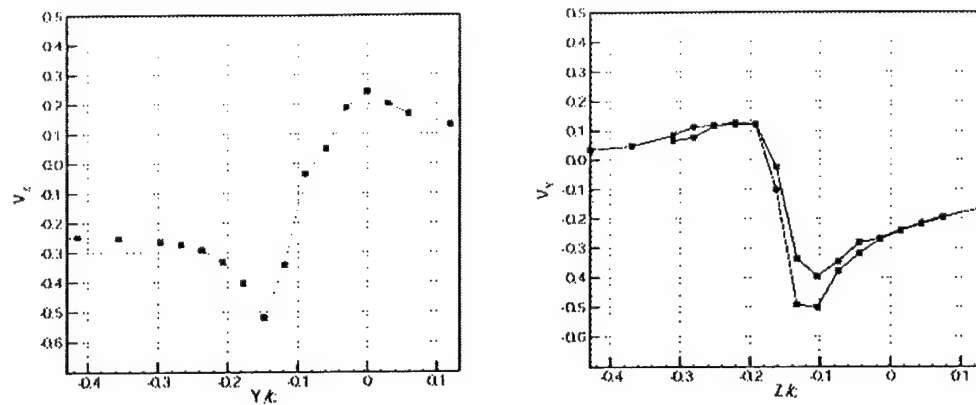


Figure 7.17: Circumferential velocity profile. Horizontal cut (left), Vertical cut (right), $x/c = 0.93$.

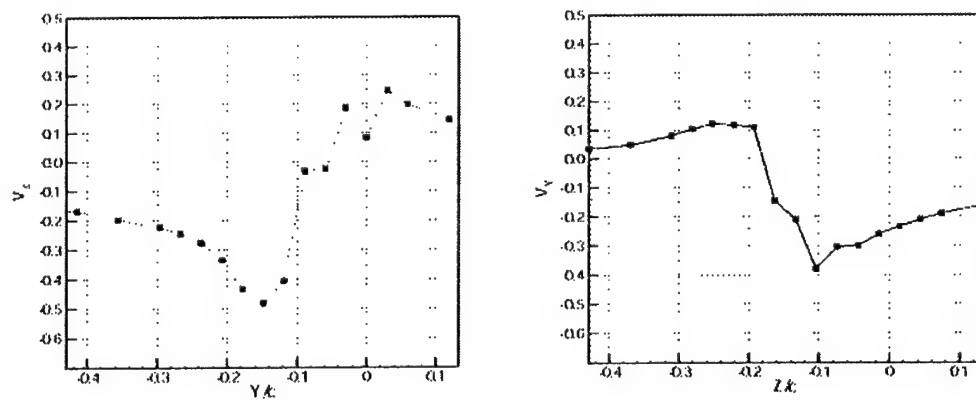


Figure 7.18: Circumferential velocity profile. Horizontal cut (left), Vertical cut (right), $x/c = 0.97$.

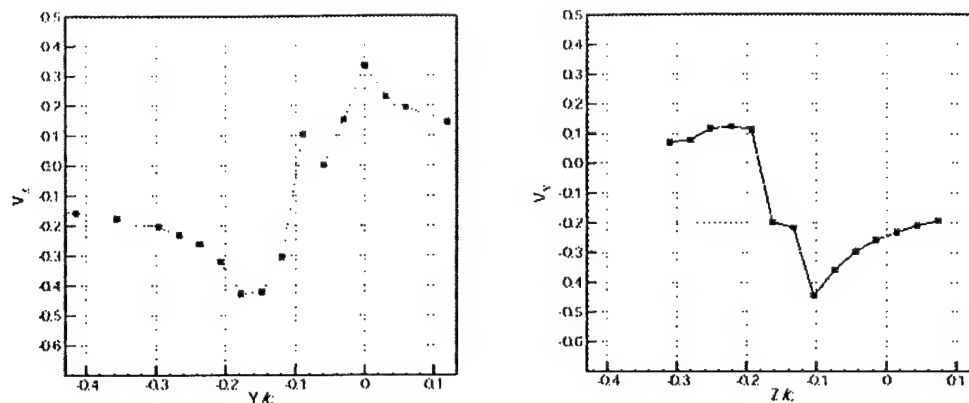


Figure 7.19: Circumferential velocity profile. Horizontal cut (left), Vertical cut (right), $x/c = 1.02$.

at the bottom and outboard side are weaker than at the other locations. By a chordwise location of 0.59 they are approximately 50% of the velocities at the other locations. Kinks in the velocity profile are also apparent at some chordwise locations.

7.3.3 Circulation and Core Size

Circulation and core size were determined from the presented circumferential velocity profiles. Due to the asymmetry, a single value of circulation or core radius does not accurately represent the true nature of the vortex. Circulation and core size were computed for velocity profiles along both axes. Circulation was computed using half of the difference in the peak velocities. Figure 7.20 and Figure 7.21 show the results from the profiles along the horizontal and vertical directions respectively. Data from the horizontal axis show the circulation increasing from $0.2m^2/s$ at $x/c = 0.47$ to $0.9m^2/s$ at the trailing edge. Likewise, the core width increased from 3% of the chord at $x/c = 0.47$ to 9% of the chord at the trailing edge. Few data points were obtained from the velocity profiles along the vertical axis. This was due to the ambiguous peak velocity near the bottom of the vortex and the uncertainty in the peak magnitude and location for vortex centers that did not coincide with a measurement line. However, the data from these profiles show that

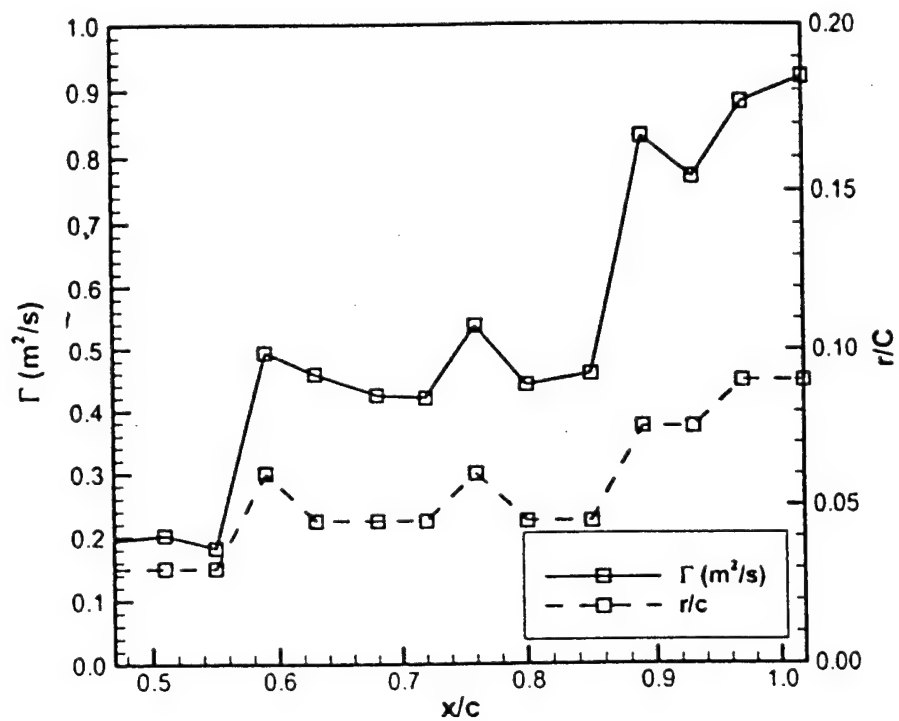


Figure 7.20: Evolution of circulation and width/2.

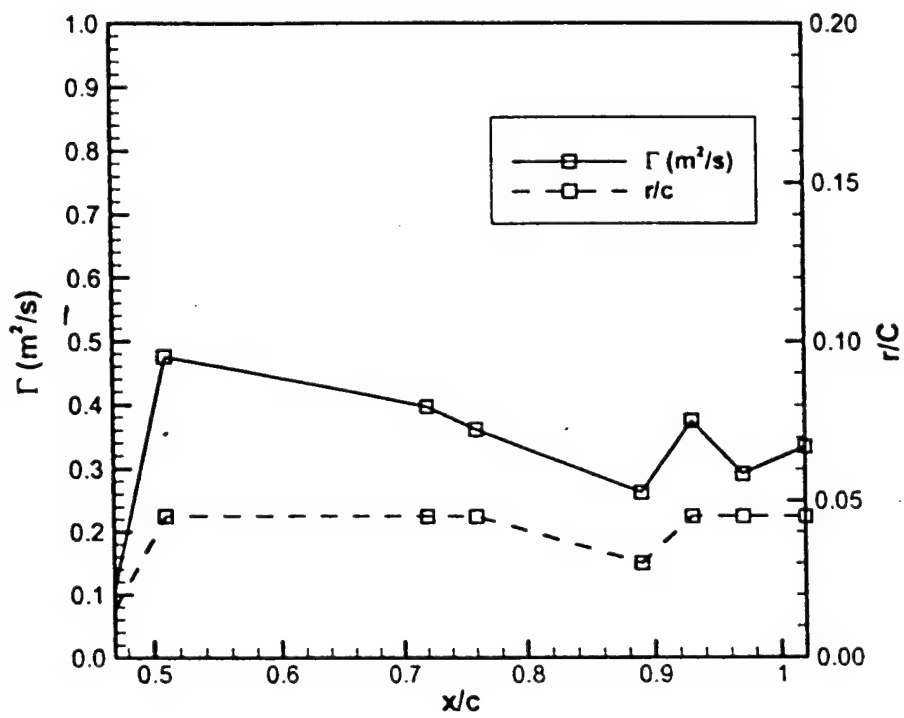


Figure 7.21: Evolution of circulation and height/2.

the circulation starts near $0.105m^2/s$ at an $x/c = 0.47$. There is a sudden increase to nearly $0.5m^2/s$ at $x/c = 0.51$. This is then followed by a decay to $0.335m^2/s$ at the trailing edge. The height of the vortex remains nearly constant at 4.5% of the chord.

7.3.4 Axial Velocity

Most of the chordwise planes measured show regions within the core having axial velocities approaching that of the blade tip. Velocities up to 0.96 of the tip speed were measured. At this point however, since the exact location of the blade is not known, there is some ambiguity regarding the region of large axial velocities. It cannot be determined if these regions are fluid or the blade itself. In the blade tip velocity field shown in Figure 5E, the region of the flow close to tip speed is nearly 0.09 non-dimensional units tall. However, the non-dimensional blade thickness at that chordwise location is 0.04. This indicates that at least some of that region is fluid moving at tip speed. At the other chordwise locations it is not as clear. As the planes move toward the leading edge, the size of the high velocity region approach the thickness of the blade. In those planes no conclusions can be drawn.

The magnitude of the axial velocities also suggest that they are of the fluid and not the blade. If the LV were measuring the surface velocity it should measure 1.0. To verify this, velocity measurements of the blade velocity will be made by repeating the measurements without seeding. This will also provide another method, in addition to the code to be discussed, to determine the exact location of the blade in the measurement grid.

7.3.5 Vortex Location During Formation

The asymmetry of the vortex again presents problems when locating its center. Two methods were used to do so. The first searched for a vortex signature in the circumferential velocity profiles. The center was assumed to be located half way between the peaks. The second method located the region of peak axial velocity. The horizontal location during formation is shown in Figure 7.22 and the vertical location is shown in Figure 7.23. Both of these plots are relative to the measurement grid origin. At this point, nothing can be said about the vortex center relative to the blade since the exact blade

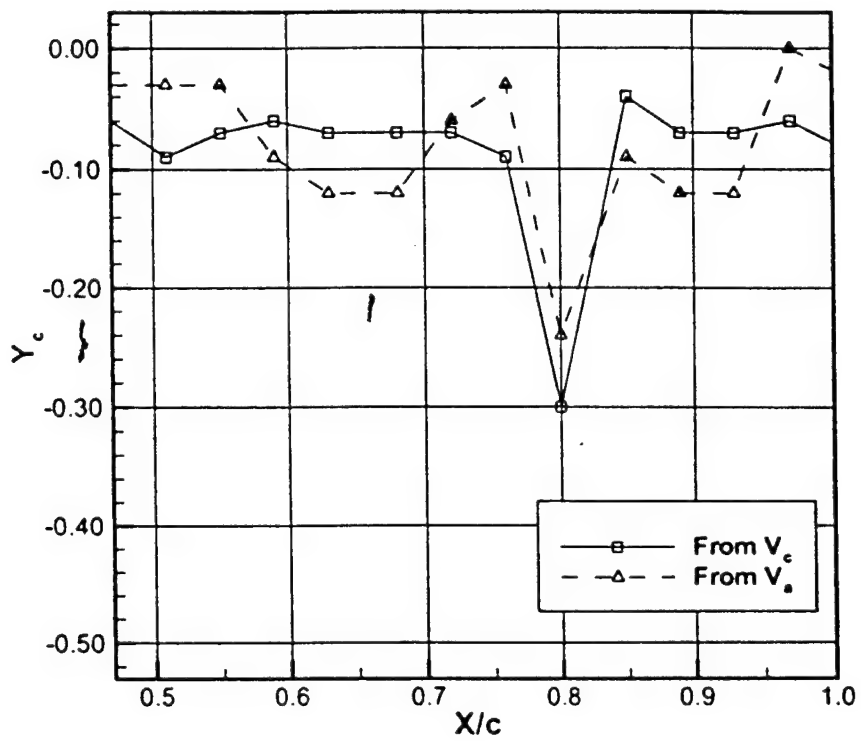


Figure 7.22: Horizontal vortex location.

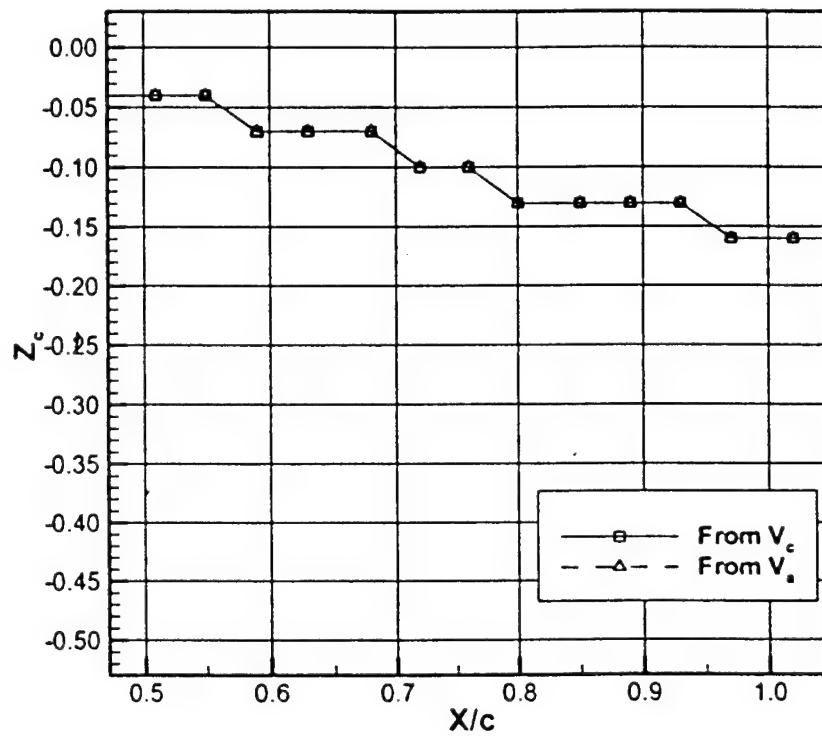


Figure 7.23: Vertical vortex location.

position is not yet known.

Comparison of the two methods shows good correlation considering the asymmetry of the vortex. In the lateral direction both methods place the center oscillating about a y/c location of -0.06. There is however an excursion seen in both methods at x/c of 0.79 to -0.30. The maximum difference between the two methods is 0.06, or two measurement points. An important feature to notice is that one method does not consistently under or over predict the other method. If this were the case, it would suggest that there was a registration problem in the data. However, since neither seems to consistently over or under predict the other, a registration problem is unlikely. Therefore, the asymmetry observed in the position of the peak axial velocity is likely a physical feature of the flow.

In the vertical direction, both methods produce identical results. A downward movement relative the measurement origin is observed.

7.3.6 Observations on the Vortex Formation Process

The resolution of the LV system becomes an issue for these measurements. At the trailing edge, there are nine measurement points across the core. However, the length scales of the vortex near the midchord position are approaching the resolution of the LDV system. At the chord location where the first clear velocity profile appears, there are only three measurement points in the core. Presumably the vortex formation process starts closer to the leading edge, but with the current LDV system, it cannot be captured.

The asymmetry of the vortex causes differences in the vortex strength depending on which velocity profiles are used. If the results are averaged, however, it can be used as an indication of the overall changes in vortex strength. In general, an increase in vortex strength is observed. Coupled with the secondary features, or kinks, in the velocity profiles, this suggests that the formation process may be due to a rollup of individual vortex filaments.

7.3.7 Blade Tip Location

Knowledge of the blade position as it passes through the measurement grid is critical if the vortex position relative to the blade is to be captured and

Location	Flapping Angle
Rear	2.13°
ABS	-1.41°
Front	-2.13°
RBS	1.41°

Table 7.2: Measured flapping angles, $\mu = 0.10$, 1050RPM

phenomenon near the blade surface are to be observed. The location of the blade in the measurement grid is a function of the blade flapping angles, azimuth and airfoil section. Liou[1988] measured the tip path plane (TPP) of this rotor at an advance ratio of 0.10 and at 2100 RPM. However, since these tests were conducted at 1050 RPM, it was felt that the measurements should be repeated to verify the TPP.

The TPP was measured by lowering a horizontal laser beam until it touched the tip of the rotor. The test section lights were turned off so that the intersection of the laser and the blade tip could easily be determined. This test was conducted on the ABS and the rear of the rotor. The measured flapping angles match those measured by Liou and are shown in Table 7.2. A code is being written to numerically solve for the position of the blade in the measurement grid. The results will be used to filter out locations that correspond to blade interference.

7.4 Evolution to the Near Wake

7.4.1 Evolution of Core Axial Velocity

The variation in the axial velocity on the ABS, RBS and rear of the rotor are shown in Figure 7.24. On the ABS, the peak core axial velocity increases linearly from 25% of tip-speed to 50% of tip-speed from a vortex age of 0 degrees to about 24 degrees, after which it drops slowly back to 25% of tip-speed by an age of 120 degrees and levels off. On the RBS, velocities reaching nearly 80% of tip speed are observed immediately following formation. This suggests that core axial velocity reaches tip speed during formation due to the no-slip condition on the blade. The peak sharply drops within 6 degrees

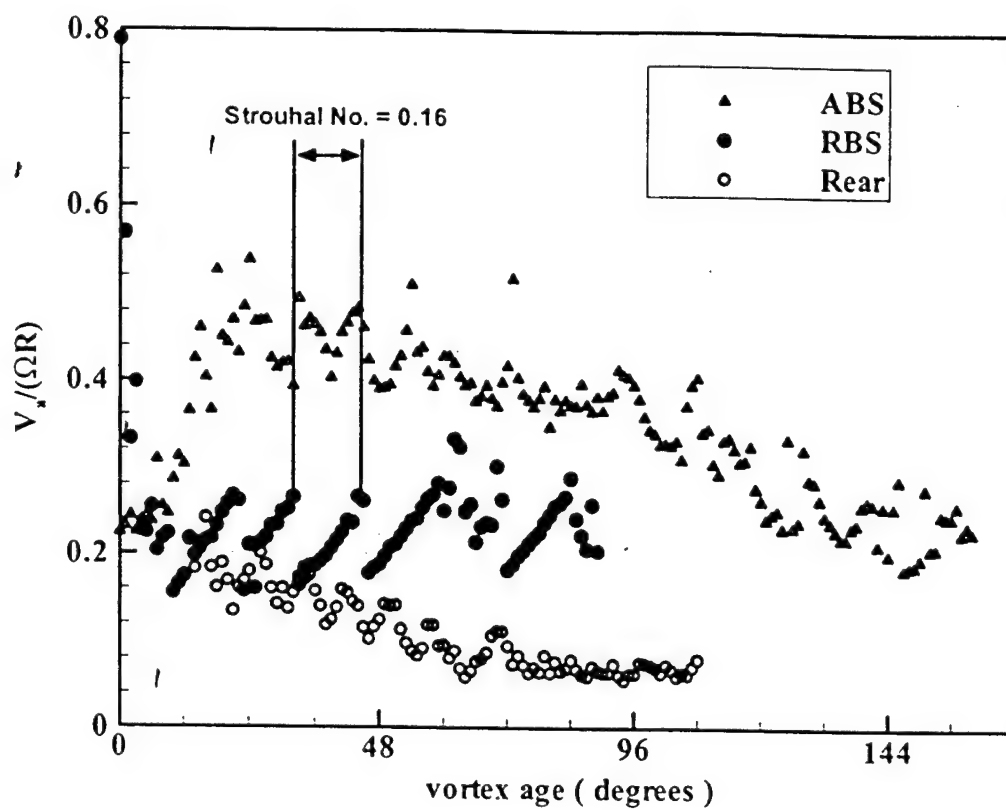


Figure 7.24: Evolution of the peak axial velocity.

of azimuth, and is replaced by a wave like pattern of evolution as seen on the ABS. The mean of this wave like pattern levels off at 25% of tip-speed. At the rear of the rotor, the peak axial velocity is much smaller, starting out at 20% of tip-speed and leveling off at about 8% of tip-speed by the time the vortex is 72 degrees old.

There are distinct differences in the evolution of the core axial velocity distribution on the ABS and the RBS. These differences might be in part due to the differences in seed particle dynamics. On the ABS the seed particles have to reverse direction to follow the core flow, thus taking more time to adjust to the local velocity when compared to the RBS. On the RBS, seed particles traveling along with the freestream flow are more easily entrained in the blade-tip boundary layer.

There appears to be a lot of scatter in the data. On closer inspection, there is a periodic pattern to the core axial velocity evolution. The period of this pattern is about 10 degrees of rotor azimuth, or a time of 1.62ms. The Strouhal Number based on this period, tip-speed and blade tip thickness is 0.16, which suggests a shedding pattern very similar to the shedding in the wake behind a cylinder.

Measurements were made to extend the data on the evolution of the axial velocity out to vortex age of 540°. By a vortex age of 160° the number of data points inside the vortex core had diminished to the point that no conclusion could be made on the peak axial velocity.

7.4.2 Evolution of Circumferential Velocity

Figure 7.25 shows the evolution of the peak core circumferential velocity on the four azimuths of the rotor. The velocities on the front and RBS of the rotor are about 10% higher than the velocities at the ABS at all vortex ages. On the RBS and front of the rotor disk, within the first 6 degrees of vortex age the peak velocities reach 45% of tip-speed on the RBS and 35% of the tip-speed on the ABS. After that, the peak velocities drop slowly, reaching 30% of tip-speed by an age of 72 degrees on the RBS and 20% of tip-speed by an age 160 degrees. On the rear the velocities stay level at 20% of tip-speed. There is decay in the maximum core circumferential velocities. Several researchers have decay in the core velocities and have proposed that it is due

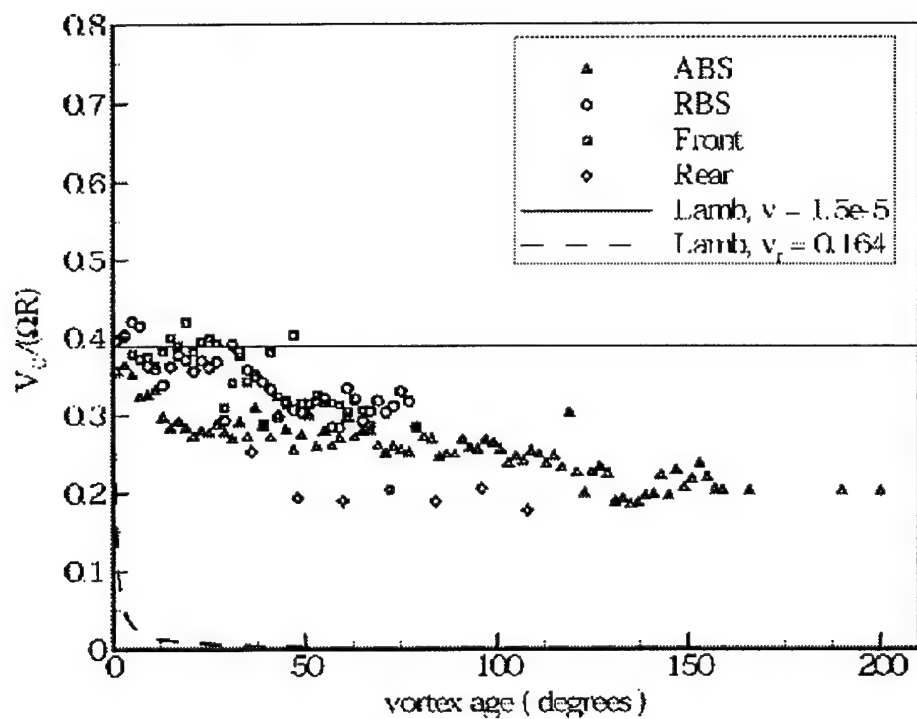


Figure 7.25: Evolution of the peak circumferential velocity.

to the diffusion of the vortex core. Lamb[1932], derived an expression for the core circumferential velocity as a function of circulation, core radius and downstream distance from the trailing edge of the generating blade, given as:

$$V_c(r, x) = \frac{\Gamma}{2\pi r} \left[1 - e^{-\frac{V_{tip}}{4\nu x} r^2} \right]$$

Non-dimensionalized with V_{tip} , using thickness of the rotor blade for core diameter, and replacing the distance x with the vortex age, ψ , the expression can be rewritten as:

$$\frac{V_c(\psi)}{V_{tip}} = k_1 \left[1 - e^{-\frac{0.0675}{\psi x}} \right]$$

Note that Lamb derived this equation making assumptions of small axial gradients, small core velocities compared to free-stream velocities, and a rectilinear vortex. None of these assumptions are valid for vortices shed from a rotor blade.

Under these considerations, the value of k_1 was obtained as 0.39 from Figure 25E. Using a value of ν equal to the kinematic viscosity of $1.5e^{-5}$ gives the flat line in Figure 25E, indicating that viscous diffusion cannot be the cause of the decay of the vortices.

A value of eddy viscosity was obtained for this flow using Prandtl's mixing length model:

$$\nu_t = l^2 \left| \frac{du}{dy} \right|$$

For the vortex core in these tests, the mixing length is taken as the blade thickness, and the velocity gradient is obtained from measurements, giving $\nu_t = 0.164$. Using this value in Lamb's model results in a drop of peak core velocity to 1% of tip-speed within 12 degrees of vortex age. Thus, the levels of turbulence in the flow-field are much lower than those associated with the scales of the tip-vortex.

Measurements of peak circumferential velocity were made out to a vortex age of 488° on the ABS (Figure 7.26). These measurements show that the peak circumferential velocity remains reasonably constant for nearly one and a half turns of the rotor.

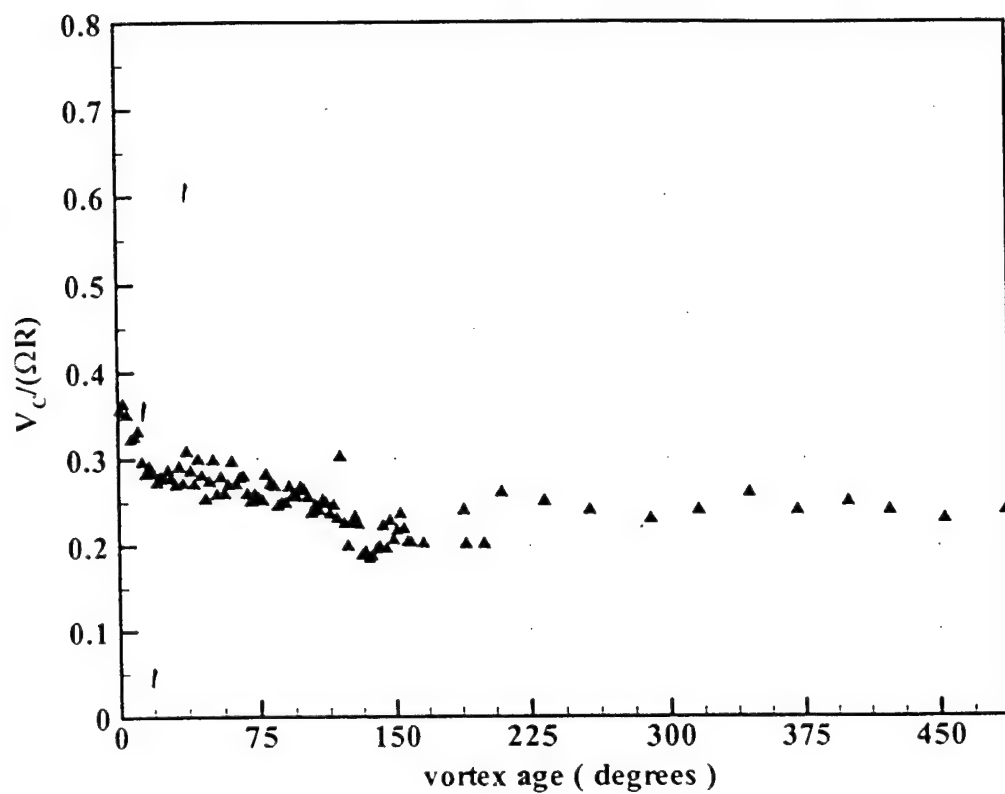


Figure 7.26: Peak Circumferential velocity, ABS.

7.4.3 Vortex Size

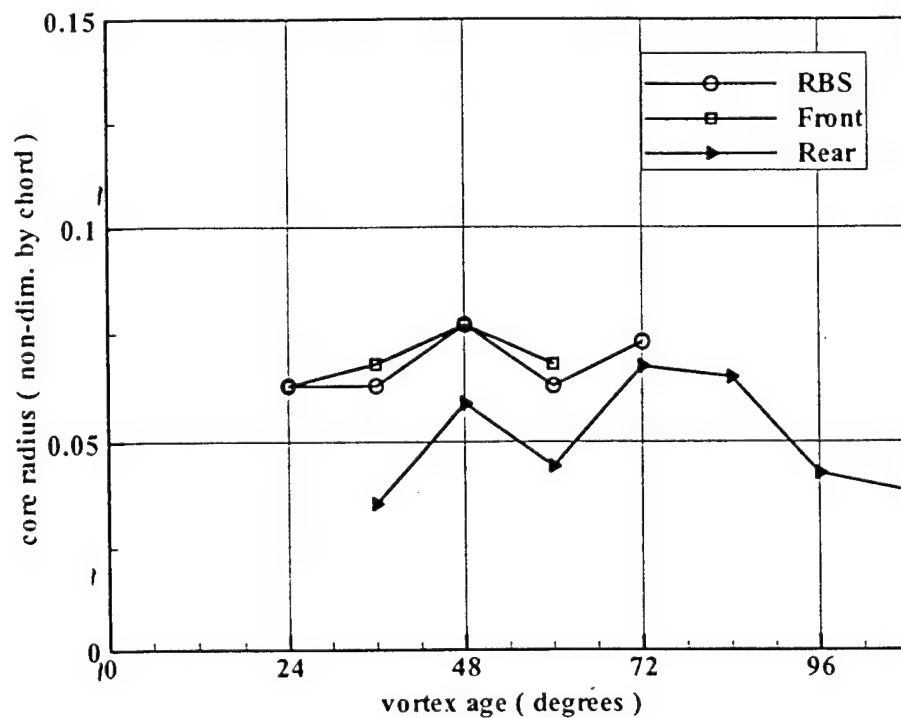


Figure 7.27: Evolution of the vortex core radius.

On the RBS and the front of the rotor, the core radius varies between 6% and 7% of the chord (Figure 7.27). At rear of the rotor, the radius increases from 4% of the chord to 6% by an age of 72° , and then decreases back to 4% at an age of 108° . On the ABS, there is an increase from 5.5% to 6.5% between 24° and 36° of vortex age followed by decay to 4.5% at an age of 96° (Figure 7.28). For vortex ages between 189° and 488° , the radius oscillates between 4 and 7% of the chord.

Recall from the vortex formation measurements that the core radius at the trailing edge was 9% of the chord. The reason for this discrepancy is not yet known; further analysis of the data is still needed. One possible explanation is that the vortex may not be completely rolled up. It may take several chord lengths for the vortex to completely form.

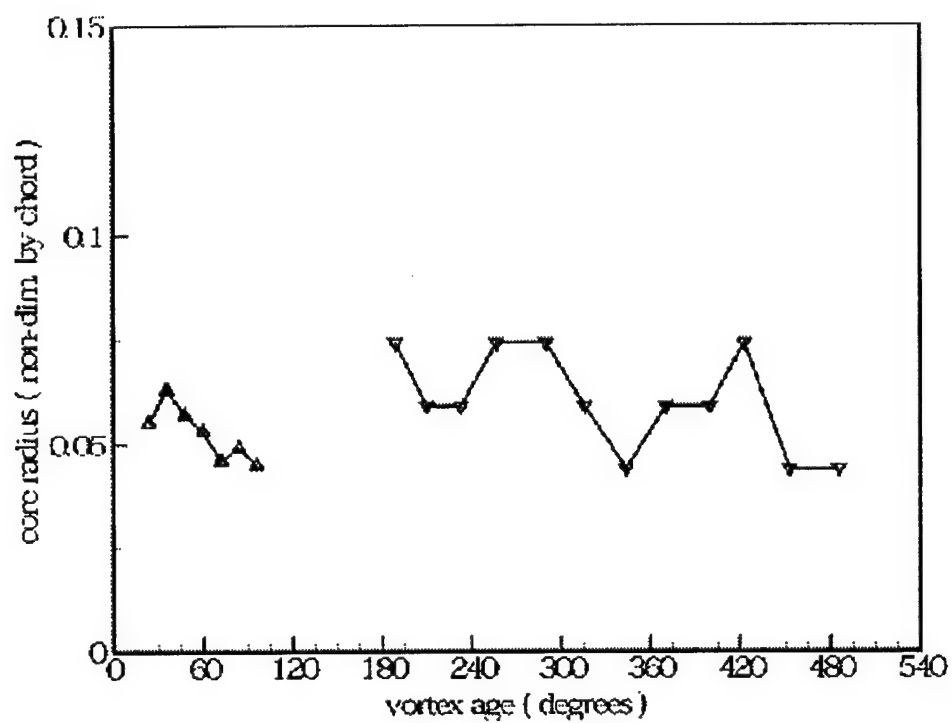


Figure 7.28: Evolution of the vortex core radius, ABS

7.4.4 Wake Boundaries

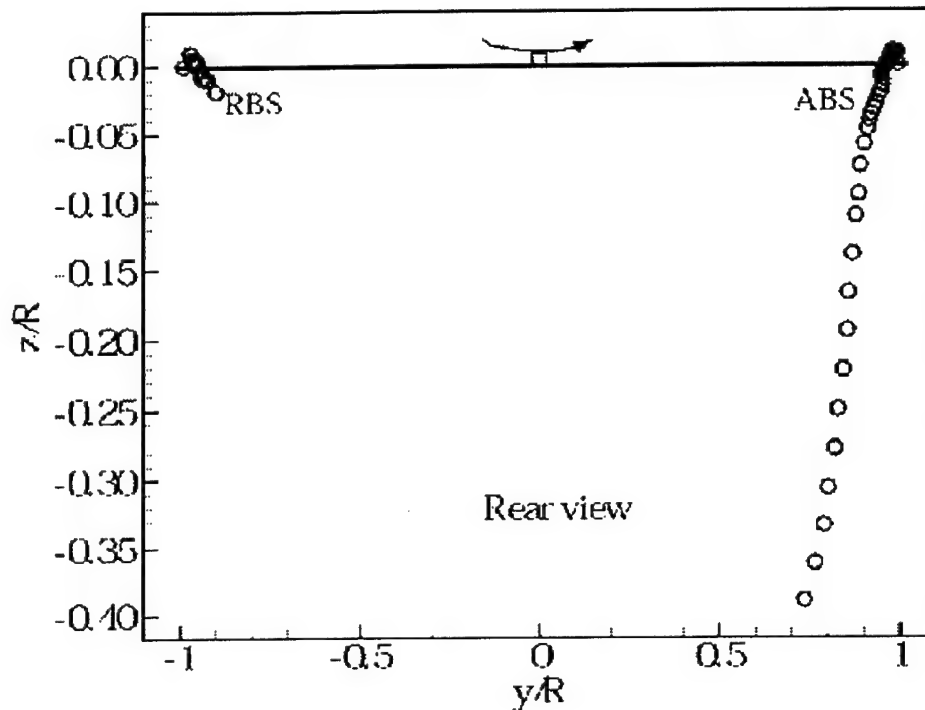


Figure 7.29: Wake boundaries on the ABS and RBS.

The wake boundaries are shown in Figure 7.29 and Figure 7.30. On the ABS and RBS, the boundaries are dominated by contraction. In the far wake on the ABS, the boundary exhibits a slight change of slope at z/R of -0.30. The boundaries at the front and rear of the rotor are dominated by convection.

7.4.5 Tip Vortex Turbulence

There are several factors that affect the measurement of the RMS velocities. At very early vortex ages, when the vortex is not completely rolled up, very high values of RMS fluctuations are observed, sometimes reaching 50% of the mean. This is in large part due to the lack of seed particles within the core. The core velocities are thus averaged over a very few number of particles, resulting in a large RMS velocity. With the exception of the rear station, the fluctuations reduce to a value typically around 10% of the mean velocity,

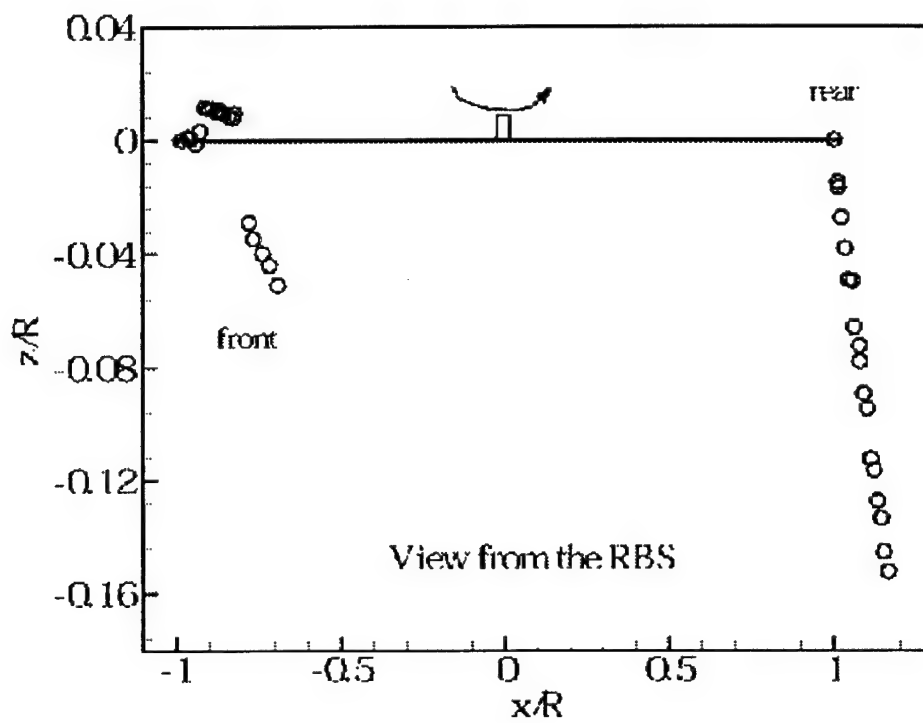


Figure 7.30: Wake boundaries on the front and rear.

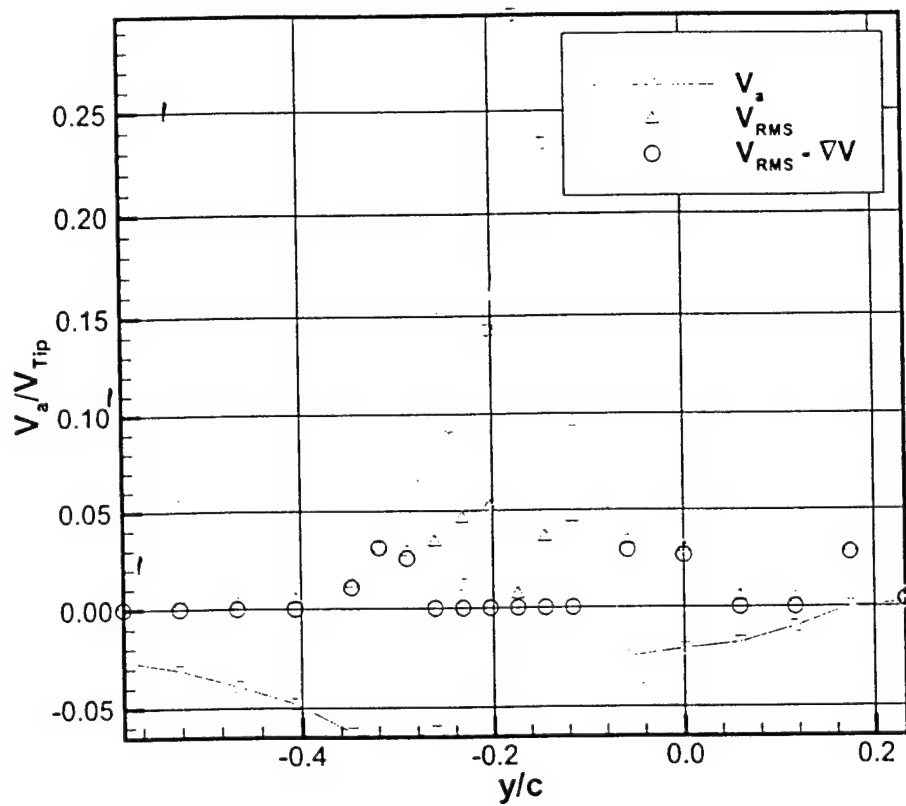


Figure 7.31: Core axial velocity profile, ABS, Age = 12°

after about 30 degrees of vortex age. The azimuth resolution used for acquiring the data and the large velocity gradient in the core also contributed to the measured RMS velocity. All the tests here used an azimuth resolution of 1 degree. The time taken by the tip-vortex to cross the measurement volume is about 6 degrees (0.95 ms). In this time, the velocity variation is about 50% of tip-speed, or 20 m/s. This corresponds to a velocity variation of 4.17 m/s per degree. Therefore when the data is acquired with an azimuth resolution of 1 degree, it already has RMS fluctuations on the order of 10% of the tip-speed. If these fluctuations are taken out of the RMS values, it is clear that fluctuation levels within the vortex core are lesser than the freestream turbulence levels (Figure 7.31). This indicates that there is no turbulence generated in the tip-vortex core. Furthermore, absence of turbulence generation within the core is demonstrated by the fact that at all locations on the rotor disk, except the rear, the RMS fluctuations drop with increasing vortex age. This phenomenon could only result from a decay of turbulence if any is present. On the rear of the rotor, the generating blade is in the turbulent wake of the rotor hub and shaft. Some of this turbulence might be wrapped into the core, resulting in large RMS fluctuations.

7.5 Seed Particle Dynamics

7.5.1 Formulation of the Seed Particle Dynamics Problem

Radial force due to the fluid rotation, and aerodynamic drag are assumed to be the only forces acting on the particle. Particles are assumed spherical. Aerodynamic drag acting on the particle is obtained from Stokes relationship. The particle at time t is shown in Figure ??.

The angle ϕ is the rotation of the fluid and θ is the angle of particle lag behind the gas rotation. The vectors u and v are the X and Y components, respectively, of the gas velocity V at the particle's position. The particle's velocity is represented by \dot{x} and \dot{y} . Summing the forces in the X and Y directions and assuming Stokes drag results in:

$$\sum F_X = m\ddot{x} = F_{X_{drag}} = 6\pi\mu r V_{rX}$$

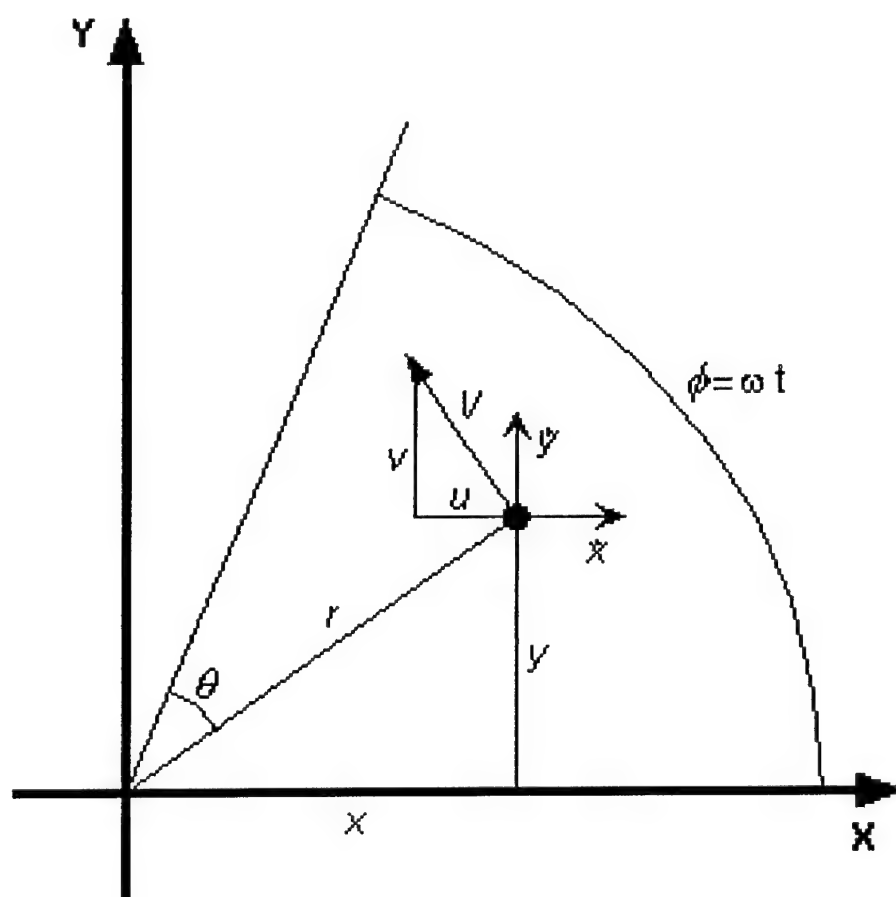


Figure 7.32: Particle at time t .

$$\sum F_Y = m\ddot{y} = F_{Y_{drag}} = 6\pi\mu r V_{rY}$$

where V_r is the velocity relative to the particle. From the diagram it can easily be shown that the relative velocity of the particle is given by:

$$V_{rX} = u - \dot{x} = -V \frac{y}{r} - \dot{x}$$

and

$$V_{rY} = u - \dot{y} = -V \frac{x}{r} - \dot{y}$$

The gas velocity was modeled assuming solid body rotation in the vortex core and then switched to a potential model outside of the vortex core. The resulting equations of motion are:

$$\ddot{x} + \beta\dot{x} + \beta\frac{V}{r}\dot{y} = 0 \quad \ddot{y} + \beta\dot{y} + \beta\frac{V}{r}\dot{x} = 0$$

where

$$\beta = \frac{18\mu}{\rho_p d_p^2}$$

$$V = \omega_o r \quad \text{for} \quad 0 \leq r \leq R_c$$

$$V = \frac{\Gamma_o}{2\pi r} \quad \text{for} \quad r > R_c$$

The subscripts p and o represent the characteristics of the particle and conditions at $t = 0$, respectively.

These equations were numerically integrated using Matlab software. Particles with diameters of 1.0, 2.0, 3.0, 4.0 and 5.0 microns were examined. All particles were "released" at $r/R_c = 0.01$ with an angular velocity equal to that of the gas. The numerical integration was stopped when $r/R_c = 3.0$. Initial angular velocity, ω_o , vortex circulation, Γ_o , and core radius were determined from experimental data. These correspond to 3333 rad/s, 0.754 m^2/s and 0.006 m respectively. The Stokes numbers for these particles based on the initial angular velocity are listed in Table 7.3.

Particle Diameter (μm)	Stokes Number= $\frac{\rho_p \omega_o D_p^2}{18\mu}$
1	0.0088
2	0.0351
3	0.0789
4	0.1402
5	0.2191

Table 7.3: Particle's Stokes numbers

7.5.2 Predicted Difference Between Seed Particle and Fluid Velocity

Results of simulating the dynamics of seed particles of mineral oil in a 2-D vortex are shown in the following figures. The radial and tangential velocity components are shown in Figure 7.33. The non-dimensional air velocity is also superimposed on the chart. The error in tangential velocity is seen on the upper part of the figure as differences from 1.0. The error in radial velocity is shown at the bottom of the figure as differences from 0.

True tangential velocity in the vortex core is under-represented by particles measuring $3\mu m$ and larger. The velocity error ranges from approximately 2% – 8%. Particles smaller than $2\mu m$ showed better than 99% accuracy in representing the tangential velocity. Outside the vortex core, where velocities and centrifugal forces acting on the particles are lower, all particles rapidly adjust to the new conditions and then travel at the same speed as the fluid. The larger particles do, however, have a slight lag before they adjust to the proper velocity. All of the particles in the core obtain a radial velocity due to the centrifugal forces acting on them. This results in errors ranging between approximately 1% and 18% of the fluid velocity. The error decays in the potential region of the vortex. The decay, however, is not as strong as that of the tangential velocity.

7.5.3 Error in Radial Growth of Vortex Core

The increase of the particle's radial position is shown in Figure 7.34. As illustrated in the figure, particles experience the greatest increase in radial

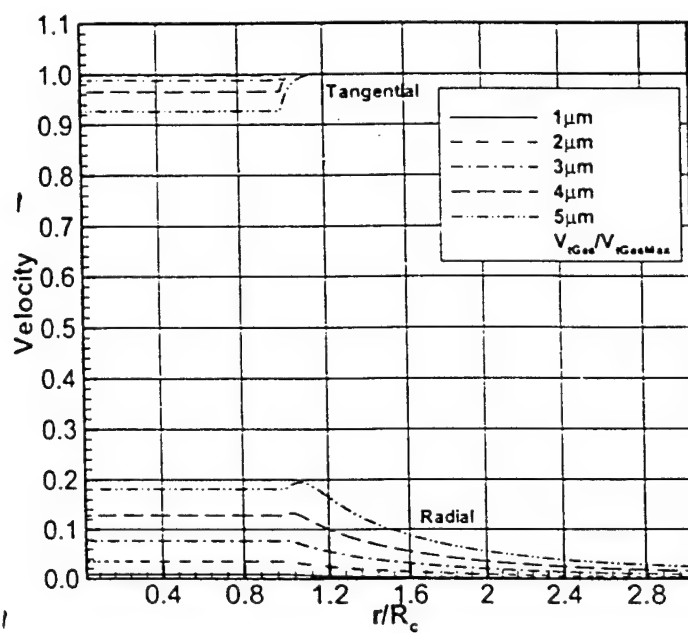


Figure 7.33: Non-dimensional velocity.

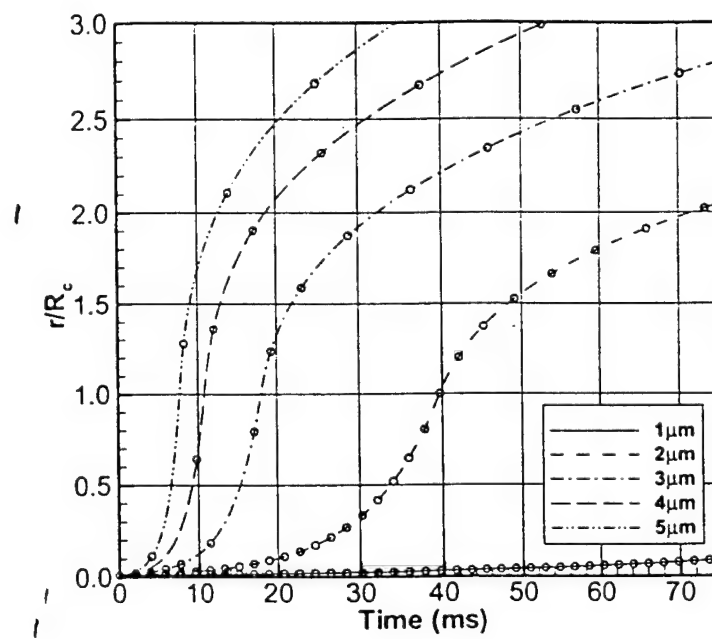


Figure 7.34: Radial position. Circles represent one revolution.

Particle Dia. (μm)	Time (ms) $r/R_c = 0.1$	Time (ms) $r/R_c = 0.5$	Time (ms) $r/R_c = 1.0$
1	78	133	159
2	20	34	40
3	9	15	18
4	5	9	11
5	4	6	8

Table 7.4: Time to reach various radial locations

position while in the vortex core. Outside of the core, the rate of radial position growth decreases. The circles indicate each revolution of a particle. Table 7.4 shows the amount of time required for particles to reach several radial locations. As expected, large particles are rapidly centrifuged from the vortex core.

7.5.4 Velocity Error

These simulations show that the tangential velocity of seed particles entrained in the vortex core closely represents the true tangential velocity of the gas. The maximum error is approximately 8% lower than the true velocity for $5\mu m$ particles. There is also a substantial radial component of velocity due to the centrifugal force acting on the particles. Again, the largest errors are due to the 4 and $5\mu m$ particles.

One issue to consider is the amount of time required to centrifuge the largest particles out of the core. In 11 ms, or a vortex age of 69.3° , nearly all of the 4 and $5\mu m$ particles have been ejected from the core. At that point, the maximum tangential error is about 2% and the radial velocity error is approximately 8%.

7.5.5 Particle Number Density

Another issue that affects LV measurements is particle density in the core. Since particles are required to obtain measurements, low seeding densities in the core will result in low data rates. The presented results show that particles are rapidly evacuated from the core. By 159ms, or a vortex age of 1002° ,

the vortex core is nearly completely void of particles. At first glance, this would seem to indicate that one could make vortex core measurements up to vortex ages of about 1000° . However, since the peak axial velocity occurs in the center of the vortex, the maximum age that allows for measurements of the maximum axial velocity is significantly less. Additionally, note that the axial velocity is directed towards the blade, and thus fluid with the particles evacuated, moves towards segments of the vortex with lower vortex ages.

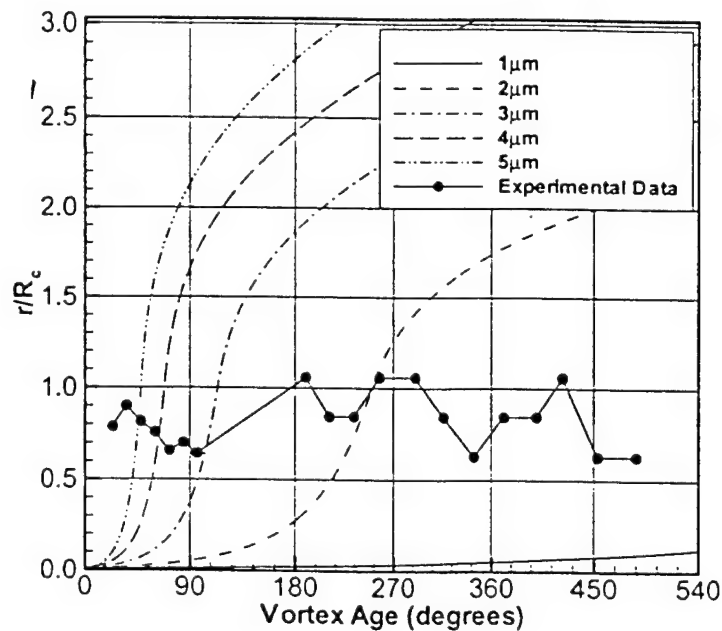


Figure 7.35: Comparison of measured core size with 2-D predictions for various sizes of particles.

The predictions of particle dynamics are compared with the actual experimental data obtained (Figure 7.35). As mentioned before, the core tangential velocity could be measured up to 540 degrees of vortex age. From these, the

core size could be obtained. Going back to the calculation of particle dynamics for particles of various sizes starting from near the core center, we are able to predict the vortex age at which these particles would have gone beyond the real vortex core edge. Thus, for ages beyond this, the measured core size should keep increasing. Comparing with the actual data for core size, we see that the size stays essentially constant beyond 450 degrees of vortex age. The predicted conical increase of core size due to particle spinout does not occur. This indicates that either the particles used are less than 2 microns in diameter, or the predictions of error are extremely conservative.

Given the above comparison, the upper bound of error in tangential velocity due to particle spinout must be revised downwards, to the values corresponding to particles of 1 to 2 microns, for the above simulation approach. Thus the upper bound from Figure 7.33 is seen to be on the order of 1 to 2 percent, an insignificant source of error in these measurements.

As mentioned before, the actual vortex has a strong axial velocity component that should be taken into account in future simulations of seed particle spinout. Two competing effects may be expected: Firstly, the presence of axial flow towards the blade tip would cause spinout to occur at smaller ages than predicted by the 2-D model. However, the axial flow would also cause a sink-like radial fluid velocity. This would reduce the radial drift of particles from the core, and keep them at locations inside the core where the acceleration is lower. This would reduce the drift error.

7.5.6 Accuracy of the Simulation

The Stokes relationship used for particle drag was developed under the assumption that the Reynolds number, based on the particle relative velocity and diameter, is less than 1. The Reynolds number of the particles as they are centrifuged from the core is shown in Figure 7.36. According to Dring[1978], for $Re_p > 1$, Stokes relationship tends to under predict drag.

Figure 7.37 compares CD predicted by Stokes relationship and the drag models used by Dring[1978]. Stokes relationship under-predicts drag by 50% for the largest particles near the edge of the core. This under-prediction of the drag means that the trajectories and velocity errors are conservative estimates.

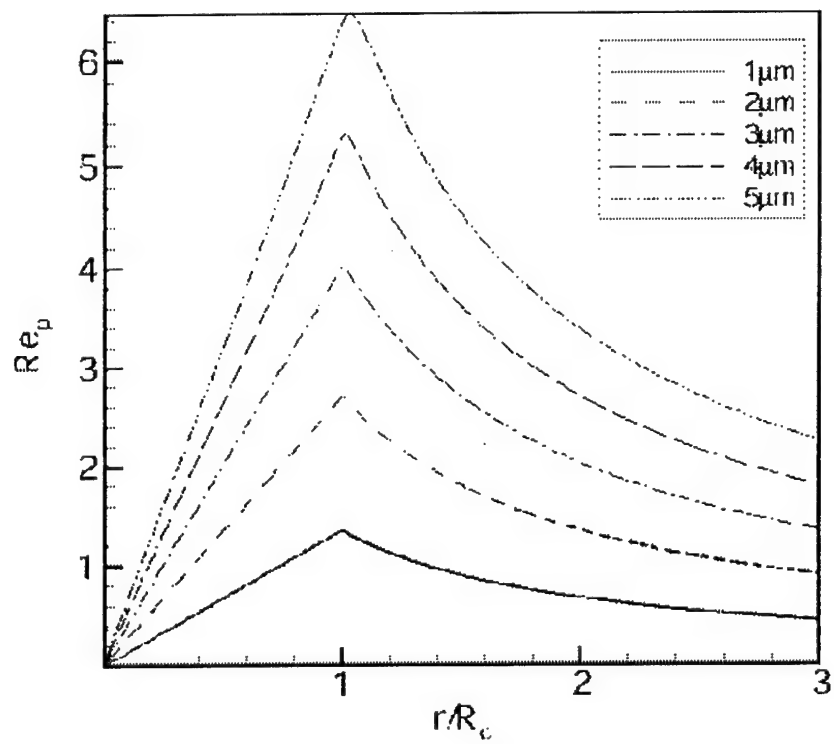


Figure 7.36: Reynolds numbers of the particles.

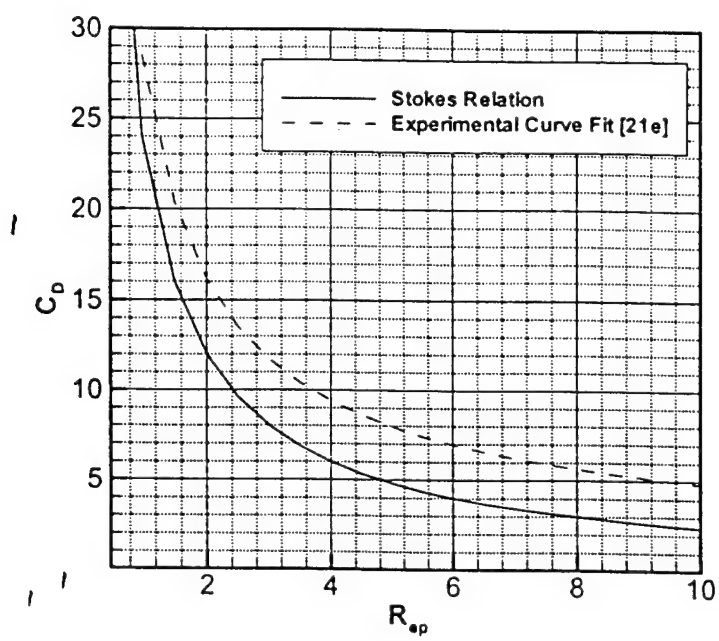


Figure 7.37: Comparison of drag predictions.

As the tip speed increases, the vortex strength increases rapidly, so that smaller particles would be needed to keep the level of error low. However, the Reynolds number of the relative flow might also increase, making the Stokes flow simulation less accurate. As mentioned previously, and as shown by comparison with the core size measurements, the axial velocity in the core should also be considered to perform a useful simulation of seed particle dynamics in rotor tip vortices.

7.6 Density Variations in the Vortex Core

7.6.1 Analytical Model

We start by considering the governing equations, in cylindrical coordinates (r, θ, z) , for the structure of a slender, axisymmetric, compressible, viscous vortex. With the quasi-cylindrical approximation, only radial derivatives of the viscous term are retained. Due to assumption of slenderness, the radial velocity is much smaller than the other velocity components, thus in the radial momentum equation, the pressure gradient balances the centrifugal force. The equations reduce to (Orangi *et al.* [2001])

$$\frac{\partial \rho V_r}{\partial r} + \frac{\rho V_r}{r} + \frac{\partial \rho V_z}{\partial z} = 0 \quad (7.1)$$

$$\frac{\partial p}{\partial r} - \frac{\rho V_\theta^2}{r} = 0 \quad (7.2)$$

$$\rho V_r \frac{\partial V_\theta}{\partial r} + \rho V_z \frac{\partial V_\theta}{\partial z} + \frac{\rho V_r V_\theta}{r} = \frac{1}{Re} \frac{1}{r} \frac{\partial}{\partial r} \left[\mu r^2 \frac{\partial}{\partial r} \left(\frac{V_\theta}{r} \right) \right] + \frac{1}{Re} \mu \frac{\partial}{\partial r} \left(\frac{V_\theta}{r} \right) \quad (7.3)$$

$$\rho V_r \frac{\partial V_z}{\partial r} + \rho V_z \frac{\partial V_z}{\partial z} = -\frac{\partial p}{\partial z} + \frac{1}{Re} \frac{1}{r} \frac{\partial}{\partial r} \left(\mu r \frac{\partial V_z}{\partial r} \right) \quad (7.4)$$

$$\begin{aligned} \rho V_r \frac{\partial T}{\partial r} + \rho V_z \frac{\partial T}{\partial z} = & (\gamma - 1) M^2 \left(V_r \frac{\partial p}{\partial r} + V_z \frac{\partial p}{\partial z} \right) + \frac{1}{(Pr)(Re)} \frac{1}{r} \frac{\partial}{\partial r} \left(\mu r \frac{\partial T}{\partial r} \right) + \\ & \frac{(\gamma - 1) M^2}{Re} \mu r \left(\frac{\partial V_z}{\partial r} \right)^2 + \frac{(\gamma - 1) M^2}{Re} \left[\mu r \frac{\partial}{\partial r} \left(\frac{V_\theta}{r} \right) \frac{\partial V_\theta}{\partial r} - \mu V_\theta \frac{\partial}{\partial r} \left(\frac{V_\theta}{r} \right) \right] \end{aligned} \quad (7.5)$$

This system of equations is closed by the equation of state for a calorically perfect gas.

$$p = \frac{1}{\gamma M^2} \rho T \quad (7.6)$$

Due to the axial symmetry assumption, the boundary and initial conditions are

$$\begin{aligned} V_r &= 0 \\ V_\theta &= 0 \\ \frac{\partial V_z}{\partial r} &= 0 \\ \frac{\partial T}{\partial r} &= 0 \end{aligned} \quad (7.7)$$

and the conditions at the outer vortex edge are for $r \rightarrow \infty$

$$\begin{aligned} V_\theta &\rightarrow V_{\theta\infty}(z) \\ V_z &\rightarrow V_{z\infty}(z) \\ p &\rightarrow p_\infty(z) \\ T &\rightarrow T_\infty(z) \end{aligned} \quad (7.8)$$

The solutions to these equations require the initial condition on V_θ, V_z, T and p as functions of r at some axial location. It is very difficult to obtain the analytical solution of such a complex system of equations. Orangi, *et al.* [2001] recommends using similarity equations to simplify the problem. However, it is still very hard to solve the similarity equations analytically. Numerical methods are preferred for this purpose (see Orangi[2001] for more detail of numerical procedure).

Again, the aim of this work is still to find simpler analytical solutions for this problem. Hence, to simply or make the analytical solutions possible, some assumptions and modifications are needed in this system of equations. Our method is applying the known solution for the velocity profile of an incompressible viscous vortex to the momentum equation of a compressible vortex to obtain a solution for the density field in the vortex.

Consider the r-momentum equation for compressible vortex, Eq. (7.2). To determine the pressure distribution, the circumferential velocity profile is needed. Furthermore, by assuming isentropic flow, the pressure p can be expressed in terms of density, ρ , as

$$\left(\frac{p}{p_\infty}\right) = \left(\frac{\rho}{\rho_\infty}\right)^\gamma \quad (7.9)$$

Therefore, to obtain the density distribution in the vortex, it is necessary to know the velocity profile V_θ . The simplest model of a viscous vortex is the Lamb vortex. Lamb[1932] developed an expression for the circumferential velocity of a trailing vortex core as a function of circulation Γ_∞ , radial distance r and time t . It can be shown as

$$V_\theta(r) = \frac{\Gamma_\infty}{2\pi r} \left[1 - \exp(-r^2/4\nu t)\right] \quad (7.10)$$

and, the Lamb result for viscous core growth is

$$r_c = 2\sqrt{\alpha\nu t} \quad (7.11)$$

where r_c is the core radius and $\alpha = 1.25643$

The steady three-dimensional problem is customarily replaced by a conceptually and numerically simpler unsteady two-dimensional problem where $t = z/V_\infty$ for trailing vortex from a fixed wing(Saffman [1992]) or for tip vortex from a rotor blade(Wong *et al.* [2000]). Thus, Eq.(7.11) shows that the vortex core radius is a function of downstream distance given by

For the trailing vortex of fixed wing,

$$r_c = 2\sqrt{\alpha\nu \frac{z}{V_\infty}} \quad (7.12)$$

For tip vortex of rotor blade,

$$r_c = 2\sqrt{\alpha\nu \frac{z}{V_{tip}}} \quad (7.13)$$

With Eq.(7.10) and (7.11), in terms of non-dimensional radial distance, $\bar{r} = r/r_c$, a simpler expression for three-dimensional viscous vortex and can be written as

$$V_\theta = \frac{\Gamma_\infty}{2\pi r_c} \left(\frac{1 - \exp(-\alpha\bar{r}^2)}{\bar{r}} \right) \quad (7.14)$$

It should be noted that Lamb's expression assumed small axial gradient, small core velocities compared to freestream and a rectilinear vortex. Moreover, for rotor-blade tip vortex, z also depends on the vortex age.[2000]

Vatistas, *et al.*[1991] gave a series of general "desingularized" velocity profiles, where the circumferential velocity in a two-dimensional cross-sectional plane of the vortex is expressed as

$$V_{\theta}(r) = \frac{\Gamma_{\infty}}{2\pi} \frac{r}{(r_c^{2n} + r^{2n})^{1/n}} \quad \text{or} \quad V_{\theta}(\bar{r}) = \frac{\Gamma_{\infty}}{2\pi r_c} \frac{\bar{r}}{(1 + \bar{r}^{2n})^{1/n}} \quad (7.15)$$

and n is an integer variable.

Consider the velocity profile for Lamb's vortex and three special vortex models of Eq.(7.15) with a particular value of n ; Rankine vortex $n = \infty$, Scully[1975] vortex $n = 1$ and $n = 2$ model.

From Eq.(7.15), $n \rightarrow \infty$, Rankine vortex:

$$V_{\theta}(\bar{r}) = \begin{cases} \frac{\Gamma_{\infty}}{2\pi r_c} \bar{r} & 0 \leq \bar{r} \leq 1 \\ \frac{\Gamma_{\infty}}{2\pi r_c} \frac{1}{\bar{r}} & \bar{r} \geq 1 \end{cases} \quad (7.16)$$

For $n = 1$ Scully vortex:

$$V_{\theta}(\bar{r}) = \frac{\Gamma_{\infty}}{2\pi r_c} \frac{\bar{r}}{(1 + \bar{r}^2)} \quad (7.17)$$

For $n = 2$ profile:

$$V_{\theta}(\bar{r}) = \frac{\Gamma_{\infty}}{2\pi r_c} \frac{\bar{r}}{\sqrt{1 + \bar{r}^4}} \quad (7.18)$$

All these vortex models satisfy the boundary conditions

$$V_{\theta}(\bar{r}) = \begin{cases} 0 & \bar{r} = 0 \\ V_{\theta_{max}} & \bar{r} = 1 \end{cases}$$

$$V_{\theta}(\bar{r}) \rightarrow 0 \text{ as } \bar{r} \rightarrow \infty$$

The normalized circumferential velocity profiles of these four vortex models are shown in Figure 7.38. From Figure 7.38 we clearly see that, in each model, the maximum circumferential velocity occurs at $\bar{r} = r/r_c = 1$. Note that the Lamb vortex and Vatistas's $n = 2$ vortex profile show very good agreement. This agreement is also seen in Bhagwat and Leishman's

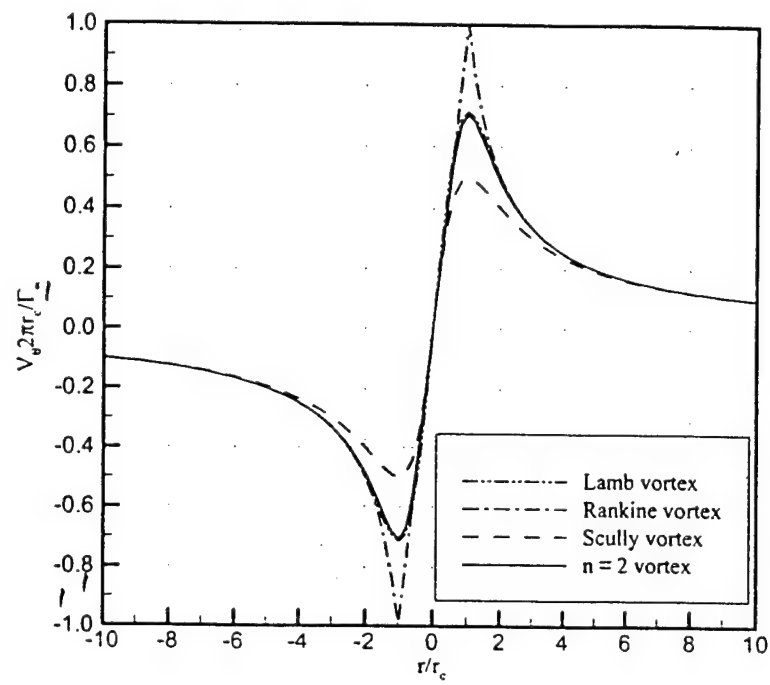


Figure 7.38: Vortex velocity profiles.

results[1998]. Moreover, it has also been shown by Vatistas, et al.[1991] that the best fit of the simpler model to the experimental circumferential velocity component is obtained if $n = 2$. Thus, to avoid complexity of mathematical solution, we now consider the $n = 2$ model as a simpler model of the Lamb vortex.

7.6.2 Vortex Density Distribution

From Eq.(4.2), we can rewrite it in terms of \bar{r} as following

$$\frac{\partial p}{\partial \bar{r}} - \frac{\rho V_\theta^2}{\bar{r}} = 0 \quad (7.19)$$

By differentiating Eq.(7.9) with respect to \bar{r} , we obtain

$$\frac{\partial p}{\partial \bar{r}} = \frac{\gamma p_\infty}{\rho_\infty^\gamma} \rho^{\gamma-1} \frac{\partial \rho}{\partial \bar{r}} \quad (7.20)$$

Substituting Eq.(??) into Eq.(??) for $\frac{\partial p}{\partial \bar{r}}$ results in

$$\frac{V_\theta^2}{\bar{r}} = \frac{\gamma p_\infty}{\rho_\infty^\gamma} \rho^{\gamma-2} \frac{\partial \rho}{\partial \bar{r}} \quad (7.21)$$

Then integrating both sides of Eq.(7.21) with respect to \bar{r} gives

$$\int \frac{V_\theta^2}{\bar{r}} d\bar{r} = \frac{\gamma p_\infty}{(\gamma-1)\rho_\infty^\gamma} \rho^{\gamma-1} + c \quad (7.22)$$

where c is a constant of integration determined by the boundary condition $\rho(\bar{r}) \rightarrow \rho_\infty$ as $\bar{r} \rightarrow \infty$. Substituting the three vortex velocity profiles, given in Eq.(7.16)-(7.18), and finding the first and second derivatives of density, we finally obtain in non-dimensional form

1. $n \rightarrow \infty$, Rankine vortex:

$$\bar{\rho} = \frac{\rho}{\rho_\infty} = \begin{cases} [1 + (\gamma-1)\lambda(\bar{r}^2 - 2)]^{\frac{1}{\gamma-1}} & 0 \leq \bar{r} \leq 1 \\ \left[1 - \frac{(\gamma-1)\lambda}{\bar{r}^2}\right]^{\frac{1}{\gamma-1}} & \bar{r} \geq 1 \end{cases} \quad (7.23)$$

$$\frac{\partial \bar{\rho}}{\partial \bar{r}} = \begin{cases} 2\lambda\bar{r}[(\gamma-1)\lambda(\bar{r}^2 - 2) + 1]^{\frac{2-\gamma}{\gamma-1}} & 0 \leq \bar{r} \leq 1 \\ \frac{2\lambda}{\bar{r}^3} \left[1 - \frac{(\gamma-1)\lambda}{\bar{r}^2}\right]^{\frac{2-\gamma}{\gamma-1}} & \bar{r} \geq 1 \end{cases} \quad (7.24)$$

$$\frac{\partial^2 \bar{\rho}}{\partial \bar{r}^2} = \begin{cases} 2\lambda [1 + (\gamma - 1)\lambda(\bar{r}^2 - 2)]^{\frac{2-\gamma}{\gamma-1}} \left[1 + \frac{2(2-\gamma)\lambda\bar{r}^2}{1+(\bar{r}^2-2)(\gamma-1)\lambda}\right] & 0 \leq \bar{r} \leq 1 \\ \frac{2\lambda}{\bar{r}^4} \left[1 - \frac{(\gamma-1)\lambda}{\bar{r}^2}\right]^{\frac{2-\gamma}{\gamma-1}} \left[\frac{2(2-\gamma)\lambda}{\bar{r}^2} \left(1 - \frac{\gamma-1}{\bar{r}^2}\lambda\right) - 3\right] & \bar{r} \geq 1 \end{cases} \quad (7.25)$$

2. $n = 1$, Scully vortex:

$$\bar{\rho} = \frac{\rho}{\rho_\infty} = \left[1 - \frac{\gamma - 1}{1 + \bar{r}^2}\lambda\right]^{\frac{1}{\gamma-1}} \quad (7.26)$$

$$\frac{\partial \bar{\rho}}{\partial \bar{r}} = \frac{2\lambda\bar{r}}{(1 + \bar{r}^2)^2} \left[1 - \frac{\gamma - 1}{1 + \bar{r}^2}\lambda\right]^{\frac{2-\gamma}{\gamma-1}} \quad (7.27)$$

$$\begin{aligned} \frac{\partial^2 \bar{\rho}}{\partial \bar{r}^2} &= \frac{2\lambda}{(1 + \bar{r}^2)^2} \left[1 - \frac{\gamma - 1}{1 + \bar{r}^2}\lambda\right]^{\frac{2-\gamma}{\gamma-1}} \\ &\quad \left[1 - \frac{4\bar{r}^2}{1 + \bar{r}^2} + \frac{2(2-\gamma)\lambda\bar{r}^2}{(1 + \bar{r}^2)^2} \left(1 - \frac{\gamma - 1}{1 + \bar{r}^2}\lambda\right)^{-1}\right] \end{aligned} \quad (7.28)$$

3. $n = 2$ profile:

$$\bar{\rho} = \frac{\rho}{\rho_\infty} = \left[(\gamma - 1)\lambda \left(\tan^{-1}(\bar{r}^2) - \frac{\pi}{2}\right) + 1\right]^{\frac{1}{\gamma-1}} \quad (7.29)$$

$$\frac{\partial \bar{\rho}}{\partial \bar{r}} = 2\lambda \left[\frac{\bar{r}}{1 + \bar{r}^4}\right] \left[(\gamma - 1)\lambda \left(\tan^{-1}(\bar{r}^2) - \frac{\pi}{2}\right) + 1\right]^{\frac{2-\gamma}{\gamma-1}} \quad (7.30)$$

$$\begin{aligned} \frac{\partial^2 \bar{\rho}}{\partial \bar{r}^2} &= \frac{2\lambda}{1 + \bar{r}^4} \left[1 + (\gamma - 1)\lambda \left(\tan^{-1}(\bar{r}^2) - \frac{\pi}{2}\right)\right]^{\frac{2-\gamma}{\gamma-1}} \\ &\quad \left[1 - \frac{4\bar{r}^4}{1 + \bar{r}^4} + \frac{2(2-\gamma)\lambda\bar{r}^2}{(1 + \bar{r}^4)^3} \left[1 + (\gamma - 1)\lambda \left(\tan^{-1}(\bar{r}^2) - \frac{\pi}{2}\right)\right]^{-1}\right] \end{aligned} \quad (7.31)$$

where $\lambda = \Gamma_\infty^2 \rho_\infty / 8\pi^2 \gamma p_\infty r_c^2$ is a non-dimensional term. Therefore, the density variation and its first and second derivatives depend on the circulation of vortex, Γ_∞ , which depends on the freestream velocity (fixed wing) or rotor-tip velocity (rotary wing).

Computed density profiles are plotted in Figure 7.39 for each of the three vortex profiles in our interested cases. Also, by changing λ , the effect of circulation to the density variation is shown in Figure 7.40.

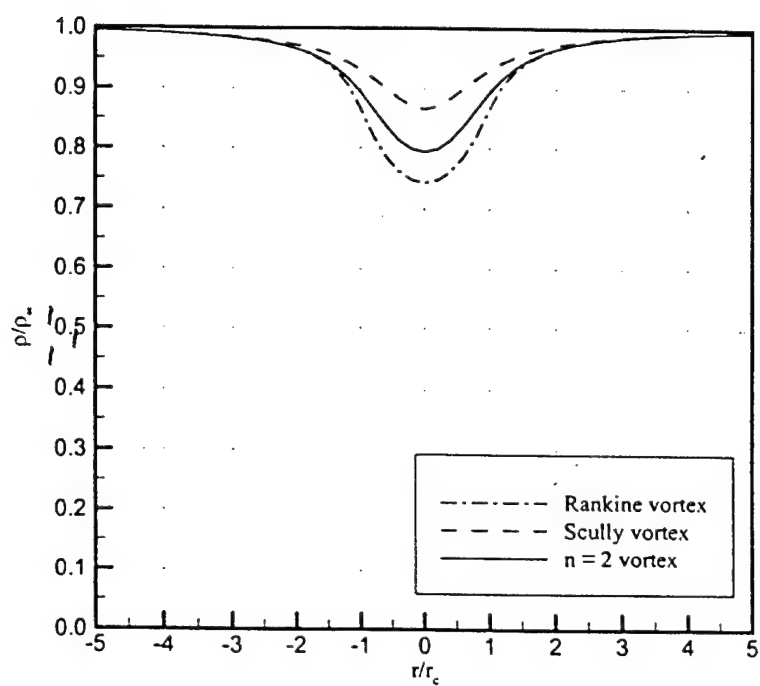


Figure 7.39: Density distribution for Rankine($n = \infty$), Scully($n = 1$) and $n = 2$ vortex models, $\lambda = 0.14$.

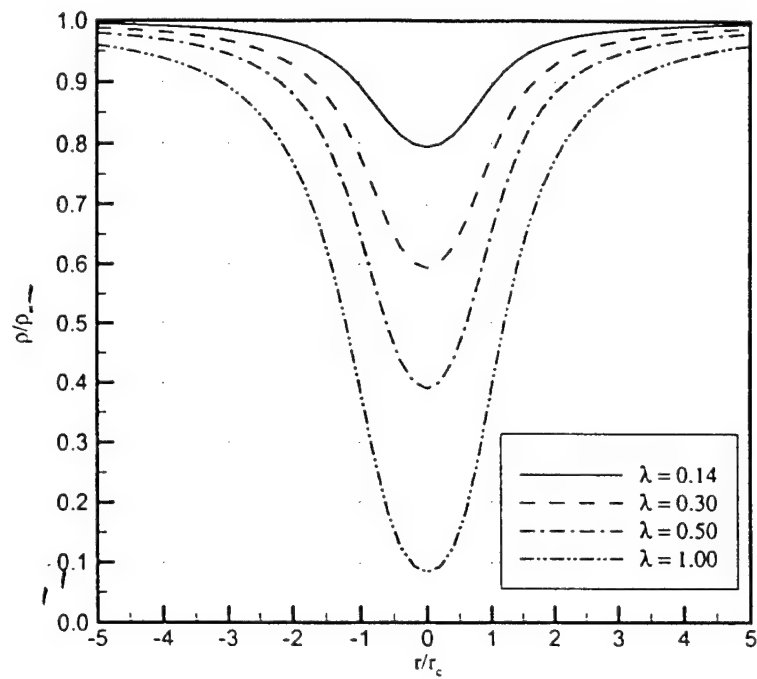


Figure 7.40: The effect of λ on the density distribution for $n = 2$ vortex model.

7.6.3 Relation Between Vortex Density and Light Intensity

We are interested in measuring the intensity of light or laser, which is directly effected by the refractive effects of incident light. The refractive effects are produced by local density variations in the flow field. Thus, knowing relationship between the fluid density ρ (or $\bar{\rho}$) and the refractive index, η , is needed. This relationship is expressed by, using the Gladstone-Dale relation

$$\frac{\eta - 1}{\rho} = \kappa \quad (7.32)$$

with sufficient accuracy where κ is the Gladstone-Dale constant which varies with both the fluid property and the wavelength of the transmitted light. The value of this constant for air is $2.28 \times 10^{-4} m^3/kg$ (Reddy [1999]).

Eq.(7.32) shows that the refractive index of the fluid is proportional to its density. Thus, if there are regions of density variation in the flow field, such as in a vortex, the incident light normal to the plane will be refracted, producing diverging or converging light rays onto a recording screen or receiving plane. The angular deflection of these light rays depends on the first derivative of density with respect to distance. These deflected light rays will produce regions of decreased or increased illumination or intensity. A simple ray diagram of this process is shown in Figure 7.41.

By assuming symmetric flow in the radial direction, the light intensity distribution due to density variation in the flow field can be written in cylindrical coordinates as

$$\frac{\Delta I}{I} = -\frac{l\kappa}{\eta_o} \int_{l_1}^{l_2} \left(\frac{1}{r} \frac{\partial \rho}{\partial r} + \frac{\partial^2 \rho}{\partial r^2} \right) dz \quad (7.33)$$

where l_1 to l_2 is the light path length through the density variation and η_o is the refractive index at reference conditions. By rewriting Eq.(7.33) in non-dimensional form, we obtain for the light intensity of compressible vortex

$$\frac{\Delta I}{I} = -\frac{l\kappa\rho_\infty}{\eta_o r_c^2} \int_{l_1}^{l_2} \left(\frac{1}{\bar{r}} \frac{\partial \bar{\rho}}{\partial \bar{r}} + \frac{\partial^2 \bar{\rho}}{\partial \bar{r}^2} \right) dz \quad (7.34)$$

Integrating along the light path results in

$$\frac{\Delta I}{I} = -\frac{\kappa\rho_\infty}{\eta_o r_c^2} l(l_2 - l_1) \left(\frac{1}{\bar{r}} \frac{\partial \bar{\rho}}{\partial \bar{r}} + \frac{\partial^2 \bar{\rho}}{\partial \bar{r}^2} \right) \quad (7.35)$$

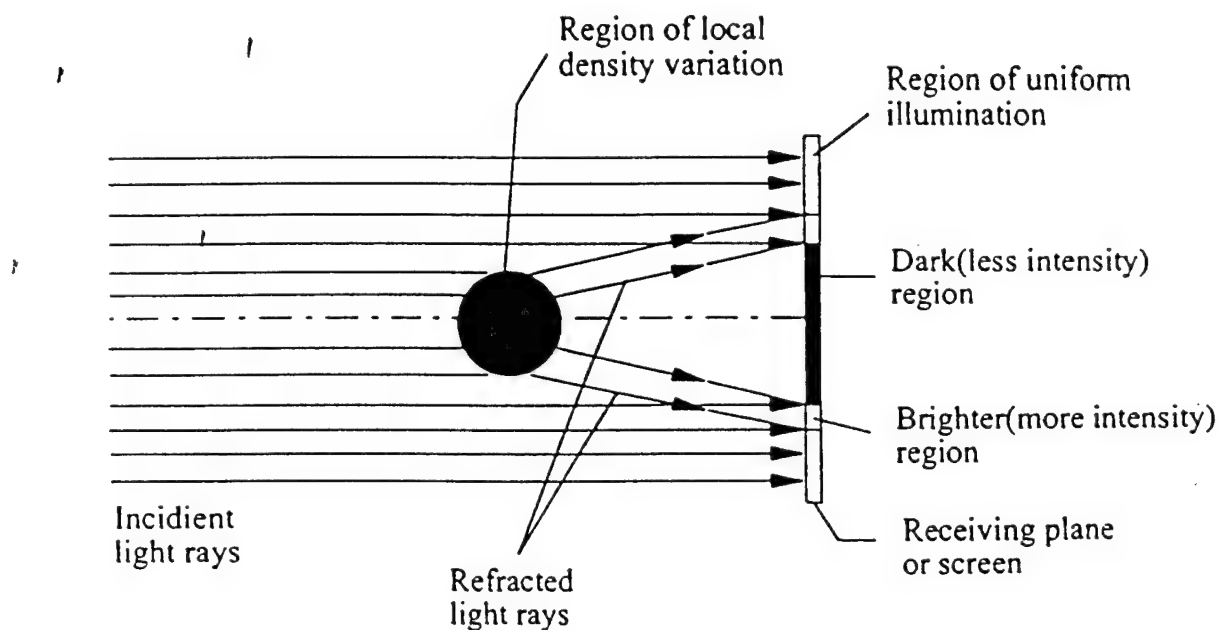


Figure 7.41: Refraction of light passing through a local density variation (Bagai *et al.* [1993]).

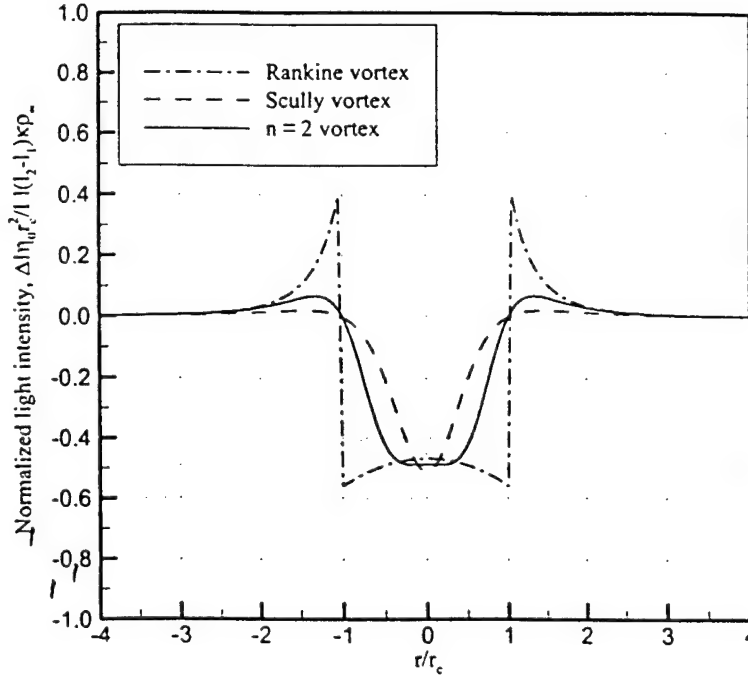


Figure 7.42: Computed light intensity for Rankine($n = \infty$), Scully($n = 1$) and $n = 2$ vortex models, $\lambda = 0.14$.

By substituting for density variation and its gradient for each of three vortex profiles in to Eq.(7.35), we obtain results of light intensity associated with each vortex models shown in Figure 7.42. In addition, by changing λ , the effect of circulation to the light intensity is shown in Figure 7.43.

7.6.4 Observations

Figure 7.39 shows that the fluid density within the vortex is significantly lower than the ambient density. Different vortex model yields considerably different value of vortex density profile. However, every vortex models gives the minimum density at the same position, the center of vortex, but different values. The Rankine vortex model has a lowest minimum density value.

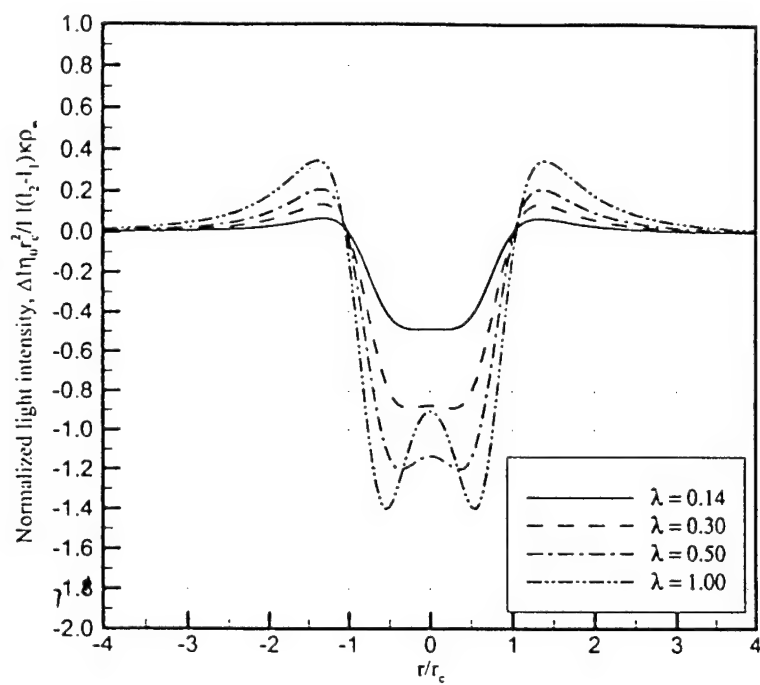


Figure 7.43: The effect of λ on the light intensity profile for $n = 2$ vortex model.

Since the density within a vortex is less than the ambient density, the incident light rays passing through the vortex are deflected outward radially. In Figure 7.40, increasing the value of λ (or the circulation) yields the fluid density decreasing. Due to the force balance between pressure gradient and centrifugal force, the more λ increases, the more density is reduced.

From Figure 7.42, there are both areas of negative and positive intensity within vortex in each case. The negative intensity values are recognized as regions of deficient light relative to ambient, whereas the positive intensity values are regions of brighter illumination. We see in Figure 7.42 that the negative intensity values are inside the core and the brighter intensity are the outside. Thus, the shadow or speckle of a vortex projected on the receiving screen consists of a dark central circular spot surrounded by a brighter periphery or halo.

As shown in Figure 7.43, within the core, the light intensity reduces and the value of λ goes up whereas the intensity outside the core increases as λ goes down. However, at $\lambda = 1$, the $n = 2$ vortex model yields a unique intensity distribution with a slightly more illumination (but it is still less than the ambient) around the vortex center. Thus, the peak or minimum illumination does not necessarily occur at the vortex center. Moreover, as λ increases, the regions of dark spot get slightly bigger than the vortex core radius. This increasing of dark regions should not be interpreted as the growth of the size of vortex core. Hence, theoretically, either the dimension of dark circular spot or the inner diameter of the bright halo is not necessarily equal to the dimension of vortex core.

7.7 Web-based Tip Vortex Database

A database for the rotary, fixed and oscillating-wing vortices has been setup on the Internet in order to integrate observations from various tests over decades. This knowledge base serves not only the purpose of a look-up table for vortex-data, but can be used to compare results from different configurations. This web site can be accessed at

www.ae.gatech.edu/research/windtunnel/vortorgn/vortorgn.html

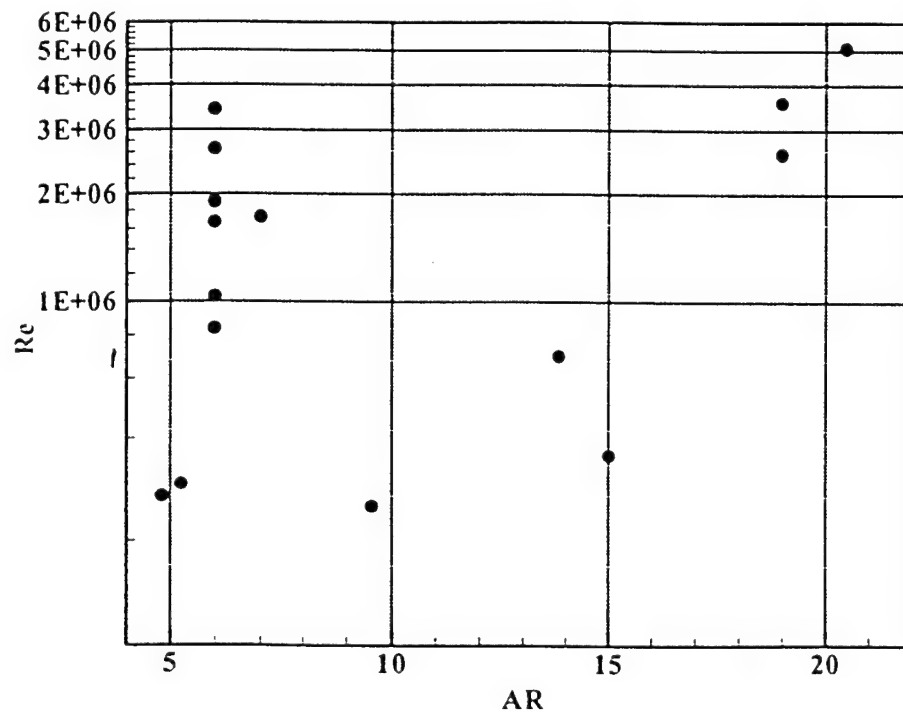


Figure 7.44: Range of aspect ratio and Reynolds number over which data exist.

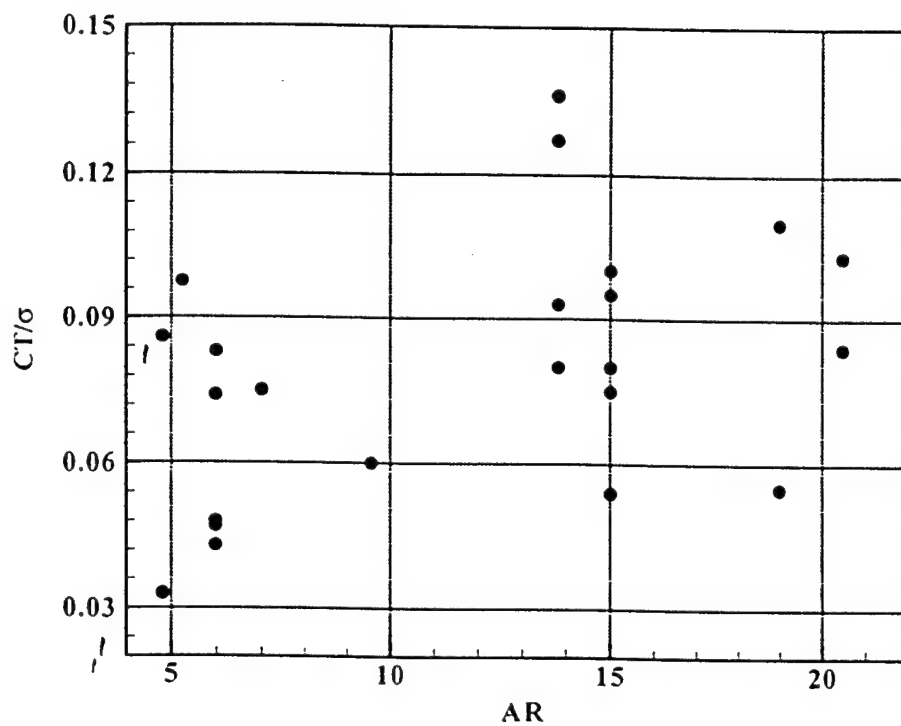


Figure 7.45: Range of aspect ratio and thrust coefficients over which data exist.

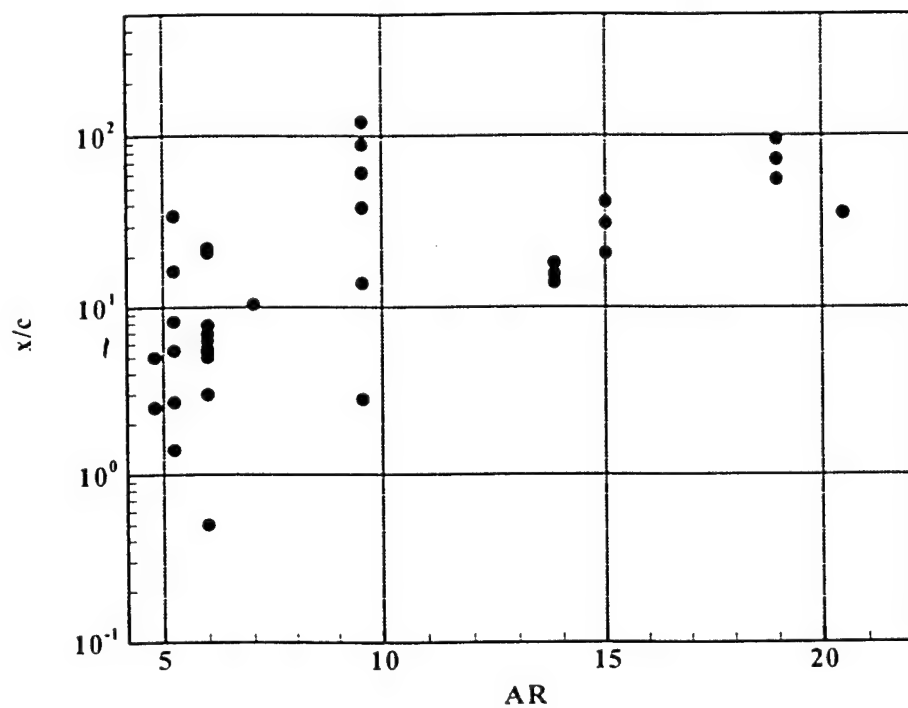


Figure 7.46: Range of aspect ratio and downstream distance over which data exist.

The database contains tabulated data for fixed, oscillating and rotary wings. As can be seen from the web site, there are a large number of tests on tip-vortices over a wide range of test-parameters. This is shown in Figure 7.44 - Figure 7.46 for four parameters, aspect ratio, Reynolds number, downstream distance from the trailing edge and thrust coefficient. Aspect ratios tested vary between 5 for model rotors to 20 for full-scale rotors. Tests have been conducted over an order of magnitude variation in Reynolds number. Data exists for downstream locations of the tip-vortex from fractions of chord lengths to hundreds of chord lengths behind the trailing edge. Thrust coefficients vary over an order of magnitude.

7.7.1 Correlation of Circulation Measurements from Several Rotary Wing Experiments

In spite of all these studies, there has been no success in developing general theoretical models for determining the tip-vortex characteristics from the basic loading parameters on the generating wing. An expression was developed to estimate the circulation contained in the tip-vortex in terms of the Reynolds number, aspect ratio and the geometric angle of attack of the generating wing. Circulation data from several researchers is then compared to this theoretical model.

There are several factors that effect the circulation of the tip vortex trailed from a wing or a rotor blade. Four primary factors that can be identified as having first order effects on core properties are the aspect ratio, Reynolds number, downstream distance and thrust coefficient. There are factors over which there might be lesser control, such as facility unsteadiness and measurement techniques.

In the following paragraphs, a derivation is presented for the strength of the tip-vortex in terms of tip Reynolds Number, aspect ratio and the geometric angle of attack of the rotor blade. Then the results of circulation measurements from several researchers are correlated with the estimated values obtained from the test conditions. The deviations of the experimental values from the estimated values stem from parameters not included in the derivation. These include deviations due to measurement techniques and facility unsteadiness as well as core decay.

Let Γ_v be the strength of the tip-vortex after roll-up is complete and let Γ_{max} be the maximum bound circulation on the rotor blade. Then, as a general case,

$$\tilde{A}_v = k \tilde{A}_{max}$$

Let the spanwise location on the rotor blade where the maximum bound circulation occurs be R^* . Then at $r = R^*$, Kutta-Joukowski theorem gives,

$$\tilde{n}U^* \tilde{A}_{max} = \frac{1}{2} \tilde{n}U^{*2} c^* C_l^*$$

where c^* is the chord length, V^* is the incoming velocity, C_l^* is the lift coefficient of the blade section at $r = R^*$. This results in an expression for the trailed vorticity in the vortex,

$$\tilde{A}_v = \frac{k}{2} (U^* c^*) (a^* \dot{a}^*)$$

where, a^* is the section lift curve slope, α^* is the section angle of attack. Letting $Re^* v = V^* c^*$, and absorbing $a^* k = k_1$,

$$\Gamma_v = \left(\frac{k_1}{2} \right) (Re^* v) (\alpha_g - \alpha_i)^*$$

where α_g is the geometric and α_i is the induced angle of attack. Now, if we make an assumption that the induced angle of attack is primarily due to the tip vortex and is of the form,

$$\alpha_i^* = \frac{V_i}{U^*}$$

and we assume most of the induced velocity is caused by the tip-vortex and use the span b as a characteristic length,

$$V_i = \frac{\Gamma_v}{k_2 b}$$

we can write,

$$\alpha_i^* = \frac{\Gamma_v}{k_2} \left(\frac{1}{ARRe^*v} \right)$$

Substituting this into the expression for the tip vortex strength, we get,

$$\Gamma_v = \left(\frac{k_1}{2} \right) (Re^*v) \left(\alpha_g - \frac{\Gamma_v}{k_2} \left(\frac{1}{ARRe^*v} \right) \right)^*$$

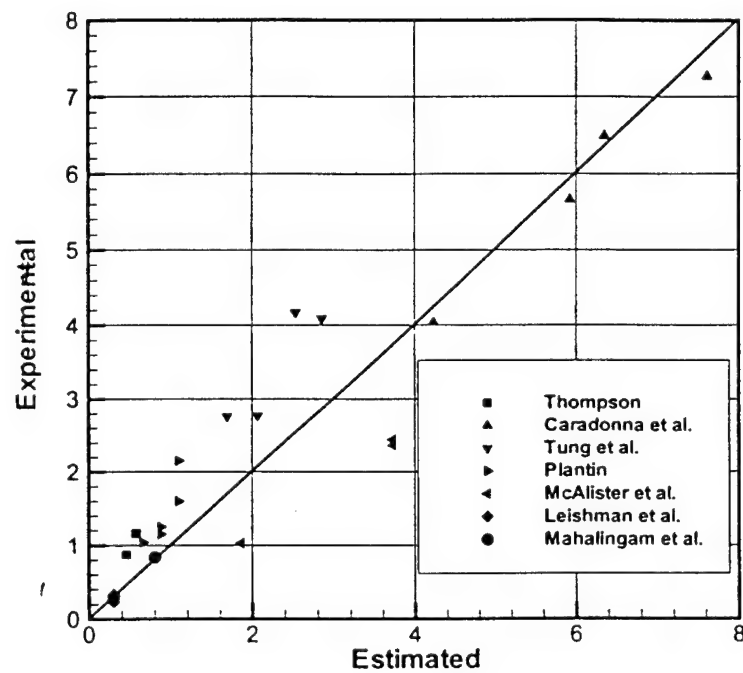
Simplifying this for the tip-vortex strength, and absorbing all the constants into two constants, K and K_1 , we get,

$$\Gamma_v = (K)(Re^*v)(\alpha_g^*) \frac{1}{1 + \frac{K_1}{AR}}$$

This expression indicates that the tip vortex circulation should be proportional to Re^*v , the geometric angle of attack and AR . The utility of this result is that the tip-vortex strength is related directly to the geometric angle of attack at an arbitrary rotor blade section. Re^* and section angle of attack can be easily replaced by an arbitrary factor multiplied by corresponding values at the tip and the factors can be absorbed into the constants. Thus the tip-vortex circulation is easily expressed in terms of Re , AR and geometric angle of attack.

This relation was used to estimate the circulation for several tests on rotary wings. Figure 7.47 shows the plot for the estimated circulation versus the measured values. The experimentally measured circulation values match closely with the estimated circulation. Significantly, it was found that data belonging to a particular test clumped together on one side of the theoretical line and did not scatter all over. The data available fits the above expression very well for values of $K = 1.24$ and $K_1 = 1$. Using this value of K , we obtain a value for k as, $k = \frac{2K}{a^*}$. This results in a value of $k = 0.395$. This implies that the circulation in the tip-vortex is only about 40% of the maximum bound circulation on the rotor-blade.

Thus, it is clear that for most rotor configurations, in hover as well as forward flight, the circulation contained in the tip-vortex core is about 40% of the maximum bound circulation on the rotor-blade. This value appears to be very small compared to standard models where the tip-vortex circulation is assumed to be equal to the maximum bound circulation. The reasons for



this can be attributed to the approximations in the calculation of the bound circulation distribution. The flow field the rotor blade operates in is highly unsteady, with a time varying freestream as well as inflow. Added to this is the complexity of the three-dimensional velocity field that exists over most of the rotor blade. The use of the Kutta-Joukowski theorem coupled with blade element theory is an over simplification of the flow occurring in a rotor blade. Thus, a rigorous analysis including unsteady and three-dimensional effects is necessary for the calculation of the blade bound circulation using inflow.

7.8 Summary

The experiments have shown that the vortex increases in strength and size during the formation process. This, coupled with secondary features observed in the velocity profiles, suggests that the formation process may be due to the rollup of discrete vortex filaments. This is precisely what is seen in the computations.

Chapter 8

Summary and Future Work

8.1 Summary

The helicopter rotor wake is among the most complex flow fields in aerodynamics, perhaps because the wake is fully three dimensional and unsteady. The rotor wake is composed of the tip-vortex and inboard sheets. The strong tip-vortex is by far the most dominant feature of the rotor wake and thus the main consideration in this work.

Owing to the rotation of the blade, the lift and the circulation are concentrated in the tip region. Moreover, the zero-pressure difference between upper and lower blade surfaces at the rotor tip requires that the bound circulation drop to zero at the tip. Therefore, the rate of the spanwise variation of the bound circulation is very high at the tip, causing the strong trailing vortices there to quickly roll up into a single tip-vortex. This strong tip-vortex has a great effect on the rotor performance. When a rotor blade encounters the tip vortex shed by the preceding blade, Blade-Vortex Interaction (BVI) will occur and BVI is the principal source of vibrations and noise.

This work has focused on the formation and downstream development of the tip-vortex for both fixed and rotary wings. The classical inviscid lifting-line and lifting-surface methods are applied locally near the wing tip to describe the origin of the tip vortex.

After a brief introduction to the panel method in Chapter 2, the case of the fixed wing was discussed in Chapter 3. First, we defined the asymptotic expansion of the solution for the bound circulation near the wingtip. It was shown in particular that to leading-order, in the tip region, the flow

over a fixed wing is equivalent to the flow over a semi-infinite wing and the bound circulation has an analytical solution obtained from that given by Stewartson [1960]. Next, a similar analysis was performed for the lifting-surface model of the semi-infinite wing based on the Schlichting-Thomas [1947] vortex-panel method model is formulated. The numerical results for the bound circulation were compared with the experimental data of McAlister and Takahashi [1991] and the comparison is fairly good. Results were also presented for the roll-up structure of the tip-vortex. It was shown that the tip-vortex develops downstream of the wing and its circulation approaches the peak bound circulation value asymptotically. The computed induced-vertical velocity was compared with the experimental data of McAlister and Takahashi [1991] and the comparison is encouraging. No turbulence model is necessary despite the fact that for the Reynolds numbers of the experiment, the flow would be expected to be turbulent.

The major difference between the fixed and rotary-wing wake is the wake geometry. For a fixed wing, the wake convects downstream and away from the generating wing. However, the shed vortices from a rotary wing stay in the vicinity of the rotor blades for a few revolutions and significantly affect the distribution of the bound circulation on the rotor blade. Thus, the shed-vorticity field near a rotary wing-tip is considerably different from that for a fixed wing. This difference was discussed in Chapter 4.

In Chapter 4, it was shown that to leading-order, the flow near the tip of a large aspect ratio rotary wing is equivalent to the flow past a semi-infinite wing. The leading-order inner solution for the bound circulation is similar to that for the fixed wing, except that there is a parameter involved that is dependent on the geometric angle of attack, the aspect ratio and the number of blades. The lifting-surface model was used to represent the tip region of the rotary wing and the roll-up process of the trailing vortices was treated. The formation and downstream development of the rotor tip-vortex was described. It was found that the tip-vortex does not roll up completely at the trailing edge of the rotor blade as assumed in many wake models; instead, the circulation develops downstream and approaches the peak bound-circulation value asymptotically. It was also found that the fixed wing tip-vortex develops more quickly than the rotor tip-vortex and this is due to the steeper gradient of the bound circulation for the rotary wing.

It is observed that the rotor wake is not a perfect helix. The rotor wake is fully contracted within about one rotor radius below the rotor tip-path plane. In Chapter 5, two wake models were applied to consider the effects of

the rotor-wake contraction on the bound circulation. First, a crude vortex-cylinder model was applied to represent the rotor-wake contraction and the resulting bound circulations compared surprisingly well with Caradonna and Tung [1981]. Then a discrete vortex-ring model was used to represent the rotor wake and its results for the wake slipstream compare well with Landgrebe's [1972] formula.

Preliminary boundary layer calculations were made and these calculations are described in Chapter 6.

Laser velocimetry measurements were conducted on the wake of a two bladed teetering rotor in forward flight to gain an understanding of both the vortex formation process and how the vortex properties evolve into the near wake. These experiments are described in Chapter 7. Circumferential velocity profiles of the vortex during the formation process were first observed at a chordwise location of 0.47. In the early stages, outside of the vortex core, the typical $1/r$ decay is not present. Due to asymmetry, velocity profiles along the horizontal and vertical directions were examined. Peak circumferential velocity and core size were determined from these profiles. These values were averaged to gain a general idea of the vortex behavior. The vortex increases in strength and size during the formation process. This, coupled with secondary features observed in the velocity profiles, suggests that the formation process may be due to the rollup of discrete vortex filaments.

The axial velocity in several regions in the vortex core approached 96% of the tip speed. In some planes, especially those near the trailing edge, the region of high axial velocity is much larger than the blade thickness. This clearly shows that it is the fluid velocity being measured. As the planes get closer to the leading edge, the region of high axial velocity approaches the size as the blade thickness. In these planes it not clear what is the fluid and what is the blade since the exact location of the blade is not known. Planned experiments and a numerical code will be used to determine the exact location of the blade.

Measurements of the near wake show a distinct periodic pattern in the evolution of the peak core axial velocities. The Strouhal Number based on this period, tip speed and blade tip thickness is 0.16. This suggests that it is caused by a shedding phenomenon. Comparison with a turbulent Lamb vortex shows that the expected decay of the circumferential velocity is significantly faster than the measured decay rate. Furthermore, measurements in the core axial velocity also show no evidence of turbulent within the core.

The dynamics of LV seed particles entrained in a 2D vortex were simulated

numerically to determine an upper bound on errors associated with particle "spinout". For a vortex representative of that found in these experiments, errors in the circumferential velocity up to 8% for the largest particle size were estimated. The rotation of the fluid also imparted a radial velocity up to 20% of the circumferential velocity. Comparison with the measured core size shows that the seed particle spinout predictions are extremely conservative. Based on the comparison with measured vortex size, it is seen that the actual magnitude of error in the core tangential velocity due to seed particle spinout is negligible.

Stokes drag predictions used for the simulations underestimated the drag acting on the particles near the edge of the core; the velocity error and particle trajectories are therefore conservative estimates. Predictions of seed particle dynamics for rotor tip vortices should also incorporate the substantial effects of core axial velocity, and proper models for particle drag appropriate for the actual Reynolds number range.

Flow diagnostic techniques utilizing changes in the index of refraction of the fluid such as shadowgraphy and scintillameters might be used to efficiently determine vortex strength and observe structures within the vortex. A relationship between the flow properties and the intensity of light passing through must be known, however. A simple analytical model to establish the relationship between density gradient and intensity was developed for a three-dimensional compressible viscous vortex. This model could enable the use of these techniques for efficient measurement of the vortex properties and structure.

Rotary wing circulation measurements from several researchers were correlated. An expression for the core circulation was obtained in terms of AR , Re and geometric angle of attack. The experimental core circulation values match the prediction well. A significant fact is that data taken in a particular test always clump together and are not scattered around the theoretical value. Furthermore, the expression implies that the circulation in the tip-vortex is only about 40% of the maximum bound circulation on the rotor-blade. The reason for the discrepancy between the calculations and the experiments is unknown.

The primary results and major accomplishments of this work are

- A lifting surface code for a semi-infinite three-dimensional fixed and rotary wing has been developed for use as the inner solution at the wing tip and the formation of the vortex has been described by rollover

of vortex filaments near the wing tip.

- An analytical lifting-line analysis for the semi-infinite fixed wing has been compared with the full lifting surface code and the results are very good.
- The analytical lifting surface code results for the development of the tip vortex shed by both fixed and rotary wings have been compared with experiment and the results are encouraging.
- The calculations show that the circulation of the tip-vortex is about 80 – 90% of the maximum bound circulation in hover and the tip-vortex is formed within one revolution. The experiments suggest that the circulation is $\sim 40\%$ of the maximum bound circulation in low-speed forward flight. The reason for the large discrepancy is unknown.
- Experimental data obtained in the last few decades by researchers all over the world has been correlated.
- An internet database has been setup where results from several fixed-, rotary- and oscillating- wing tests have been tabulated.
- Circulation measurements from this database have been correlated with an expression developed for trailed circulation in the vortex in terms of geometric angle of attack and aspect ratio.
- Laser velocimetry has been performed near the blade tip on the advancing side of a 2-bladed rotor in forward flight in the Harper Wind Tunnel. Vortex trajectories over the blade tip, as well as velocity fields in the vortex formation region have been obtained from these measurements.
- The experiments have shown that the vortex increases in strength and size during the formation process. This, coupled with secondary features observed in the velocity profiles, suggests that the formation process may be due to the rollup of discrete vortex filaments. This is precisely what is seen in the computations.
- Laser velocimetry was also used to obtain velocity data in the very near wake of the rotor blade in a fixed wing configuration. These are

intended to serve as direct comparisons to the rotary wing data under the same free-stream turbulence levels.

- Axial velocity values within the vortex can reach 96% of the tip speed.

8.2 Future Work

The following are some suggestions for future work that can be built on the present work.

1. A further step on this work would be to include more realistic wing geometry. In the current work, only the rectangular, zero thickness wing is considered. However, as shown in Srinivasan *et al* [1993], the wing planform has a significant effect on the distribution of the bound circulation. Correspondingly, the downstream development of the core radius and the circulation of the tip-vortex will be changed. To deal with different wing configurations, the distribution of the horseshoe panels needs to be adjusted.
2. Another addition to the this work would be to consider the effect of viscosity on the formation of the tip-vortex. A boundary-layer solution in the tip region might be introduced into the current potential-flow model. The current potential-flow solution on the wing surface in the tip region can be taken as the outer-flow condition of the boundary layer and the set of the three-dimensional boundary-layer equations solved numerically. By taking account of the viscous effect, the core radius, the axial flow in the viscous core and the position of the flow separation on the wing surface can be obtained. In addition, it is believed that viscosity is a factor in determining the axial velocity in the core of the vortex.
3. The numerical calculations can easily be extended to forward-flight and this is currently being done.

Appendix A

Papers, Presentations, and Degrees Awarded

Archival Papers

A. T. Conlisk, "The Vortex Dynamics of Rotor Wakes", to appear *The International Journal of Computational Fluid Dynamics*, 2000.

Hui Li, O. R. Burggraf, and A. T. Conlisk, "On the Formation of a Rotor Tip-Vortex", submitted to *J. Aircraft*.

A. T. Conlisk, "Modern Helicopter Rotor Aerodynamics", to appear in *Progress in Aerospace Sciences*.

Conference Papers

A. T. Conlisk, "The Fluid Dynamics of Rotor Wakes: Theory, Computation and Experiment", 29th Fluid Dynamics Conference, Norfolk, VA, June 1999(Invited).

Hui Li, O. R. Burggraf and A. T. Conlisk, "On the Formation of a Tip-Vortex", paper 2000-0282, 38th AIAA Aerospace Sciences Meeting, Reno, Nev., January 2000.

Mahalingam, R., Wong, O.D., Komerath, N.M., "Experiments on the Origins of Tip-Vortices", AIAA Paper 2000-0278, 38th Aerospace Sciences Meeting and Exhibit, Reno, NV, Jan. 2000.

Hui Li, O. R. Burggraf and A. T. Conlisk, "On the Formation of a Rotor Tip-Vortex", American Helicopter Society Aeromechanics Specialists' Meeting, Atlanta, Georgia, November 13, 14, 2000.

Wong, O.D., Mahalingam, R., Tongchitpakdee, C., Komerath, N.M., "The Near Wake Of A 2-Bladed Rotor In Forward Flight", AHS Aeromechanics Specialists Meeting, Atlanta, GA, Nov. 2000.

Wong, O.D., Komerath, N.M., "Tip Vortex Formation and Evolution to the Near Wake of a Rotor in Forward Flight", AHS 57th Annual Forum, Washington, DC, May 2001.

Kini, S., Godavarty, V., and Conlisk, A.T., "Comparison of Two Distinct Models of Rotor Wakes with Experiment", submitted to the 40th AIAA Aerospace Sciences Meeting and Exhibit, 2002.

Presentations

Hui Li, Ning Mei, O. R. Burggraf and **A. T. Conlisk**, "The Formation of a Rotor Tip-Vortex", American Physical Society Division of Fluid Dynamics Meeting, November 21-23, 1999, New Orleans, La.

Degrees Awarded

R. Mahalingam, PhDAE, June 1999, GT.

Hui Li, MSME, June 2000, OSU

Santosh Kini, MSME August 2001, OSU(partial support)

Oliver Wong, PhD, GT(partial support)

Chanin Tongchitpakdee, MSAE, GT(partial support)

Technology Transfer

Discussions with Al Egolf of Sikorsky are ongoing in attempts to acquire a copy of GENHEL to incorporate the results described in this report.

Modeling of Vortex-Airframe Interaction, November 12, 1999, Sikorsky Aircraft Corporation, Stratford, Connecticut. Including a discussion of tip-vortex formation.

Appendix B

Lifting-line Theory for a Multi-bladed Rotor in Hover for the Untwisted Rectangular Blade

Burggraf[1999] applied the concepts of Prandtl's lifting-line theory to formulate and solve the corresponding integro-differential equation for a helicopter rotor operating in the hover condition. In Prandtl's theory, the high aspect-ratio wing is represented by a line vortex (the bound vortex) and the aerodynamic properties of each spanwise section are approximated locally by the two-dimensional characteristics from linearized airfoil theory. However, the free stream of the local section is replaced by the relative wind, i.e., the effective angle of attack is the geometric angle of attack reduced by the local downwash induced by the trailing vortices.

For the case of the rotor blade in hover, two modifications must be made:

- (1) the "free stream" of Prandtl's theory is replaced by the angular velocity of rotation of the blade, and
- (2) the trailing vortices follow a more-or-less helical path.

Consistent with the variation of bound circulation across the span, vortices are shed all across the rotor, forming an approximately cylindrical slipstream filled with concentric helical vortices. To simplify the analysis, we approximate these discrete helical vortices by uniform cylindrical sheets of

vorticity, corresponding to an assumption of a lightly-loaded rotor. For purposes of computing the downwash, these elemental vortex cylinders may be viewed as composed of vortex rings, whose strength is approximately constant on each cylinder. The axial component of the helical vortices may be ignored, since it does not contribute to the downwash.

B.1 Derivation of the Integral Equation

A cylindrical coordinate system (r, θ, z) is convenient, where r is the radial coordinate, θ the azimuthal coordinate, z the axial coordinate, and a represents the radius of the rotor (see figure 4.1).

We have shown previously that a semi-infinite cylinder of radius r' composed of vortex rings of constant circulation per unit length γ_θ induces the vertical velocity

$$v_z(r) = \begin{cases} \gamma_\theta/2 & \text{for } r < r' \\ \gamma_\theta/4 & \text{for } r = r' \\ 0 & \text{for } r > r' \end{cases} \quad (\text{B.1})$$

Now these elemental vortex-ring cylinders, formed from the inboard vortex sheet, are superposed with the vortex cylinder generated by the tip vortex to form the complete rotor slipstream. Since the downwash at radius r in the rotor plane is induced only by those cylinders of larger radius, the net downwash is given by

$$v_z(r) = \frac{1}{2} \int_r^a \gamma_{\theta i}(r') dr' + \frac{1}{2} \gamma_{\theta t} \quad (\text{B.2})$$

where the subscripts i and t refer to the inboard vortex sheet and to the tip vortex, respectively.

The circulation per unit length γ_θ is estimated by smearing out each successive loop of the vortex helix over the distance it advances in one turn of the rotor. The time for one revolution is $2\pi/\Omega$, where Ω is the angular velocity of the rotor. The distance the vortex at radius r is swept downward in one rotor revolution is then $2\pi v_z/\Omega$. Let Γ be the value of the bound circulation along the rotor. Then the strength of the shed circulation per unit length along the rotor is $-d\Gamma/dr$, and hence the vorticity of the cylindrical sheet at radius r for n blades is

$$\gamma_\theta(r) = -\frac{n\Omega}{2\pi v_z(r)} \frac{d\Gamma}{dr} \quad (\text{B.3})$$

The tip-vortex is translated downward only by its own self-induced downwash, since the interior vortex cylinders do not induce downwash at the tip. The downwash induced by a vortex cylinder at its own radius is only half that induced at interior points, so that from Eq.(B.1) the downwash at the tip is just $\gamma_{\theta t}/4$. Hence one loop of the tip vortex winds a distance downward

$$\Delta_z = 2\pi v_z(a)/\Omega = \pi\gamma_{\theta t}/2\Omega$$

and so the strength of the tip vortex cylinder for n blades, corresponding to the circulation Γ_t at the tip for each blade, is just

$$\gamma_{\theta t} = n\Gamma_t/\Delta_z = 2n\Gamma_t\Omega/\pi\gamma_{\theta t}$$

Solving for $\gamma_{\theta t}$ gives the result

$$\gamma_{\theta t} = \sqrt{\frac{2n}{\pi}\Gamma_t\Omega} \quad (\text{B.4})$$

The bound circulation Γ is related to the downwash velocity v_z through the airfoil section properties. From two-dimensional linearized airfoil theory, the lift coefficient is given by

$$C_l = m\alpha_e$$

where m has the value 2π for a flat-plate airfoil, and has slightly different values for airfoils with thickness (for airfoils with camber, a bias shift must be included). We use the flat-plate value, and then find for the circulator

$$\Gamma = \pi u_\infty c \alpha_e$$

where u_∞ is replaced by Ωr for the rotor in hover, and α_e is the effective angle of attack

$$\alpha_e = \alpha_o - \frac{v_z}{\Omega r}$$

Here α_o is the geometric angle of attack of the airfoil section. Combining these results gives

$$\Gamma(r) = \pi\Omega c [\alpha_o r - \frac{1}{\Omega}v_z(r)] \quad (\text{B.5})$$

For simplicity, we now assume both chord c and geometric angle of attack α_o constant across the blade radius. Then from Eq.(B.3), the vorticity of the inboard vortex cylinders is given by

$$\gamma_\theta(r) = -\frac{n\Omega^2 c}{2v_z(r)} [\alpha_o - \frac{1}{\Omega} \frac{dv_z}{dr}] \quad (\text{B.6})$$

Substituting this expression for γ_θ into Eq.(B.2) yields the integro-differential equation for the induced downwash:

$$v_z(r) = -\frac{n\Omega^2 c}{4} \int_r^a \left[\alpha_o - \frac{1}{\Omega} \frac{dv_z(r')}{dr'} \right] \frac{dr'}{v_z(r')} + \sqrt{\frac{n\Gamma_t \Omega}{2\pi}} \quad (\text{B.7})$$

Here Γ_t is given in terms of v_z at the tip by Eq.(B.5).

The simplicity of the solution may be more easily recognized by use of the following non-dimensional variables. Let

$$R = \frac{r}{a}, \quad W(R) = \frac{v_z(r)}{\Omega a \alpha_o}, \quad \lambda = \frac{\alpha_o}{n} \cdot \frac{a}{c} \quad (\text{B.8})$$

Then with Γ_t evaluated as $\Gamma(a)$ from Eq.(B.5), Eq.(B.7) takes the simpler form

$$W(R) = -\frac{1}{4\lambda} \int_R^1 \left[1 - \frac{dW(R')}{dR'} \right] \frac{dR'}{W(R')} + \sqrt{\frac{1}{2\lambda} [1 - W(1)]} \quad (\text{B.9})$$

It is clear from Eq.(B.9) that the solution for the downwash function W depends on the radius function R and only the one aspect-ratio parameter λ .

B.2 Solution of the Integral Equation

The integro-differential equation may be converted to an ordinary differential equation simply by differentiating term-by-term, as

$$\frac{dW}{dR} = \frac{1}{4\lambda W(R)} \left[1 - \frac{dW}{dR} \right]$$

Collecting terms in dW/dR , the nonlinear equation is reconfigured into standard form:

$$[1 + 4\lambda W(R)] \frac{dW}{dR} = 1 \quad (\text{B.10})$$

In this revised form the solution is found easily, by integrating term-by-term:

$$W(R) = \frac{1}{4\lambda} \left[\pm \sqrt{1 + 8\lambda(R + K)} - 1 \right]$$

This form of $W(R)$ satisfies the integral equation (B.9) if and only if the constant of integration K is zero. Choosing the sign of the radical to require positive downwash (positive lift), the solution of the integral equation becomes¹

$$W(R) = \frac{1}{4\lambda} [\sqrt{1 + 8\lambda R} - 1] \quad (\text{B.11})$$

The corresponding circulation distribution for an individual blade is obtained from Eq.(B.5):

$$\frac{\Gamma}{\Omega a \alpha_o} = \pi c [R - W(R)] \quad (\text{B.12})$$

¹If the negative sign is chosen, the downwash is negative everywhere in $0 < R < 1$.

Appendix C

The Velocity Induced by a Rotor Wake Modelled as a Discrete Distribution of Vortex Rings

In this appendix, Burggraf's discrete vortex ring model is illustrated.

C.1 The Elementary Vortex Ring

The rotor slipstream is formed from the aggregate of more-or-less helical trailing vortices shed by the rotor. The continuous distribution of these "helical" trailing vortices across the rotor forms a screwlike surface winding down below the rotor. It is possible to fit a rotationally symmetrical surface, to the space curve traced out on this screw surface by a single trailing vortex. We shall refer to this individual rotationally symmetric surface as an elemental slipstream surface, and denote it by S_m which is shown on Figure 5.4.

We take a cylindrical-polar coordinate system with z the distance measured along the axis of the cylinder, r the radius, and θ the azimuthal angle. The origin is located in the plane of the rotor.

The circulation of the vortex Γ' may be resolved into axial and azimuthal components. The axial vorticity induces an azimuthal flow, and the azimuthal vorticity induce radial and axial flow. Since the downwash is small compared with the rotational speed of the rotor (except near the hub), we

shall neglect the axial component, treating each loop of the trailing vortex as a discrete ring vortex.

Now we calculate the induced downwash of the rotor wake modelled by such a distribution of vortex rings. We first consider the velocity at a point $P(r, z)$, in cylindrical coordinates, induced by an elementary vortex ring of radius a_{mk} . The axis of the ring is the axis of rotation of the rotor. The ring under consideration is located a distance z_{mk} below the rotor disk, which lies in the plane $z = 0$. The axial velocity induced by this elementary ring vortex of circulation Γ_m' is given in terms of elliptic integrals in the form*

$$u_{mk}(r, z) = -\frac{\Gamma_m}{2\pi r} \frac{z - z_{mk}}{\sqrt{(r + a_{mk})^2 + (z - z_{mk})^2 + \mu^2}} \left\{ K(k_{mk}) - \left[1 + \frac{2a_{mk}r}{(r - a_{mk})^2 + (z - z_{mk})^2 + \mu^2} \right] E(k_{mk}) \right\} \quad (C.1)$$

$$w_{mk}(r, z) = \frac{\Gamma_m'}{2\pi} \frac{1}{\sqrt{(r + a_{mk})^2 + (z - z_{mk})^2 + \mu^2}} \left\{ K(k_{mk}) + \left[\frac{2a_{mk}(a_{mk} - r)}{(r - a_{mk})^2 + (z - z_{mk})^2 + \mu^2} - 1 \right] E(k_{mk}) \right\} \quad (C.2)$$

where μ is the vortex cut-off parameter and k , the modulus of the elliptic integrals, is given by

$$k_{mk}^2 = \frac{4a_{mk}r}{(r + a_{mk})^2 + (z - z_{mk})^2 + \mu^2} \quad (C.3)$$

The complete slipstream surface S_m is accounted for by summing the induced velocity for all the vortex loops, $k = 1$ to K , from the rotor disk to downstream infinity. It should be noted that the circulation Γ_m' is the same for each of the vortex rings on S_m , but the radius a_{mk} of the vortex rings on S_m varies with distance below the rotor plane; i.e., a_{mk} varies with k for fixed m . The complete rotor slipstream is then modelled from hub to rotor tip as a discrete set of such elemental slipstream surfaces, $m = 0$ to M . In addition the final contracted slipstream for large z will be represented by a continuous distribution of vortex rings along a semi-infinite cylindrical surface.

*See Küchemann, D., and Weber, J., *Aerodynamics of Propulsion*, McGraw-Hill Book Co., 1953. The derivation has been modified to include the effect of the artificial cut-off parameter μ .

C.2 The Strength and Location of the Trailing Vortices

The trailing vortices arise because of variation of the bound circulation of the rotor blade. The simplest model would be to represent the bound circulation by a piecewise constant distribution of vortices $\Gamma_m, m = 1$ to M , with each constant element of bound circulation continued into the wake with a pair of trailing vortices; i.e., a set of "horseshoe vortices." Thus the vortex rings on the innermost elemental slipstream surface S_0 have the circulation

$$\Gamma'_0 = -\Gamma_1 \quad (C.4)$$

while for the outermost surface S_M

$$\Gamma'_M = \Gamma_M \quad (C.5)$$

and for the intermediate surfaces $S_m, m = 1$ to $M - 1$, the values are

$$\Gamma'_m = \Gamma_m - \Gamma_{m+1} \quad (C.6)$$

If we represent each loop of the trailing vortex by its own vortex ring, then the rings are not uniformly spaced, owing to the variation of the induced downwash velocity with distance below the rotor disk. Let w_{mk} be the downwash velocity at the k th vortex ring on the m th elemental slipstream surface S_m . For each complete rotation of an n -bladed rotor, there are n new vortex loops generated. In that time points on a vortex loop will be translated downward a distance $2\pi w/\Omega$, where Ω is the angular velocity of the rotor. Hence for closely-spaced rings in steady flow the distance between successive vortex rings is

$$z_{m,k+1} - z_{mk} = \frac{2\pi}{n\Omega} w_m \quad (C.7)$$

Again for steady flow the elemental slipstream surfaces correspond to the streamlines of the flow. Thus

$$\frac{dr}{dz} = \frac{u}{w}$$

For closely spaced rings we have

$$r_{m,k+1} - r_{mk} = \frac{2\pi}{n\Omega} u_m \quad (C.8)$$

equation (C.7) and (C.8) are solved using Runge-Kutta method.

C.3 The Asymptotic Slipstream

An accurate representation of the rotor slipstream, as described above, would require a very large number of vortex rings. We may estimate the truncation error for M rings on a single elemental slipstream by approximating the discrete rings by a continuous distribution of azimuthal vorticity along a circular cylinder. The corresponding induced velocity is given below. Thus if w_∞ is the downwash induced at the rotor by a semi-infinite vortex cylinder, a cylinder of large but finite length L and radius a will induce downwash at the rotor in the amount

$$w \approx w_\infty \left(1 - \frac{a^2}{2L^2} + \dots\right)$$

Thus for one percent accuracy, the vortex rings must extend to at least seven radii below the rotor disk.

To improve accuracy, we shall include vortex rings to a distance L below the rotor disk, but then extend the slipstream from that point to infinity by a continuous distribution of azimuthal vorticity wound around a semi-infinite cylinder. The linear density of vorticity along the cylinder is denoted as γ'_m , which is equivalent to $\Gamma'_m/\Delta z$.

A semi-infinite cylindrical distribution of μ -vortices of the ring type induce the axial and radial velocity components are given by Burggraf [1999]

$$\bar{u}_m(r, z) = -\frac{\gamma'_m}{2\pi r} \sqrt{(r + \bar{a}_m)^2 + (z - \bar{z}_m)^2 + \mu^2} \left[\frac{r^2 + \bar{a}_m^2 + (z - \bar{z}_m)^2 + \mu^2}{(r + \bar{a}_m)^2 + (z - \bar{z}_m)^2 + \mu^2} K(\bar{k}_m) - E(\bar{k}_m) \right] \quad (\text{C.9})$$

$$\begin{aligned} \bar{w}_m(r, z) = & \frac{\gamma'_m}{4} \left\{ \left[1 + \frac{\bar{a}_m^2 - r^2 - \mu^2}{\sqrt{(r^2 + \bar{a}_m^2 + \mu^2)^2 - 4\bar{a}_m^2 r^2}} \right] \right. \\ & + \frac{2}{\pi} \frac{z - \bar{z}_m}{\sqrt{(r + \bar{a}_m)^2 + (z - \bar{z}_m)^2 + \mu^2}} \\ & \times \left. \left[K(\bar{k}_m) + \frac{\bar{a}_m^2 - r^2 - \mu^2}{(r + \bar{a}_m)^2 + \mu^2} \Pi(\bar{\sigma}_m^2, \bar{k}_m) \right] \right\} \quad (\text{C.10}) \end{aligned}$$

Here \bar{a}_m represents the final radius of the m th elemental slipstream surface, and \bar{z}_m is the distance below the rotor disk at which the vortex cylinder begins, say at a distance

$$\bar{z}_m = z_{mK} + \frac{1}{2} \Delta z$$

where z_{mK} is the z -location of the last vortex ring and Δz represents the final spacing of the ring vortices, $\Delta z = (z_{mK} - z_{m,K-1})$. The elliptic-integral parameters of Eqs. (C.9) and (C.10) are defined as

$$\bar{k}_m^2 = \frac{4\bar{a}_m r}{(r + \bar{a}_m)^2 + (z - \bar{z}_m)^2 + \mu^2} \quad (\text{C.11})$$

$$\bar{\sigma}_m^2 = \frac{4\bar{a}_m r}{(r + \bar{a}_m)^2 + \mu^2} \quad (\text{C.12})$$

Bibliography

- [1993] Bagai, A., Moedersheim, E.P., Leishman, J.G., "Developments in the Visualization of Rotor Wakes Using the Wide-Field Shadowgraph Method", *Experimental and Numerical Flow Visualization*, vol. 172, pp. 149 - 163, 1993.
- [1964] Batchelor, G. K., "Axial Flow in Trailing Line Vortices", *Journal of Fluid Mechanics*, vol. 20, part 4, pp. 645-658, 1964.
- [1980] Berry, John, D. and Mineck, R. E., "Wind Tunnel Test of an Articulated Helicopter Rotor Model with Several Tip-Shapes", NASA TM 80080, 1980.
- [1998] Bhagwat, M. J., and Leishman, J. G., "On the Relationship between Blade Circulation and Tip Vortex Characteristics", 54th Annual Forum of the American Helicopter Society, May, 1998.
- [1972] Boatwright, D. W., "Measurements of Velocity Components in the Wake of a Full-Scale Helicopter Rotor in Hover", USAAMRDL TR 72-33, 1972.
- [1989] Brand, A.G., Komerath, N.M., and McMahon, H.M., "Results from the Laser Sheet Visualization of an Incompressible Vortex Wake", *Journal of Aircraft*, vol. 26, no. 5, pp. 438-443, May 1989.
- [1990] Brand, A.G., McMahon, H.M., and Komerath, N.M. "Correlations of Rotor/Wake - Airframe Interactions with Flow Visualization Data", *Journal of the American Helicopter Society*, vol. 35, no. 4, pp. 4-15, October 1990.
- [1973] Brown, C. E., "Aerodynamics of Wake Vortices", AIAA J., vol. 11, no. 4, pp. 531-536, April, 1973.

- [1999] Burggraf, O. R., "Lifting-line Theory for a Rotor in Hover", notes, 1997.
- [1999] Burggraf, O. R., Private Communication, 1999.
- [1997] Caradonna, F., Henley, E., Silva, M., Huang, S., Komerath, N.M., Reddy, U., Mahalingam, R., Funk, R., Wong, O., Ames, R., Darden, L., Villareal, L., Gregory, J., "An Experimental Study of a Rotor in Axial Flight". AHS Specialists' Meeting on Rotorcraft Aerodynamics and Aeroacoustics, Williamsburg, VA, October 1997.
- [1999] Caradonna, F., Henley, E., Silva, M., Huang, S., Komerath, N.M., Reddy, U., Mahalingam, R., Funk, R., Wong, O., Ames, R., Darden, L., Villareal, L., Gregory, J., "Performance Measurements and Wake Characteristics of a Model Rotor in Axial Flight", *AHS Journal*, Oct. 1999.
- [1981] Caradonna, F. X. and Tung, C., "Experimental and Analytical Studies of a Model Helicopter Rotor in Hover", NASA Technical Memorandum 81232, September, 1981.
- [1992] Caradonna, F. X., "The Application of CFD to Rotary Wing Aircraft", NASA Technical Memorandum 102803, 1992.
- [1971] Chigier, N. A. and Corsiglia, V. R., "Tip Vortices - Velocity Distributions", 27th Annual National Forum of the American Helicopter Society, May 1971.
- [1999] Christopher M. H. and Lyle, N. L., "Higher-Order Accurate Simulations of Wake and Tip Vortex Flowfields", *Proceedings of the 55th Annual Forum of the American Helicopter Society*, pp. 1984-1997, May, 1999.
- [1997] Conlisk, A. T., "Modern Helicopter Aerodynamics", *Annual Review of Fluid Mechanics*, vol. 29, pp. 515-567, 1997.
- [1972] Cook, C. V., "The Structure of the Rotor Blade Tip Vortex", AGARD Conference Proceedings No. 111 on Aerodynamics of Rotary Wings, AGARD CP 111, 1972.
- [1995] Dacles-Mariani, Jennifer, R. S., Kwak, D. and Zilliac, G., "A Computational Study of Wingtip Vortex Flowfield", AIAA 93-3010, 1995.

- [1996] Devenport, W. J., Rife, M. C., Liapis, S. I. and Follin, G. J., "The Structure and Development of a Wing-tip Vortex", *Journal of Fluid Mechanics*, vol. 312, pp. 67-106, 1996.
- [1979] Dring, R.P., Casper, J.R., Suo, M., "Particle Trajectories in Turbine Cascades", *Journal of Energy*, vol. 3, no. 3, pp. 161-6, May-June 1979.
- [1982] Dring, R.P., "Sizing Criteria for Laser Anemometry Particles", *Journal of Fluids Engineering*, vol. 104, pp. 15-17, March 1982.
- [1978] Dring, R.P., Suo, M., "Particle Trajectories in Swirling Flows", *Journal of Energy*, vol. 2, no. 4, pp. 232-237, July-August 1978.
- [1971] Dwyer, H.A. and McCroskey, W.J., "Crossflow and Unsteady Boundary-Layer Effects on Rotating Blades", *AIAA J.*, Vol. 9, no. 8, pp. 1498-1505, 1971.
- [1953] Escudier, "Vortex Breakdown: Observations and Explanations", *Progress in Aerospace Sciences*, vol. 25, pp. 189, 1953.
- [1950] Fogarty, L.E. and Sears, W.R., "Potential Flow Around Rotating Advancing Cylindrical Blade", *J. Aero. Sci.*, Vol. 17, no. 9, pp. 599, 1950.
- [1951] Fogarty, L.E., "The Laminar Boundary Layer on Rotating Blade", *J. Aero. Sci.*, Vol. 18, no. 4, Apr 1951 pp. 247-252, 1951.
- [1978] Francis, Michael S. and Kennedy, Donald A., "Formation of a trailing Vortex", *J. Aircraft*, Vol. 16, no. 3, pp. 148-154, 1978.
- [1995] Funk, R.B., Komerath, N.M., "Rotor Wake Interaction with a Lifting Surface", *Proceedings of the American Helicopter Society Annual Forum*, Ft. Worth, TX, May 1995.
- [1961] all, M. G., "A Theory for the Core of a Leading Edge Vortex", *J. Fluid Mech*, Vol. 11, pp. 209-228, 1961
- [1948] Glauert, H., *The Elements of Aerofoil and Airscrew theory*, 2nd edition, Cambridge University Press, 1948.
- [1956] Gray, R. B., "An Aerodynamic Analysis of a Single-Bladed Rotor in Hovering and Low-Speed Forward Flight as Determination from Smoke Studies of the Vorticity Distribution in the Wake", Princeton University Aero. Engr. Dept., Report No. 356, September, 1956.

- [1991] Gray, R. B., "Vortex Modeling for Rotor Aerodynamics -The 1991 Alexander A. Nikolsky Lecture", *Journal of American Helicopter Society*, vol. 27, no. 1, pp. 3 - 14, 1992.
- [1995] Hariharan, N., PhD. Thesis, School of Aerospace Engineering, Georgia Institute of Technology, 1995.
- [1999] Hariharan, N. and Sanker, L. N., "First-Principles Based High Order Methodologies for Rotorcraft Flowfield Studies", *Proceedings of the 55th Annual Forum of the American Helicopter Society*, pp. 1921-1933, May, 1999.
- [1982] Head, M. R. In *Flow Visualization II*, W. Merzkirch, ed., pp. 399-403, Hemisphere, Washington, 1982. Also pg. 51 of *An Album of Fluid Motion*, M. Van Dyke, The Parabolic Press, Stanford, California.
- [1985] Hess, J. L. and Valarezo, W. O., "Calculation of Steady Flow About Propellers Using a Surface Panel Method", *Journal of Propulsions and Power*, vol.1, no. 6, 1985.
- [1992] Jain-Ming J. W., "On Controlling the Tip Vortex Flow of a Lifting Wing", Southern Conference on Theoretical and Applied Mechanics, April, 1992.
- [2000] Jain, R., Conlisk, A.T., "Interaction of Tip-Vortices in the Wake of a Two-Bladed Rotor in Axial Flight", *Journal of the American Helicopter Society*, no. 3, pp. 157-164, July 2000.
- [1977] James, C. B., Albert, L., Kenneth, L. O. and Opal, J. L., "Measurements of Helicopter Rotor Tip Vortices", *Proceedings of the 33th Annual Forum of the American Helicopter Society*, May, 1977.
- [1980] Johnson, W., *Helicopter Theory*, Princeton University Press, New Jersey, 1980.
- [1986] Katz, J. and Maskew, B., "Unsteady Low-Speed Aerodynamic Model for Complete Aircraft Configurations", AIAA, vol. 25, no. 4, 1986.
- [1991] Katz, J. and Plotkin, A., *Low - speed Aerodynamics: from Wing Theory to Panel Methods*, McGraw - Hill, 1991.

- [2002] Kini, S., Vishwanath, G. and Conlisk, A.T., "Comparison of Two Distinct Models of Rotor Wakes with Experiments", submitted to the 40th AIAA Aerospace Sciences Meeting and Exhibit, January, 2002.
- [1976] Kocurek, J. D. and Tangler, J. L., "A Prescribed Wake Lifting Surface Hover Performance Analysis", 32nd Annual Forum of the American Helicopter Society, May, 1976.
- [1991] Komerath, N.M., Liou, S-G., Hyun, J-S., "Flowfield of a Swept Blade Tip at High Pitch Angles", AIAA 91-0704, Meeting, Jan. 1991.
- [1990] Komerath, N.M., Liou, S.G., Thompson, T.L., "A Remote-Aligned Off-Axis Receiving System for Laser Velocimetry in Large Facilities", *Experimental Techniques*. vol. 14, no. 4, pp. 29-33, July, 1990.
- [1998] Komerath, N. M., Thompson, T. L., Kwon, O. J., and Gray, R. B., "The Velocity Field of a Lifting Model Rotor Blade in Hover". *Journal of Aircraft*, vol. 25, pp. 250 - 257, March, 1988.
- [1961] Kriebel, A.R., "Particle Trajectories in a Gas Centrifuge", *Journal of Basic Engineering*, vol. 83, no. 3, pp. 333-340, September 1961.
- [1932] Lamb, Sir Horace, *Hydrodynamics*, Cambridge University Press, 6th Edition, pp. 592-593, 668-669, 1932.
- [1932] Lamb, Sir Horace, *Hydrodynamics*, Cambridge University Press, 6th Edition, 1932.
- [1991] Lanchester, F. W., *Aerodynamics*, quoted in Anderson, J.D., *Fundamentals of Aerodynamics*, Fig. 5.42, pp. 366, 2nd Edition, McGraw-Hill, 1991.
- [1972] Landgrebe, A. J., "The Wake Geometry of a Hovering Helicopter Rotor and Its Influence on Rotor Performance", *Journal of the American Helicopter Society*, vol. 17, no. 4, pp. 2-15, October, 1972.
- [1995] Leishman, J. G., Baker, A. and Coyne, A., "Measurements of Rotor Tip Vortices", *Journal of the American Helicopter Society*, vol. 41, no. 4, pp. 342-353, October, 1996.

- [1995] Leishman, J.G., Baker, A., Coyne, A., "Measurement of Rotor Tip Vortices Using Three-Component Laser Doppler Velocimetry", AHS Aeromechanics Specialists Conference, Oct. 1995.
- [1996] Leishman, J.G., "Seed Particle Dynamics in Tip Vortex Flows", *Journal of Aircraft*, vol. 33, no. 4, pp. 823-825, July-August 1996.
- [1988] Liou, S.G., "Velocity Measurements on a Lifting Rotor/Airframe Configuration in Low Speed Forward Flight", PhD Thesis Georgia Institute of Technology, 1988.
- [1989] Liou, S.G., Komerath, N.M., and McMahon, H.M., "Velocity Measurements of Airframe Effects on a Rotor in Low-Speed Forward Flight", *Journal of Aircraft*, vol. 26, no. 4, pp. 340 - 348, April 1989.
- [1990] Liou, S.G., Komerath, N.M., McMahon, H.M., "The Velocity Field of a Circular Cylinder in the Wake of a Rotor in Forward Flight", *Journal of Aircraft*, vol. 27, no. 9, pp. 804-809, Sep. 1990.
- [1990] Liou, S.G., Komerath, N.M., and McMahon, H.M., "Measurement of Transient Vortex-Surface Interaction Phenomena", *AIAA Journal*, vol. 28, no. 6, pp. 975-981, June 1990.
- [1964] Mager, Artur 1964 "Three-Dimensional Laminar Boundary Layers", Theory of Laminar Flows, Section C, High Speed Aerodynamics and Jet Propulsion, Vol. 4, Princeton.
- [1996] Mahalingam, R. and Komerath, N. M., "Rotor Tip Vortex/Airframe Collision Effects on the Vortex and Airframe", AIAA 96-2013, June, 1996.
- [1998] Mahalingam, R., Komerath, N.M., "Measurements of the Near Wake of a Rotor in Forward Flight", AIAA 98-0692, January 1998.
- [1998] Mahalingam, R., Komerath, N.M., "Characterization of the Near Wake of a Helicopter", AIAA 98-2909, Fluid Dynamics Conference, June 1998.
- [2000] Mahalingam, R., Wong, O.D., Komerath, N.M., "Experiments on the Origins of Tip-Vortices", AIAA Paper 2000-0278, Reno, NV, January 2000.

- [1998] Mahalingam, Raghav, Private Communication, 1998.
- [1991] McAlister, K. W., and Takahashi, R. K., "NACA 0015 Wing Pressure and Trailing Vortex Measurements", NASA Technical Paper 3151, AVSCOM Technical Report 91-A-003, 1991.
- [1995] McAlister, K. W., Schuler, C. A., Branum, L., and Wu, J. C., "3-D Measurements Near a Hovering Rotor for Determining Profile and Induced Drag", NASA TP 3577, August, 1995.
- [1996] McAlister, K. W., "Measurements in the Near Wake of a Hovering Rotor", AIAA 96-1958, June, 1996.
- [2001] McAlister, K., Tung, C., and Heineck, J.T., "Devices that Alter the Tip Vortex of a Rotor," NASA/TM-2001-209625, AFDD/TR-01-A-003, 2001.
- [1968] McCormick, B. W., Tangler, J. L., and Sherrier, H. E., "Structure of Trailing Vortices", *Journal of Aircraft*, vol. 5, no. 3, pp. 260-267, 1968.
- [1968] McCroskey, W.J. and Yaggy, P.F. 1968 "Laminar Boundary Layers on Helicopter Rotors in Forward Flight", *AIAA J.*, Vol. 6, no. 10, pp. 1919-1926.
- [1982] Miller, R. H., "Application of Fast Free Wake Analysis Techniques to Rotors", *Vertica*, vol. 8, no. 3, pp. 255-261, 1984.
- [1973] Moore, D. W. and Saffman, P. G., "Axial Flow in Trailing Line Vortices", *Proc. Roy. Soc. A*, vol. 333, pp. 491-508, 1973.
- [2001] Orangi, S., Foster, M. R. and Bodonyi, R. J., "On the Structure of a Three-Dimensional Compressible Vortex", *Computers and Fluids*, vol. 30, pp. 115-135, 2001.
- [1983] Osama, A. K., Li-Chuan C. and Thomas, T., "A Nolinear Hybrid Vortex Method for Wings at Large Angle of Attack", AIAA 82-0351, March, 1983.
- [2000] Radcliff, T. D., Burggraf, O. R. and Conlisk, A. T., "On the Three-Dimensional Interaction of a Rotor-Tip Vortex with a Cylindrical Surface", under consideration for publication in *Journal of Fluid Mechanics*, 2000.

- [1999] Reddy, U. C., "Whole Field Velocity Measurements in Three-Dimensional Periodic Flows", PhD. Thesis, Georgia Institute of Technology, Atlanta, GA, 1999.
- [1991] Roger, C. S., "Wing Tip Vortex Calculation with an Unstructured Adaptive-Grid Euler Solver", 47th Annual Forum of the American Helicopter Society, May, 1991.
- [1996] Rule, J. and Bliss, D., "Prediction of Turbulent Trailing Vortex Structure from Basic Loading Parameters", AIAA 96-2495, June 1996.
- [1992] Saffman, P. G., *Vortex Dynamics*, Cambridge University Press, 1st Edition, 1992.
- [1947] Schlichting, H., and Thomas, H. H. B. M., "Note on the calculation of lift distribution of swept wings", Royal Aircraft Establishment Rpt., No. Aero. 2236, 1947.
- [1975] Scully, M. P., "Computation of Helicopter Wake Geometry and its Influence of Rotor Harmonic Airloads", MIT Report ASR:TR178-1, 1975.
- [1948] Sears, W.R. 1948 "The Boundary Layer of Yawed Cylinders", *J. Aero. Sci.*, Vol. 15, no. 1, pp. 49-52, 1948.
- [1980] Shenoy, K. R. and Gray, R. B., "Iterative Lifting Surface Method for Thick Bladed Hovering Helicopter Rotors", *Journal of Aircraft*, vol. 18, no. 6, June, 1981.
- [1978] Shivananda, T.P., McMahon, H. M., and Gray, R. B., "Surface Pressure Measurements at the Tip of a Model Helicopter Rotor in Hover", *Journal of Aircraft*, vol. 15, no. 8, pp. 460-467, 1978.
- [1993] Srinivasan, G. R., Raghavan, V., Duque, E. P. N. and McCroskey, W. J., "Flowfield Analysis of Modern Helicopter Rotors in Hover by Navier-Stokes Method", *Journal of the American Helicopter Society*, vol. 38, no. 3, pp. 3-13, 1993.
- [1960] Stewartson, K., "A Note On Lifting Line Theory", *Quart., Journ. Mech. and Applied Math.*, vol. XIII, pt. 1, 1960.

- [1976] Suciu, E. O. and Morino, L., "A Nonlinear Finite Element Analysis of Wings in Steady Incompressible Flows with Wake Rollup", AIAA 76-74, 1976.
- [1953] Tan, H.S. 1953 "On Laminar Boundary Layer over a Rotating Blade", *J. Aero. Sci.*, Vol. 20, pp. 780-781, 1953.
- [1999] Tang, L. and Baeder, J. D., "Improved Euler Simulation of Hovering Rotor Tip Vortices with Validation", *Proceedings of the 55th Annual Forum of the American Helicopter Society*, pp. 1934-1941, May, 1999.
- [1988] Thompson, T.L., Komerath, N.M., and Gray, R.B., "Visualization and Measurement of the Tip Vortex Core of a Rotor Blade in Hover", *Journal of Aircraft*, vol. 25, no. 12, pp. 1113 - 21, December, 1988.
- [1983] Tung, C., Pucci, S. L., Caradonna, F. X. and Morse, H. A., "The Structure of Trailing Vortices Generated by Model Helicopter Rotor Blades", *Vertical*, vol. 7, no. 1, pp. 33-43, 1983.
- [1994] Tung, C. and Lee, S., "Evaluation of Hover Prediction Codes", *Proceedings of the 50th Annual Forum of the American Helicopter Society*, pp. 829-844, May, 1994.
- [1996] Tung, C., Yu, Y. and Low, S., "The Aerodynamic Aspect of Blade/Vortex Interaction", AIAA 96-2010, June, 1996.
- [1964] Van Dyke, M., "Lifting-Line Theory As a Singular Perturbation Problem." *Arch. Mech. Stos*, vol. 16, no. 3, pp. 173, 1964.
- [1975] Van Dyke, M., *Perturbation Methods in Fluid Mechanics*, Annotated Edition, Parabolic Press, 1975.
- [1991] Vatistas, G. H., Kozel, V. and Mih, W. C., "A Simpler Model for Concentrated Vortices", *Experiments in Fluids*, vol. 11, pp. 73-76, 1991.
- [2000] Wong, O., Mahalingam, R., Tongchitpakdee, C. and Komerath, N. M., "The Near Wake of a 2-Bladed Rotor in Forward Flight", AHS Aeromechanics Specialist Meeting, Atlanta, Georgia, Nov 13-14, 2000.
- [1994] Xiao, Z., Affes, H., and Conlisk, A. T., "The Boundary Layer Flow due to a Vortex Approaching a Cylinder", *J. Fluid Mech.*, vol. 275, pp. 33-58, 1994.

- [1985] Yeh, D. T. and Plotkin, A., "Vortex Panel Calculation of Wake Rollup Behind a Large Aspect Ratio Wing", AIAA 85-1561, December, 1985.